The reducibility of mixed Mo/V oxide materials to carbides and their reactivity in the activation of propane

vorgelegt von
BSc.(Hons) Chemiker
Thomas Cotter
aus Christchurch (Neuseeland)

Von der Fakultät II - Mathematik und Naturwissenschaften
der Technischen Universität Berlin
zur Erlangung des akademischen Grades
Doktor der Naturwissenschaften
Dr.rer.nat.

genehmigte Dissertation

Promotionsausschuss:

Vorsitzender: Prof. Dr. Arne Thomas
Berichter/Gutachter: Prof. Dr. Reinhard Schomäcker
Berichter/Gutachter: Prof. Dr.Robert Schlögl
Berichter/Gutachter: Prof. Dr.Klaus Christmann

Tag der wissenschaftlichen Aussprache: 19. August 2011

Berlin 2011

D 83

“There is nothing like looking, if you want to find something…

You certainly usually find something if you look, but it is not always quite the something you were after.”

– *Thorin (The Hobbit)*

Preface and Acknowledgments

The work presented in this thesis was carried out from July 2007 to June 2011 at the Department of Inorganic Chemistry at the Fritz Haber Institute in Berlin. Herein I would like to give thanks to the numerous people who have made it a pleasure to work here as well as to those people who have supported me in my studies.

First and foremost I would like to thank Professor Dr. Robert Schlögl for giving me the opportunity to carry out my studies at this wonderful institution, imbued with such a deep sense of history and academic excellence. Your energy and capacious intellect has strongly influenced my thinking and I am indebted to you. I would also like to thank my supervisor, Dr. Annette Trunschke, for her kind and unwavering support over the last four years, guiding me to the endpoint while allowing me to explore interesting topics along the way.

In the organization and defense of my thesis at the Technical University of Berlin I would like to especially thank Professor Dr. Reinhard Schomäcker for taking me on as an external student. In addition I am very grateful to Professor Dr. Klaus Christmann of the Freie University and Professor Dr. Arne Thomas of the Technical University for agreeing to be part of my examining committee.

Without the help of a number of people this thesis would not have been possible. For their help with regards to measurements, advice and technical assistance I would like to acknowledge the following people (in no particular order); Gisela Lorenz, Raoul Naumann, Daniel Brennecke, Doreen Steffen, Gisela Weinberg, Wei Zhang, Manfred Schuster, Almudena Celaya, Edith Kitzelmann, Frank Girgsdies, Andrey Tarasov, Olaf Timpe, Malte Behrens, Yury Kolen'ko, Kazuhiko Amakawa, Maike Hashagen, Jean-Phillippe Tessonier, Ed Kunkes, Lénárd-Istvan Csepei, and Siegfried Engelschalt. A special thank you goes out to Manfred Schuster who donated a lot of his time for the acquisition and analysis of microscopy data presented here.

For their help in writing and correcting this dissertation I owe a debt of gratitude to my sister Rosie Cotter for correcting the entire thesis for grammar. I would also like to thank Maricruz Sanchez, Kazuhiko Amakawa and Andrey Tarasov for correcting individual chapters for content.

For their support and interesting discussion I would like to acknowledge the members of the Reactivity group and the AC department, and additionally Yury, Till and Peter for their friendship early on and for helping me to settle in a new city. I would like to thank my flatmates, Tallulah and Veronica (the ‘Neukölln Princesses’), for their good humour for the last two years and I especially thank my girlfriend Maricruz for her love, support and consideration over the last 12 months.

Finally I would like to thank my parents for their unceasing encouragement and belief in me. You inspire me to always look for the best in life and I owe everything that I have and that I am to you.

To my parents

Eidesstattliche Versicherung

Hiermit erkläre ich, dass ich die Dissertation selbst angefertigt habe. Die Arbeit enthält– auch in Anteilen – keine Kopien andere Arbeiten. Verwendete Hilfsmittel und Quellen sind vollständig angegeben. Die Namen alle Wissenschaftler die mit mir zusammengearbeiten haben, sind in den Anlagen vollständig genannt.

Abstract:

A series of mixed Mo/V oxide materials was treated under varying carbon-rich, reducing conditions in order to model conditions found when high-performance multi-metal oxide catalysts are operated at high conversion in selective oxidation reactions. The objectives were twofold: to better understand the mechanism of reduction-carburisation in the bimetallic oxide system, and to determine the influence of chemical composition and oxidation state on the reactivity in propane activation.

Bimetallic carbides of the form $(Mo_{1-x}V_x)_2C$ were synthesised by carbothermal reduction of the corresponding *h*-$Mo_{1-x}V_xO_3$ oxide precursors. The reduction was followed by *in situ* X-ray diffraction and the mechanism was investigated using solid-state kinetic modeling techniques. The reactivity of the resultant carbides for the catalytic dehydrogenation of propane was measured under various conditions including CO_2- and H_2O-containing feeds. To probe the surface structure-activity relationships, *in situ* reaction methods were applied as characterisation tools in addition to the standard structural and surface analysis techniques.

The kinetic and structural analysis of carbothermal reduction revealed a strong stabilising influence of the vanadium dopant via modification of the oxygen mobility in the lattice. With respect to the catalytic dehydrogenation of propane, it was observed that vanadium doping increased the initial conversion of propane but decreased selectivity to propylene. In soft-oxidative feeds (CO_2, H_2O) the carbide surface is oxidised, promoting the dehydrogenation reaction. Notably, Mo_2C is an excellent catalyst for the hydrogenation of CO_2 via reverse water-gas-shift reaction. *In situ* XPS experiments correlate propane dehydrogenation activity with an oxycarbide surface modification and alkyl-recombinative products are observed in concert with clear changes in the valence band spectra. Post-mortem analyses of the catalysts by transmission electron microscopy reveal significant surface and bulk restructuring as well as the recrystallisation of metastable phases and inhomogeneous bloating of the structure by aliphatic carbon.

Vanadium is proposed to exert a stabilising influence due to its strongly oxophilic nature, resulting in the formation of V=O moieties which kinetically hinder the mobility of oxygen and carbon through the oxide/carbide lattice. The resulting higher initial activity for propane activation is attributed to the increased activity of sites selective to hydrogenolysis. Hexagonal $(Mo/V)_2C$ is proposed to be a reasonable model for bronze-like multi-metal oxide catalysts in propane activation due to the recrystallisation of the metastable fcc carbide structure observed under reaction conditions.

The reducibility of mixed Mo/V oxide materials to carbides and their reactivity in the activation of propane

vorgelegt von Thomas Cotter

Zusammenfassung

Der Effekt von Vanadium auf die chemische Beständigkeit und Reaktivität von Molybdänoxid-basierten Hochleistungskatalysatoren, die in Selektivoxidationen unter hohem Umsatz gefahren werden, wurde an einer Serie von gemischten Mo/V Oxidmaterialien modelliert.
Dabei standen folgende Fragen im Mittelpunkt des Interesses:

1. Nach welchem Mechanismus verläuft die Carbidbildung?
2. Welchen Einfluss hat die chemische Zusammensetzung des gebildeten Carbids auf die Aktivierung von Propan an seiner Oberfläche?

Bimetallische Carbide der Form $(Mo_{1-x}V_x)_2C$ wurden durch carbothermische Reduktion der entsprechenden oxidischen Vorstufen der allgemeinen Zusammensetzung *h*-$Mo_{1-x}V_xO_3$ synthetisiert. Die Reduktion wurde mittels in situ Röntgenbeugung verfolgt und der Mechanismus wurde unter Heranziehung festkörperkinetischer Modelle studiert. Die Reaktivität der erhaltenen Carbide in der katalytischen Dehydrierung von Propan wurde unter verschiedenen Bedingungen, unter anderem auch in Gegenwart von eingespeistem CO_2 und H_2O-Dampf, getestet. Neben herkömmlichen Struktur- und Oberflächenanalysemethoden, wurden zur Aufklärung von Struktur-Reaktivitätsbeziehungen auch oberflächensensitive in-situ Methoden zur Charakterisierung der Katalysatoren unter Reaktionsbedingungen verwendet.
Die kinetische und strukturelle Analyse der carbothermischen Reduktion zeigte einen starken stabilisierenden Effekt der Vanadiumdotierung, die auf eine Veränderung der Sauerstoffmobilität im Kristallgitter zurückzuführen ist.
In der katalytischen Dehydrierung von Propan konnte beobachtet werden, dass die Vanadiumdotierung den anfänglichen Umsatz von Propan erhöht aber die Selektivität zu Propen reduziert.
In leicht-oxidierender Umgebung (CO_2, H_2O) wird die Carbidoberfläche oxidiert, was die Dehydrierungsreaktion fördert. Mo_2C ist ein hervorragender Katalysator für die Hydrierung von CO_2 in der umgekehrten Wassergasreaktion.
In situ XPS Experimente zeigen, dass die Aktivität in der Dehydrierung von Propan mit der Umwandlung in eine Oxicarbidoberfläche korreliert und dass Hochtemperatur-Metathese-Produkte gemeinsam mit signifikanten Veränderungen in den Valenzbandspektren beobachtet werden. Die hohe Anfangsaktivität wird der erhöhten Aktivität von carbidischen Zentren für die Hydrogenolyse des Propans zugeschrieben.
Die Untersuchung der gebrauchten Katalysatoren durch Transmissionselektronenmikroskopie macht signifikante Oberflächen- und Volumen-Restrukturierungen sowie eine Rekristallisation der metastabilen Phasen und eine Bildung inhomogener, blasenartiger Strukturen durch den aliphatischen Kohlenstoff deutlich.
Es wird vorgeschlagen, dass Vanadium aufgrund seiner stärkeren „oxophilen“ Natur als Stabilisator wirkt, indem die Bildung von V=O Gruppen die Mobilität des Kohlenstoffs und Sauerstoffs durch das Oxid/Karbid Gitter kinetisch hemmt.

Table of Contents

Chapter 1: Introduction and Overview

1.1 Introduction

The catalytic properties of a given material depend upon the chemical and physical nature of the surface as well as the chemical environment and temperature. These conditions determine the dynamic nature of the catalyst surface and control the subsequent; adsorption, bond-breaking, diffusion and bond-forming processes. The interplay of thermodynamic and kinetic processes at the nanoscale can mean that the activity of a single catalytic site for an undesired pathway exceeds that of the desired pathway by many orders of magnitude. The implications of this are such that the consideration of all possible surface species must be taken into account when modeling the kinetics of a reaction, and that small inhomogeneities in the chemical potential of a system may lead to measurable differences in reactivity.

The selective or partial oxidation of light hydrocarbons is an increasingly important field in industrial heterogeneous catalysis, and molybdenum and vanadium-based oxide materials have long been recognised as key components owing to their manifold structural and electronic complexity.[1, 2] Oxydehydrogenation and partial oxidation reactions already play an important role in this emerging chemical economy.[1] On an industrial scale at high conversions these catalysts are subject to a wide range of conditions which can vary considerably in chemical potential and composition as well as temperature.[3] From an extensive body of research it is recognised that these influences control the oxidation state at the surface and subsequently the phase composition of the catalyst active surface.[4, 5]

In Table 1.1 the partial and total oxidation reactions for propane and butane are listed along with their enthalpies of formation and the adiabatic temperature change in the reaction mixture. In the oxidation reactions of these two alkanes it can be seen that even the selective (dehydrogenation) pathway is highly exothermic and results in a considerable adiabatic temperature rise. This generated heat energy serves to greatly increase the local temperature and greatly decrease the oxygen concentration over an atomic area scale. Locally, the conditions are vastly different from that observed for the integrated bulk of the catalyst. Subsequently it can be expected that the catalyst surface responds dynamically by means of electron exchange and potentially atomic

rearrangement as well. On a mesoscopic scale, this phenomenon is referred to as 'hot spot' formation.

Table 1.1: Partial and total oxidation reactions of propane and butane with enthalpy and adiabatic temperature change.

Reaction	$\Delta H°$, kJ/mol	ΔT_{ad}, °C
$C_3H_8 + ½O_2 \rightarrow C_3H_6 + H_2O$	-117	1000
$C_3H_8 + 1½O_2 \rightarrow 3CO + 4H_2$	-226	900
$C_3H_8 + 5O_2 \rightarrow 3CO_2 + 4H_2O$	-2050	2800
$C_4H_{10} + ½O_2 \rightarrow C_4H_8 + H_2O$	-117	800
$C_4H_{10} + 2O_2 \rightarrow 4CO + 5H_2$	-569	1700
$C_4H_{10} + 6½O_2 \rightarrow 4CO_2 + 5H_2O$	-2636	2700

In the case of partial oxidation reactions, it can be expected that the chemical potential over local areas will average out and hypoxic areas will be rapidly reoxidised upon the introduction of oxygen, however, this is not necessarily the case. In any plug-flow gas reactor there is necessarily a gradient of chemical potential ranging from the inlet conditions to outlet conditions, which may be at complete oxygen conversion and at high concentrations of product gases.

It is demonstrated in literature regarding partial oxidation reactions that conversion of oxygen in fixed bed reactors results in a strongly varying profile of reactive atmosphere along the direction of gas flow.[6, 7] Under conditions of total oxygen consumption it is evident that the gas potential of the atmosphere will become reducing, however, this phenomenon is widely ignored in studies which cite partial oxygen conversion in order to remain in a regime whereby the reaction kinetics may be analysed by conventional means. Several studies by Sinev and others, however, point to the persistent presence of hydrogen (not commonly measured in catalytic studies) in reactions in which only partial conversion of oxygen is demonstrated.[8-10] These studies as well as others suggest that the conventional kinetic models which integrate over the entire reactor do not account for all observed species in these reactions. On a mesoscopic scale, highly exothermic total oxidation reactions in the often rich mixtures applied may hypothetically result in the generation of transient

and dynamic pockets of reduced surface species which are easily reoxidised upon cooldown and are also not evident spectroscopically.

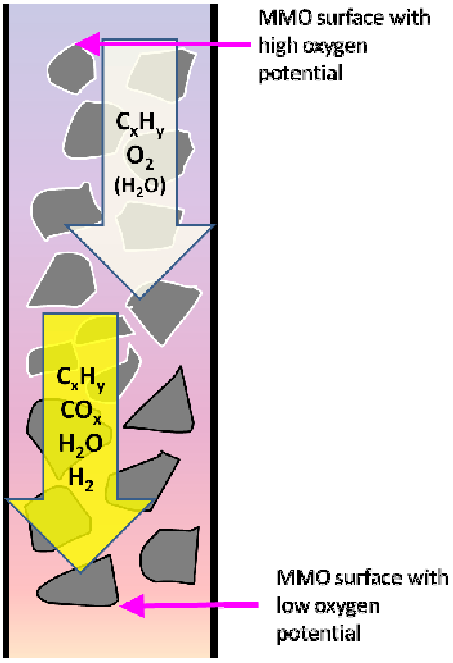

Figure 1.1: Schematic diagram of a partial oxidation reactor at high conversion.

Vanadium substituted molybdenum carbide (α-Mo_2C) is chosen as a model for a highly reduced catalyst for the reasons that molybdenum and vanadium are widely found as a components in oxidation catalysts, such as Mo_5O_{14}-type catalysts for acrolein oxidation, and more recently the novel class of $MoVNbTeO_x$ materials for the partial oxidation of propane to acrylic acid.[11, 12] Furthermore, because the chemistry of Mo_2C is now widely studied there exist a number of studies detailing the synthesis and structural characterization of such materials.[13-15]

1.2 Preface

The partial oxidation of paraffins to industrially useful oxygenates has been studied intensively over the last twenty-five years.[16] A number of industrially important advances have been made in this field but most still rely on alkene feedstocks which are generally derived from non-renewable petrochemical resources. A currently applied and industrially important reaction in this class is the partial (amm)oxidation of propene to acrylic acid and acrylonitrile. To meet the growing demands for such materials, more readily available and renewable feedstocks must be considered.

Development of catalytic systems for the direct oxyfunctionalisation of propane to acrylic acid is therefore an important step in the progression of this field.

With respect to the selective oxidation of light alkanes over reducible oxides (i.e. Mo, V), there are a number of mechanisms and pathways proposed in the literature. However, it is generally agreed that first step of oxyfunctionalisation is the oxidative dehydrogenation of the substrate alkane.[1] For example, in the case of the selective oxidation of propane to acrylic acid, propane is initially dehydrogenated and the propene reacts further to the oxygenated product, in this case acrylic acid.

$$C_3H_8 \rightarrow C_3H_6 \rightarrow C_3H_4O_2$$

However, for considering a simplified surface redox chemistry in such reactions we may consider the initial oxidative dehydrogenation (ODH) alone. The efficient ODH of light alkanes has long been a goal of researchers and industry and as a result many potential catalysts for this process are being explored. The catalysts currently being developed with the goal of industrialization can be divided into two categories: [1,17, 18]

- Redox catalysts based on oxides of transition metals such as: Mo, V, W. These are active at relatively low temperatures (350-400°C)
- Non-redox metal oxide catalysts such as alkaline-earth and rare-earth oxides (also B, Sn, and Si). Generally active at temperatures above 500°C

For the ODH of propane, Mo/V-based oxides are most commonly used and indeed MoVTe catalysts are high performing materials for the ODH of propane under the appropriate conditions.[19] In the case of ODH of propane to propene, the overall reaction can be characterised by the following general steps which have been surmised from previous studies.[18]

1. Propane adsorption/interaction with the catalyst surface
2. Scission of the methylene C-H bond resulting in an isopropyllic radical species
3. Reaction of a methyl C-H bond with a neighbouring oxygen atom resulting in β-elimination and the formation of a C=C bond
4. Desorption of propene
5. Elimination of H_2O from the catalyst surface resulting in an oxygen vacancy
6. Reoxidation of the catalyst surface

The general steps outlined above, along with the diffusion of educts and products to and from from the catalytic site make up the basis of our understanding of these reaction processes and allow us with an extension of theory to develop appropriate rate equations and kinetic models for the oxidative dehydrogenation (ODH) of light alkanes.

There are five commonly cited kinetic models which are used to describe the kinetics of light alkane ODH: a) Eley-Rideal (ER) model; b) Langmuir-Hinshelwood (LH) model; c) The 'rake' model; d) Mars Van Krevelen (MVK) or redox model and; e) the power law model. Of these models, the first two (ER, LH) involve the direct reaction of oxygen with the adsorbed alkane either on the surface (LH), or from oxygen in the gas phase (ER). These models are largely discounted because they involve the direct reaction of oxygen with the alkane or the activation of oxygen on the surface to form a peroxide species, the first of which is spin-prohibited while the second is indicated to result in deep oxidation.[20, 21] Of the remaining models, the 'rake' model and the power law models are purely phenomenological approaches to describe the rates of reaction and can be used to determine rate constants for theoretical reactions steps in the absence of a true mechanistic model.

The remaining model which is very commonly applied in the case of selective oxidation over reducible metal oxide catalysts[22] is the Mars Van Krevelen model, sometimes referred to as the redox model.[23] This approach makes the assumption that the oxygen of reaction is derived from the lattice and that the subsequently reduced surface is reoxidised by oxygen which is adsorbed in the vicinity of the reduced site. The concerted action of the catalyst surface is such that in a steady state:

$$rate\ of\ O_2\ adsorption = rate\ of\ surface\ reduction$$

This model is claimed to be supported by studies for various catalyst systems[24, 25] but it does not provide a complete understanding of the mechanism of reoxidation and is frequently cited without strong evidence. Further to this, the model can be criticised for failing to describe elementary steps adequately. Dioxygen must be adsorbed on the surface and activated before it dissociates and is incorporated into the vacancies of the solid.

The process must also be reversible, allowing the oxygen to diffuse out of the surface and react with adsorbed gaseous species. In some catalytic studies it is purportedly shown, by isotopic labeling and transient analysis of products, that the redox vacancies may be replenished from the oxygen in the bulk of the catalyst.[24, 26, 27] This is contrary to the assumption of a direct reoxidation of the surface vacancy and there appear to be disagreement as to the validity of this mechanism in some selective oxidation reactions which is as yet unresolved.[28, 29]

It has been observed that the surface of the well-studied $MoVTeNbO_x$ catalyst is dynamic and changes under reaction conditions to give the active surface.[30] In general the complexity of the material has defied attempts to elucidate the catalytic mechanism however it is widely believed that the redox chemistry of vanadium is the key to its performance. In the standard models of propane selective oxidation over transition metal oxides there are commonly discussed mechanisms for the formation of propylene, acetone, acrolein, acrylic acid and 'CO_x'. However the C_2 oxygenate, acetic acid, is commonly the second most abundant oxygenate and under certain condition maleic anhydride may be observed in the outlet gas.[19, 31, 32] There is no commonly accepted mechanism to account for this C-C bond breaking and formation. Further to this, the balance of CO/CO_2 in the outlet gas of such catalyst systems freqently favours CO despite strongly oxidising conditions. It is hereby proposed that there may be other contributing phases or sites (possibly micro-crystalline or amorphous) that participate in these catalytic reactions. A possibility exists that carbides or nitrides formed during preparation (from NH_4^+), or under reaction conditions (C_3H_8), may contribute to the overall activity of the catalyst.[9]

Metal carbides are well known to undergo facile surface oxidation[33-37] and molybdenum carbide has been explored as a potential catalyst in a number of hydrocarbon transformation reactions.[38-43] Mo_2C may therefore provide a non-oxidic support material by which we can understand not only aspects of the surface reactivity of complex oxides in reduced/carburised states, but also draw some conclusions regarding oxygen mobility in the oxide lattice as we study the formation of these materials and their catalytic activity in conditions relevant to selective oxidation catalysis.

1.3 Aims of this work and thesis structure

The overall goal of this project is to develop an understanding of the reduction/carburisation process with respect to Mo-based multi-metal oxide (MMO) catalysts used in alkane and alkene selective oxidation processes. Of particular interest is the catalyst class of MoVTe oxides used for the partial oxidation of propane to acrylic acid. By generating a simplified model for the MoVTe catalyst it can subsequently be studied in the TPR-carburisation and for reactivity of the reduced system in the activation of propane. To simplify this goal it may be broken down into parts:

- To synthesise a series of well-defined mixed-metal oxide precursors for carburisation
- Characterise the precursors and understand the carburisation process with respect to the dopant element
- Prepare the model carbide system in sufficient quantities for characterisation and catalytic testing
- Design and construct an apparatus for the catalytic testing of the carbides
- Test the catalytic properties of the series of catalysts and gain an insight into the nature and influence of the secondary metal constituent
- Characterise the catalysts using *in situ* techniques to gain a mechanistic understanding of the catalytic properties with relation to those observed for the functioning MoVTe system

In order to address this broad thesis, the realisation of the above goals is described over three chapters with each chapter constructed as a self-contained story; containing: introduction, literature review, methods, results, discussion and conclusions. The structure is as follows:

Chapter Two — The synthesis of mixed Mo-V carbides is a study of the reduction-carburisation of mixed Mo/V oxides. The experimental section describes the synthesis and characterisation of molybdenum carbide materials as well as the measurement of kinetic data with regards to the reduction-carburisation. Structural and mechanistic aspects of the reactions are discussed with reference to the solid-state kinetics.

Chapter Three — Reactivity of propane over Mo/V carbide I: Catalytic reactivity and temperature programmed studies is concerned with the measurement and analysis of the catalytic properties of molybdenum carbide materials in the activation of propane. The various reaction pathways are discussed with respect to the changing dynamics of the surface and also the influence of differing feed compositions. This chapter is also tied to Chapter Two by a series *in situ* oxide carburisation experiments (temperature-programmed reactions) which explore the simultaneous activation of propane and carburisation of the model oxide material.

Chapter Four — Reactivity of propane over Mo/V carbide II: Surface reactivity studies and post-catalytic characterisation seeks to connect the observed reactivity of the Mo/V materials with a picture of the surface and bulk chemistry and also electronic structure. The final chapter is connected to Chapters 2 & 3 by the discussion of alkane activation and post-mortem characterisation of the carbides and oxides after high temperature reaction in propane environments.

Chapter Five — Summary and Conclusions gives a brief synopsis of each chapter's results followed by a summary of the combined findings and the conclusions that can be drawn from this work.

Although finding relevant connection to the multi-metallic oxide MoVTe is a motivation of this thesis, it must be stressed here that it is not a goal of this work to definitively prove the existence of a carbidic overlayer in such materials. Nor is it to explore the reactivity of the MoVTe system. The two primary goals of this thesis are principally to: discuss the mechanistic aspects of carbide formation in the aforementioned Mo/V oxides and thereby relate the influence of carbon potential and chemical complexity to such oxidic materials. Secondly, it is to determine the reactivity of these reduced carbidic systems with respect to alkane activation in conditions which bear some relevance to selective oxidation catalysis. To achieve these goals and develop a less ambiguous understanding of the surface processes has frequently required the use of conditions more forcing than those found in oxidation catalysis. It is stressed that these conditions are chosen purely because they reflect and preserve the extremes of chemical potential which may be found in the boundaries of the reaction.

1.4 Introduction to early transition metal carbides

Early transition metal carbides have been shown to have promising catalytic properties in a number of hydrocarbon transformation reactions.[44, 45] Since Levy and Boudart first demonstrated the Pt-like catalytic properties of WC,[46] there has been increasing interest in these materials as substitutes for noble metals in industrial catalytic reactions. The progress of this research has been primarily driven by innovation in the synthesis of such carbides and nitrides, allowing researchers to make materials with reproducible physical properties and chemical compositions. Formerly, transition metal carbides were formed only at very high temperatures by direct combination of the component elements. This inevitably produces materials with low surface area, as the temperatures involved generally lead to extensive sintering, and relatively high levels of carbon impurity. Lee *et al.* successfully developed a temperature programmed reduction (TPR) method[47] that allowed for carbide and nitride materials of appreciably high surface area to be formed under a wide range of conditions. Many catalytic studies since have made use of this technique to synthesise transition metal (TM) carbides and nitrides material. More recently, a number of groups have made group V and VI carbides via the high-temperature decomposition of various solution-based precursors.[48-50] This technique looks to be promising because the precursor solutions provide a definite stoichiometry which can be manipulated before treatment. Also, there is potential for the facile synthesis of mixed metal precursors.[51-57] Various other synthetic techniques include; chemical vapour deposition,[58, 59] organometallic-based syntheses,[60] and solid state substitutions.[61]

The reactions of light hydrocarbons over group V and VI TM carbides are highly varied and the reported catalytic activities include; Fischer-Tropsch chemistry,[62] isomerisation,[44, 63] hydrodesulfurisation (HDS),[39, 53, 64, 65] hydrodenitrogenation (HDN),[54, 66] hydrogenolysis,[67, 68] oxidative dehydrogenation,[69, 70] hydrogenation,[71] methane reforming,[72-74] and dehydroaromatisation.[75-77] The catalytic activity of carbides in some cases exceeds that of the noble metals and they have been shown to be resistant to poisoning by reaction byproducts such as carbon and sulfur.[78-80]

In contrast to industrially produced carbides which are relatively inert, high surface area TM carbides are reactive to oxygen and must be passivated to prevent extensive oxidation. Numerous studies have been carried out probing the active surfaces and the

conditions under which they are formed but it seems to be consensus that excess carbon must be removed to fully activate the catalyst and that oxidation of the carbide surface dramatically reduces catalytic activity in many cases.

The use of characterisation techniques for transition metal carbides is relatively limited in the literature, perhaps owing to the fact that the unsupported material is opaque to many spectroscopic techniques. X-ray diffraction (XRD) is widely used as a tool to confirm the bulk composition in many papers and its use *in situ* is discussed. X-ray absorption fine structure (XAFS) can be very useful in confirming the extent of reaction throughout the solid and it is discussed with regards to supported and unsupported materials. Other bulk analyses include the use of differential thermal analysis (DTA), usually in conjunction with thermogravimetry (TG) and mass spectroscopy (MS). These techniques may be used *in situ* during the carburisation reaction or in various oxidative tests. Further methods primarily involve probing the surface composition and structure using spectroscopic techniques such as: X-ray photoelectron spectroscopy (XPS), UV, Raman, diffuse reflectance infrared Fourier transform spectroscopy (DRIFTS), and reflection absorption infrared spectroscopy (RAIRS). Some of these techniques commonly make use of the adsorption of small probe molecules in order to titrate/investigate the active sites on the catalyst surface.

1.5 Structure of molybdenum carbide

Early transition metals of the groups; IVa (Ti, Zr, Hf), Va (V, Nb, Ta), VIa (Cr, Mo, W), VIIa (Mn), and VIII (Fe, Co, Ni) all react under certain conditions to form stable carbides.[81] These materials have been investigated thoroughly due to their unique physical properties and the role which they play in the field of metallurgy. More recently this has role has grown to include phenomena such as superconductivity and catalysis. These binary compounds are often termed ‘refractory materials’ and in general such transition metal carbides are known for their:

i. Extreme hardness/brittleness
ii. High melting points
iii. Good electrical and thermal conductivities

The first two features, i. and ii., are reminiscent of the properties of covalently or ionically bonded compounds while iii., along with the observation that many carbides

exhibit non-stoichiometry, would suggest that the bonding is metallic. In reality the properties reflect a mixture of these characteristics and as such are not easily understood purely on the basis of electronic structure.

With respect to the simple binary carbide structures observed for these elements the atomic arrangement can be in part determined by Hägg's rule which states that the structure depends on the ratio of the radii of the nonmetal (r_x) and metal (r_m) atoms, respectively. For $r = r_x/r_m < 0.59$, the following structures may arise: face-centered cubic (*fcc*), hexagonal closed packed (*hcp*) or simple hexagonal (SH). The carbon atoms reside in the large interstitial sites of octahedral or cubic prismatic geometry. For $r > 0.59$ the metallic arrangement distorts to accommodate the larger nonmetal atoms and preserve metal-metal interactions. Further to this, Engel-Brewer theory may be used to predict the structures of some compounds according to the electronic structures of the parent metals. However, overall there exist a range of structures for each element and no simple rules exist to predict every possibility.

Molybdenum along with tungsten is known to form simple carbides with varying structures depending upon the synthesis conditions. Due to the low scattering power of interstitial C atoms, a search of the historical literature reveals a wide variety of binary phases for the Mo/C system, some of which have been duplicated. In reality there are a range of stoichiometries and degrees of ordering in many of the crystal systems, however, a synopsis of the primary crystalline phases is given in Table 1.2.

Table 1.2: Six known molybdenum phases.[81]

Phase	Metal lattice structure	Space Group	C atom position	Stacking sequence	Remarks
α-Mo_2C	*ortho.*	Pbcn	Oct.	ABAB	
β-Mo_2C	*hcp*	$P6_3/mmc$	Oct.	ABAB	α-W_2C
η-MoC_{1-x}	*hcp*	$P6_3/mmc$	Oct.	ABCACB	(η-Mo_3C_2)
α-MoC_{1-x}	*fcc*	Pm3m	Oct.	ABCABC	β-W_2C $x = 0.54$
γ-MoC	*sh*	$P\bar{6}m2$	Prism	AAAA	WC
γ'-MoC	*hcp*	$P6_3/mmc$	Oct, and prism	AABB	

The most stable and commonly reported modification is α-Mo_2C which is differentiated from β-Mo_2C by a slight orthorhombic distortion of the metal lattice, resulting in a 'pseudo-hexagonal' lattice. β-Mo_2C is a high temperature variation of this phase in which the lattice is purely *hcp*, however, in the literature α- & β- are frequently interchanged and in practice the phases are not easily distinguishable. Of the phases in Table 1.2, two are commonly found in the literature regarding catalysis — orthorhombic/pseudo-hexagonal α-Mo_2C (often referred to as β-Mo_2C), and face-centred cubic α-MoC_{1-x} (see Figure 1.2). For ease of reference, these phases will be referred to as *hcp* and *fcc*, respectively, hereafter. In a large number of publications these distinctions are either not referred to or contradict other sources. This confusion almost certainly arises due to the indefinite stoichiometries and the fact that the *fcc* carbide is often formed with a stoichiometry very close to Mo_2C. These problems are further exacerbated by a lack of consistency in the XRD reference diffractograms. A full discussion of the structural characteristics of molybdenum carbide is beyond the scope of this literature review at present but further analysis will be given as appropriate.

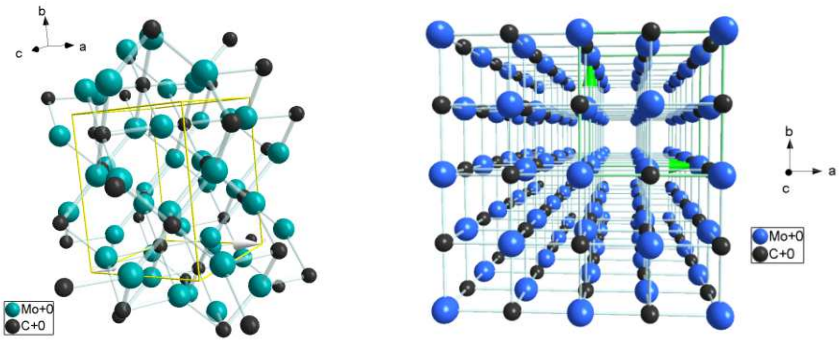

Figure 1.2: crystallographic views of the structures of; (left) orthorhombic α-Mo_2C and (right) *fcc* α-MoC_{1-x}. Note that α-MoC_{1-x} displays a Mo:C stoichiometry of 1:1 and represents all possible positions for interstitial carbon in the structure.

1.6 Synthesis of molybdenum carbide

Metal carbides are traditionally used in tool manufacture and in mechanical applications where considerable hardness is required. Most commonly the materials are synthesised by combining the native elements at very high temperatures, resulting in a heavily sintered product. These materials are not useful in catalysis as they

exhibit low surface areas and significant impurities which serve to reduce the overall activity. For the purpose of catalysis, transition metal carbides with high purity and high surface area must by synthesised. This can be done in several ways; the decomposition of organometallic precursors,[60] chemical vapour deposition using volatile precursors,[58, 59] heat-treatment of solution-based precursors,[82-85] and among others, the reduction and carburization of metal oxide powders.[47] The final two methods are of particular interest because they have been shown to produce high surface area materials and are also processes which are potentially scalable.

1.6.1 Temperature programmed reduction (TPR) of metal oxides

For the last twenty years the principle method that researchers have used to produce high surface area carbides is the temperature-programmed reaction (TPR) of precursor metal oxides. In a landmark paper, Lee *et al.* outline the synthesis of molybdenum carbide and molybdenum nitride from MoO_3.[47] The resultant carbide and nitrides exhibit high surface areas (50-200m^2g^{-1}), consistent stoichiometry, and are largely free from graphitic carbon. This is achieved using temperature programmed reduction (TPR) under a CH_4/H_2 stream (NH_3 in the case of nitrides) of a high purity starting material. All products are characterized by XRD, BET surface area measurement, and the reaction monitored using gas chromatography (GC). It is shown that the reduction occurs in two steps — the first being the reaction $MoO_3 \rightarrow MoO_2$, and the second corresponds to the synthesis of the carbide, $MoO_2 \rightarrow Mo_2C$ (see Figure 1.3).

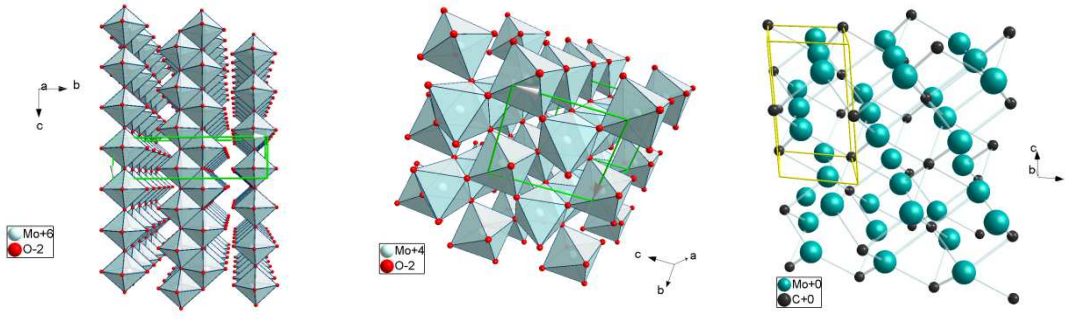

Figure 1.3: From left, crystallographic representations of: α-MoO_3, MoO_2, and β-Mo_2C.

The second reduction is dependent on the ratio of CH_4/H_2 used: a high ratio (up to 100% CH_4) will result in a higher surface area material but there will be deposition of graphitic carbon, at lower ratios the deposition of coke is less favourable but the

surface area is lower. At very low ratios, it is observed that the oxide is reduced to Mo metal.

This technique has been applied and developed extensively for the carburisation (and nitridation) of other transition metal oxides. Of particular note is the use of higher carbon content alkanes in the carburisation process. By utilizing higher alkanes (C2, C3, C4, C6)[14, 86, 87] in combination with hydrogen, the carburisation temperature can be lowered significantly, therefore reducing the potential for particle sintering and increasing the resultant surface area. The thermodynamics of this process are not entirely clear with larger alkanes but it appears that dissociation of the alkane species and subsequent incorporation of carbon into the lattice is a more facile process than the incorporation of methane.

A further aspect to this process is that molybdenum carbide produced by the action of methane/hydrogen mixtures result in the thermodynamically stable *hcp* Mo_2C whereas the use of higher alkanes result in the metastable *fcc* MoC_{1-x} (in the case of ethane a mixture of both phases is produced).[88] Both carbides exhibit a roughly 2:1 stoichiometry of Mo:C however the *fcc* MoC_{1-x} is stabilised by the persistent presence of oxygen and is better described as an oxycarbide.[89] *In situ* XRD studies have shown that both processes involve the initial formation of MoO_2 after which carbon is introduced into the structure. However, the *fcc* MoC_{1-x} shares similar lattice parameters with regards to MoO_2 which results in a topotactic exchange to give the carbide, as is also the case in the formation of Mo_2N. This is seen in SEM images of the final product which show very similar morphologies to the starting oxide material. In the case of *hcp* Mo_2C the lattice undergoes a rearrangement to give a very different morphology to that of MoO_3. In both cases the surface area of the carbide or nitride is significantly higher than that of the starting oxide but this can be explained by the observation that the initial crystallites are degraded to highly porous aggregates of nanocrystalline material while retaining the overall morphology. From the results of BET surface area analysis it can be seen that the highest surface area materials result from the topotactic exchange and that the formation of the hexagonal phase results in a decreased surface area (ca. 200 m^2g^{-1} compared with ~50 m^2g^{-1}). This can be observed directly in the case where Mo_2N of high surface area is carburized using a methane/hydrogen mixture to give the *fcc* carbide with very similar surface area.[14]

The different catalytic activities/stabilities of these two phases have not been explored thoroughly but the evidence that *fcc* MoC_{1-x} is stabilized by oxygen inclusion and may be more prone to forming oxycarbides helps to explain the observed phase instability at high temperatures.[89] Furthermore it has been observed that the *fcc* carbide is more effective for dehydrogenation whereas the *hcp* phase exhibits greater performance in reforming reactions or oxidizing conditions.[90]

1.6.2 Stability

In recent papers by Li *et al.*, the surface reactivity of Mo_2C/Al_2O_3 with regards to oxidation and subsequent reduction is probed by *in situ* FTIR spectroscopy.[91] In an initial study, alumina supported Mo_2C was synthesised by TPR method in a quartz cell whilst monitored using FTIR spectroscopy. This allowed characterization of the freshly synthesised Mo_2C surface by monitoring the CO stretching frequency. As a control, the experiment was repeated in a conventional fashion and the product was passivated under a 1% O_2/N_2 mixture at RT and then activated under H_2 at 873K. The IR spectrum of each material was very different with respect to the CO stretching frequency. The freshly prepared material had a steady, strong absorbance at 2054cm^{-1} indicating that the CO molecule was adsorbed linearly on a Mo surface site and that the Mo was in a reduced state ($Mo^{\delta+}$, $0 < \delta < 2$). CO adsorbed on the passivated sample had a much higher stretching frequency (2180 cm^{-1}) indicating a more heavily oxidized state. The spectra of the fresh sample also bore some resemblance to similar studies of group VIII metals adding credence to the idea that early TMCs resemble noble metals in their electronic structure and activity.

The effects of carburisation temperature and the time at which the final temperature is held were also shown to have a strong influence on the adsorption of CO. XPS studies of both the passivated and subsequently reduced catalyst material back up the FTIR data, showing that even in the reduced form, the majority of the Mo sites are in a high valence state (Mo^{+6} and Mo^{+4}). This indicates that the surface layer is predominantly oxycarbidic. Although it was accepted that activation at elevated temperatures (873K) using H_2 was effective in removing the surface oxide, it was demonstrated by TPR-MS that the loss of interstitial carbon also occurs. Lower temperatures were ineffective at entirely reducing the oxide layer. Hence, it was concluded that passivation of Mo_2C using molecular oxygen as the source was too severe and

resulted in a surface which could not be fully reduced without losing the original surface. In a previous communication, Li *et al.* have established that the reactivity of a similar nitride material is analogous.[91]

In a follow-up paper[34] Li *et al.* worked around the question of passivation and compared three potential passivating systems for the alumina-supported Mo_2C. It was found that by replacing oxygen with water or carbon dioxide as the oxidant, it was possible to produce a mild oxidic layer that could subsequently be reduced more easily. FTIR studies of CO molecules over oxygen-passivated material and CO_2/water-passivated material show a significant difference in their ability to reattain the low oxidation state in surface Mo atoms characteristic of freshly prepared carbides.

These results are in agreement with the findings of Reimer *et al.*, who in an extensive article in 1987 have explored the syntheses of Mo_2N, *hcp* Mo_2C, and *fcc* MoC_{1-x}.[67, 92] In the article they prepare the nitride using the TPR method of Volpe and Boudart (1985)[13, 93] and the carbides by the carburisation of Mo powder and Mo_2N, respectively. The question of removing surface oxygen and/or carbon is dealt with and it is concluded that surface carbon may be removed by treatment with oxygen but at the expense of the inclusion of oxygen atoms to the carbide lattice. Likewise the removal oxygen, it is stated, cannot be effected without significant removal of carbide carbon atoms from the lattice. However, it is considered to be possible to remove oxygen from the near surface region by heat-treatment with a CH_4/H_2 mixture at elevated temperatures.

1.7 Activation of light alkanes over molybdenum-based catalysts

1.7.1 Conversion of methane to synthesis gas

The conversion of methane to synthesis gas is catalysed over high surface area Mo and W carbides. It is discussed as an attractive alternative to Ni-based catalysts, which suffer from coke build up and eventual deactivation, and comparable in activity/selectivity to some platinum-group metals whilst being cheap to produce.

The conversion of methane to synthesis gas over Mo and W carbides was demonstrated by Green *et al.* using dry reforming (carbon dioxide), partial oxidation

(oxygen), and steam reforming.[72, 94-96] A stoichiometric feed ratio is used at elevated pressure. The catalyst material was prepared by TPR of high surface area metal oxides and the reactions are carried out in modified microreactor.

The activity of the catalysts in the dry reforming of methane is largely dependent on the pressure and gas hourly space velocity (GHSV) of reactant mixture. At ambient pressure the catalysts are deactivated after a short time due to oxide formation (observed via *in situ* XRD analysis). At higher pressures (~8 bar), the system is stable as observed over 60-70 hours. Mo_2C was the more effective of the two carbides, comparable in relative activity to Rh-based catalysts.

The carbides were also studied in the partial oxidation of methane to carbon monoxide. In the presence of oxygen at elevated temperatures and ambient pressure the catalyst materials deactivated. This was overcome by operating at an elevated pressure and with an initial gas mixture of CH_4/CO_2 which was switched to a CH_4/air mixture over the course of an hour. Under these conditions, Mo_2C, WC, and 5% Mo_2C/Al_2O_3 catalyst systems catalysed the partial oxidation of methane with high selectivity and exhibited stability over the course of 12 hours.

Similarly in the steam and mixed reforming conditions, the catalysts performed ably, showing high selectivities for the production of hydrogen and carbon monoxide. It was found that elevated temperatures and optimised flow rates prevented any detectable deterioration of the catalyst activity over the course of 72 hours.

It is seen throughout the study that the carbide catalysts are deactivated at ambient temperature due to oxide formation, and that this mechanism is suppressed at elevated pressures. The phenomenon can be explained by the relative rates of oxidation and carburization.

$$Mo_2C + 5CO_2 = 2MoO_2 + 6CO \qquad (\text{rate} = k_1) \qquad (1)$$

$$2MoO_2 + 5CH_4 = Mo_2C + 4CO + 10H_2 \qquad (\text{rate} = k_2) \qquad (2)$$

In Figure 1.4 it can be seen that the consumption of the feed gases CH_4 and CO_2 drops dramatically with increasing GHSV. The lowest GHSV remains active for just over 1000 minutes before deactivating. The diamond points represent an increased GHSV

but with a diluted feed stock such that the molar quantity of reactants is identical to the optimised conditions.

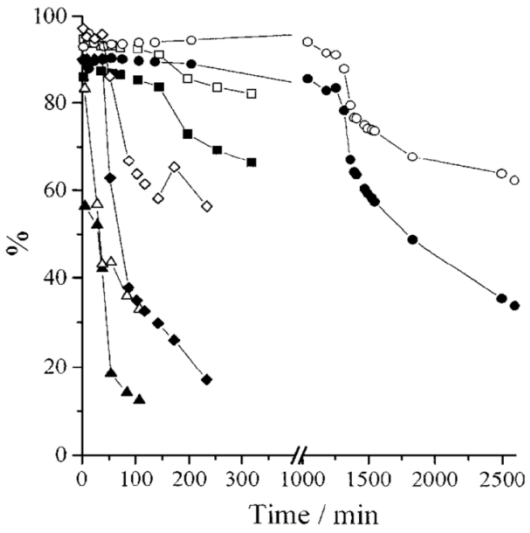

Figure 1.4: Effect of GHSV on the stability of the Mo_2C catalyst at 1123K and 1 bar. Open symbols = χ_{CO2}; closed symbols = χ_{CH4}. GHSV (h^{-1}):○ — 1.91 x 10^3; □ — 3.97 x 10^3; Δ — 6.36 x 10^3; ◊ — (1.91 x 10^3 + Ar = 8.79 x 10^3). Reprinted from [72] with the permission of Elsevier.

At higher pressure (8 bar) and operating at optimised GHSV, deactivation of the catalyst material is not observed. From this graph and other experimental data it was concluded that the reaction rate which governs the rate of carbide oxidation (1) is faster than that of oxide carburisation (2). At lower GHSVs and higher pressures, there is an increased contact time which allows the two reactions to reach equilibrium.

1.7.2 Dehydrogenation Reactions

Dehydrogenation is the rate determining step in the partial oxidation reaction of propane to acrylic acid. This reaction is generally carried out over oxidic catalysts such as the mixed metal oxide MoVTe system and it represents a fundamental advance from the use of propene as a feed stock. A number of studies have investigated carbides for their activity with respect to dehydrogenation reactions and they appear to show some promise.

1.7.2.1 Molybdenum oxycarbides

MoO_3 was reduced under a mixture of butane/H_2 at 550°C and found to be active in the dehydrogenation and simultaneous isomerisation of n-butane.[90] Under the n-

butane/H_2 stream, the catalytic surface was unstable leading to total carburisation of the surface layer and subsequent coke deposition. This surface remained active but the selectivity was entirely towards hydrogenolysis to methane. The addition of steam to the reactant mixture was found to stabilize the surface composition and prevent coking, however, a reduction in the catalytic activity was also noted.

1.7.2.2 Supported molybdenum carbides

Solymosi *et al.* have carried out the dehydrogenation of propane over ZSM-5 and SiO_2 supported molybdenum carbide.[97, 98] In the case of the SiO_2 supported material, dehydrogenation was the dominant reaction and propylene selectivity approached 50% at a conversion of ca. 25%. The selectivity decreased with increasing temperature which was attributed to deactivation of the catalyst through further carburisation. The ZSM-5 supported carbide however, showed very low selectivity to propylene and the principal reactions observed were aromatization and cracking. In this case, much of the activity could be attributed to the support material ZSM-5 which is selective towards cracking and aromatization in the absence of Mo_2C. Although increased selectivity for aromatization was observed.

1.7.2.3 Vanadium Carbides and Nitrides

Thompson *et al.* have presented some relevant work on vanadium carbides and nitrides in the dehydrogenation of butane.[99, 100] V_2O_5 is reduced using TPR under CH_4/H_2 and likewise under NH_3 to yield the corresponding carbide and nitride. The carbide is sub-stoichiometric with the formula V_8C_7 and the nitride has the formula VN. In a stream of n-butane/H_2 (in He carrier gas), both catalysts displayed an increased selectivity to the formation of olefins in comparison with Mo_2C, which was highly unselective. The bonding in the compounds was investigated using NEXAFS and there was seen to be substantial charge transfer from the vanadium to the non-metal atom. It was suggested that this ionicity, which is not seen in other TM carbides, was in part responsible for the increased selectivity observed.

1.7.3 Isomerisation reactions

Isomerisation of short chain alkanes (C4–C7) is an important reaction in petroleum chemistry to increase octane content and produce cleaner-burning fuels. One of the challenges in this area of chemistry is the development of catalysts that can isomerise

n-heptane with high selectivity while minimising hydrogenolysis, or 'cracking'. Ledoux *et al.* have reported high selectivity in the isomerisation of *n*-heptane over a Mo_2C catalyst which was pretreated in air at elevated temperatures.[44] Prior to this study, Ribeiro *et al.* reported the effect of surface oxygen on the selectivity of tungsten carbide powders in isomerisation reactions.[101, 102] Isomerisation was not observed on freshly prepared catalysts but it is observed with high selectivity over oxygen modified carbides. It can be seen from these and other papers that the reactivity is strongly dependant on the carbidic surface and that varying degrees of oxidation will modify the selectivity substantially.

1.7.4 Interaction of light alkanes on supported Mo_2C catalysts

Recent papers by Solymosi *et al.*, have reported on the catalytic activity of TPR-prepared β-Mo_2C supported on SiO_2 and ZSM-5, respectively.[75]

In the former case, the oxidative dehydrogenation of ethane is carried out over a silica supported catalyst showing high selectivity (90-95%) for the formation of ethylene at moderate conversion (8-30%). The oxygen source used was CO_2 with the predominant reaction being:

$$C_2H_6 + CO_2 \leftrightarrow C_2H_4 + CO \qquad (3)$$

The Mo_2C catalyst was prepared according to the method of Boudart *et al.* and ethane (12.5% in Ar) was passed over the material at temperatures between 550–690°C. The partial pressure of CO_2 was varied but the most reliable results were obtained for the ratio C_2H_6:CO_2 = 1:1. At 873K these conditions resulted in selectivity of 87% at 14% conversion with a turnover rate for ethylene of 2.7×10^{-3}. By contrast, the precursor to the carbide material, MoO_3 supported on SiO_2, showed very little catalytic activity for the reaction $C_2H_6 + CO_2$. The conversion rate for similar temperatures was around 3% with a selectivity of 25-30%. Increasing the flow rate or GHSV decreased the selectivity to ethylene while increasing the rate of formation of undesirable products.

The more recent paper of relevance by Solymosi *et al.* details the reactions of propane over three Mo_2C catalyst systems: unsupported β-Mo_2C, ZSM-5 supported Mo_2C, and SiO_2 supported Mo_2C.[97, 98] The interaction of propane and propylene on the surface of the catalyst was probed using FTIR spectroscopy on a sample of Mo_2C/SiO_2 at

reduced pressures. The results show that propane was physisorbed on the surface at lower temperatures (150-250K) but at higher temperatures, the spectrum more closely resembles that of adsorbed propylene. This is supported by temperature programmed desorption (TPD) measurements in which propane adsorbed onto supported Mo_2C is seen to be converted to propylene and ethylene at higher temperatures.

The catalytic reactivity of the three systems was compared over a range of temperatures and flow rates. Additionally, the reactivity of the support materials was tested to provide comparison.

Over bulk β-Mo_2C at 600°C, the predominant reaction is dehydrogenation to propylene. This occurs with ca. 44% selectivity, but with a low conversion (~7%) which may in part be due to the low surface area of the unsupported material.

The silica-supported catalyst material was tested over the same temperature range and it was found that initially, the predominant reaction was hydrogenolysis, resulting in the production of methane and ethane. After some time on line, the dehydrogenation reaction became more prevalent and propylene was produced with a selectivity of 50%. It is suggested that the hydrogenolysis reaction is inhibited by coke deposition on the catalyst surface.

The reactions of propane over ZSM-5 and Mo_2C/ZSM-5 were found to be quite different. On untreated ZSM-5, from around 500°C, dehydrogenation and cracking reactions predominate. Above 550°C, however, the production of benzene and toluene by aromatization reactions is observed. At 700°C the selectivity is at a maximum of 34%. In the Mo_2C/ZSM-5 system, however, selectivity of 46% is achieved at the lower temperature of 600°C with only a slight decrease in conversion. The difference in the reactivity is attributed to the β-Mo_2C activity for dehydrogenation combined with the ability of ZSM-5 to aromatize the intermediate propylidyne species.

1.7.5 Partial oxidation reactions

Highly relevant to the proposed experimental work is the oxidation of light alkanes over early transition metal carbide surfaces. Very few studies have been carried out regarding this reaction but some research of note was performed by Ledoux *et al.*, examining the partial oxidation of butane to maleic anhydride over supported

vanadium carbide.[103, 104] The carbide was synthesised by depositing a volatile metallic precursor (liquid V_2O_5) over a high surface area carbonaceous support. The system is heated in the absence of oxygen to 1300°C, reducing the oxide to form a carbon-supported VC catalyst. This surface is then passivated in air resulting in an amorphous surface layer of vanadium oxycarbide as revealed by HRTEM.

Catalytic tests with butane reveal that the under varying conditions the material showed some selectivity towards maleic anhydride. Passing an enriched mixture of butane (O_2/Bu = 1.1) over the catalyst resulted in total combustion but a leaner mixture (O_2/Bu = 6), produced maleic anhydride with ca. 30% selectivity at ca. 45% butane conversion.

1.8 References

[1] S. Albonetti, F. Cavani, F. Trifiro, Catalysis Reviews-Science and Engineering 1996, 38, 413.

[2] A. M. El-Awad, E. A. Hassan, A. A. Said, K. M. Abd El-Salaam, Monatshefte für Chemie / Chemical Monthly 1989, 120, 199.

[3] F. Cavani, F. Trifiro, Catalysis Today 1999, 51, 561.

[4] J. S. Lee, M. Boudart, Catalysis Letters 1993, 20, 97.

[5] R. Schlögl, A. Knop-Gericke, M. Hävecker, U. Wild, D. Frickel, T. Ressler, R. E. Jentoft, J. Wienold, G. Mestl, A. Blume, O. Timpe, Y. Uchida, Topics in Catalysis 2001, 15, 219.

[6] N. Ballarini, A. Battisti, F. Cavani, A. Cericola, C. Lucarelli, S. Racioppi, P. Arpentinier, Catalysis Today 2006, 116, 313.

[7] R. Horn, N. Degenstein, K. Williams, L. Schmidt, Catalysis Letters 2006, 110, 169.

[8] M. Y. Sinev, G. A. Vorobeva, V. N. Korchak, Kinetics and Catalysis 1986, 27, 1007.

[9] M. Y. Sinev, Z. T. Fattakhova, Y. P. Tulenin, P. S. Stennikov, V. P. Vislovskii, Catalysis Today 2003, 81, 107.

[10] B. Savova, D. Filkova, D. Crisan, M. Crisan, M. Raileanu, N. Dragan, L. Petrov, J. C. Védrine, Applied Catalysis A: General 2009, 359, 55.

[11] P. Botella, B. Solsona, A. Martinez-Arias, J. M. L. Nieto, Catalysis Letters 2001, 74, 149.

[12] P. Beato, A. Blume, E. Girgsdies, R. E. Jentoft, R. Schlogel, O. Timpe, A. Trunschke, G. Weinberg, Q. Basher, F. A. Hamid, S. B. A. Hamid, E. Omar, L. M. Salim, Applied Catalysis a-General 2006, 307, 137.

[13] J. S. Lee, L. Volpe, F. H. Ribeiro, M. Boudart, Journal of Catalysis 1988, 112, 44.

[14] C. Bouchy, S. B. D. A. Hamid, E. G. Derouane, Chemical Communications 2000, 125.

[15] K. Page, J. Li, R. Savinelli, H. N. Szumila, J. P. Zhang, J. K. Stalick, T. Proffen, S. L. Scott, R. Seshadri, Solid State Sciences 2008, 10, 1499.

[16] C. F. Cullis, Industrial and Engineering Chemistry 1967, 59, 18.

[17] F. Cavani, F. Trifiro, Catalysis Today 1995, 24, 307.

[18] R. Grabowski, Catalysis Reviews-Science and Engineering 2006, 48, 199.

[19] A. T. L. Csepei, R. Schloegl private discussions 2011.

[20] S. T. Oyama, J. W. Hightower, American Chemical Society National Meeting, Catalytic selective oxidation, American Chemical Society, Washington, 1993.

[21] S. T. Oyama, B. K. Warren, American Chemical Society National Meeting, Heterogeneous hydrocarbon oxidation, American Chemical Society, Washington, 1996.

[22] R. K. Grasselli, Catalysis Today 1999, 49, 141.

[23] P. Mars, D. W. van Krevelen, Chemical Engineering Science 1954, 3, 41.

[24] R. K. Grasselli, D. J. Buttrey, J. D. Burrington, A. Andersson, J. Holmberg, W. Ueda, J. Kubo, C. G. Lugmair, A. F. Volpe, Topics in Catalysis 2006, 38, 7.

[25] M. G. O'Brien, A. M. Beale, S. D. M. Jacques, T. Buslaps, V. Honkimaki, B. M. Weckhuysen, The Journal of Physical Chemistry C 2009, 113, 4890.

[26] U. Rodemerck, B. Kubias, H. W. Zanthoff, M. Baerns, Applied Catalysis a-General 1997, 153, 203.

[27] M. Abon, K. E. Bere, P. Delichere, Catalysis Today 1997, 33, 15.
[28] X. Liu, B. Frank, W. Zhang, T. P. Cotter, R. Schlogl, D. S. Su, Angewandte Chemie-International Edition 2011, 50, 3318.
[29] B. Frank, R. Fortrie, C. Hess, R. Schlogl, R. Schomacker, Applied Catalysis a-General 2009, 353, 288.
[30] A. C. Sanfiz, T. W. Hansen, D. Teschner, P. Schnorch, F. Girgsdies, A. Trunschke, R. Schlogl, M. H. Looi, S. B. A. Hamid, Journal of Physical Chemistry C 2010, 114, 1912.
[31] F. Ivars, B. Solsona, M. Soriano, J. López Nieto, Topics in Catalysis 2008, 50, 74.
[32] F. Naraschewski, A. Jentys, J. Lercher, Topics in Catalysis, 54, 639.
[33] H. Oudghiri-Hassani, E. Zahidi, M. Siaj, J. Wang, P. H. McBreen, Applied Surface Science 2003, 212, 4.
[34] W. C. Wu, Z. L. Wu, C. H. Liang, P. L. Ying, Z. C. Feng, C. Li, Physical Chemistry Chemical Physics 2004, 6, 5603.
[35] K. J. Leary, J. N. Michaels, A. M. Stacy, Journal of Catalysis 1986, 101, 301.
[36] K. J. Leary, J. N. Michaels, A. M. Stacy, Journal of Catalysis 1987, 107, 393.
[37] J. S. Lee, K. H. Lee, J. Y. Lee, Journal of Physical Chemistry 1992, 96, 362.
[38] V. V. Nemoshkalenko, V. P. Krivitskii, A. P. Nesenjuk, L. I. Nikolajev, A. P. Shpak, Journal of Physics and Chemistry of Solids 1975, 36, 277.
[39] B. Dhandapani, T. St Clair, S. T. Oyama, Applied Catalysis a-General 1998, 168, 219.
[40] C. Bouchy, C. Pham-Huu, B. Heinrich, C. Chaumont, M. J. Ledoux, Journal of Catalysis 2000, 190, 92.
[41] J.-S. Choi, G. Bugli, G. Djéga-Mariadassou, Journal of Catalysis 2000, 193, 238.
[42] D. C. LaMont, A. J. Gilligan, A. R. S. Darujati, A. S. Chellappa, W. J. Thomson, Applied Catalysis a-General 2003, 255, 239.
[43] S. Liu, R. Ohnishi, M. Ichikawa, Journal of Catalysis 2003, 220, 57.
[44] E. A. Blekkan, P. H. Cuong, M. J. Ledoux, J. Guille, Industrial & Engineering Chemistry Research 1994, 33, 1657.
[45] A. Katrib, V. Logie, N. Saurel, P. Wehrer, L. Hilaire, G. Maire, Surface Science 1997, 377, 754.
[46] R. B. Levy, M. Boudart, Science 1973, 181, 547.
[47] J. S. Lee, S. T. Oyama, M. Boudart, Journal of Catalysis 1987, 106, 125.
[48] H. Preiss, B. Meyer, C. Olschewski, Journal of Materials Science 1998, 33, 713.
[49] H. Preiss, D. Schultze, K. Szulzewsky, Journal of the European Ceramic Society 1999, 19, 187.
[50] A. M. Stux, C. Laberty-Robert, K. E. Swider-Lyons, Journal of Solid State Chemistry 2008, 181, 2741.
[51] C. C. Yu, S. Ramanathan, F. Sherif, S. T. Oyama, Journal of Physical Chemistry 1994, 98, 13038.
[52] E. Boellaard, A. M. vanderKraan, J. W. Geus, in Preparation of Catalysts Vi, Vol. 91, 1995, pp. 931.
[53] C. C. Yu, S. Ramanathan, B. Dhandapani, J. G. Chen, S. T. Oyama, J. Phys. Chem. B 1997, 101, 512.
[54] S. T. Oyama, C. C. Yu, S. Ramanathan, Journal of Catalysis 1999, 184, 535.
[55] V. Schwartz, S. T. Oyama, J. G. G. Chen, Journal of Physical Chemistry B 2000, 104, 8800.

[56] S. Korlann, B. Diaz, M. E. Bussell, Chemistry of Materials 2002, 14, 4049.
[57] S. Chouzier, P. Afanasiev, M. Vrinat, T. Cseri, M. Roy-Auberger, Journal of Solid State Chemistry 2006, 179, 3314.
[58] M. Nagai, I. Shishikura, S. Omi, Japanese Journal of Applied Physics Part 1-Regular Papers Short Notes & Review Papers 2000, 39, 4528.
[59] J. Lu, U. Jansson, Thin Solid Films 2001, 396, 53.
[60] J. M. Giraudon, L. Leclercq, G. Leclercq, A. Lofberg, A. Frennet, Journal of Materials Science 1993, 28, 2449.
[61] I. P. P. A. J. C. M. M. Artur M. Nartowski, Advanced Materials 1998, 10, 805.
[62] K. Y. Park, W. K. Seo, J. S. Lee, Catalysis Letters 1991, 11, 349.
[63] P. Delporte, C. PhamHuu, M. J. Ledoux, Applied Catalysis a-General 1997, 149, 151.
[64] J. C. Edwards, P. D. Ellis, Langmuir 1991, 7, 2117.
[65] G. M. Dolce, P. E. Savage, L. T. Thompson, Energy & Fuels 1997, 11, 668.
[66] J. G. Choi, J. R. Brenner, L. T. Thompson, Journal of Catalysis 1995, 154, 33.
[67] G. S. Ranhotra, A. T. Bell, J. A. Reimer, Journal of Catalysis 1987, 108, 40.
[68] S. T. Oyama, Catalysis Today 1992, 15, 179.
[69] F. C. Meunier, A. Yasmeen, J. R. H. Ross, Catalysis Today 1997, 37, 33.
[70] F. Solymosi, R. Nemeth, Catalysis Letters 1999, 62, 197.
[71] C. Phamhuu, M. J. Ledoux, J. Guille, Journal of Catalysis 1993, 143, 249.
[72] J. B. Claridge, A. P. E. York, A. J. Brungs, C. Marquez-Alvarez, J. Sloan, S. C. Tsang, M. L. H. Green, Journal of Catalysis 1998, 180, 85.
[73] K. Oshikawa, M. Nagai, S. Omi, J. Phys. Chem. B 2001, 105, 9124.
[74] S. Naito, M. Tsuji, Y. Sakamoto, T. Miyao, Scientific Bases for the Preparation of Heterogeneous Catalysts 2002, 143, 415.
[75] F. Solymosi, J. Cserényi, A. Szöke, T. Bánsági, A. Oszkó, Journal of Catalysis 1997, 165, 150.
[76] D. Wang, J. H. Lunsford, M. P. Rosynek, Journal of Catalysis 1997, 169, 347.
[77] S. Liu, L. Wang, R. Ohnishi, M. Ichikawa, Journal of Catalysis 1999, 181, 175.
[78] P. Liu, J. A. Rodriguez, The Journal of Physical Chemistry B 2006, 110, 19418.
[79] D. J. Ham, Y. K. Kim, S. H. Han, J. S. Lee, Catalysis Today 2008, 132, 117.
[80] J. A. Schaidle, A. C. Lausche, L. T. Thompson, Journal of Catalysis 2010, 272, 235.
[81] S. Nagakura, S. Oketani, Transactions of the Iron and Steel Institute of Japan 1968, 8, 265.
[82] P. Afanasiev, Inorg. Chem. 2002, 41, 5317.
[83] H. M. Wang, X. H. Wang, M. H. Zhang, X. Y. Du, W. Li, K. Y. Tao, Chemistry of Materials 2007, 19, 1801.
[84] L. Aladko, V. Komarov, A. Manakov, A. Ancharov, Journal of Inclusion Phenomena and Macrocyclic Chemistry 2007.
[85] X.-H. Wang, M.-H. Zhang, W. Li, K.-Y. Tao, Catalysis Today 2008, 131, 111.
[86] T. C. Xiao, A. P. E. York, V. C. Williams, H. Al-Megren, A. Hanif, X. Y. Zhou, M. L. H. Green, Chemistry of Materials 2000, 12, 3896.
[87] T. C. Xiao, H. T. Wang, J. W. Da, K. S. Coleman, M. L. H. Green, Journal of Catalysis 2002, 211, 183.
[88] T. Xiao, A. P. E. York, K. S. Coleman, J. B. Claridge, J. Sloan, J. Charnock, M. L. H. Green, Journal of Materials Chemistry 2001, 11, 3094.

[89] A. Hanif, T. C. Xiao, A. P. E. York, J. Sloan, M. L. H. Green, Chemistry of Materials 2002, 14, 1009.
[90] M. K. Neylon, S. Choi, H. Kwon, K. E. Curry, L. T. Thompson, Applied Catalysis a-General 1999, 183, 253.
[91] W. C. Wu, Z. L. Wu, C. H. Liang, X. W. Chen, P. L. Ying, C. Li, Journal of Physical Chemistry B 2003, 107, 7088.
[92] G. S. Ranhotra, G. W. Haddix, A. T. Bell, J. A. Reimer, Journal of Catalysis 1987, 108, 24.
[93] L. Volpe, M. Boudart, Journal of Solid State Chemistry 1985, 59, 348.
[94] A. P. E. York, J. B. Claridge, A. J. Brungs, S. C. Tsang, M. L. H. Green, Chemical Communications 1997, 39.
[95] T.-C. Xiao, H.-T. Wang, A. P. E. York, M. L. H. Green, Catalysis Letters 2002, 83, 241.
[96] A. P. E. York, T.-c. Xiao, M. L. H. Green, J. B. Claridge, Catalysis Reviews 2007, 49, 511
[97] E. Solymosi, R. Nemeth, L. Ovari, L. Egri, Journal of Catalysis 2000, 195, 316.
[98] F. Solymosi, R. Németh, A. Oszkó, J. J. S. E. Iglesia, T. H. Fleisch, in Studies in Surface Science and Catalysis, Vol. Volume 136, Elsevier, 2001, pp. 339.
[99] H. Kwon, S. Choi, L. T. Thompson, Journal of Catalysis 1999, 184, 236.
[100] H. Kwon, L. T. Thompson, J. Eng, J. G. Chen, Journal of Catalysis 2000, 190, 60.
[101] F. H. Ribeiro, M. Boudart, R. A. Dallabetta, E. Iglesia, Journal of Catalysis 1991, 130, 498.
[102] E. Iglesia, F. H. Ribeiro, M. Boudart, J. E. Baumgartner, Catalysis Today 1992, 15, 455.
[103] F. Meunier, P. Delporte, B. Heinrich, C. Bouchy, C. Crouzet, C. PhamHuu, P. Panissod, J. J. Lerou, P. L. Mills, M. J. Ledoux, Journal of Catalysis 1997, 169, 33.
[104] M. J. Ledoux, F. Meunier, B. Heinrich, C. Pham-Huu, M. E. Harlin, A. O. I. Krause, Applied Catalysis a-General 1999, 181, 157.

Chapter 2: The synthesis of mixed Mo-V carbides

2.1 Abstract

A series of bimetallic carbides of the form $(Mo_{1-x}V_x)_2C$ ($0 < x < 0.12$) was synthesised by carbothermal reduction of corresponding *h*-$Mo_{1-x}V_xO_3$ mixed metal oxide (MMO) precursors. The oxides were synthesised by precipitation and the subsequent carbide phase development was monitored using *in situ* X-ray diffraction (XRD) and outgas analysis of the temperature-programmed reduction-carburisation. The observed structural evolution is combined with analysis of the solid state kinetic data and the reduction mechanism is discussed.

Inclusion of vanadium is observed to retard the onset of reduction as well as strongly influencing the kinetics of oxide reduction. The reduction is observed to proceed via a complex mechanism involving initial formation of a monoclinic suboxide, MoO_{3-x}. Increasing the content of vanadium retards the onset of reduction as well as the onset of carburisation in the step $MoO_2 \rightarrow Mo_2C$.

The carbides exhibit a trend in the growth morphology with vanadium concentration, from a particulate-agglomerate material to a packed, nano-fibrous morphology. Transmission electron microscopy investigation of the fibrous material using selected area electron diffraction (SAED) reveals that the high aspect-ratio crystallites exhibit pseudomorphism, and in the case of the vanadium containing materials, it is observed that there is some preferential orientation of crystal grains. Characterisation of the materials by N_2 adsorption reveals an increasing mesoporosity associated with the fibrous morphology, as well as an exceptionally high surface area (80–110m^2/g).

The synthesis was subsequently scaled up from the *in situ* XRD preparation using a specially adapted rotary furnace to perform the temperature-programmed reduction-carburisation. By adapting the heating rate, gas flow and pre-treatment conditions it was possible to produce carbide materials with comparable physical properties to those obtained from the small scale. As a result, it was possible to synthesise Mo_2C materials in multi-gram quantities (5–15 g) with BET surface areas ranging from 50–100 m_2/g, among the highest values reported in literature.

In addition to the development of the synthesis parameters, air-free techniques and equipment were developed for the handling of freshly-reduced carbide materials.

These tools are readily adaptable for high-temperature syntheses and allow the user to transfer material from the reactor directly to the glovebox without exposure to atmosphere.

2.1.1 Introduction

Since it was observed that early transition metal carbides display noble metal-like properties,[1, 2] there has been a renewed interest in these materials in the field of catalysis, especially so in the case of group V and VI carbides. It is hoped that such materials may be able to substitute scarcer and more expensive noble metals in a growing field of applications, including fuel cells and energy-related catalysis. This resurgence is largely due to the discovery of facile routes to highly dispersed bulk carbides and supported carbides by which transition metal oxides are reduced using a temperature-programmed reaction in the presence of a carbon containing gas.[3] Depending on the conditions, this approach yields stoichiometric materials of high purity with relatively high surface areas.

Molybdenum carbide exhibits interesting activity in a number of catalytic reactions including isomerisation,[4] hydrogenation and hydrogenolysis,[5] methanol reforming[6] and hydrotreating reactions.[7] It can also be formed under relatively mild conditions making it an ideal material for the study of carbides in catalysis. In addition, molybdenum participates in an extensive chemistry with oxygen providing various potential approaches to mono- and polymetallic carbides *via* multi-metal oxide (MMO) precursors. In this study, we explore an approach to a ternary carbide (Mo,V) through the use of Mo/V mixed oxides.

Various approaches to polymetallic carbides are outlined in the literature for their potential in hydrotreatment catalysis, including established variations of M_6C-type carbides (*i.e.* A_xB_yC; x = 2, 3, 4; y = 6-x; A, B = Ti, V, Cr, Mn, Fe, Co, Ni, Nb, Mo, W, Ta).[8, 9] Of more relevance to the present study is the preparation of carbide solid solutions related to the simple *hcp* and *fcc* carbide phases.[10] In two studies by Oyama *et al.*, a series of bimetallic transition metal oxide precursors of the form $M_1M_2O_x$ (M_1 = Mo, W; M_2 = V, Cr, Fe, Co, Ni, Nb, Mo, W) was prepared by the solid state fusion of simple oxide components. The oxides were subsequently carburised as per the literature method resulting in bimetallic oxycarbide materials.[11, 12] Also, recently,

Bastos *et al.* have synthesised mixed Mo/W carbides by varying the synthesis method of the precursor compounds including co-precipitation of mixed metal oxides.[13]

In this study, a bimetallic modification of the hexagonal molybdate *h*-MoO_3 was chosen as a starting material with vanadium as the substituting dopant metal. In this way it was expected to reduce potential segregation under the conditions of carburisation. The variably substituted oxides, in the form $(NH_4)_xMo_{1-x}V_xO_3$, were prepared by coprecipitation[14] and the resulting precursors subsequently carburised in an *in situ* XRD cell to give a series of samples of the form $(Mo,V)C_x$. From the characterisation of the intermediate and resultant products it can be seen that the composition and structure of the precursor oxide influences the mechanism of reaction as well as the surface area, morphology and grain size of the product carbides.

2.1.2 Motivation

As outlined in the introductory chapter, the primary motivation for this work is to study the potential influence that a reduced metal oxide catalyst operating in a carbon-rich environment may have on catalytic activity. The study has particular relevance to the MoVTe M1 catalyst for the partial oxidation of propane to acrylic acid[15, 16] and to Mo_5O_{14}-type catalysts used in the selective oxidation of acrolein to acrylic acid.[17]

The primary elements apart from oxygen in all of the aforementioned catalysts are molybdenum and vanadium, which due to their reducibility and electronic flexibility have been studied extensively in the catalytic literature, especially with respect to oxidation chemistry. In general, the reducible nature of molybdenum oxide lends itself to the formation of carbides due to the relatively low temperatures required to substitute carbon in the lattice *cf.* other transition metals.[18-20]

The temperature-programmed reduction-carburisation of MoO_3 to β-Mo_2C under H_2/CH_4 (as developed by Oyama *et al.*[3]) is carried out in two steps. The first involves the reduction of MoO_3 to MoO_2 which is carried out by the action of hydrogen alone. The second step is the reduction-carburisation of MoO_2 to Mo_2C which is performed by the hydrogen and methane in concert. It is also possible to carry out the carburisation with methane alone, however, it requires higher temperatures to allow the decomposition of CH_4 to release atomic hydrogen and

perform the requisite reduction steps.[3] Furthermore, higher hydrocarbons may be used to effect the carburisation of MoO_x. Each successive increase in chain length decreases the required temperature to decompose the hydrocarbon and incorporate carbon into the oxide matrix.[21-24] Additionally, it is possible to carburise MoO_x using carbon alone as the reducing-carburising agent.[25-27]

The stability of MoO_3 to the initial reduction is a function of the (generally) low surface area and the strength of the H-H bond, which must be activated to combine with lattice oxygen. Therefore, the use of longer chain hydrocarbons, which decompose over MoO_x at temperatures < 400°C, are able to reduce the oxide at lower temperatures than pure H_2 by the generation of atomic hydrogen at the site of decomposition. Depending upon the specific nature of this reduction-carburisation it is possible to form either the *fcc* α-Mo_2C or *hcp* β-Mo_2C. Hence, the action of propane upon molybdenum oxide is observed to result in a mixture of *fcc* and *hcp* molybdenum carbide phases at between 500-600°C, ca. 100°C lower than that observed for H_2/CH_4. This temperature range is certainly not beyond that which is achieved in hotspots observed for selective oxidation catalysts.[28]

Thus, the need for a detailed and mechanistic picture of the reduction-carburisation process lies at the heart of this study. The point of difference maintained here is that the mechanism and kinetics of formation has not before been approached for bimetallic/polymetallic systems that reflect the chemical nature of selective oxidation catalysts.

2.1.3 Experimental goals and approach

As is stated in the motivation section, it is desired to produce a study that elucidates the role and influence of vanadium in the carburisation process. To do this, it is necessary to have a defined series of precursor oxides with which to carry out the carburisation study. The conditions of the TPR-carburisation must be defined, and the composition and structure of the starting materials and products should be well-understood. Furthermore, to gain mechanistic insight, the reaction must be monitored *in situ* to determine the extent of reaction and the nature of intermediate phases. To satisify these requirements, an outline of the experimental approach is as follows:

- Prepare a well-defined series of oxide precursors based on the hexagonal molybdate *h*-MoO_3 with V progressively substituting Mo to give a mixed Mo/V oxide precursor *h*-$Mo_{1-x}V_xO_3$
- Characterise the oxide precursors using: XRD, N_2-physisorption, SEM (& SEM-EDX), TEM and TG-DSC
- Carburise the oxide precursors using CH_4/H_2 in a TPR-carburisation based on the preparation by Oyama *et al.*[3]
- Monitor the evolution of of crystalline phases using *in situ* XRD during the temperature-programmed reduction-carburisation
- Carry out kinetic studies on the oxide reduction-carburisation using different heating rates with quantative analysis of the outgas
- Use solid-state kinetic modeling to gains insight into the mechanism of reduction-carburisation by comparison with the *in situ* XRD data
- Characterise the carbide products using: XRD, N_2-physisorption, CHN analysis, SEM (& SEM-EDX), XPS, TEM and TG-DSC
- Develop a scaled-up synthesis method based on the understanding gained from plug-flow experiments

In the study of molybdenum carbide, the preparation of well-defined material with homogeneous surface properties is important because the reactive nature of the surface makes it difficult to characterise exactly. Only limited information can be inferred if the chemical nature of the surface is dynamic or unknown. On the basis of these criteria we can generally define the ideal carbidic surface as being representative of the bulk structure of the material, ie. an interstitial arrangement of only molybdenum and carbon at which the surface is ideally terminated as a crystallographic plane, and also importantly, free of adventitious carbon species such that every surface site is accessible to reaction. Previous studies have shown that this can be achieved through the judicious use of thermodynamic parameters derived from an analysis of the Gibbs free energy equations for carbon formation and methane reforming.[3]

2.2 Experimental

2.2.1 Synthesis

2.2.1.1 Synthesis of precursor oxides

The series of *h*-MoO_3 precursors (of the form *h*-$Mo_{1-x}V_xO_3$) was prepared in an automated laboratory reactor (LABMAX, Mettler, Toledo) by the precipitation of a 0.032 M aqueous solution (total metals) of ammonium heptamolybdate $(NH_4)_6Mo_7O_{24}\cdot 4H_2O$ (Merck, > 99%) and ammonium metavanadate $(NH_4)VO_3$ (Aldrich, > 99%) at constant pH and temperature. The precipitation pH of the mixed AHM/AMT solutions was determined using a Mettler DL77 laboratory titrator at the desired temperature (75°C) titrated with 1M HNO_3. As can be seen in Figure 2.1 the curves are not very sharp, but from the differential it was decided to choose pH = 0.5.

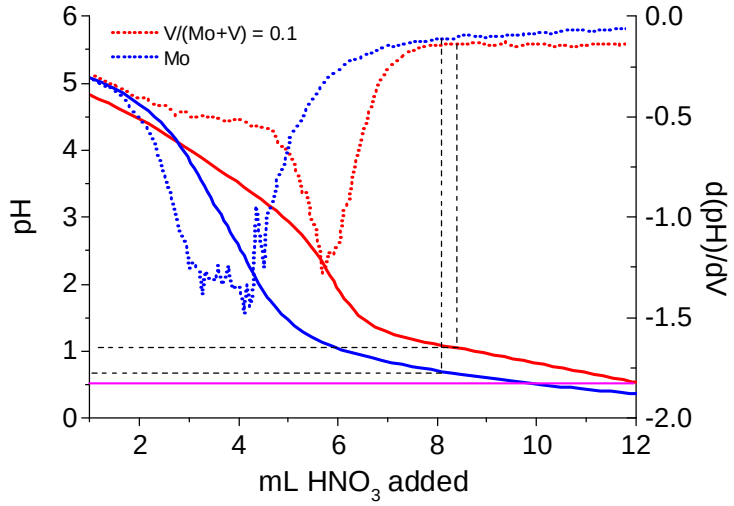

Figure 2.1: Titration curves for 1M (metals basis) AHM (blue) and AHM/AMT (red) solutions at 75°C.

The metal-containing solution (1000mL) was automatically added stepwise to aqueous HNO_3 (ph = 1; 300mL) maintained at a temperature of 75°C throughout addition. The pH was maintained at 0.5 by automated monitoring and via addition of 3M HNO_3 from a reserve. The precipitate was aged for 2 hours at 75°C, collected by filtration, washed with water (2 x 100mL) and washed once with EtOH (100mL) before drying overnight at 80°C. It was observed that molybdenum was preferentially precipitated from the reactant solution and therefore the applied and received Mo/V ratios, and the physical properties of the oxides, are detailed in Table 2.2.

An example of the LABMAX protocol can be seen in Figure 2.2. The protocol can be interpreted as follows; 1) initial acification to pH = 5 (red line); 2) addition of metal salt solution (1000 g over 100 mins); 3) nucleation → t = 03:40; 4) precipitation (endothermic event) @ 03:40; 5) post-aging at temperature.

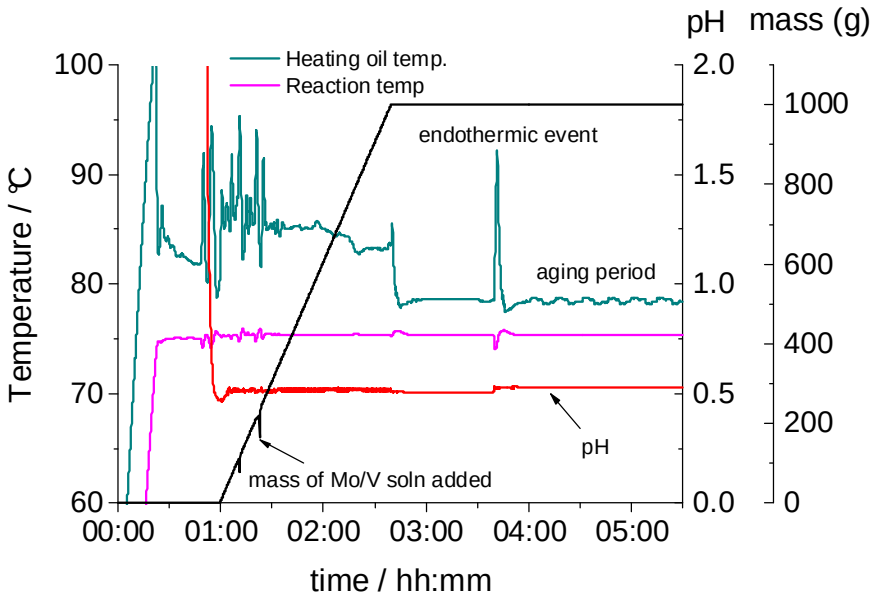

Figure 2.2: A typical LABMAX protocol for the synthesis of *h*-$Mo_{1-x}V_xO_3$.

α-MoO_3 used for *in situ* XRD experiments was obtained by spray drying a 0.3 M solution of ammonium heptamolybdate (AHM) in a Büchi Mini Spray Dryer B290 (Inlet temperature = 433 K; Outlet temperature = 376 K; Pumping rate = 15% of maximum) followed by calcination in a muffle furnace at 773 K for 10 hours. For the temperature-programmed reduction-carburisation experiments *α*-MoO_3 was used as received (Sigma Aldrich).

2.2.1.2 In situ reduction-carburisation of Mo/V oxides

The carbide materials were synthesised *via* a temperature-programmed reduction-carburisation (TPR-C) under a flowing atmosphere; 50 ml/min He (> 99.9%), 40 ml/min H_2 (> 99.9%), and 10 ml/min CH_4 (> 99.9%). The reduction and subsequent phase formation was observed *in situ* using powder XRD. The precursor oxides (170–230 mg) were loaded into the *in situ* cell and initially ramped to 300°C (no structural changes were observed) where a diffraction pattern was recorded under isothermal conditions. Subsequently, the temperature was ramped at 1°C/min and scans were recorded isothermally every 50°C to a final hold temperature of 750°C for 4 hours

before cooling to room temperature at which point a final scan was recorded (see Figure 2.3). The sample was passivated under 0.5 % O_2 in He (total flow 100 ml/min) for 2 hours before removing the sample. The conditions of the *in situ* experiment were chosen in order to balance the temperature resolution and the overall heating rate (0.56°C/min) with the apparatus limitations, as well as recording a functional 2θ range for Rietveld analysis.

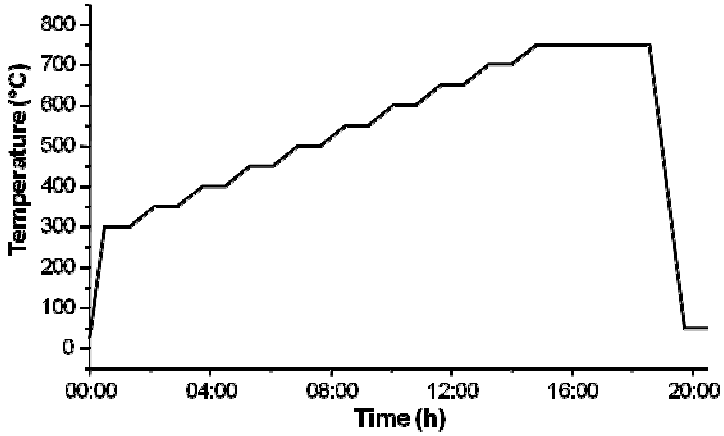

Figure 2.3: Temperature program for in situ XRD studies.

The *in situ* powder XRD studies were performed in a STOE Theta/Theta diffractometer with reflection geometry (secondary graphite monochromator, Cu $K\alpha_{1+2}$ radiation (λ = 1.5419 Å), scintillation counter) equipped with an Anton Paar XRK 900 *in situ* XRD cell. *In situ* scans were carried out in the range 22° < 2θ < 43° for the temperature program and a longer scan (5° < 2θ < 60°) at room temperature after passivation. The temperature program was combined with analysis of the outgas stream using a Pfeiffer OmniStar quadrupole mass spectrometer.

2.2.1.3 Large scale preparation of $(Mo_{1-x}V_x)_2C$

The goal of upscaling was to retain the high surface area of materials synthesised *in situ* and to produce catalytically active carbides with low levels of adventitious carbon for materials testing and use in future studies. The conditions were therefore modified with respect to the *in situ* synthesis.

In this study we have utilised a custom-built rotary furnace produced by Xerion, combined with a bespoke quartz reaction vessel which integrates by means of a stainless steel flange with attached KF butterfly valves. The furnace and reactor

assembly is contained within a sealed stainless steel hood which is continuously purged with N2 gas to provide an inert shield in case of rupture. A gas manifold assembly allows for the purging of the reaction chamber and a flexible range of gaseous atmospheres. The temperature of the furnace is moderated by a Eurotherm 2704 PID controller with a three zone furnace coupled with feedback from three embedded thermopiles. The isothermal zone of the reactor is measured across the central zone of the reactor (12–14cm) and is measured to be +/- 5°C with an offset of -25°C from the PID displayed values.

The materials synthesis was scaled up to multi-gram (~10g) quantities using a custom built rotary furnace with 3 heating zones (Xerion Advanced Heating GmbH), equipped with mass flow controllers for Ar, O_2, H_2 and CH_4 (Bronkhorst) and a PID heating controller (Eurotherm 2704). In each case 10.0 g of *h*-$Mo_{1-x}V_xO_3$ precursor was introduced to the modified SiO_2 tube reactor and subjected to a temperature program under flowing CH_4/H_2 (1:4; 450 sccm) as follows: RT → 350°C @ 1°C/min; 350°C → 500°C @ 0.2°C/min; 500°C → 550°C @ 1°C/min; 550°C → 675°C @ 0.2°C/min ; hold 4 hours → RT. Following the temperature program, the KF butterfly valves on the flange ends were closed and the sealed reactor was introduced to the glove box. A photograph of the furnace set-up as well as the air-free transfer device is shown in Figure 2.4.

Figure 2.4: (left) 'Hindenburg' rotary furnace used for upscaled synthesis of $(Mo_{1-x}V_x)_2C$. (right) Custom-designed flanges for air-free reactor transfer.

2.2.1.4 Temperature programmed reduction-carburisation

Temperature-programmed reduction-carburisation experiments were carried out using 500mg of precursor oxide in a SiO_2 U-tube reactor heated in the isothermal zone of a tube furnace (Carbolite). The heating was controlled by a PID controller (Eurotherm 2416) and the temperature monitored by a thermocouple in the reactor bed. The gas analysis was carried out with heated lines using an in-line IR CO_x detector (ABB) and a mass spectrometer (Pfeiffer Omnistar) to monitor reaction products. The oxides were carburised in a flowing atmosphere of 200 sccm $Ar/H_2/CH_4$ (5:4:1) under temperature ramps of 1, 2 & 5 °C/min to a final hold temperature of 675°C for two hours. Quantitative product analysis for H_2O and CO_x was carried out by normalising the MS signals to the calibrated CO_x detector and by summation of the total oxygen content of the precursor oxides.

For solid state kinetic modeling of the reduction process, the TPR data was analysed using 'NETSCH — Thermokinetics' software to give the conversion-dependent activation energy using the technique of Ozawa-Flynn and Wall.[29] The derived activation energies were subsequently used to generate reaction curves for $\theta/\theta_{0.5}$ vs. α for mechanism comparison using the masterplot method.

2.2.1.5 In situ and ex situ characterisation

The *in situ* powder XRD studies were performed in a STOE Theta/Theta diffractometer with reflection geometry (secondary graphite monochromator, Cu $K\alpha_{1+2}$ radiation (λ = 1.5419 Å), scintillation counter) equipped with an Anton Paar XRK 900 *in situ* XRD cell. *In situ* scans were carried out in the range $22° < 2\theta < 43°$ for the temperature program and a longer scan ($5° < 2\theta < 60°$) at room temperature after passivation. The temperature program was combined with analysis of the outgas stream using a Pfeiffer OmniStar quadrupole mass spectrometer.

Ex situ powder XRD was carried out on the precursor oxides and for full scans on the as-synthesised carbides using a STOE STADI P diffractometer in transmission geometry (primary focusing Ge monochromator, Cu $K\alpha_1$ radiation (λ = 1.5406 Å), linear position sensitive detector). Full pattern analysis of the XRD data was performed using TOPAS software.[30] The pattern fit for each material was carried out using a Pawley refinement based on a hexagonal unit cell. The information on

crystallite sizes was subsequently obtained as L_{Vol}-IB values (volume-weighted average column height based on integral breadth) according to the double-Voigt approach.[31]

Differential scanning calorimetry (DSC) combined with thermo-gravimetric analysis (TGA) was used to study the thermal decomposition of the precursor oxides. The study was carried out on a Netsch Jupiter STA 449C calorimeter equipped with a Pfeiffer OmniStar quadrupole mass spectrometer for analysis of out gases.

The carbon content of the carbide samples was measured by CHN analysis carried out using a FlashEA 1112 Elemental Analyzer. In the case of V-containing materials pure oxygen is used to effect total combustion of the samples.

All oxide and carbide samples were analysed by full N_2-adsorption-desorption isotherms using a Quantachrome Autosorb AS-6B measured after a pre-treatment in vacuum at 200°C for 2 hours. The specific surface areas were determined applying the Brunauer-Emmet-Teller (BET) method using 11 data points in the relative pressure p/p_0 range between 0.05 and 0.3. The pore size distributions were calculated using the Barrett-Joiner-Halenda (BJH) method from the desorption branch of the N_2 isotherm.

Analysis of the carbide morphologies was investigated on a HITACHI S 4000 FEG scanning electron microscope (SEM). To determine elemental concentrations, electron dispersive X-ray spectroscopy (EDX) was carried out using the EDAX DX-4 analysis system.

Transmission electron microscopy (TEM) investigation of the Mo/V carbide was carried out with a Philips CM 200 FEG (Philips, Eindhoven, The Netherlands) TEM operated at 200 kV and equipped with a Gatan Image Filter (Gatan, Warrendale, PA) and a charge-coupled device (CCD) camera.

2.3 Results and discussion

2.3.1 Hexagonal precursor oxides

h-MoO_3 is a metastable, complex molybdate defined by zigzag edge-sharing MoO_6 octahedral chains which extend down the length of the *c*-axis and are edge connected

to form a superstructure in which hexagonal channels travel down the length of the c-axis. The channels are partially occupied by monovalent cationic species (H_3O^+, NH_4^+, K^+, Rb^+, Cs^+ are reported) that are intrinsic to the stability of the structure and presumably serve a templating role for the crystallization of the phase. The synthesis was first described by Olenkova in 1981 and subsequently characterised in detail by Caiger.[32-34] In contrast, $K_{0.13}Mo_{0.87}V_{0.13}O_3$, a mixed Mo/V analogue is described by Darriet *et al.* [35] in 1973 (see Figure 2.5) and the phase stability of $H_{0.13}Mo_{0.87}V_{0.13}O_3$ is more recently demonstrated by Dupont.[36, 37] In this study we have used a synthetic method resulting in NH_4^+-containing mixed Mo/V molybdates previously described by Mougin *et al.*[14] The characterisation and description of this oxide series are outlined in Table 2.2.

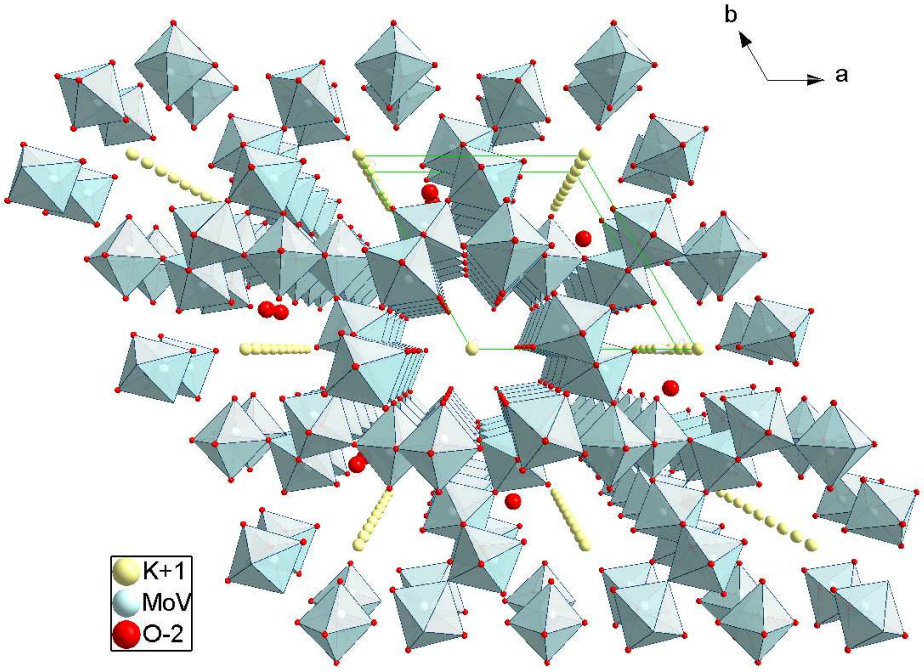

Figure 2.5: Crystal structure of $K_{0.13}Mo_{0.87}V_{0.13}O_3$ as decribed by Darriet and Galy.[35]

As can be seen from Figure 2.6(a), the result of V substitution is an increase of stability of the structure to oxidative degradation (*h*-MoO_3 → *α*-MoO_3), which is observed in the profiles of the TG-DTA analysis of the oxides 0Vox and 8Vox. The increase in stability is observed to increase to a maximum at ca. 10% vanadium substitution and is in accordance with a previous study.[14] The case for a statistical distribution of V atoms throughout the Mo sublattice is further strengthened in Figure 2.6(b) which shows the divergence of the overlapping [120] and [101] diffraction peaks at $2\theta = 25.8°$ with increasing vanadium content.

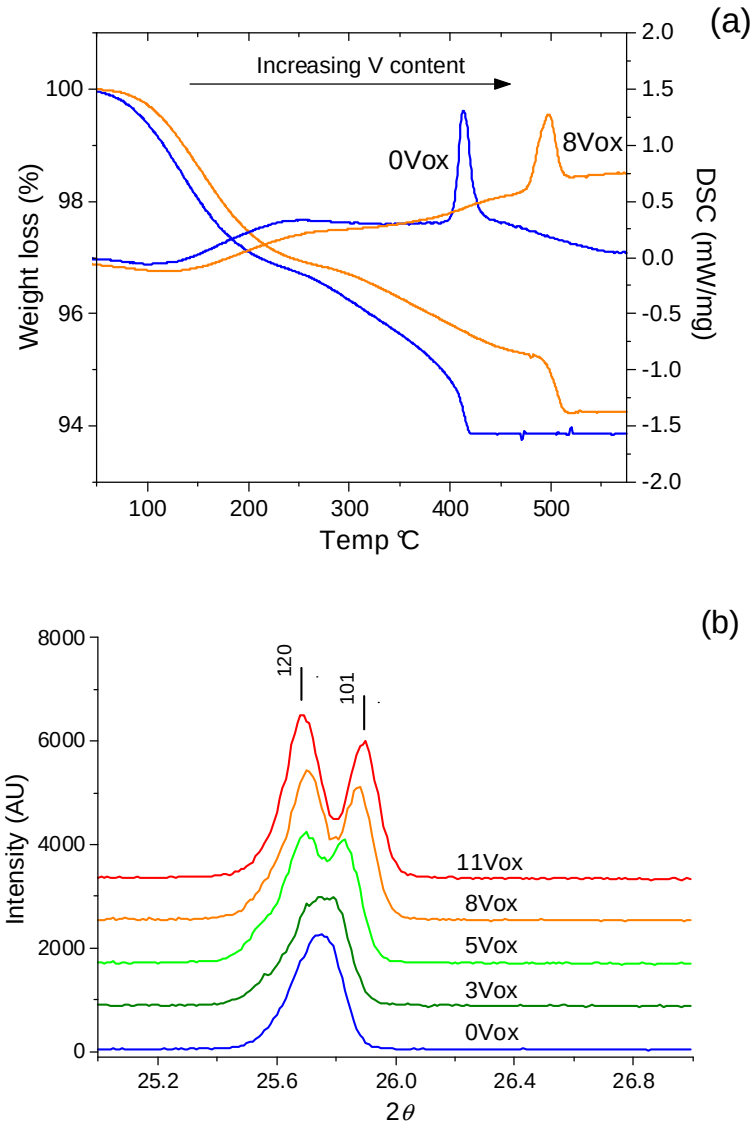

Figure 2.6: (a) TGA-DSC traces for the oxidative degradation (*h*-MoO_3 → *α*-MoO3) of precursor oxides 0Vox and 8Vox. (b) X-ray diffraction patterns of the precursor oxides (0Vox-11Vox) between 25° < 2*θ*< 27° illustrating the divergence of overlapping peaks with increasing V content.

The series of Mo-V precursors based on *h*-MoO_3 structure were comparatively analysed using a Rietveld refinement carried out using TOPAS software. The structural model used is that found by Galy *et al.* for the compound $K_xMo_{1-x}V_xO_3$. The model has been modified to include NH_4^+ in place of K^+ and the parameters refined. It was observed that especially in the case of V-substituted oxides, the structural model best approximated the pattern when a mixture of two identical phases was taken into account. The inclusion of this minority phase (20-30%) helped to account for various shoulder peaks and asymmetric peak shapes. The two phases are

labeled H^1 (majority) and H^2 (minority) for distinction (Table 2.1). From Figure 2.7a we can se from the Rietveld fit for 8Vox that the fit is reasonable but in some cases does not fully describe the peak shapes. The plots in Figure 2.7b & c help us to understand this trend further: for the 'c' parameter the oxide series obeys Vegard's law[38] with regards to a linear relationship between the dopant concentration and the lattice parameter and the trend is observed to be identical for both calculated phases. In Figure 2.7b however we see a relation between the phases H1 and H2 with a distinct maximum for 5Vox. In this case the 'a' parameter describes the a-b lattice plane in which the octahedra are hexagonally arranged. This plane can be expected to swell/shrink depending upon the occupation of the channels with H_2O and NH_4 and we therefore see this variation which is explainable by increasing cation (NH_4^+) density in the hexagonal channels with V content. This reaches a maxima and then shrinks as the influence of vanadium's smaller ionic diameter increasingly dominates.

2.1: Lattice parameters for the *h*-Mo(V)O_3 series as determined by Rietveld fitting

Sample	H1%	H2%	a (H1)	c (H1)	a (H2)	c (H2)
0Vox (6600)	75	25	10.5750(2)	3.7271(1)	10.6107(4)	3.7281(3)
3Vox (6702)	73	27	10.5735(2)	3.7231(1)	10.6221(4)	3.7232(3)
5Vox (6271)	76	24	10.5861(2)	3.7201(1)	10.6324(4)	3.7193(3)
8Vox (6697)	78	22	10.5791(1)	3.7120(1)	10.6189(4)	3.7117(3)
11Vox (6601)	80	20	10.5838(1)	3.7091(1)	10.6143(5)	3.7095(3)

The observed difference in the cell parameter (~0.05Å) as well as the imperfect Rietveld fit may be explained by a bicontinuous variation in the cell parameter generated by slight inhomogeneieties in the crystalline structure. This is likely to due inhomogeneieties which originate from the point of nucleation. We see however that the 'c' parameter provides us a better measure of the statistical distribution of V throughout the structure as the layer-layer distances in the c-axis exhibit the same trends in variation.

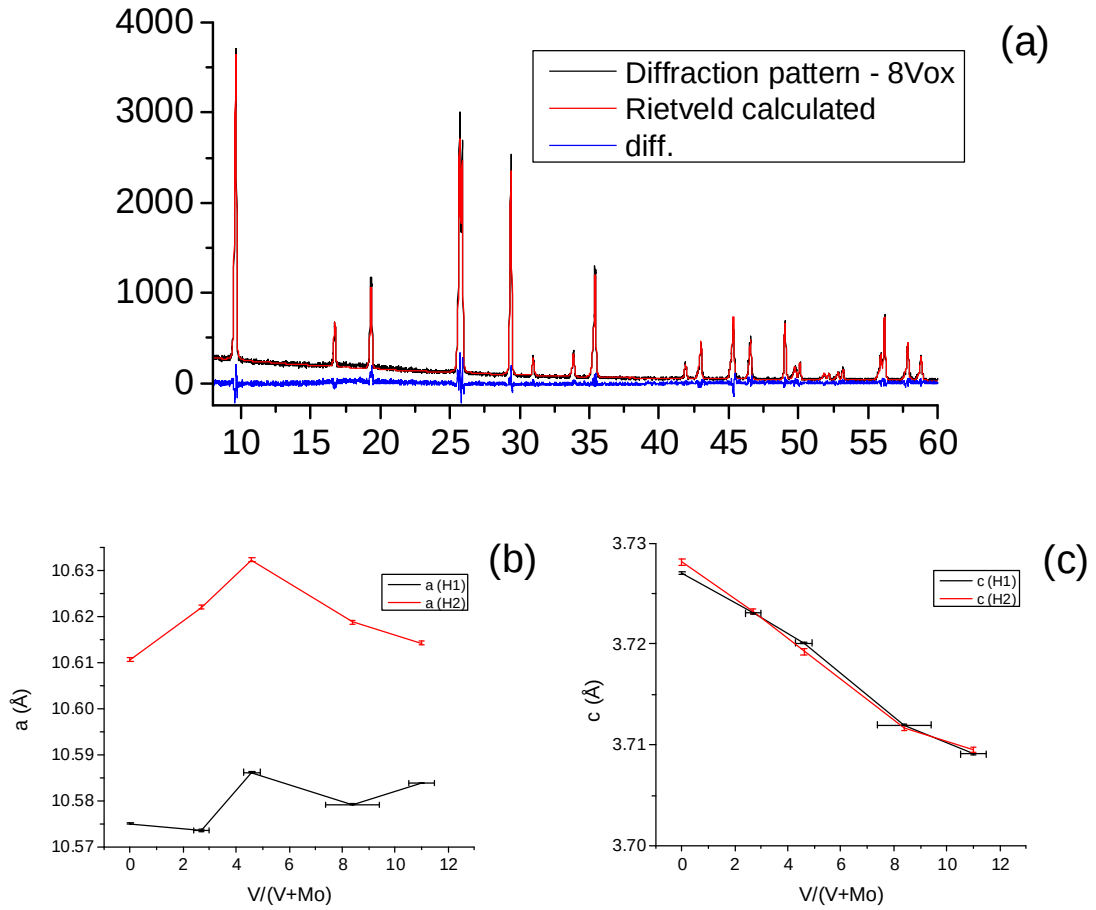

Figure 2.7: (a) Rietveld refinement for 8Vox; (b) 'a' parameter vs. V content as calculated for the phases H1 and H2 (c) 'c' parameter vs. V content as calculated for the phases H1 and H2

As one would expect, the crystalline morphology of the hexagonal oxides, seen in Figure 2.8 2.8, is hexagonal prismatic. Increasing vanadium content distorts the crystal habit, tending towards flattened hexagonal crystallites of a more polydisperse nature. The nucleation-precipitation-aging growth of the oxides results in spherical polycrystallites ca. 100-150μm in diameter with flat terminations and an observed decrease in packing density with increasing vanadium content.

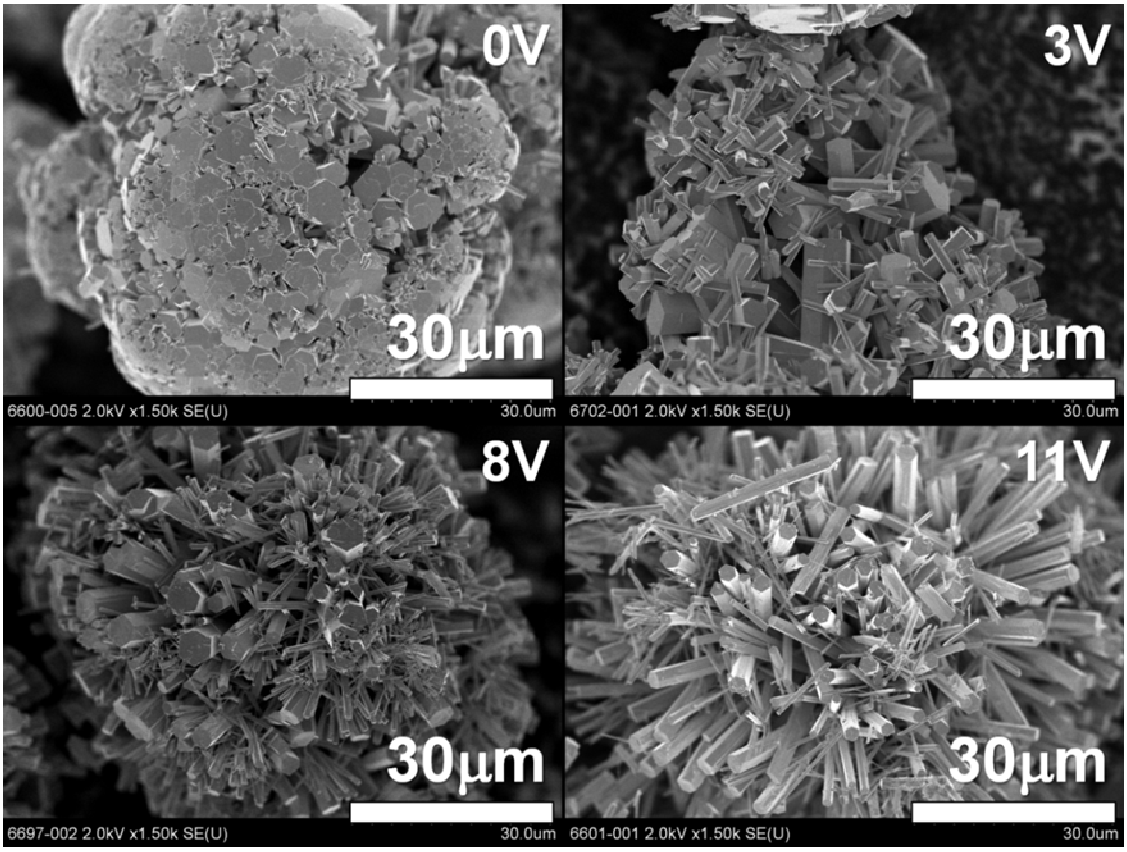

Figure 2.8: Scanning electron micrographs of the hexagonal oxides 0Vox, 3Vox, 8Vox & 11Vox.

This is in accordance with the physical attributes of the oxides, varying from the denser, white, crystalline *h*-MoO_3 to a yellow-orange for the doped materials. The surface areas (see Table 2.2), as calculated by the Brunauer-Emmet-Teller (BET) isotherm from N_2 adsorption, are uniformly low (< 1 m^2/g) with the exception of the highest loaded oxide 11Vox, which is slightly higher at 2 m^2/g. This sample shows evidence of vandadium saturation in the TG-DTA plots and the crystal morphology exhibits some delamination and structural distortions from the hexagonal geometry which may account for the higher surface area.

We can conclude that we have a well-defined series of mixed Mo/V oxide precursors. These materials form the basis for this study on the structural and mechanistic aspects of the reduction-carburisation of Mo/V oxides.

Table 2.2: Properties of the precursor oxides α-MoO_3 (Rox) , h-MoO_3 (0Vox), and h-$Mo_{(1-x)}V_xO_3$ (3Vox–11Vox)

[a] as determined by SEM-EDX

[b] as determined by Rietveld refinement

Precursor ID	Phase	Internal ID	x applied V/(V+Mo)* 100	x recieved[a] V/(V+Mo)* 100	Lattice parameters[b]		Oxidation temperature[c] h->α (°C)	BET surface area (m^2/g)
					a (Å)	c (Å)		
Rox	α-MoO_3	5201	-	0	-	-	-	1.6
0Vox	h-MoO_3	6600	0	0	10.5750(2)	3.7271(1)	403	<1
3Vox	h-$Mo_{(1-x)}V_xO_3$	6702	4	2.7±0.3	10.5735(2)	3.7231(1)	434	<1
5Vox	h-$Mo_{(1-x)}V_xO_3$	6271	10	4.6±0.3	10.5861(2)	3.7201(1)	452	1.1
8Vox	h-$Mo_{(1-x)}V_xO_3$	6697	15	8.4±1	10.5791(1)	3.7119(1)	479	<1
11Vox	h-$Mo_{(1-x)}V_xO_3$	6601	20	11±0.5	10.5838(1)	3.7091(1)	481	1.8

[c] as determined by thermo-gravimetric analysis

Table 2.3: Synthesis conditions and physical properties of resultant carbides Rc, 0Vc–11Vc.

[a] as calculated from a Pawley fit carried out using TOPAS software

[b] As determined by EDX

[c] L_{Vol}-IB – derived from Pawley refinement

Sample name	Int. ID	Precursor ID	Final temp. (K)	Phase	Lattice parameters[a] (Å)		V/(V+Mo) *100[b]	C theor. (%w/w)	C meas. (%w/w)	Crystal size[c] (nm)	BET (m^2/g)	Pore volume (cc/g)
					a	*c*						
Rc	5661	Rox	1023	Mo_2C (*hcp*)	3.008(1)	4.761(1)	0	5.89	-	6.3	71	-
0Vc	6713	0V (6600)	1023	Mo_2C (*hcp*)	3.007(1)	4.778(1)	0	5.89	13.6	4.9	80	0.152
3Vc	6708	3V (6702)	1023	Mo_2C (*hcp*)	3.007(1)	4.818(2)	2.7±0.7	5.97	14.1	3.8	99	0.139
5Vc	6704	5V (6271)	1023	Mo_2C (*hcp*)	3.006(1)	4.797(2)	4.4±0.5	6.01	13.7	4.1	107	0.175
8Vc	6703	8V (6697)	1023	Mo_2C (*hcp*)	3.004(1)	4.786(2)	8.0±0.7	6.11	13.5	3.8	101	0.194
11Vc	6701	11V (6601)	1023	Mo_2C (*hcp*)	3.017(1)	4.857(3)	11.3±1	6.18	13.2	3.3	97	0.184

2.3.2 Carburisation of hexagonal Mo/V oxides

In the case of all of the precursor oxides (Rox, 0Vox—11Vox) it was observed that hexagonal β-Mo_2C is obtained as a result of temperature-programmed reduction-carburisation under H_2/CH_4 (Figure 2.9). The resulting carbides, prepared in the *in situ* cell of the X-ray diffractometer are referred to as; Rc, 0Vc, 3Vc, 5Vc, 8Vc, 11Vc and the physical properties are outlined in Table 2.3.

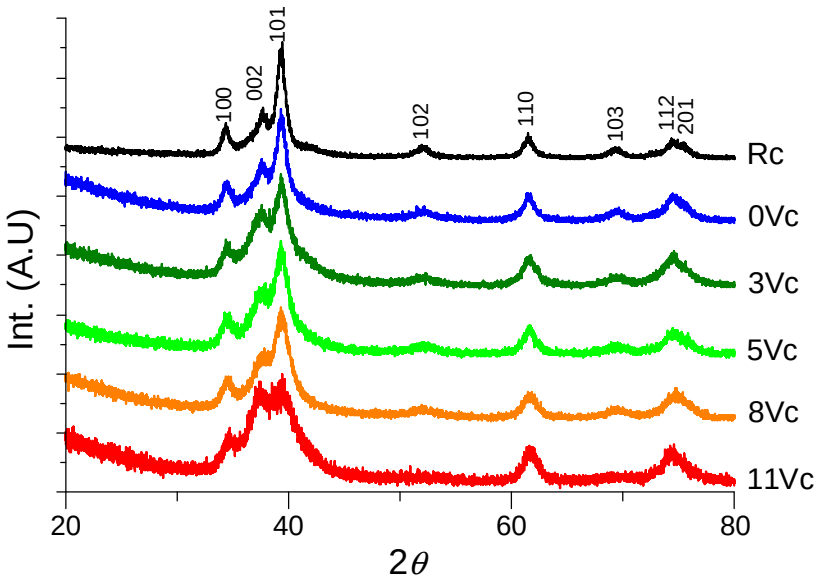

Figure 2.9: Normalised powder X-ray diffractograms of the product carbides Rc, 0Vc – 11Vc measured at T = 25°C.

In Figure 2.10, the phase evolution of the precursor reduction-carburisation is illustrated by waterfall plots of the diffraction patterns recorded *in situ* at 50°C intervals. The reduction proceeds from the precursor oxide structure (α-MoO_3, *h*-MoO_3) consecutively reducing to MoO_2 between 350–450°C and to the carbide between 550–600 °C. From the plots it is observed that the temperature observed for the initial reduction of the *h*-$Mo(V)O_3$ precursors to $Mo(V)O_2$ increases with vanadium content.

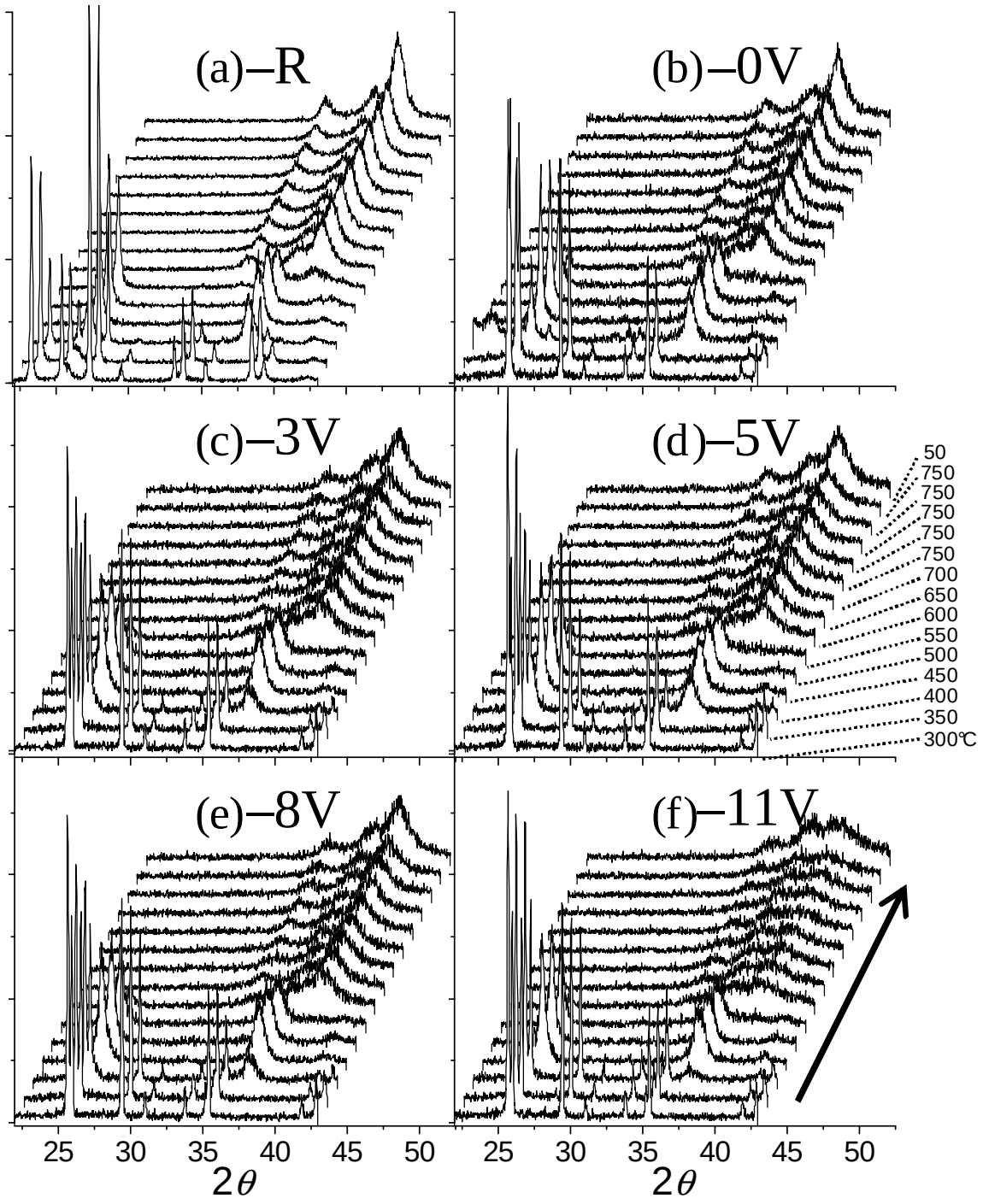

Figure 2.10: Evolution of *in situ* XRD patterns during the temperature programmed reaction under He-H_2-CH_4. (a) Rox → Rc; (b) 0Vox → 0Vc; (c) 3Vox → 3Vc; (d) 5Vox → 5Vc; (e) 8Vox → 8Vc; (f) 11Vox → 11Vc.

In Figure 2.11, the diffraction patterns of the precursor oxides are presented as a top-down plot of 2θ vs. temperature with the normalised square root of the intensity to enhance peak visibility. From this plot it is evident that the stability of the oxides to reduction increases with vanadium loading. At this temperature resolution no difference in the final carburisation temperature is observed, however, significant

peak broadening is observed for the carburisation of α-MoO_3 *cf.* *h*-MoO_3 and increasingly broad diffraction peaks are seen with dopant vanadium concentration. Analysis of the products physical properties is presented in the next section.

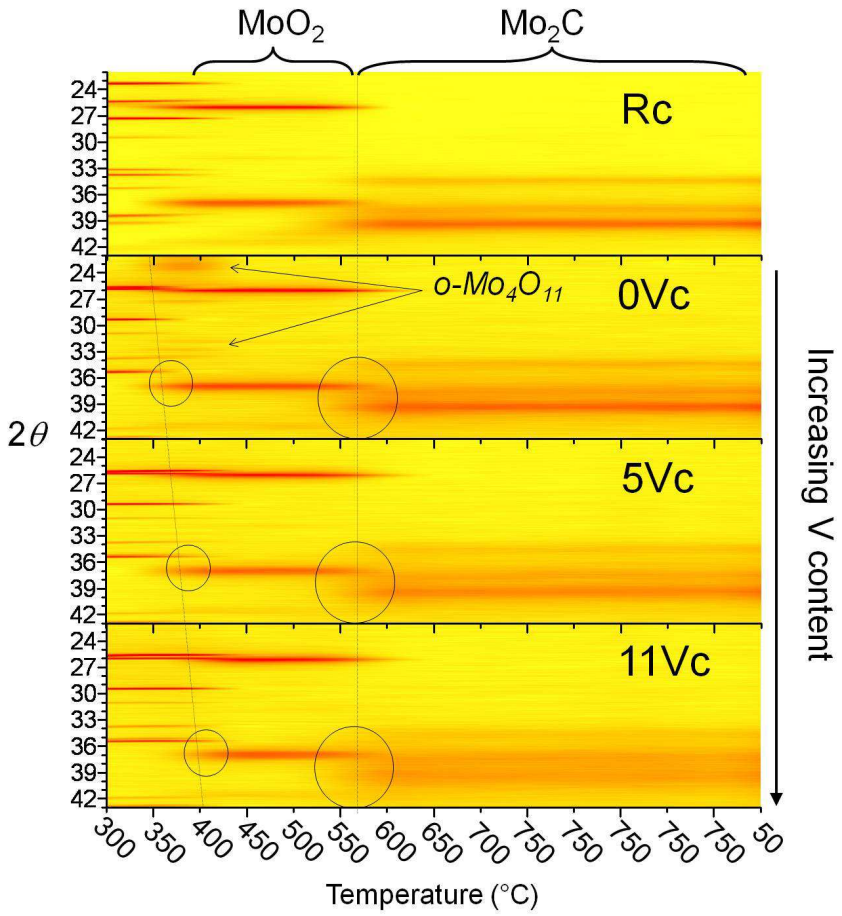

Figure 2.11: Contrast plot of the normalized √Intensity vs. temperature over the phase evolution of R, 1, 3 & 5 from MoO_3 → (Mo_4O_{11}) → MoO_2 → Mo_2C. The outlined areas emphasise the observed phase changes in the *h*-Mo(V)O_3 reduction-carburisation.

In the top-down plot (Figure 2.11) for 0Vc there is observed an intermediate phase not observed for the other precursors. To determine the nature of this intermediate phase the *in situ* carburisation experiments were repeated with an offset temperature of 25°C to interpolate the data and provide an effective increase in the time resolution. The intermediate scan at T = 375°C is shown in Figure 2.12 and the unknown phase was determined to be orthorhombic *o*-Mo_4O_{11}, which has also been observed by Choi *et al.* as an intermediate in the reduction-carburisation of a structurally similar ammonium molybdate.[39]

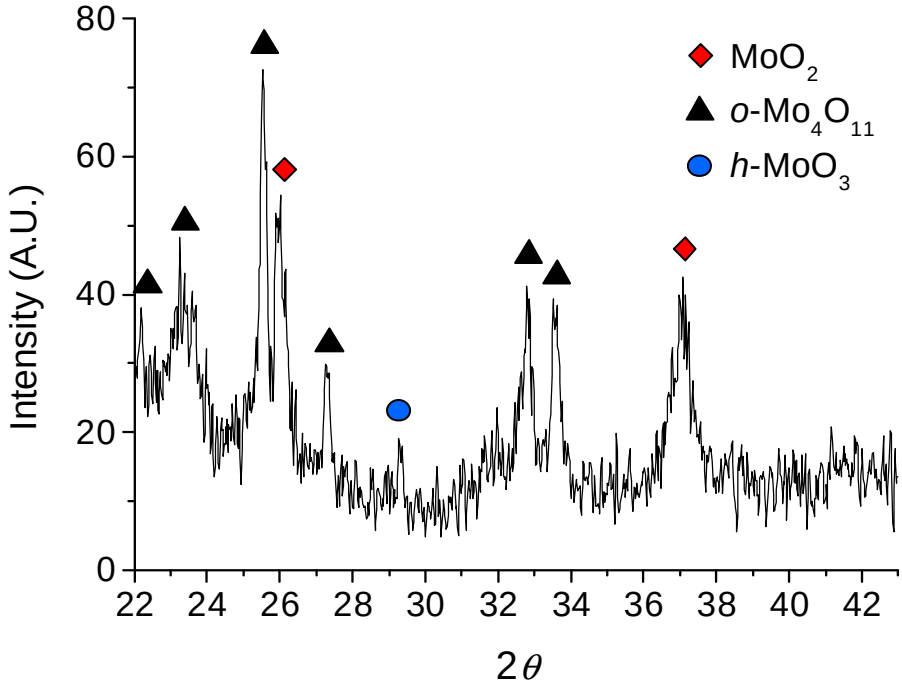

Figure 2.12: *In situ* XRD scan of *h*-MoO_3 (0Vox) TPR-carburisation at 375°C showing intermediate *o*-Mo_4O_{11} phase.

Formation of the closely related monoclinic *m*-Mo_4O_{11} can be observed in the reduction of α-MoO_3 → MoO_2, the first step in the industrial production of molybdenum metal. The role of *m*-Mo_4O_{11} in this reaction was long believed to be as an intermediate in the reduction of Mo^{VI} → Mo^{IV} which is thermodynamically stabilised under certain conditions of temperature and H_2 partial pressure.[40] More recently this has been disputed and it is demonstrated in separate studies to be a result of the comproportionation of α-MoO_3 and MoO_2 via an oxygen exchange mechanism.[40-42] It was shown by Ressler *et al.* that the reaction:

$$3MoO_3 + MoO_2 \rightarrow Mo_4O_{11}$$

occurs in reducing conditions at temperatures > 425°C depending on the partial pressure of H_2.[40] In the same study, an Arrhenius plot generated from a series of isothermal reduction experiments gives two apparent activation energies for the reduction depending on the temperature. At temperatures > 425°C, the reduction MoO_3 → MoO_2 is observed to occur with apparent activation energy of 103kJ/mol. Below 425°C the reduced activation energy of 34kJ/mol is observed. It was concluded from this study that the activation energies corresponded to the kinetic regime with

and without the by-production of Mo_4O_{11} respectively. This would imply that the reduction of Mo_4O_{11} to MoO_2 is kinetically more difficult than the direct reduction of MoO_3.

The question as to why Mo_4O_{11} is not usually observed in the reduction of α-MoO_3 (also not in this study) is addressed by Lalik[43] in a recent study of the kinetics. It is proposed that the layered MoO_3 structure is reduced in a topotactic reaction to MoO_2 via a shear mechanism of the interlayer planes of α-MoO_3. The resulting interfacial boundary between the Mo(VI) and Mo(IV) may then collapse to the intermediate Mo_4O_{11} given sufficient oxygen mobility. The thickness of this interfacial layer (and therefore the XRD visibility) is dependent upon the external conditions.

2.3.3 Temperature-programmed reduction-carburisation

To obtain further understanding of the mechanistic picture in our system TPR-carburisation profiles were obtained to determine the overall extent of reduction α. This extent was calculated by integrating the total oxygen which was observed to evolve from the structure according to the overall equations:

$$MoO_3 + H_2 \rightarrow MoO_2 + H_2O \qquad (1) \qquad T = 300–500°C$$

$$2MoO_2 + CH_4 + 2H_2 \rightarrow Mo_2C + 4H_2O \qquad (2) \qquad T > 550°C$$

As well as H_2O, CO is observed to evolve during (2) from steam reforming of CH_4 over the readily forming carbide via outgassed H_2O. Additionally, a small amount of CO_2 is detected due the water-gas shift reaction:

$$CH_4 + H_2O \rightarrow CO + 3H_2 \qquad (3)$$

$$CO + H_2O \rightarrow CO_2 + H_2 \qquad (4)$$

The total oxygen content of the precursor systems was calculated from the mass loss observed for the oxides upon heating in synthetic air to 500°C (decomposed to α-MoO_3*) and derived from the stoichiometry Mo:O = 1:3 (*V:O = 2:5) to give a defined oxygen content for each sample. This was also correlated against the observed mass loss after reaction. The extent of reduction at each point was determined by integration of the total of the MS signals at m/z = 18 & 28 which were normalised

relative to the known CO concentration from the CO_x IR detector. For simplicity CO_2 can be disregarded as it was found to contribute < 1% to the total oxygen evolved.

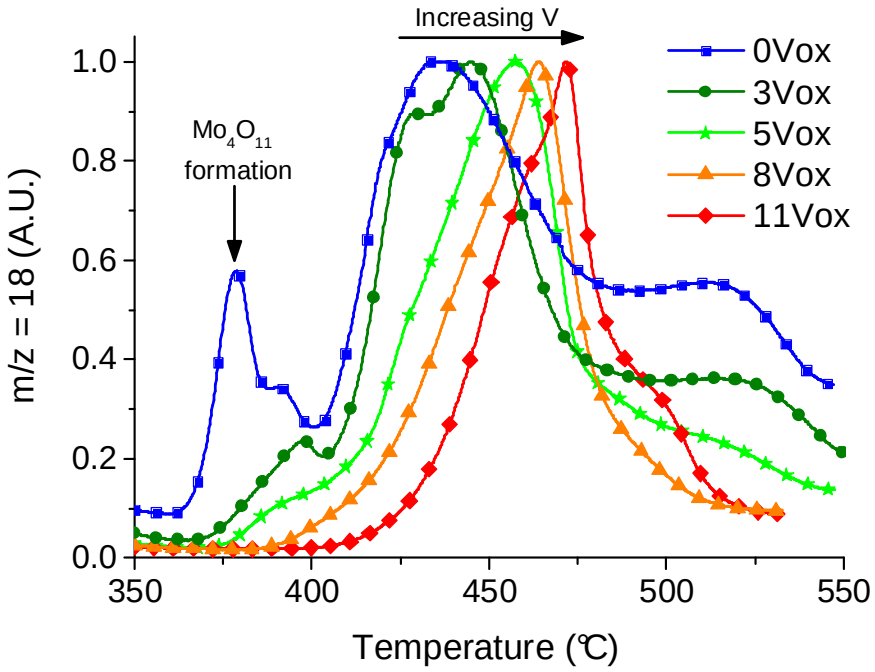

Figure 2.13: Temperature-programmed reduction-carburisation profiles of the normalized H_2O (m/z = 18) signal for *h*-$Mo_{1-x}V_xO_3$.

Figure 2.13 shows the evolution of H_2O (the only O-containing educt detected in the initial reduction [1]) for the hexagonal oxide series. In agreement with the *in situ* XRD study we observe an increase in the water peak to higher temperatures with increasing V content. Additionally, it is apparent that at lower vanadium loadings there are additional peaks which appear to be related to the observed '*o*-Mo_4O_{11}' phase at 375–400°C. This peak disappears entirely for the 8Vox sample which also presents the most uniform reduction peak. The 11Vox shows a slight shoulder at higher temperatures (475-500°C) which may be related to the reduction of VO_x moieties.

In Figure 2.14 the reduction profiles vs. temperature at different heating rates are contrasted for the α-MoO_3, 0Vox and 8Vox samples. Comparison of each reduction profile at 1°C/min shows most clearly the influence of the precursor structure on the reduction kinetics. For the reduction of α-MoO_3 (Figure 2.14a) an initial exponential increase in reduction is observed between 375 – 425°C.

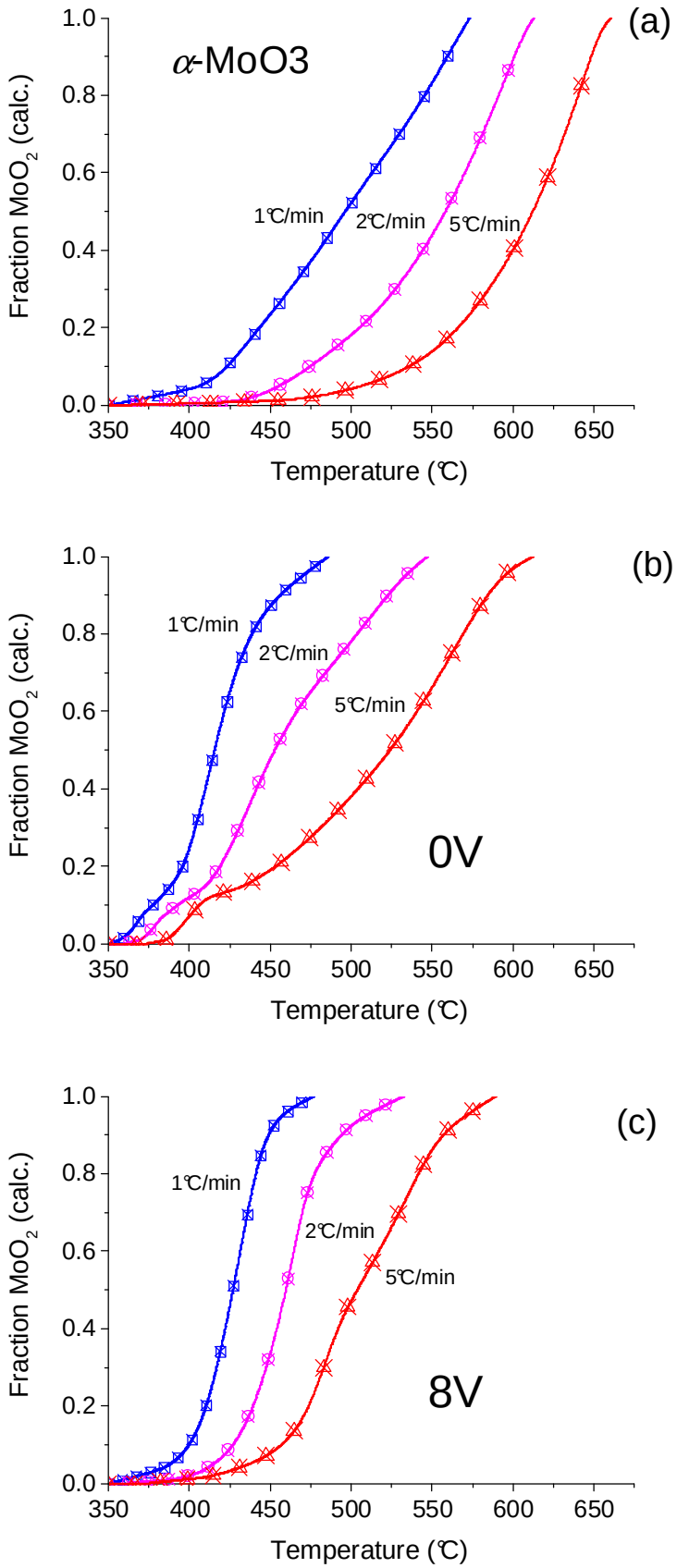

Figure 2.14: Extent of reduction vs. temperature at different heating rates for: (a) α-MoO_3, (b) 0Vox and (c) 8Vox.

This could be associated with an increase in reacting surface area, followed by an almost linear reduction to MoO_2. This is in contrast to the 0Vox sample (Figure 2.14b) which exhibits an initial fast reduction to orthorhombic Mo_4O_{11} between 350 – 400°C followed by a relatively steep reduction curve to MoO_2 which is almost complete by 425°C. The vanadium containing precursor 8Vox (Figure 2.14c) has a delayed onset of reduction but is reduced smoothly to MoO_2 between 400 – 450°C. Increasing the temperature rate in the case of α-MoO_3 and 0Vox has the effect of distorting the reduction curve to an overall exponential shape which is most pronounced in the case of α-MoO_3 but also observed for the 5°C/min heating rate of 0Vox. The vanadium containing precursor 8Vox shows a delayed onset of reduction but overall retains the same curve shape with only slight distortion at the 5°C/min heating rate. The distortion in the reduction curve for the highest temperature rate can thus be explained as the delayed onset of oxygen mobility due to vanadium doping.

The second stage of reduction from $MoO_2 \rightarrow Mo_2C$ is illustrated in Figure 2.15 which compares the extent of reduction of the precursor oxides vs. temperature at a ramping rate of 1°C/min over the temperature range 475 – 675°C. Here we see that the influence of vanadium is to retard the reduction-carburisation process. Disregarding the case of α-MoO_3 we can see from Figure 2.15b that the initial consumption of methane (m/z = 15), indicating the onset of carbon incorporation, begins at progressively higher temperatures ranging from 578°C for 0Vox to 595°C for 8Vox. When we correlate these temperatures with the integrated reduction curve of Figure 2.15a it is apparent that the carburisation process does not begin at the completion of the reduction $MoO_3 \rightarrow MoO_2$. The average oxidation state of the Mo can be seen to be $\sim MoO_{1.33}$ which corresponds to Mo_3O_4 (or $Mo^{IV}O_2.2Mo^{II}O$; or $2Mo^{IV}O_2.Mo^0$). This can be seen from the X-ray diffractograms in Figures 2.10 and 2.11 that the crystalline phase MoO_2 persists until around this exact temperature range. Because there are no other crystalline phases observed, the implications of this are that Mo^{IV} is coexisting with a lower oxidation state of molybdenum such as metallic Mo^0 or alternatively '$Mo^{II}O$' — a cubic oxide phase which has been observed as micro-domains within stabilising matrices.[44-46] Or alternatively, an intermediate oxidation state (Mo^{III}) exists, such as that reported by Davies *et al.*[47] To date there is very little support in the literature for such an electronic state and it should be considered as merely speculative without stronger evidence.

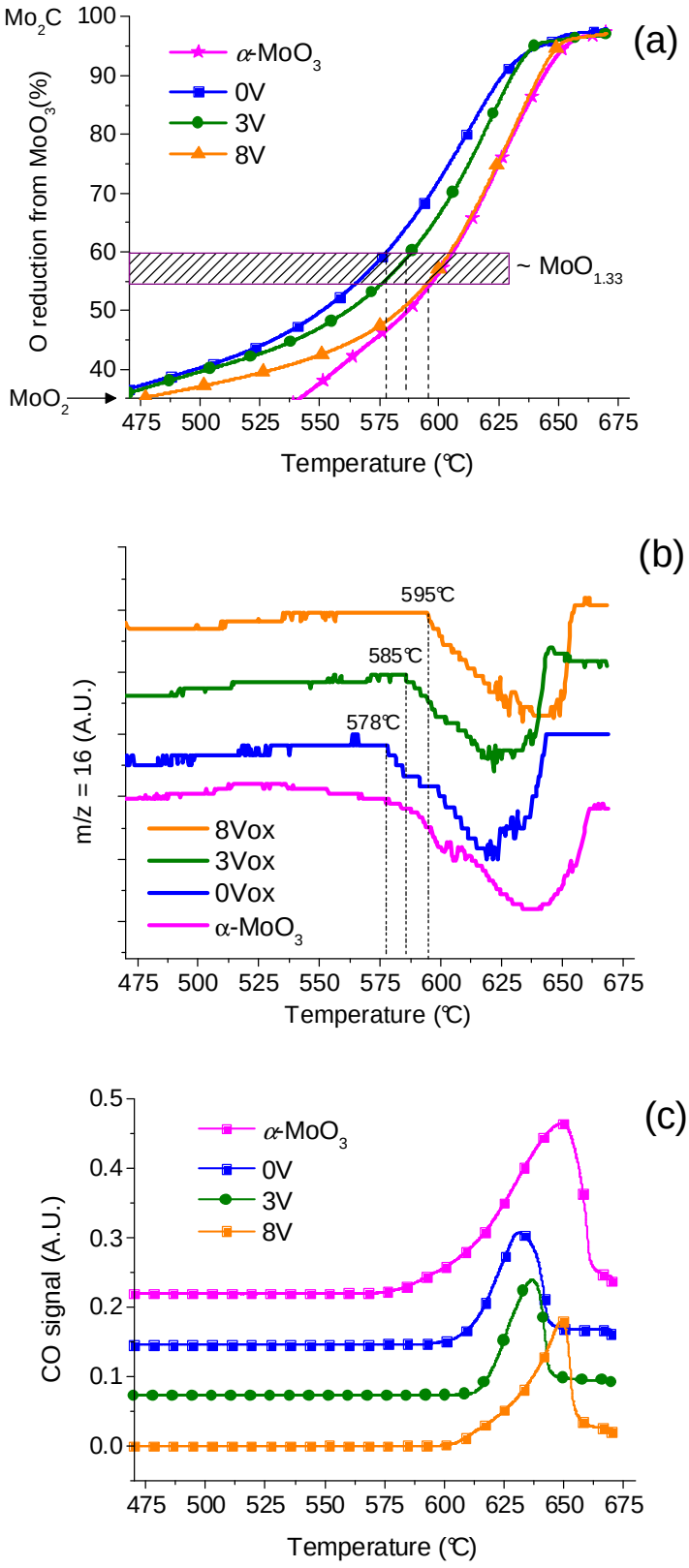

Figure 2.15: (a) TPR-carburisation profiles at 1°C/min showing the reduction MoO_2 → Mo_2C. Extent of reduction is indicated on the y-axis (MoO_3 = 0%; MoO_2 = 33%; Mo_2C =

100%). (b): Consumption of CH_4 (m/z = 15) vs. temperature at 1°C/min. (c): Evolution of CO (IR signal) vs. temperature at 1°C/min. Note – some data points are omitted for clarity.

$Mo^{II}O$ is discussed in the context of alkane isomerisation catalysis[48, 49] and is more widely accepted as an intermediate oxidation state of Mo.[50, 51] However, from the data at hand we cannot make further distinction as to the true nature of this oxidation state apart from the fact that it lies directly between the disappearance of MoO_2 crystalline phase and emergence of Mo_2C.

What is happening in the case of α-MoO_3 is less clear due to the complexity of its reduction profile (Figure 2.16). α-MoO_3 is known to incorporate hydrogen and form bronzes as well as the so-called Magnéli phases which come about through a shear mechanism of reduction. From Figure 2.15 it appears that incorporation of carbon in α-MoO_3 is at an earlier stage of reduction, however, from the *in situ* XRD diffractograms we also observe the persistence of MoO_2 phase until 575-600°C.

In parallel with the removal of oxygen in the form of water (eqn. 2) is the observation of CO which is formed via a complex reforming process (eqn. 3) involving lattice carbon substitution as demonstrated by Green.[52] Interestingly, as seen in Figure 2.15(c) formation of CO is observed at lower temperatures and is more pronounced for the α-MoO_3 *cf.* the hexagonal precursors. In all cases the peak is observed to correlate with the completion of reduction (at which point the H_2O reforming source is depleted). The CO peak area related to the TPR-carburisation of α-MoO_3 is considerably larger than those observed for the hexagonal precursor oxides implying that the reforming reaction is more effectively catalysed. The exact reasons for this relative increase and for the inclusion of carbon at lower temperatures *cf.* *h*-MoO_3 are not speculated on here.

For all of the oxides in the step: $MoO_2 \rightarrow Mo_2C$, there is an exponential increase in reduction with temperature which is consistent with an increase in available reacting surface area as reported by Green.[24] Additionally, it is seen that 0Vox and 3Vox are reduced to carbides more easily than 8Vox and α-MoO_3. These observations are in accordance with the hypothesis that vanadium reduces the mobility of oxygen in the structure and thus retards the removal of lattice oxygen and subsequently carbon inclusion.

2.3.4 Solid state kinetic analysis of TPR curves

The solid state kinetic analysis was carried out using the following approaches:

- Integration and normalisation of the TPR-carburisation data to determine 'α'
- Model-free analysis of the non-isothermal data using Friedmann and Ozawa-Flynn-Wall methods to determine the conversion-dependent activation energy
- Derivation of the 'generalised time' using calculated activation energies to give an approximation for: $\theta/\theta_{0.5} = t/t_{0.5}$
- Use of master plot methods to elucidate the reaction mechanism by comparison with the treated data

The reduction curves for α-MoO_3, *h*-MoO_3 (0Vox), *h*-$Mo_{0.97}V_{0.03}O_3$ (3Vox) and *h*-$Mo_{0.92}V_{0.08}O_3$ (8Vox) can be seen in Figure 2.16 in which $\alpha = 1$ corresponds to Mo_2C. In the ideal case therefore we can define $\alpha = 0.33$ for the case of the reduction:

$$MoO_3 \rightarrow MoO_2 \qquad \text{—} \qquad (1)$$

And the carburisation is observed for $0.33 < \alpha < 1$:

$$MoO_2 \rightarrow Mo_2C \qquad \text{—} \qquad (2)$$

To picture these mechanistic steps we have carried out the model-free kinetic analysis using a Friedmann analysis[53] which is a multi-point analysis determined by plotting $\log(d\alpha/dt)$ vs. 1/T at different iso-conversions for a range of heating rates (β). The specific advantage of this analysis is that the plot does not require a constant rate of temperature change; this is of relevance because the TPR measurements are carried out using a temperature ramp followed by a plateau. In the case of data obtained at 1°C/min, the oxide is entirely reduced by the final temperature — 675°C, however, at the highest heating rate of 5°C/min, the reduction-carburisation is not complete until sometime after the plateau. For these reasons we must use the Friedmann analysis if we are to consider the entire reduction $MoO_3 \rightarrow Mo_2C$ and observe trends. From Figure 2.17 we can see that the reduction of the orthorhombic α-MoO_3 differs from that of the hexagonal *h*-MoO_3-type oxides. The reduction of orthorhombic α-MoO_3 has an initially low apparent activation energy which gradually increases to a value of ~100 kJ/mol just before $\alpha = 0.33$.

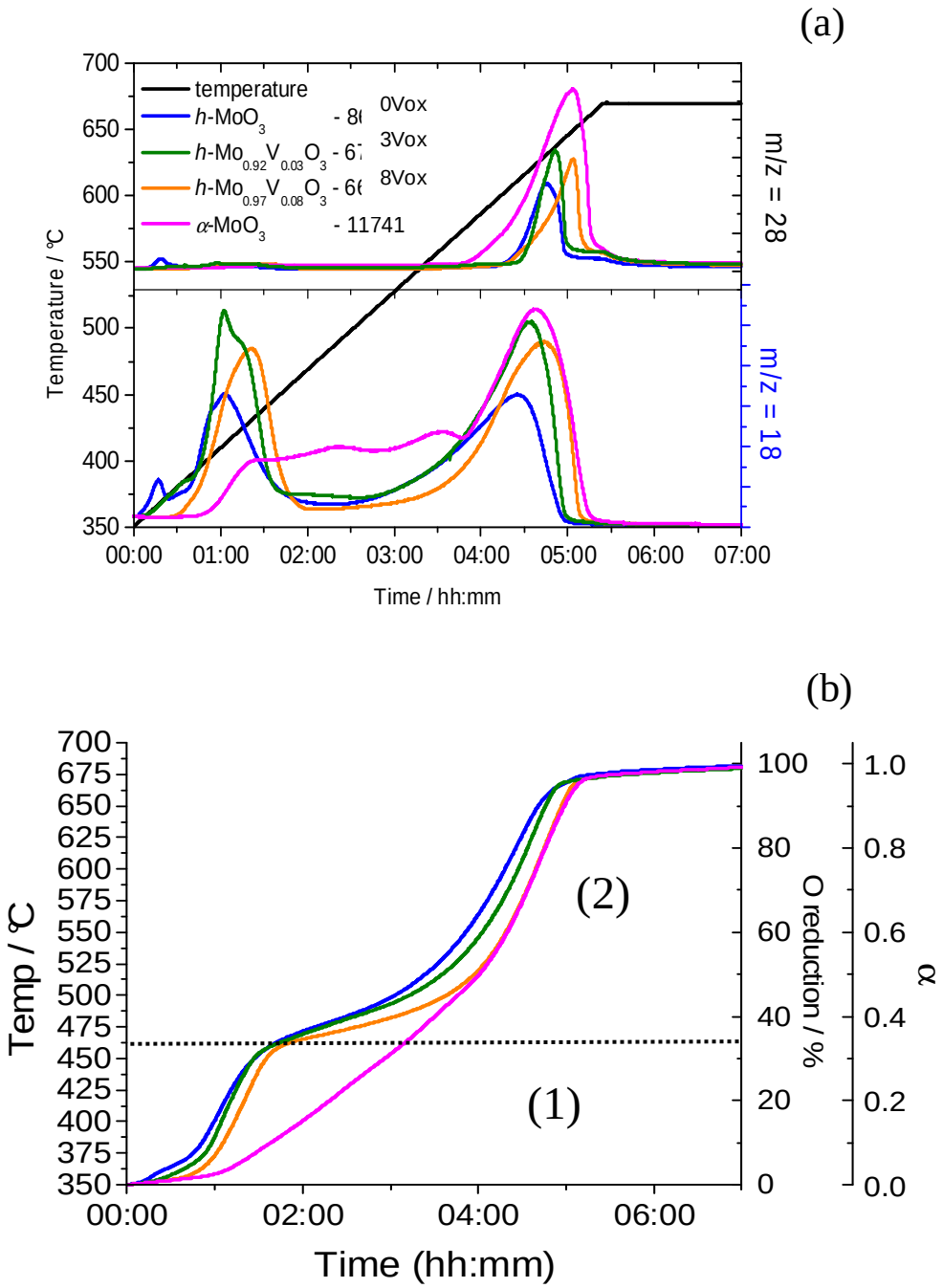

Figure 2.16: (a) Normalised MS signals (CO, H_2O) for the TPR-carburisation of oxide precursors at 1°C/min. (b) Calculated extent of reduction (α) for above conditions.

This is followed by an inflection point which indicates the beginning of carburisation. This analysis is consistent with previously reported studies such as those of Ressler *et al.* and Lalik.[40-42] The Friedmann analysis of the hexagonal oxides shows a different picture. Here we see that the initial apparent activation energy is high (> 100 kJ/mol) and decreases rapidly at around α = 0.1. From this we can conclude that for the hexagonal oxides that there are at least two mechanistic steps in the reduction MoO_3

→ MoO_2 which is further evidenced by the observed *o*-Mo_4O_{11} phase seen in the *in situ* XRD.

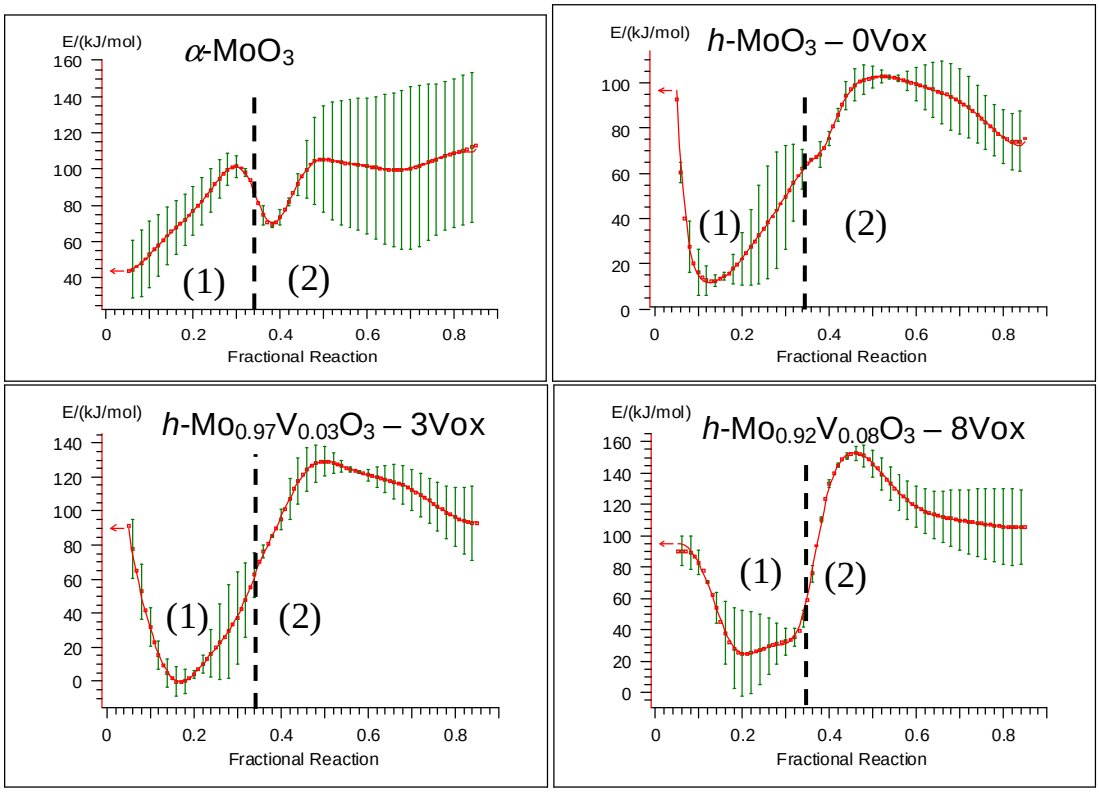

Figure 2.17: Friedmann analysis of TPR-carburisation for α-MoO_3, 0Vox, 3Vox & 8Vox showing the two steps of reduction-carburisation — (1) & (2).

As the concentration of vanadium increases we can also see that the apparent activation energy for the carburisation step (2) increases. In the case of *h*-MoO_3 the apparent activation energy of carburisation is ~100 kJ/mol — close to that observed for the orthorhombic oxide precursor. For the 3V and 8V samples this is increased to 130 and 150 kJ/mol, respectively. It is also notable that the activation energies for reduction (1) and carburisation (2) become increasingly well defined stepwise with the addition of vanadium. In the case of the carburisation of 8V we can see that the there are three clear mechanistic steps and that the carburisation is strongly separated from the reduction.

Although these activation energies help to paint a mechanistic picture we can see that there is a considerable degree of error and if we consider the calculated energies we must conclude that they are in some cases unrealistic (E_a = 0 kJ/mol). To improve the accuracy of these measurements an alternative model-free system called Ozawa-

Flynn-Wall analysis was applied.[29] Ozawa-Flynn-Wall technique is a Multi-point analysis which is determined by plotting log(dT/dt) vs. 1/T at different iso-conversions. This technique requires a constant temperature rate (dT/dt) and so we redefine a new extent of reaction, α', where α' = 0.5 α. In this way we define fractional conversions for which the temperature is changing in a constant manner.

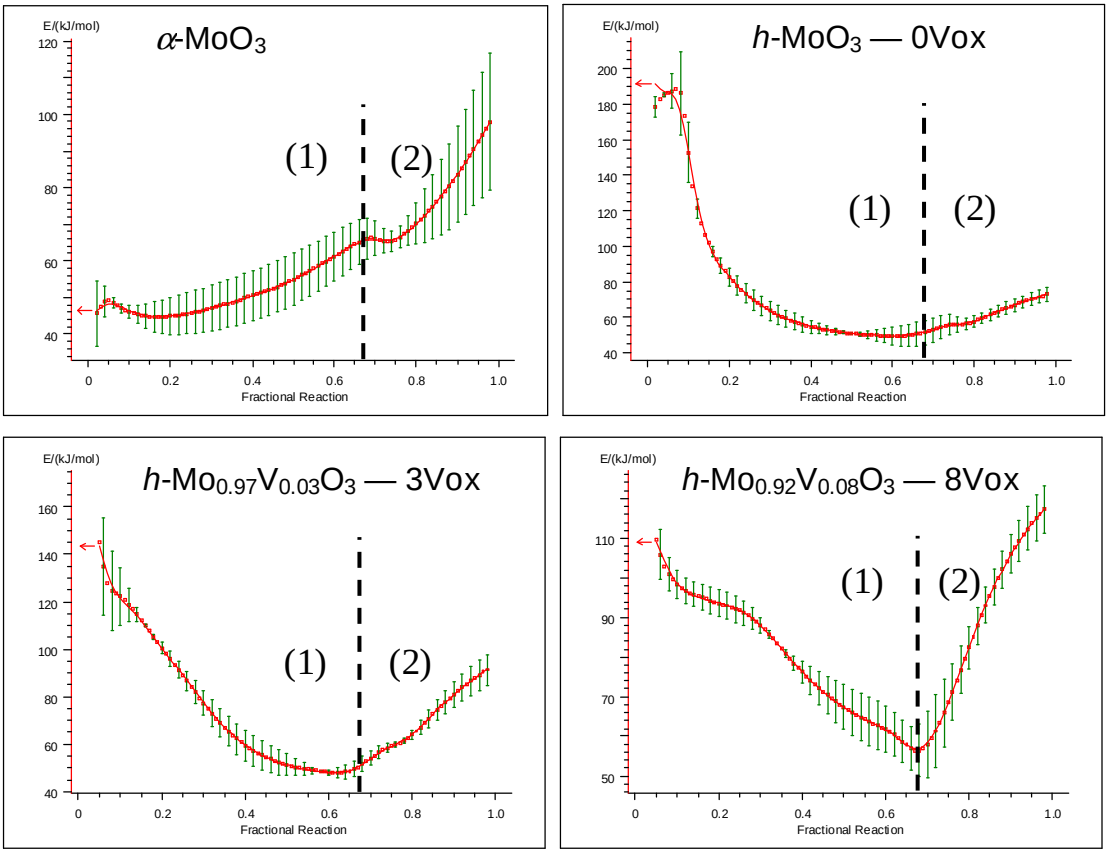

Figure 2.18: Ozawa-Flynn-Wall analysis of the TPR-carburisation as in Figure 2.16. The extent of reaction is redefined as α' = 0.5 α which gives $\alpha'_{0.66} \rightarrow MoO_2$

We see for the Ozawa-Flynn-Wall analyses in Figure 2.18 that we minimize the related error and that the calculated activation energies lie within a realistic range of values. The general trends are similar to the Friedmann analysis. We see a high activation barrier for the reduction of the hexagonal oxide *h*-MoO_3 (~180 kJ/mol) which decreases with vanadium concentration. Importantly, from these calculated values we can try to apply the data to a kinetic model.

Table 2.4: Solid-state rate and integral expressions for different reaction models.[54]

Model	Differential form f(α)	Integral form g(α)	Notes
Pm — power law	$m\alpha^{\frac{1}{m}}$	$\alpha^{\frac{1}{n}}$	$m = 2,3,4$
Am — Avrami–Erofeev	$m(1-\alpha)[-\ln(1-\alpha)]^{\frac{1}{m}}$	$[-\ln(1-\alpha)]^{\frac{1}{m}}$	$m = 2,3,4$
R2 — contracting area	$2(1-\alpha)^{\frac{1}{2}}$	$1-(1-\alpha)^{\frac{1}{2}}$	
R3 — contracting volume	$3(1-\alpha)^{\frac{1}{3}}$	$1-(1-\alpha)^{\frac{1}{3}}$	
Fm — mth-order reaction	$(1-\alpha)^m$		$m = 0,1,2,3$
D1 — one dimensional diffusion	$\frac{1}{2\alpha}$	α^2	
D2 — two dimensional diffusion	$-\left[\frac{1}{\ln(1-\alpha)}\right]$	$\big((1-\alpha)\ln(1-\alpha)\big)+\alpha$	
D3 — three dimensional diffusion (Jander equation)	$\frac{\left[3(1-\alpha)^{\frac{2}{3}}\right]}{\left[2(1-(1-\alpha)^{\frac{1}{3}})\right]}$	$(1-(1-\alpha)^{\frac{1}{3}})^2$	
D4 — three dimensional diffusion (Ginstlinge Brounshtein equation)	$\frac{3}{\left[2((1-\alpha)^{-\frac{1}{3}}-1)\right]}$	$1-\left(\frac{2}{3}\right)\alpha-(1-\alpha)^{\frac{2}{3}}$	

Table 2.4 is an overview of some of the mathematical expressions for the rate parameters for different kinetic models of solid state reactions.[54] These equations are derived from geometric models which approximate the change of reaction rate with respect to α over time. The functions $f(\alpha)$ and $g(\alpha)$ denote the differential and integral forms, respectively, of these rate equations. By plotting $f(\alpha)/f(\alpha_{0.5})$ or $g(\alpha)/g(\alpha_{0.5})$ vs. α, the resulting curves all overlap at $\alpha = 0.5$ and for the case of isothermal experiments may be compared with measured kinetic data of the form: $t/t_{0.5}$ vs. α, where t = reaction time.

In the case of non-isothermal experiments we cannot use the time of reaction but we must derive an equivalent — 'generalized time' = θ.[29] Simply put, generalised time is derived using the Arrhenius equation and is equivalent to the time of reaction at infinite temperature. To do this we define θ as:

$$\theta = \int g(T)dt$$

This gives us a new expression for the rate constant k_0 independent of temperature:

$$k = k_0 g(T)$$

Having derived k_0 we define a function $f(\alpha)$ for the reaction rate:

$$\frac{d\alpha}{d\theta} = k_0 f(\alpha)$$

Further mathematical treatment leads to the equality:

$$\frac{\theta}{\theta_{0.5}} = \frac{t}{t_{0.5}}$$

Although we cannot calculate the value of θ directly, it can be approximately related to the function p(x) as follows:

$$\frac{\theta}{\theta_{0.5}} = \frac{p(x)}{p(x)_{0.5}} \quad \text{where,} \quad p(x) = \frac{e^{-x}}{x}\pi(x) \quad \& \quad x = E/RT$$

Now, by using the apparent energies of activation calculated by model-free techniques we compare the reaction data to a suite of kinetic models and make some hypotheses with regards to the reaction mechanism.

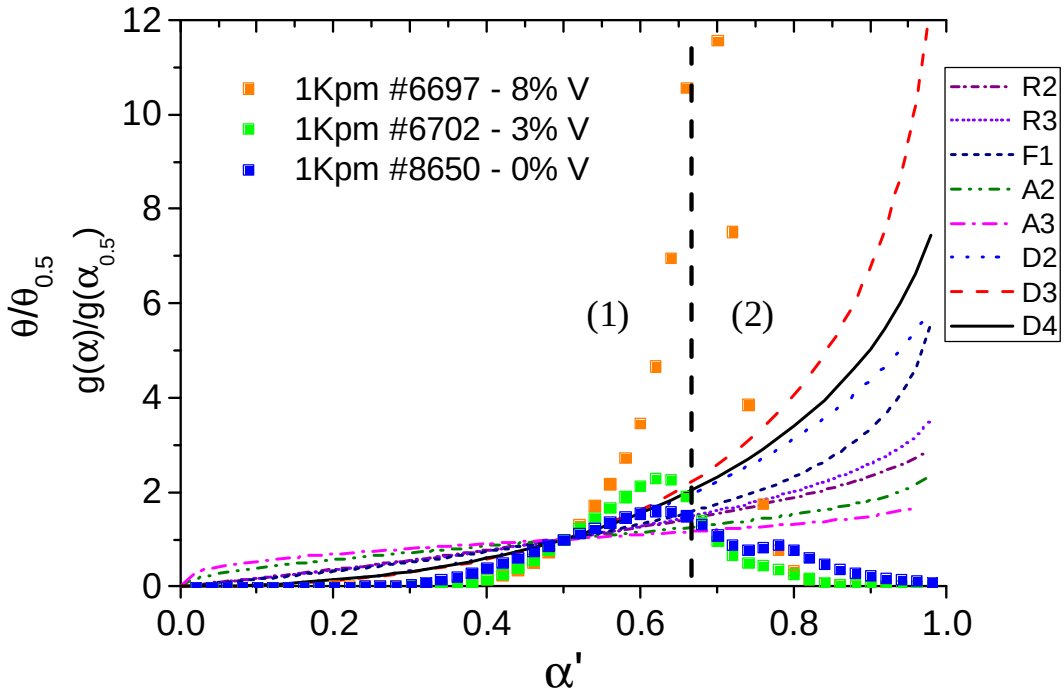

Figure 2.19: Comparison of rate data calculated using 'generalised time' derived from conversion-dependent activation energies derived from the Ozawa-Flynn and Wall analysis for the reduction-carburisation of *h*-Mo(V)O_3 oxide precursors.

In Figure 2.19 the calculated rate data are compared against a suite of reaction models (see Table 2.4). Note that the midpoints of the curve all intersect at $\alpha = 0.5$. From the degree of mismatch we can see that our curve overlaps with more than one mechanistic step. If we assume that the MoO_3 is reduced via an intermediate MoO_{3-x}, we know the initial reduction $MoO_3 \rightarrow MoO_2$ to be complete at $\alpha = 0.66$, so we have a defined endpoint for the mechanism. By differentiating the data above we can make an accurate determination for the beginning of the mechanism which is shown in Figure 2.20 as the point at which $d(\theta/\theta_{0.5})/d\alpha$' is > 1. For *h*-$MoO_3$ this mechanism is found to be $\alpha = 0.26$ and for the vanadium containing oxides it was found to be $\alpha =$

0.32. Now we are free to redefine the extent of reaction so as to encompass only the hypothesized mechanism: $MoO_{3-x} \rightarrow MoO_2$.

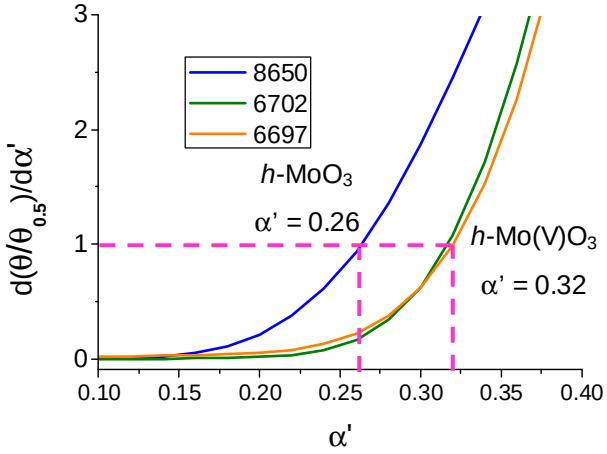

Figure 2.20: Differentiated plot of Figure 2.19 showing the beginning of the mechanism $MoO_{3-x} \rightarrow MoO_2$.

For the reaction we can now rescale our extent of reaction, α'':

α'' = 0 → MoO_{3-x} (x = 0.39 for *h*-MoO_3; x = 0.48 for *h*-$Mo(V)O_3$

α'' = 1 → MoO_2

The resulting master plots can be seen in Figure 2.21 for the oxide series 0V, 3V and 8V. For all of the reductions the most appropriate models are the diffusion models of reaction. In the case of *h*-MoO_3 and *h*-$Mo_{0.97}V_{0.03}O_3$ the comparison to the diffusion models is valid only for α'' < 0.5. For conversions above α'' = 0.5 it is observed that the model is not compatible. However, for the oxide *h*-$Mo_{0.92}V_{0.08}O_3$ (8Vox), the D3 model, or 3-dimensional diffusion model (Jander)[55] is a close match. It is therefore observed that the reaction mechanism is singular across the full range of $0 < \alpha'' < 1$.

These findings imply that for the *h*-MoO_3 (0Vox) and *h*-$Mo_{0.97}V_{0.03}O_3$ (3Vox) oxides, the initial reduction step → MoO_2 involves a more complex mechanism than we have proposed. From the model-free analyses of activation energy we could postulate that this is in regards to an early onset of carburisation or the formation less reducible species which change the diffusional mechanism. This possibility is supported by the TPR-carburisation spectra which shows a distortion in the sigmoidal reduction curves for 0Vox at higher heating rates for $\beta > 1$°C/min (Figure 2.14).

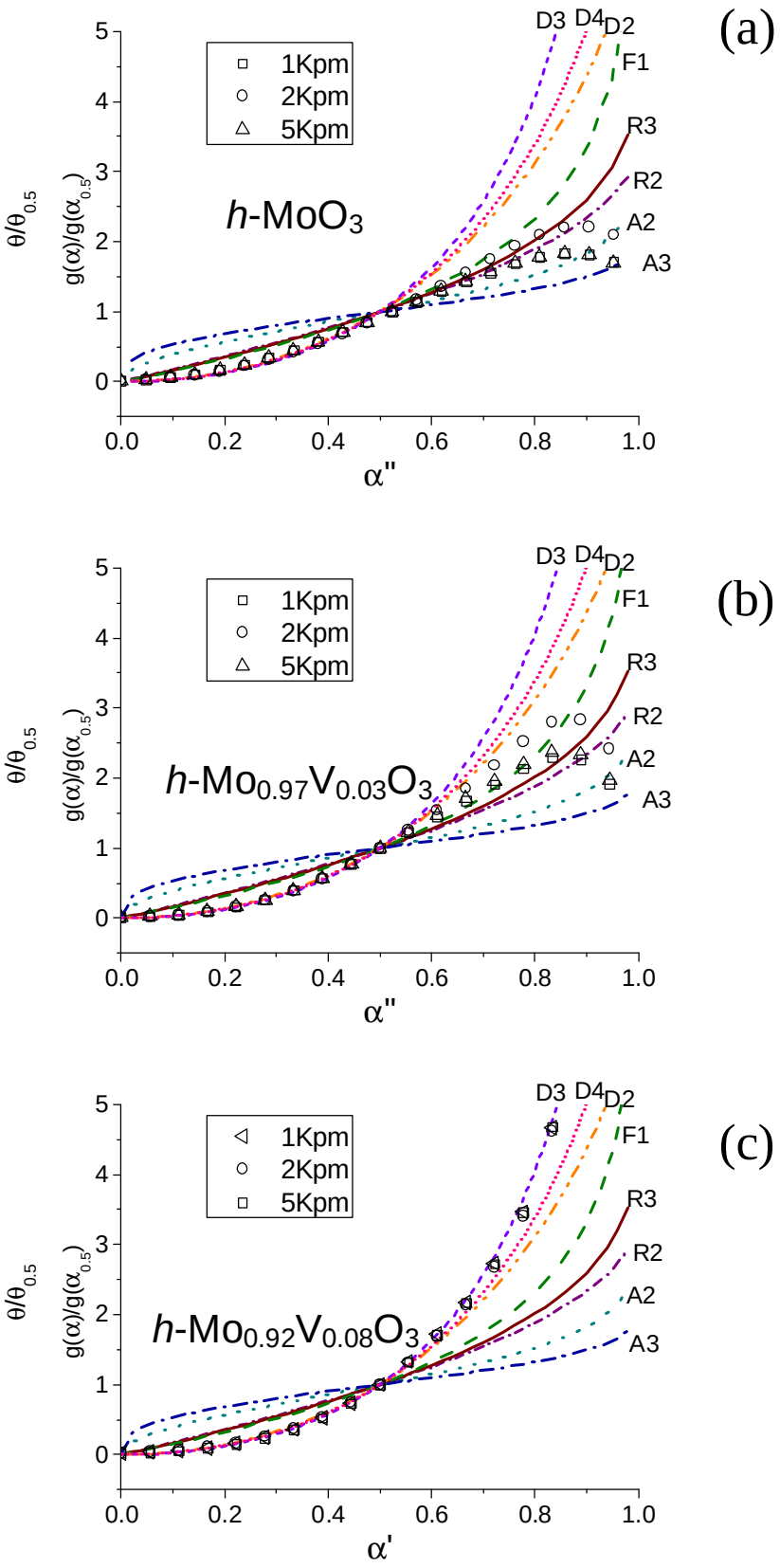

Figure 2.21: Master plot comparisons of the temperature-programmed reduction ($MoO_{3-x} \rightarrow MoO_2$) of *h*-Mo(V)$O_3$ type oxides at various heating rates. (a) *h*-MoO_3 (0Vox); (b) *h*-$Mo_{0.97}V_{0.03}O_3$ (3Vox); (c) *h*-$Mo_{0.92}V_{0.08}O_3$ (8Vox).

2.3.5 *Analysis of X-ray diffraction patterns*

The carbide derived from the *h*-MoO_3 precursor, **0V**, exhibits a broadening of the carbide peaks *cf.* the orthorhombic derived material. In the case of the vanadium-containing oxides *h*-$Mo_{1-x}V_xO_3$, it is observed that the subsequent carbide diffraction patterns are broadened significantly (Figure 2.9), implying that the carbide crystallites are smaller. Software analysis of the *ex situ* XRD data shows a trend in the particle sizes of the as-synthesised carbides. Based on the integral breadth, the volume-weighted column heights vary from 6.3 nm for the reference carbide, **R**, to 3.3 nm for the most highly substituted carbide, **5** (Table 2.3).

From software analysis of the final XRD patterns **1** – **5** (Figure 2.10) a close fit for α-Mo_2C is achieved with a hexagonal space group ($P6_3/mmc$) using a Pawley refinement with the addition of Mo metal as a minority Rietveld phase. In the case of the reference **R**, the Pawley indexed phase combined with a minority MoC_{1-x} Rietveld phase gives the most satisfactory fit. The assignment of minority phases in these samples can be rationalised by considering that in the case of molybdenum carbide synthesised from orthorhombic MoO_3, pretreatment of the oxide under H_2 leads to bronze-like hydrogenation of the structure which is subsequently carburised to the less stable cubic MoC_{1-x}.[56] This preconditioning occurs to some extent during regular carburisation of the orthorhombic oxide leading to a minority phase. In the case of the hexagonal oxides this minority phase is not observed.

As the diffraction peaks of the carbides are extremely broad, the cell parameters obtained from the diffraction patterns do not show a systematic trend as did the oxides, but it can be seen that there is no evidence of crystalline V_xO_y or VC. Further evidence for a homogenous solid solution is presented in a later section as demonstrated by elemental mapping using energy filtered TEM.

2.3.6 *Carbon determination*

CHN analysis of the carbides shows an excess of carbon with respect to the theoretical values calculated for stoichiometric M_2C (Table 2.3). The excess carbon is due to the synthetic conditions applied in the *in situ* XRD cell in which the materials are formed. These applied conditions were derived by consideration of the ideal synthesis conditions by Lee *et al.*[3] combined with consideration of the

diffractometer cell and combined analytics. The resulting dilution of the feed gas decreased the partial pressure of hydrogen, resulting in significant C deposition over the course of the synthesis.

2.3.7 Surface area, porosity and microstructure of the resulting carbides

The samples were found to exhibit relatively high surface areas (Table 2.3), ranging from 71m^2/g for the orthorhombic derived material and 80m^2/g for the undoped carbide 0Vc up to a maximum of 107 m^2/g for 5Vc. This is in contrast to the systematic trend observed in crystallite size estimated by the volume-weighted average column height (L_{Vol}-IB) seen in Table 2.3 but may be explained by analysis of the N_2 isotherms in conjunction with the morphologies observed in SEM. The full adsorption-desorption isotherms indicate an increasingly mesoporous character of the carbide materials with increasing total pore volume to a maximum of ~0.19 cm^3/g for 8Vc (Figure 2.22). The N_2 sorption isotherms are consistent with an irregular pore structure and the occurrence of slit pores. This observation is consistent with the morphological features seen in the scanning electron micrographs (Figure 2.23). It can be seen that the isotherms evolve from a purely Type III adsorption isotherm (polydisperse pore sizes, consistent with slit-micropores) in the case of 0Vc to Type IV (tighter pore size distribution, more regular mesoporous character) in the case of 8Vc. The peak in calculated surface area could be attributable to the contributions of microporous and mesoporous character which is maximised in sample 5Vc.

The mesoporosity evolves with increasing vanadium content and results in a material with an average pore diameter of between 40-50 Å (Figure 2.22). Such mesoporosity is highly relevant to the use of materials in heterogeneous catalysis because it allows for reactants to be transported to, and products to be transported from, the active sites of the catalyst.

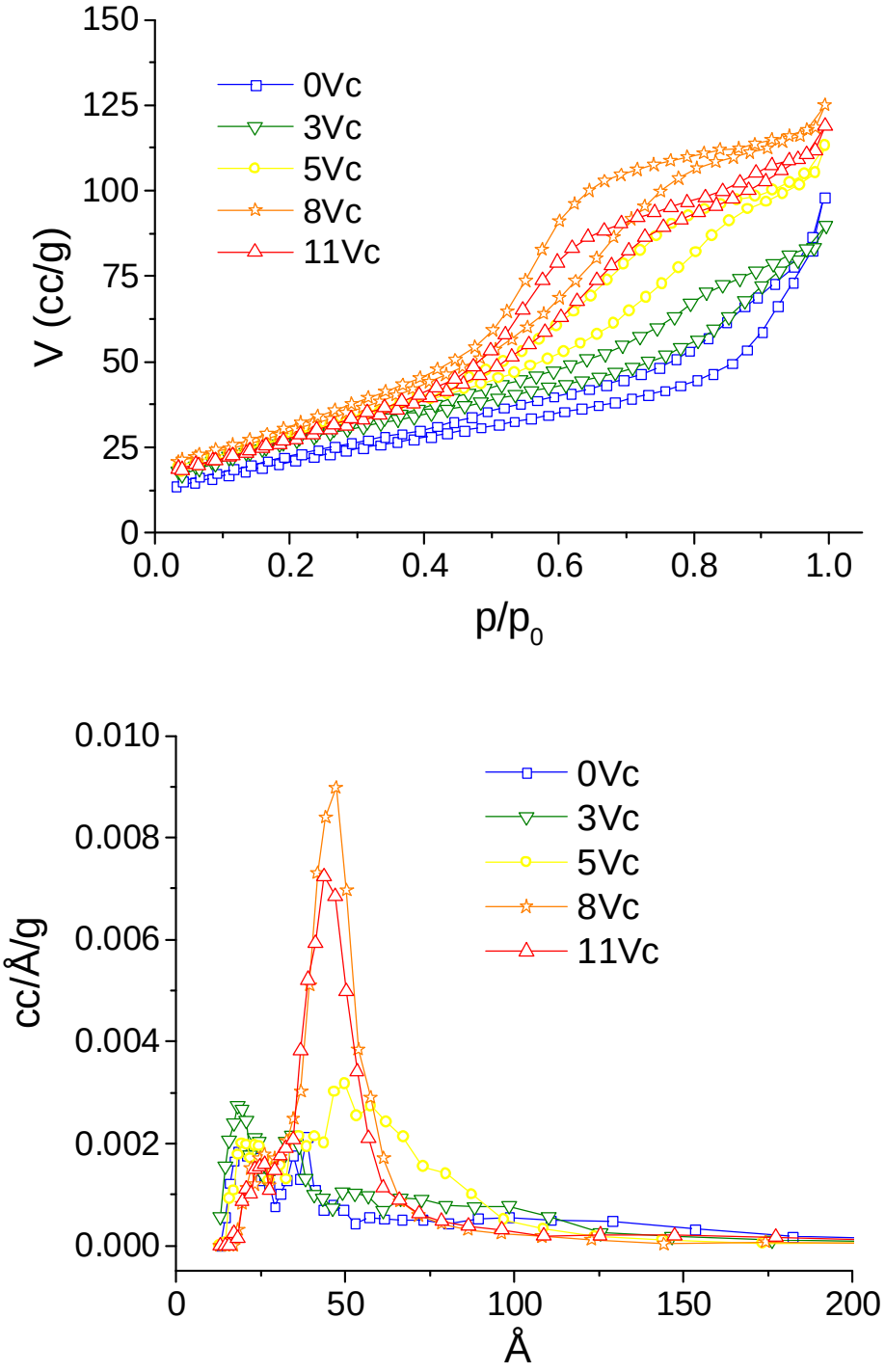

Figure 2.22: Above: comparison of N_2 adsorption-desorption isotherms for samples 0Vc – 11Vc. Below: BJH (Barett-Joyner-Halenda) approximation of pore size distributions for samples 0Vc – 11Vc.

The SEM images of the as-synthesised carbides show an interesting morphological trend. With increasing vanadium content, it is observed that the morphology evolves

from that of an agglomerated-particulate material to a densely packed nano-fibrous material with visible mesoporosity (Figure 2.2).

The apparent fibers propagate lengthwise along the *c*-axis relative to the original parent oxide crystals. To this extent pseudomorphism is evident in the preservation of the overall hexagonal prismatic structure observed in the parent oxide species.

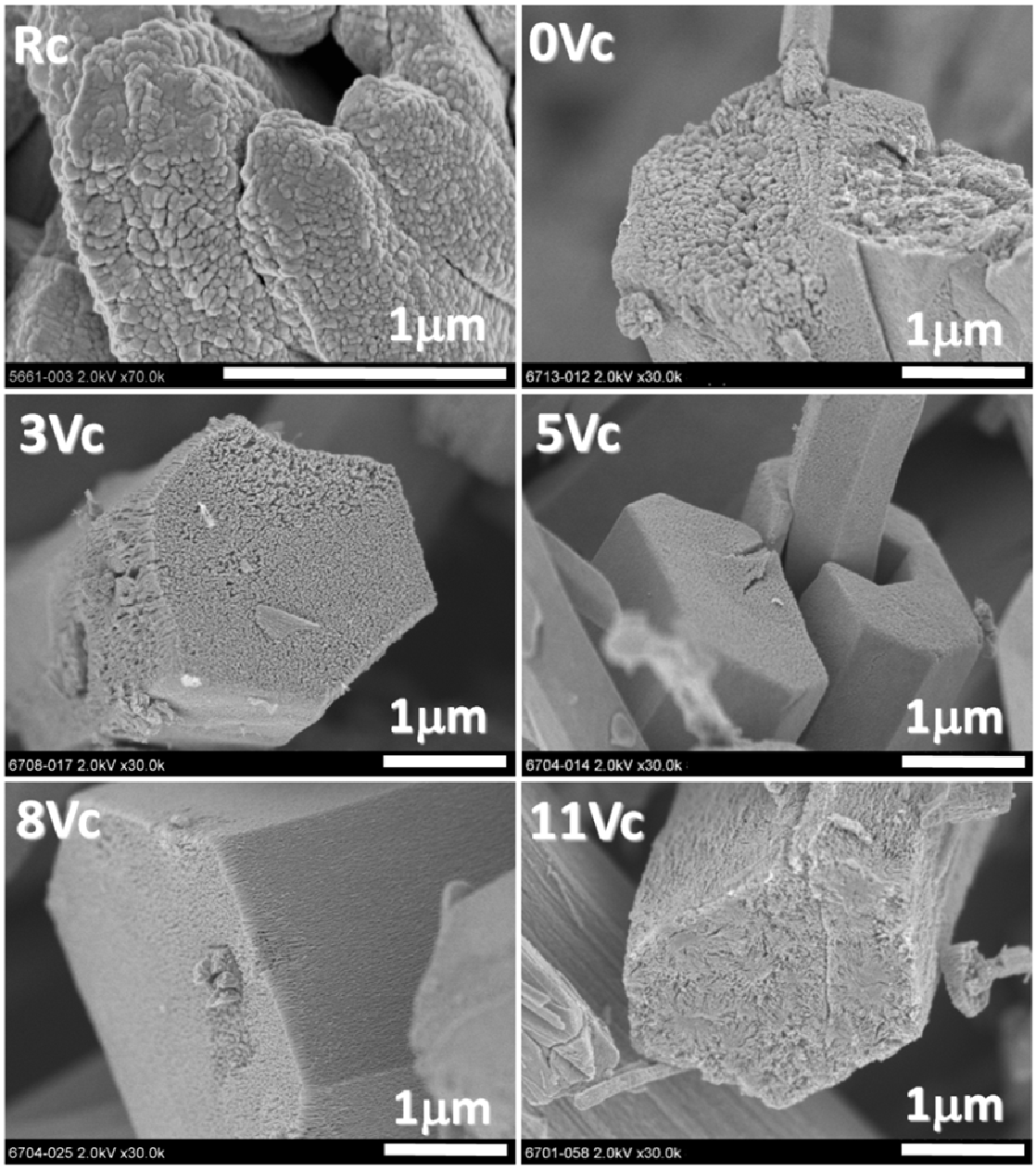

Figure 2.23: SEM images of the carburised materials Rc, 0Vc–11Vc

With increasing V content, it is observed in the SEM imagery that the carbides present an evolved mesoporosity, which originates from a smaller, more organised morphology comprised of nanocrystalline carbide. The fiber-like nature becomes increasingly dense with a trend towards a finer and more regular morphology. With reference to the temperature-programmed reduction-carburisation profiles presented in Figures 2.13–2.15, sample 8Vc, which exhibits the most uniform mesoporosity as seen in the N_2 physisorption isotherms, is characterised by the cleanest reduction profile. The trend is observed towards increasing mesoporosity with decreasing formation of intermediate *o*-Mo_4O_{11}. It is hypothesised that the kinetic 'interference' of Mo suboxide formation is linked to sintering and aggregation of particles in what is otherwise described as the topotactic reduction of $MoO_3 \rightarrow MoO_2$.[43] There are conflicting reports of the topotactic/pseudomorphic nature of this reduction,[3, 57, 58] however, these are not incommensurable with mechanisms discussed in the literature, which are highly dependent on the applied conditions and mass transport limitations.[40, 43, 59, 60]

Characterisation of the intermediately doped sample 8Vc by Transmission Electron Microscopy is consistent with the morphology observed by SEM. Figure 2.24 shows a HR-TEM image of the high-aspect ratio crystallites, which make up the fibrous bundles observed in the SEM (Figure 2.23). The low-magnification image in Figure 2.25 is a micrograph of 8Vc taken in HAADF-STEM mode (high angle annular dark field-scanning transmission electron microscopy) which shows a homogenous distribution of the elements Mo, V and C throughout the observed sample. The observed oxygen content is due to the passivation procedure.

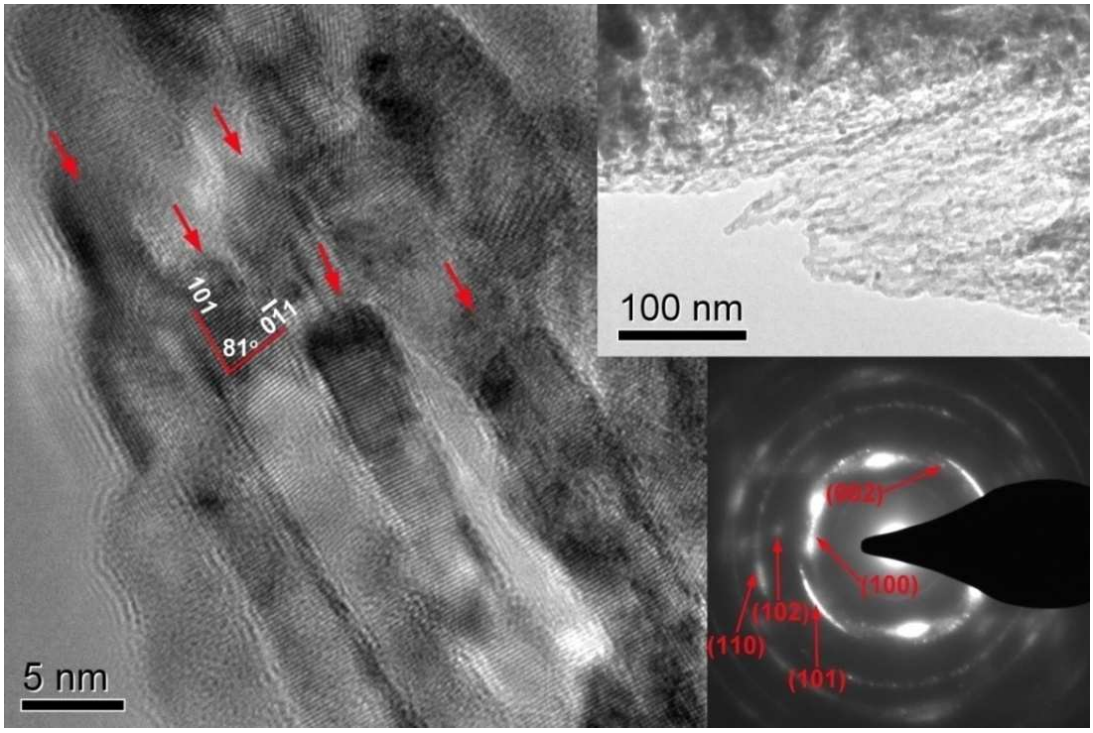

Figure 2.24: TEM image of 8Vc with low magnification image (inset top right) and spot diffraction pattern applied over a large area (inset bottom right).

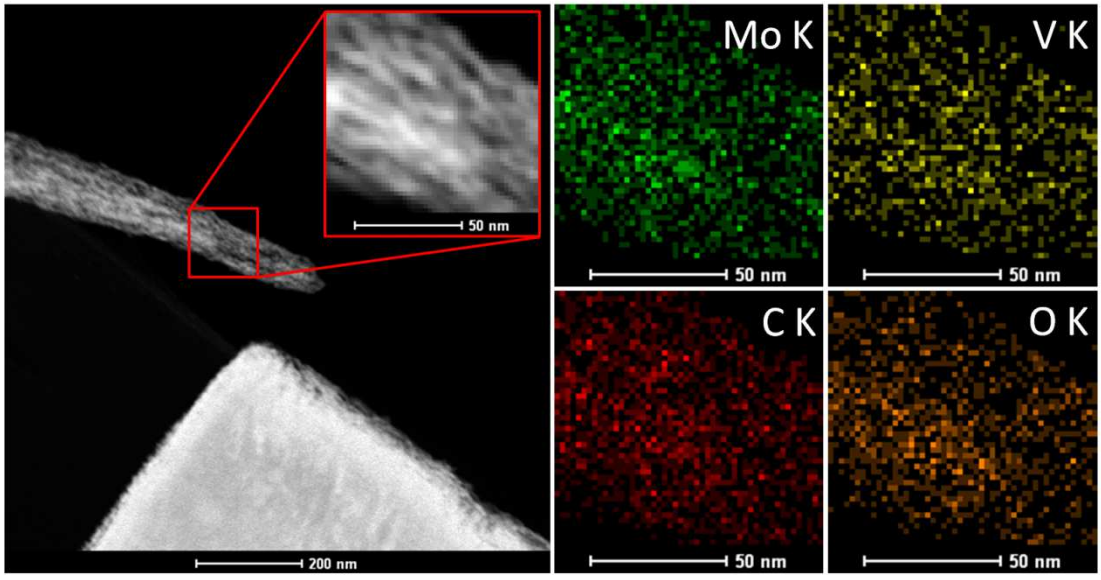

Figure 2.25: STEM-HAADF image of 8Vc combined with EDX-elemental maps for V, Mo, C and O showing a statistical distribution of elements within the sample.

Of particular interest in the TEM study was the observation that the spot diffraction pattern of the parent polycrystallite exhibits a circular pattern of elongated spots, indicating that the co-formed carbide particles have preserved crystallographic order

and exhibit preferential orientation. This retention of crystallographic order is not observed in carbides derived from undoped *h*-MoO_3 or from the carburisation of α-MoO_3. In previous studies, a range of Mo-containing oxidic materials have been used as precursors to mono- and polymetallic carbides *via* a reductive carburisation. These include α-MoO_3,[3] MoO_xH_y,[56] $(NH_4)_6Mo_7O_{24}.4H_2O$,[58] and mixed metal oxides of the form M_5O_{14} (M = Mo/V/Nb/Ta/W).[12] Topotaxy is reported in the case of the mixed metal oxide precursors, and also, in the case of the reduced oxyhydride (MoO_xH_y), the reaction under methane proceeds topotactically to the cubic carbide phase MoC_{1-x} with no observed intermediate phases. Depending on the reaction conditions used it is observed in many cases that the reaction products show pronounced pseudomorphism.

2.3.8 Upscaled synthesis of $(Mo_{1-x}V_x)_2C$

The up-scaled synthesis of $(Mo_{1-x}V_x)_2C$ materials was carried out using a series of oxide precursors analagous to that used for the *in situ* XRD study. A summary of the properties is given in Table 2.5. It can be seen from the BET surface areas of the as-synthesised carbides that a similar trend is observed for the carbides synthesised in the rotary furnace with the lowest being the Mo-only sample (8425).

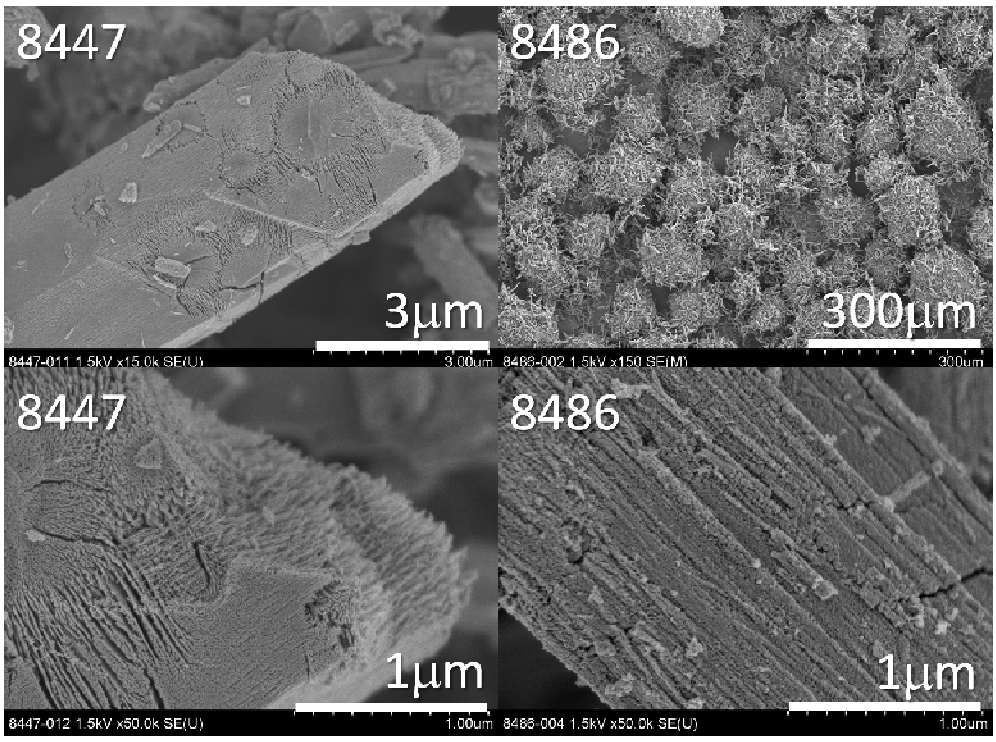

Figure 2.26: SEM micrographs of $(Mo_{1-x}V_x)_2C$.

Notably, the maximum temperature used for the synthesis is 75°C lower than that used in the *in situ* XRD study. This was done to reduce carbon deposition during the later stages of synthesis and by direct comparison with Table 2.3 it is demonstrated that the carbides exhibit a stoichiometry much closer to Mo_2C. The discrepancy between the stoichiometric value and the measured value above likely originates from the passivation procedure during which surface carbon is oxidised to CO_x.

Table 2.5: Physical properties of $(Mo_{1-x}V_x)_2C$ materials synthesised in the rotary furnace. [a]As determined by SEM-EDX

[b]Calculated column height from X-ray diffractogram refinement

Sample	Int. ID	Final temp. (°C)	Phase	Precursor ID	V/(V+Mo) [a]	C theor. (%w/w)	C meas. (%w/w)	Crystal size [b] (nm)	BET (m^2/g)
1	8425	675	Mo_2C (*hcp*)	6600	0.00	5.89	5.2	7.1	69
2	8478	675	Mo_2C (*hcp*)	6702	0.03	5.97	5.2	6.4	110
3	8447	675	Mo_2C (*hcp*)	7911	0.08	6.01	5.1	5.5	106
4	8486	675	Mo_2C (*hcp*)	6601	0.11	6.11	5.3	-	97

In the SEM images shown Figure 2.26 can be seen very similar features to those observed for the *in situ* study. In the top right, the spherical aggregates reflects the microstructure of the precipitated crystallite material of the precursor oxides. In the case of the highest V loading (#8486), surface ridging can be seen for the image in bottom right. In general the mesostructure as determined by N_2 adsorption and SEM reflect in every way the syntheses carried out in small scale in the *in situ* XRD.

TEM data from $(Mo_{0.92}V_{0.08})_2C$ is shown in Figure 2.27. The SAED patterns are in agreement with the powder XRD and there is also preferential orientation observed with a visible fault observed along the (100) plane.

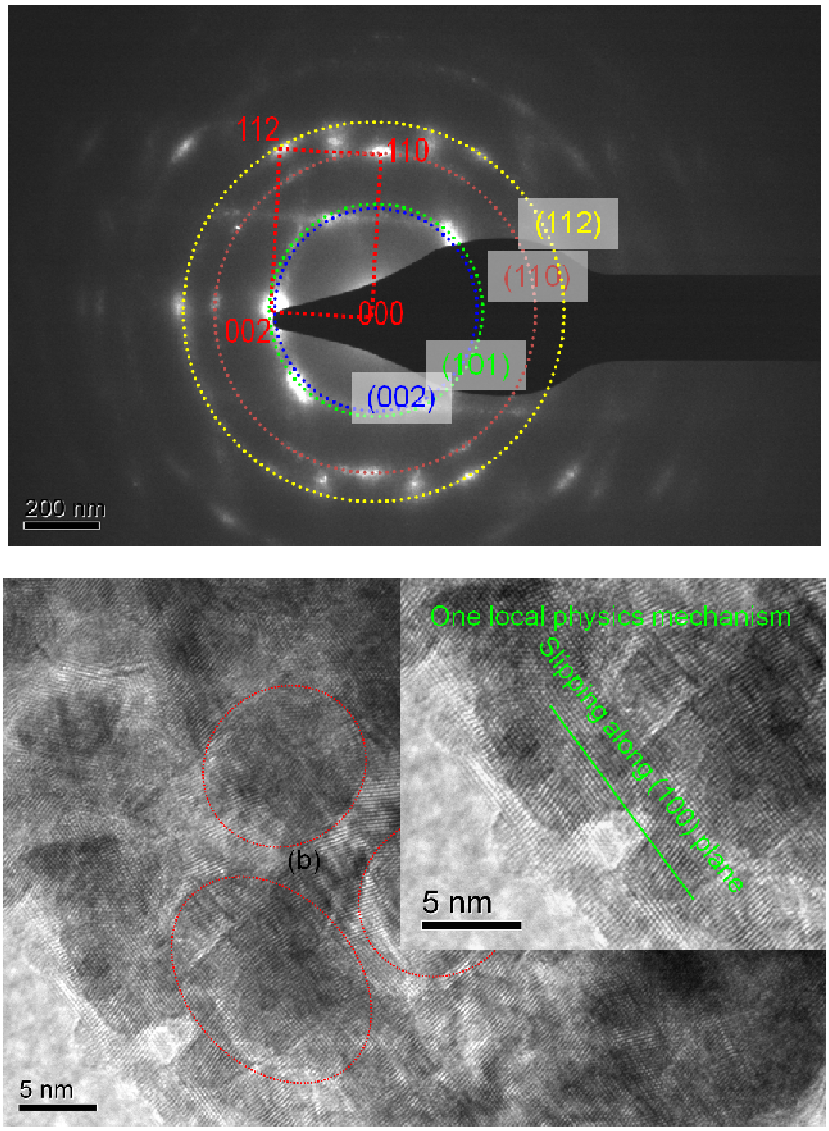

Figure 2.27: (above) SAED of spot showing *hcp* Mo_2C structure for $(Mo_{0.92}V_{0.08})_2C$ (8447); (below) HR-TEM image showing individual crystallites with observed slip plane.

2.4 Discussion

In comparing and contrasting the carburisation of α-MoO_3 and various *h*-Mo(V)O_3 type oxides we observe a number of differences. With respect to the reduction-carburisation of α-MoO_3 the measured TPR curves along with the model-free kinetic analysis support a complex mechanism whereby increasing the temperature of reduction increases the apparent activation energy. It was shown by Ressler *et al.* that the comproportionation reaction to monoclinic *m*-Mo_4O_{11} is observed at these higher temperatures.[40] This phenomenon may be explained as the oxygen becoming mobilised in the oxide lattice above a critical temperature. Above this temperature the

lattice may assume locally more stable configurations through the formation of shear structures. The layered α-MoO_3 is initially reduced via facile transport of the oxygen from the interlayer spacings of the oxide forming oxygen vacancies which lead to a slipping of the planes and reoxidation of the vacancies by parallel terminal oxygen groups.

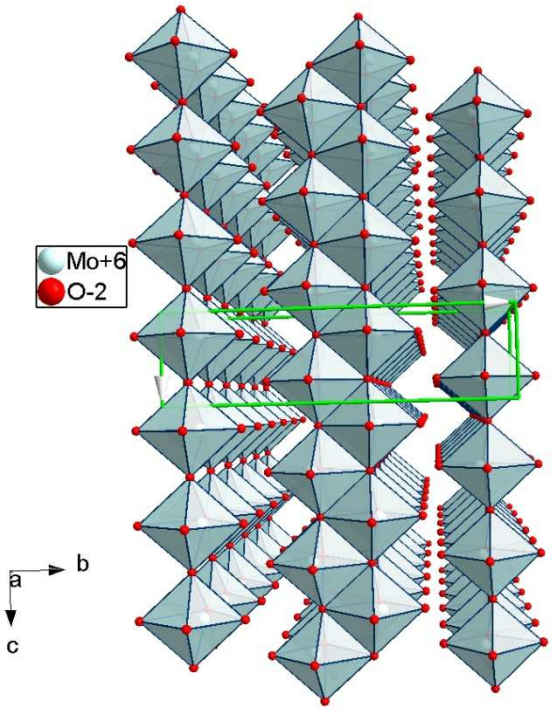

Figure 2.28: View of α-MoO_3 looking down the (100) plane at the interlayer spacings.

Increasing the temperature drives the fast reconstruction of the oxide to form a monoclinic suboxide which, depending upon reaction conditions (mass-transport limitations) may form a bulk crystalline phase, or alternatively is formed as a micro-domain of corner-linked Mo octahedra at the reaction front. The calculated apparent activation energies in Figure 2.17 & 2.18 reflect this; as the conversion increases the mechanism is changing, which also accounts for a large degree of observed error.

The reduction-carburisation of *h*-Mo(V)O_3-type oxides appears to mechanistically different to that of the orthorhombic oxide. This is not surprising because in this case the structure is 3-dimensional oxidic lattice in which all oxygen atoms are connected to at least two molybdenum atoms (Figure 2.5). The initial reduction step is observed to have the highest apparent activation energy (150–200 kJ/mol) which is because the oxide lattice has no low-energy mechanism by which it may be reduced. Initial removal of oxygen results in destabilisation of the crystal structure. The temperature

of reduction increases with increasing vanadium content which reflects the increased intrinsic stability of the V-doped materials. Due to the presence of cations in the hexagonal channels *h*-MoO_3 is non-stoichiometric with respect to Mo in order to compensate the charge in the crystal resulting in a more correct formula of: $(NH_4)_{1-x}Mo_5\square_{Mo}O_{18-x-y}\cdot H_{5-2y-x}$.[34] By substituting Mo for V, the number of crystallographic vacancies (metal) in the structure decreases, resulting in a more stable material.

More interesting to note is the general trend in activation energies for the *h*-$Mo(V)O_3$ series. The initial activation energy of reduction calculated for *h*-MoO_3 is higher than those calculated for the Mo/V precursors, while the activation energy for the reduction step $MoO_{3-x} \rightarrow MoO_2$ is lower (Figure 2.18). In the *in situ* XRD, an intermediate phase (*o*-Mo_4O_{11}) is only observed for *h*-MoO_3, however, we can see from the TPR profiles that the Mo/V oxides also share a complex mechanism. Without further evidence it is difficult to speculate on the reason for the differences in initial activation energy.

A possible explanation for these observations is related to the oxygen mobility in the oxide lattices. The effect which is then observed with the structural inclusion of vanadium is to reduce the mobility of the oxygen in the sublattice thereby increasing the energy required to reduce the oxide. The more oxophilic nature of the vanadium serves to create strongly bound V=O moieties which kinetically hinder the reduction process.

The carburisation step $MoO_2 \rightarrow Mo_2C$ is seen to increase in activation energy with the inclusion of vanadium (Figure 2.17). This phenomenon can be explained in two ways. The first is by similar argumentation as above: oxophilic vanadium moieties reduce the mobility of oxygen out of the lattice, also resisting the ingress of carbon, thereby kinetically hindering the carbide formation. Another explanation is that the reduced Mo/V oxide lacks sufficient metallic character to decompose CH_4 and thereby incorporate carbon. It is well known that MoO_2 is a metallic oxide which has electron density at the Fermi edge. For a carbide to be formed the reacting species must be metallic which is not common for transition metal oxides, even in a reduced form.

In either case we observed that in the case of *h*-$Mo_{0.92}V_{0.08}O_3$ the reduction step — $MoO_3 \rightarrow MoO_2$ — is completed entirely before the formation of the carbide. This is most clearly seen in the comparison of masterplots (Figure 2.21) which show that the reduction proceeds via a 3-dimensional diffusional mechanism. This case is also supported by the TPR profiles (Figure 2.15) which show that in the V-free oxides, CH_4 is consumed at an earlier stage of the reaction.

2.5 Summary

Reductive carburisation of a mixed metal oxide based on hexagonal MoO_3 resulted in bimetallic carbides with a novel high aspect-ratio mesostructure and ordered crystallographic nature. The Mo/V precursor oxide was synthesised by a simple precipitation reaction and the carburisation reaction was observed using *in situ* powder XRD technique. This was contrasted to the TPR-carburisation of α-MoO_3 and it was observed that all precursors were reduced via MoO_2 as an intermediate phase. The kinetics of reduction for the precursor oxides were investigated yielding insight into the mechanism of reduction. The observed TPR profiles were in agreement with the findings of Ressler and Lalik and suggest that the mobility of atomic oxygen in the lattice is affected by the inclusion of vanadium as a dopant. It is unclear as to whether it is as a structural inhibition to the comproportionation reaction:

$$3MoO_3 + MoO_2 \rightarrow Mo_4O_{11}$$

or a more fundamental electronic effect which is the origin of this observation. However, it was observed that vanadium inclusion resulted in a sharper, single reduction peak that was correlated with a more uniform evolved mesoporosity in the product carbide.

The use of multi-metal oxides as precursors for carbides is a largely unexplored area of transition metal carbide chemistry. In particular it offers interesting possibilities to produce tailored carbides with novel material properties, higher surface areas, and/or improved catalytic selectivity and performance. These goals can be achieved by either doping of bulk carbides with more active metals or by choosing precursor oxides with structural properties that influence the carbide product. The relatively high surface area of this material and the inclusion of vanadium atoms in the structure provide a basis for the investigation of a number of industrially useful reactions.

In this chapter we also present a methodology for the synthesis and characterisation of air-sensitive refractory materials produced by solid-state reaction in various gas atmospheres at elevated temperatures. The scaled-up synthesis of high surface area molybdenum carbide as characterised by XRD, CHN analysis, N_2-sorption, SEM, TEM, Raman spectroscopy (Chapter 4) and XPS (Chapter 4) is presented as an example. This technique allows us to use the materials directly in catalytic reactions without pre-treatment, providing the opportunity to characterise the materials extensively prior to reaction. This contributes to our understanding of the surface-structure-relations with catalytic activity.

2.6 References

[1] H. Bohm, Electrochimica Acta 1970, 15, 1273.
[2] R. B. Levy, M. Boudart, Science 1973, 181, 547.
[3] J. S. Lee, S. T. Oyama, M. Boudart, Journal of Catalysis 1987, 106, 125.
[4] L. Leclercq, M. Provost, H. Pastor, G. Leclercq, Journal of Catalysis 1989, 117, 384.
[5] G. S. Ranhotra, A. T. Bell, J. A. Reimer, Journal of Catalysis 1987, 108, 40.
[6] A. P. E. York, J. B. Claridge, A. J. Brungs, S. C. Tsang, M. L. H. Green, Chemical Communications 1997, 39.
[7] G. M. Dolce, P. E. Savage, L. T. Thompson, Energy & Fuels 1997, 11, 668.
[8] S. Alconchel, F. Sapina, E. Martinez, Dalton Transactions 2004, 2463.
[9] X.-H. Wang, M.-H. Zhang, W. Li, K.-Y. Tao, Catalysis Today 2008, 131, 111.
[10] S. T. Oyama, Journal of Solid State Chemistry 1992, 96, 442.
[11] C. C. Yu, S. Ramanathan, B. Dhandapani, J. G. Chen, S. T. Oyama, J. Phys. Chem. B 1997, 101, 512.
[12] S. T. Oyama, C. C. Yu, S. Ramanathan, Journal of Catalysis 1999, 184, 535.
[13] L. Bastos, W. Monteiro, M. Zacharias, G. da Cruz, J. Rodrigues, Catalysis Letters 2008, 120, 48.
[14] O. Mougin, J.-L. Dubois, F. Mathieu, A. Rousset, Journal of Solid State Chemistry 2000, 152, 353.
[15] K. O. T. Ushikubo, A. Kayo, T. Umezawa, K. Kiyona, I. Sawaki, European Patent 1992, 529.
[16] A. K. M. Hatano, European Patent 1988, 318.
[17] S. Knobl, G. A. Zenkovets, G. N. Kryukova, O. Ovsitser, D. Niemeyer, R. Schlögl, G. Mestl, Journal of Catalysis 2003, 215, 177.
[18] S. T. Oyama, J. C. Schlatter, J. E. Metcalfe, J. M. Lambert, Industrial & Engineering Chemistry Research 1988, 27, 1639.
[19] A. I. Kharlamov, V. G. Aleshin, V. M. Prokopenko, N. V. Kirillova, Theoretical and Experimental Chemistry 1981, 16, 515.
[20] S. Nagakura, S. Oketani, Transactions of the Iron and Steel Institute of Japan 1968, 8, 265.
[21] T. C. Xiao, A. P. E. York, V. C. Williams, H. Al-Megren, A. Hanif, X. Y. Zhou, M. L. H. Green, Chemistry of Materials 2000, 12, 3896.
[22] T. Xiao, A. P. E. York, K. S. Coleman, J. B. Claridge, J. Sloan, J. Charnock, M. L. H. Green, Journal of Materials Chemistry 2001, 11, 3094.
[23] T. C. Xiao, H. T. Wang, J. W. Da, K. S. Coleman, M. L. H. Green, Journal of Catalysis 2002, 211, 183.
[24] A. Hanif, T. C. Xiao, A. P. E. York, J. Sloan, M. L. H. Green, Chemistry of Materials 2002, 14, 1009.
[25] H. M. Wang, X. H. Wang, M. H. Zhang, X. Y. Du, W. Li, K. Y. Tao, Chemistry of Materials 2007, 19, 1801.
[26] X. Li, D. Ma, L. Chen, X. Bao, Catalysis Letters 2007, 116, 63.
[27] Z. W. Yao, Journal of Alloys and Compounds 2009, 475, L38.
[28] G. Centi, F. Cavani, F. Trifirò, Selective oxidation by heterogeneous catalysis, Kluwer Academic/Plenum Publishers, New York, 2001.
[29] T. Ozawa, Thermochimica Acta 1986, 100, 109.
[30] BrukerAXS, DIFFRACplus TOPAS V3.0, ©1999, p. Profile and structure analysis software.

[31] D. Balzar, in Defect and microstructure analysis by diffraction Vol. 10 (Ed.: H. J. B. R. L. Snyder, and J. Fiala), Oxford University Press, 1999.
[32] I. P. Olenkova, L. M. Plyasova, S. D. Kirik, Reaction Kinetics and Catalysis Letters 1981, 16, 81.
[33] L. M. Plyasova, S. D. Kirik, I. P. Olen'kova, Journal of Structural Chemistry 1983, 23, 590.
[34] N. A. Caiger, S. Crouch-Baker, P. G. Dickens, G. S. James, Journal of Solid State Chemistry 1987, 67, 369.
[35] B. Darriet, J. Galy, Journal of Solid State Chemistry 1973, 8, 189.
[36] L. Dupont, D. Larcher, F. Portemer, M. Figlarz, Journal of Solid State Chemistry 1996, 121, 339.
[37] L. Dupont, D. Larcher, M. Touboul, Journal of Solid State Chemistry 1999, 143, 41.
[38] A. R. Denton, N. W. Ashcroft, Physical Review A 1991, 43, 3161.
[39] J.-S. Choi, G. Bugli, G. Djéga-Mariadassou, Journal of Catalysis 2000, 193, 238.
[40] T. Ressler, R. E. Jentoft, J. Wienold, M. M. Gunter, O. Timpe, The Journal of Physical Chemistry B 2000, 104, 6360.
[41] E. Lalik, Catalysis Today 2010, In Press, Corrected Proof.
[42] E. Lalik, W. I. F. David, P. Barnes, J. F. C. Turner, The Journal of Physical Chemistry B 2001, 105, 9153.
[43] E. Lalik, Catalysis Today 2011, 169, 85.
[44] D. Wang, D. S. Su, R. Schlögl, Zeitschrift Fur Anorganische Und Allgemeine Chemie 2004, 630, 1007.
[45] E. Torres-García, G. Rodríguez-Gattorno, J. A. Ascencio, L. O. Alemá¡n-Vá¡zquez, J. L. Cano-Domínguez, A. Martánez-Hernández, P. Santiago-Jacinto, The Journal of Physical Chemistry B 2005, 109, 17518.
[46] G. Rodriguez-Gattorno, A. Martinez-Hernandez, L. O. Aleman-Vazquez, E. Torres-Garcia, Applied Catalysis a-General 2007, 321, 117.
[47] G. W. Watt, D. D. Davies, Journal of the American Chemical Society 1948, 70, 3751.
[48] H. Sakagami, Y. Asano, T. Ohno, N. Takahashi, H. Itoh, T. Matsuda, Applied Catalysis A: General 2006, 297, 189.
[49] T. Ohno, Z. Li, N. Sakai, H. Sakagami, N. Takahashi, T. Matsuda, Applied Catalysis A: General 2010
In Press, Accepted Manuscript.
[50] N. S. McIntyre, D. D. Johnston, L. L. Coatsworth, R. D. Davidson, J. R. Brown, Surface and Interface Analysis 1990, 15, 265.
[51] M. Yamada, J. Yasumaru, M. Houalla, D. M. Hercules, Journal of Physical Chemistry 1991, 95, 7037.
[52] J. B. Claridge, A. P. E. York, A. J. Brungs, C. Marquez-Alvarez, J. Sloan, S. C. Tsang, M. L. H. Green, Journal of Catalysis 1998, 180, 85.
[53] H. L. Friedman, Journal of Polymer Science Part C-Polymer Symposium 1964, 183.
[54] A. Khawam, D. R. Flanagan, The Journal of Physical Chemistry B 2006, 110, 17315.
[55] W. Jander, Zeitschrift Fur Anorganische Und Allgemeine Chemie 1927, 163, 1.
[56] C. Bouchy, C. Pham-huu, M. J. Ledoux, Journal of Molecular Catalysis a-Chemical 2000, 162, 317.

[57] C. Bouchy, C. Pham-Huu, B. Heinrich, C. Chaumont, M. J. Ledoux, Journal of Catalysis 2000, 190, 92.
[58] J. Patt, D. J. Moon, C. Phillips, L. Thompson, Catalysis Letters 2000, 65, 193.
[59] T. Ressler, O. Timpe, T. Neisius, J. Find, G. Mestl, M. Dieterle, R. Schlögl, Journal of Catalysis 2000, 191, 75.
[60] T. Ressler, J. Wienold, R. E. Jentoft, Solid State Ionics 2001, 141-142, 243.

Chapter 3: Reactivity of propane over Mo/V carbides I: Catalytic reactivity and temperature programmed studies

3.1 Abstract

In this chapter, mixed molybdenum-vanadium carbide catalysts are studied in the activation of propane. The catalysts were tested in a plug flow reactor under reducing conditions to maintain the phase composition, and the influence of temperature, surface oxidation, vanadium content and surface carbon deposition are observed on the reaction network.

In the presence of H_2/C_3H_8, Mo/V carbides are shown to catalyse the dehydrogenation of propane to propylene with a selectivity that approaches 50%, as well as carrying out the hydrogenolysis of propane to CH_4 and C_2H_6 on an apparently distinct catalytic site. Addition of H_2O or CO_2 as an oxidant to the feed greatly increases the yield and selectivity of the dehydrogenation reaction (S > 90%) and introduces products from the dry/steam reforming of propane and reverse water-gas shift. Vanadium was observed to reduce the stability of the carbide to oxidation; in the case of O_2 to α-MoO_3, and in the case of H_2O and CO_2, to MoO_2. In the activation of propane, vanadium increases the apparent activation energy for dehydrogenation and for hydrogenolysis.

In a separate study into the reverse water-gas shift reaction, Mo_2C is found to be an efficient catalyst for the hydrogenation of CO_2 with high selectivity to CO (> 90%). The reaction went to equilibrium conversion even at very high space velocities over a range of temperatures (GHSV > 200000, 500°C < T < 700°C).

In the temperature-programmed reaction of *h*-$Mo_{1-x}V_xO_3$ precursor oxide materials in H_2-C_3H_8, it was observed that the catalysts were reduced to the *fcc* α-MoC_{1-x} carbide with evidence of carbon inclusion at lower temperatures than observed for TPRC in H_2-CH_4 mixtures. On reduction, the catalytic activity was observed to increase dramatically and selectivity evolved with temperature mirroring the reduction state of the oxide.

3.2 Introduction

Selective oxidation, or oxyfunctionalisation, of alkanes is an area that has long been of interest in catalysis for reasons of energy efficiency and potential cost savings.[1] In recent years this interest has gained momentum and a number of technologies are applied industrially or are in development (Table 3.1).[2] There are a number of motivating factors for this increased focus but it is primarily dependent on the price and availability of raw materials. The increasing worldwide demand for consumer goods, combined with dwindling oil reserves, necessitate a reduced focus on the use of crude oil as a substrate material and increasing consideration of energy costs. These factors, combined with the development of environmental policy and legislation, have driven industry and academia to find innovative solutions for the chemical demands of a growing populace.

Table 3.1: Technologies for the oxidative transformation of light alkanes (C1–C6)[3]

Raw material	Product	Stage of development
Methane	Methanol	Pilot plant
Methane	Syngas	Pilot plant
Methane	Ethylene	Pilot plant
Ethane	1,2-Dichloroethane,vinyl chloride	Pilot plant
Ethane	Acetaldehyde	Research
Ethane	Acetic acid	Research
Ethane	Ethylene	Research
Propane	Acrolein, acrylic acid	Research
Propane	Propyl alcohol	Research
Propane	Acrylonitrile	Demonstrative plant
Propane	Propylene	Research
n-Butane	Acetic acid	Industrial
n-Butane	Maleic anhydride	Industrial
n-Butane	Butadiene	Industrial, abandoned
Isobutane	Methacrylic acid	Pilot plant
Isobutane	Isobutene	Research
Isobutane	t-Butyl alcohol	Research
n-Pentane	Phthalic anhydride	Research
Cyclohexane	Cyclohexanol,cyclohexanone	Industrial
Cyclohexane	Cyclohexanone	Research

Transition metal oxide-based systems are a hugely important class of materials in selective oxidation reactions due to their ability to undergo reduction oxidation cycles required for the dynamic exchange of electrons, as well as perform hydrogen abstraction and oxygen insertion. Molybdenum and vanadium form the basis for a number of mixed metal oxide (MMO) catalysts, which is unsurprising when one considers the electronic flexibility of the elements, with varying formal oxidation

states of up to VI and V respectively. Molybdenum-based oxides in particular are widely used in selective oxidation reactions due to their facile reducibility and high oxygen mobility, which can be tuned for selective reactivity through the addition of dopants and by the use of ternary (or quaternary) oxide phases.[4-7]

In industrial scale reactions these catalysts are subject to a wide range of conditions that can vary considerably in chemical potential, composition and temperature.[2] From an extensive body of research, it is recognised that these influences control the oxidation state at the surface and subsequently the phase composition of the catalyst.[8, 9]

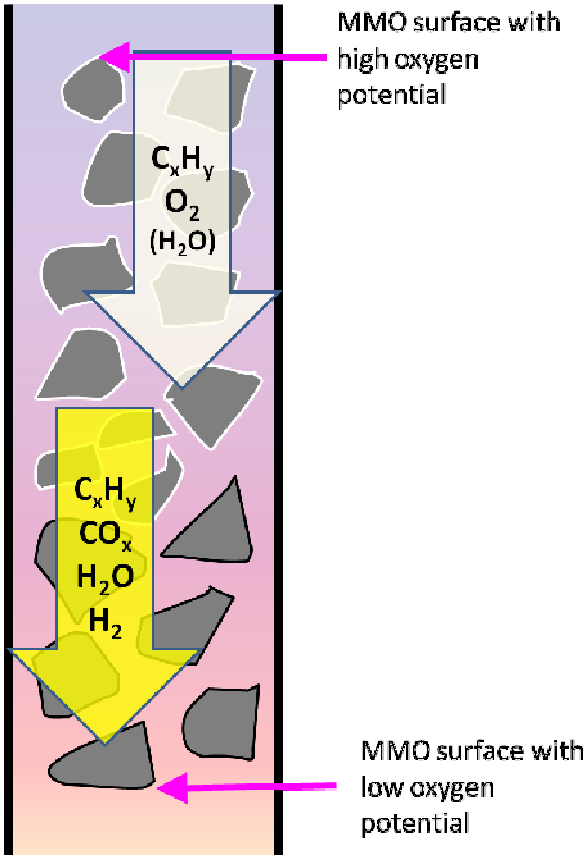

Figure 3.1: Illustration of a partial oxidation reactor operating at high oxygen conversion

It is demonstrated in the literature regarding partial oxidation reactions that the conversion of oxygen in fixed bed reactors results in a strongly varying profile of reactive atmosphere along the direction of gas flow.[10, 11] Under conditions of total oxygen consumption, it is evident that the gas potential of the atmosphere will become reducing (Figure 3.1). However, this phenomenon is widely ignored in studies that cite partial oxygen conversion in order to remain in a regime whereby the

reaction kinetics may be analysed by conventional means. Several studies by Sinev *et al.* and others point to the persistent presence of hydrogen (not commonly measured in catalytic studies) in reactions in which only partial conversion of oxygen is demonstrated.[12-14] These studies and others suggest that the conventional kinetic models that integrate over the entire reactor are not always able to account for the observed species in these reactions. These effects are mitigated by diligent practice and operation within a differential regime, taking into account the effects of mass transport limitation and heat transfer.[15] However, on a mesoscopic scale, highly exothermic total oxidation reactions in the often rich mixtures applied may hypothetically result in the generation of transiently reduced surface species. Depending on the extent of such phenomena, it could be expected that non-typical reaction products/selectivities are observed in the reaction. Currently there is a gulf between understanding the study of model catalytic systems and the operation of high-performance catalysts operating at equilibrium conversion in industrial conditions.

3.2.1 Motivation

The selective oxidation of propane to acrylic acid is a process that involves the insertion of two oxygen atoms and transfer of eight electrons. The molybdenum-based catalyst; $MoVNbTeO_x$, specifically the crystalline phase 'M1', is considered to be the most active and selective catalyst discovered to date.[16, 17] Mechanistic details of the reaction are unclear, but it is believed to occur in a concerted mechanism via the initial dehydrogenation of propane to propene.[18] The structural complexity of this catalyst is evident in Figure 3.2 in which a section of the a-b plane of M1 catalyst is shown. The M1 catalyst is a metastable-layered oxide structure comprising edge and corner sharing octahedral motifs to form a quasi-2D unit cell with six- and seven-sided channels extending through the c-axis. The Mo, V & Nb occupy the octahedral and pentagonal-bipyramidal oxygen-coordinated sites while Te sits exclusively in the channels of the structure. In general, it is observed that this structure is integral to the high performance of the catalyst, however, it is reported that the surface composition is indeed dynamic under the applied reaction conditions[19] and that the surface of the catalyst can be reversibly degraded and restored via a self-healing process.[20]

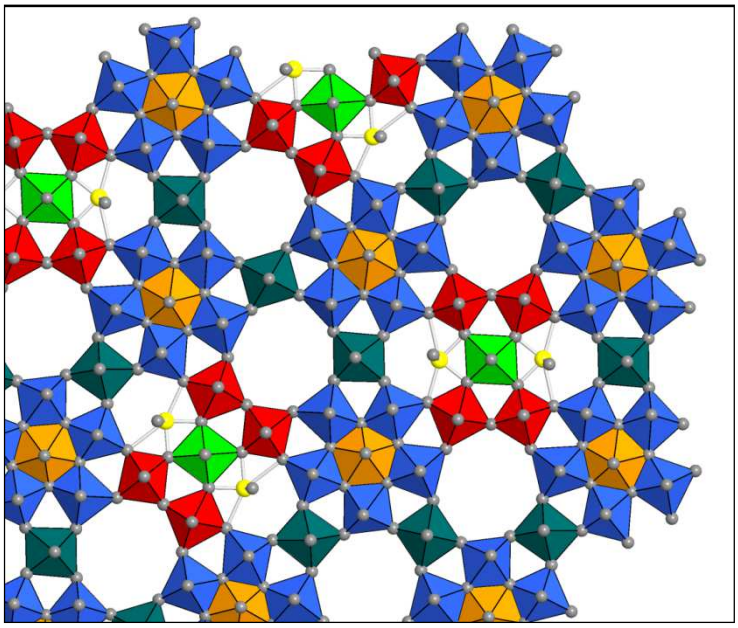

Figure 3.2: Detail of MoV(Nb)TeOx - M1 structure as viewed down the c-axis. Coloured octahedrons represent non-equivalent metal positions. Nb preferentially occupies pentagonal-bipyramidal sites; Te is preferentially bound asymmetrically in the hexagonal channels (yellow).[21]

Many proposed kinetic models for the partial oxidation of propane to acrylic acid do not fit the observed product selectivities and are inadequate to explain various features such as the high ratio of CO:CO_2 in the byproduct stream.[22] In the absence of secondary phases, it can only be assumed that all active sites are generated within the composition of the catalyst depending on the chemical potential at the surface. Hydrothermally synthesized M1 catalyst is highly efficient and the exothermic generation of acrylic acid, propene and carbon oxides at the catalytic surface results in a cascade effect, with the rapid removal of molecular oxygen from the local vicinity and the generation of heat.

Depending on the validity of the various proposed reaction schemes involving either Langmuir-Hinshelwood, Eley-Rideal or Mars-van Krewelen-type mechanisms,[23] the surface chemical potential may be reduced via direct abstraction of oxygen by carbon or by the starvation of bulk oxygen replenishment. In this case, the oxygen diffusion and reducibility of the surface will be dictated by the chemical and structural composition of the oxide.

3.2.2 Experimental goals and approach

In Chapter 2, the complex molybdate *h*-$Mo_{1-x}V_xO_3$ was presented as a precursor for TPR-carburisation to bimetallic carbide. Here we present vanadium-substituted molybdenum carbide, $(Mo_{1-x}V_x)_2C$ as a model for a highly-reduced MoVTe catalyst. As can be seen in Figure 3.3 the structure of the precursor *h*-MoO_3 bears a resemblance to the M1 structure (Figure 3.2) in that they are both channeled oxide structures with needle-like morphologies and flat, terminating a-b planes. Molybdenum may be incrementally substituted in the structure by vanadium thereby allowing for the comparison of variable chemical composition on the observed reactivity. Furthermore, because the chemistry of Mo_2C is now widely studied, there exist a number of studies detailing the synthesis, structural characterization and catalytic properties.[24-26]

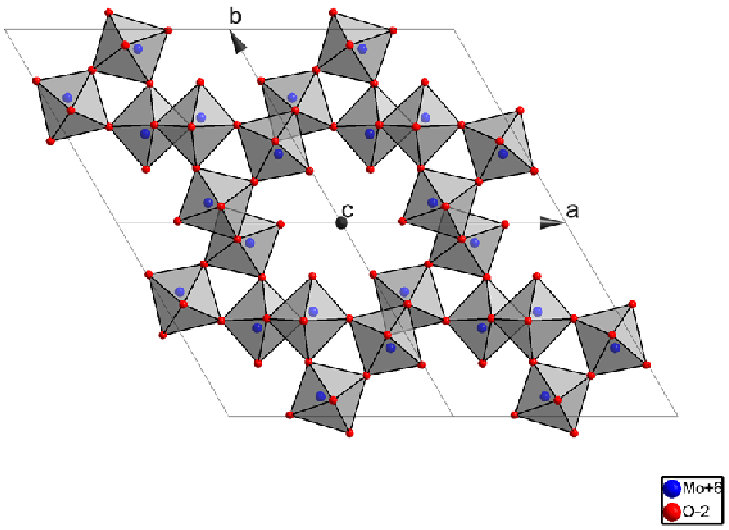

Figure 3.3: Representation of h-MoO_3 complex molybdate structure as viewed down the c-axis. Channels are partially occupied by stabilising mono-cationic species from: Na^+, K^+, Rb^+, NH_4^+, H_3O^+.[27-29] Molybdenum may be substituted by vanadium up to 13% (metal basis).[30-32]

The reaction conditions widely applied for the selective oxidation of propane over Mo-based catalysts are a mixture of 2:1 oxygen-propane (ca. 10%) in ca. 40% steam with the remaining 50% N_2, carried out at temperatures between 350-420°C.[33] However, to study the reactions of propane over a reduced oxide or carbide catalyst, it is necessary to modify the conditions so as to maintain a stable phase composition. Within this adapted regime, the roles of temperature, oxidant (O_2/CO_2/H_2O) and

vanadium concentration are explored with respect to the observed reactivity and phase stability.

The stated experimental goals are to:

- explore and understand the reactivity of propane on the Mo_2C surface
- observe the influence of surface oxidation on the reactivity of C_3H_8
- contrast the reactivity of dry C_3H_8 over Mo_2C with co-fed steam or CO_2
- apply the bimetallic system $(Mo_{1-x}V_x)_2C$ with varying *x* to determine the influence of vanadium on the reactivity
- determine the influence of dopant vanadium in a combined TPR-surface carburisation in catalytically relevant conditions.

3.2.3 Previous studies on Mo_2C

In the literature, the reactions of alkane substrates over Mo_2C (*hcp*) and MoC_{1-x} catalysts can generally be grouped into 3 categories: methane activation (C1), dehydrogenation (C3, C4) and isomerisation (C5 - C8).

3.2.3.1 Methane activation – C1

The reforming reactions of CH_4 over Mo_2C are highly relevant to the activation of higher alkanes because they serve as a fundamental model for the surface interactions of carbon containing gases as well as CO, CO_2, H_2 and H_2O.

Partial oxidation of methane (POM):

$$CH_4 + 1/2\ O_2 \leftrightarrow CO + 2H_2 \qquad — \qquad \Delta H^{\theta}_{298} = -38\ kJmol^{-1}$$

Dry methane reforming (DMR):

$$CH_4 + CO_2 \leftrightarrow 2CO + 2H_2 \qquad — \qquad \Delta H^{\theta}_{298} = 247\ kJmol^{-1}$$

Steam methane reforming (SMR):

$$CH_4 + H_2O \leftrightarrow CO + 3H_2 \qquad — \qquad \Delta H^{\theta}_{298} = 206\ kJmol^{-1}$$

Mo_2C was first demonstrated by Green *et al.* to effectively catalyse methane reforming in POM, DMR and SMR conditions.[34-36] The activities observed were

reported to be comparable with those reported for supported Ir and Ru catalysts.[35] It was also claimed that the molybdenum carbide suffers reduced deactivation from coke deposition *cf.* commercial Ni catalysts due to an increased kinetic barrier to carbon deposition.[35] There are two competing mechanisms for the formation of synthesis gas over carbides – the first is a redox mechanism and the second is a noble metal-type mechanism. In the redox mechanism (shown below for the case of DMR) the oxidant (CO_2) is dissociatively chemisorbed on the surface of the carbide to produce CO and atomic oxygen (O*) which subsequently combines with carbidic carbon in the surface and is evolved as CO leaving a vacancy (□). The vacancy may either react with an oxidant or capture C* from the decomposition of CH_4 on the surface.

$$CH_4 \leftrightarrow C^* + H_2$$

$$CO_2 \leftrightarrow CO + O^*$$

$$Mo_2C + O^* \leftrightarrow Mo_2\square + CO$$

$$Mo_2\square + O^* \rightarrow\rightarrow MoO_x$$

$$Mo_2\square + C^* \rightarrow Mo_2C$$

The alternative noble metal-like mechanism is as follows:

$$CH_4 \leftrightarrow C^* + 2H_2$$

$$CO_2 \leftrightarrow CO + O^*$$

$$O^* + C^* \rightarrow CO$$

The redox mechanism is supported by labelled $^{13}CH_4$ isotope experiments carried out by Thomson *et al.* that show the surface carbon readily undergoes exchange at reaction temperatures (> 500°C).[37] Similar labelling experiments by Xiao *et al.* confirm that ^{13}CO is observed in POM, implying a scrambling of carbon atoms commensurate with the redox mechanism.[38] In the case of DMR, a kinetic model was proposed by Thomson *et al.* which supports a cycling mechanism.[39]

This mechanism depends on the dynamic equilibrium of the surface with the gas phase; the oxycarbide interface is thermodynamically maintained with the exchange of carbon and oxygen species. For the cases of DMR and SMR the overall equilibria can be represented respectively as:[39]

$$Mo_2C + 5CO_2 \leftrightarrow 2MoO_2 + 6CO$$

$$Mo_2C + 5H_2O \leftrightarrow 2MoO_2 + CO + 5H_2$$

Additionally, the non-reversible carburisation:

$$MoO_2 + 5CH_4 \rightarrow Mo_2C + 4CO + 10H_2$$

A series of studies by LaMont *et al.* show that for the cases of SMR and DMR, bulk Mo_2C catalyst is stable in stoichiometric feeds at elevated pressures (> 8 bar) following reductive sintering and pretreatment at 700°C. [37, 39-41]

The non-oxidative reactivity of CH_4 on various molybdenum surfaces (Mo, MoO_2, MoO_3, Mo_2C (*hcp*), and MoC_{1-x} (*fcc*)) in bulk and supported systems, was reported by Solymosi *et al.*[42] Over a pre-reduced Mo_2C catalyst it was observed that initial conversion of CH_4 at 700°C was between 6-8%, dropping significantly within minutes on stream. The primary product observed was hydrogen and to a lesser extent ethane is observed to evolve after time on stream. Similar results were obtained by Oshikawa *et al.* over a series of carbide catalysts with varying structural features.[43]

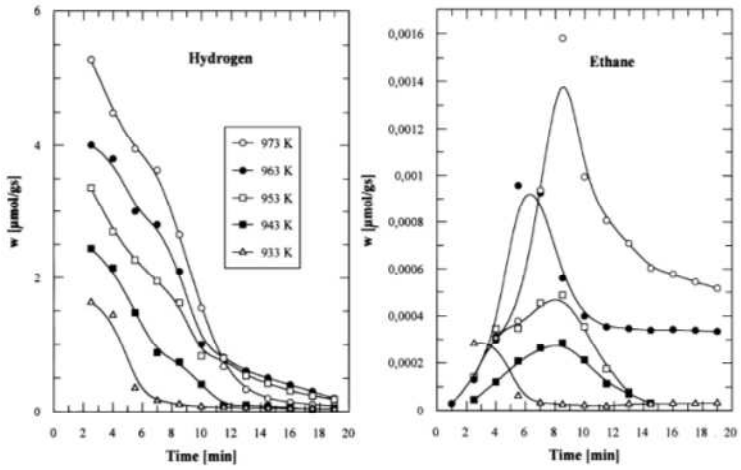

Figure 3.4: Behaviour of methane with time on stream over Mo_2C at 700°C — reprinted from [42] with permission from Elsevier.

Dehydroaromatisation of various alkanes, primarily of CH_4 to benzene, is reported for MoC_x species supported on the zeolite ZSM-5.[42, 44-53] The interaction of both phases has been shown to be necessary for the formation of aromatics via the dissociative adsorption of CH_4 over MoC_x clusters, followed by oligomerisation on the Brønsted acid sites of the HZSM-5.[47]

Both the examples of methane decomposition and dehydroaromatisation provide strong evidence that molybdenum carbides are suitable materials for reactions involving C-H bond activation. In the case of CH_4 decomposition, this results in almost immediate deactivation via carbon deposition. However in the compound system MoC_x/ZSM-5, this rapid decomposition is harnessed to provide a feedstock of carbon to the acidic zeolite catalyst, which completes the aromatisation. This example of a dynamic system is relevant to the formation of transient reduced sites, which are subsequently reoxidised resulting in a complex catalytic system.

3.2.3.2 Dehydrogenation reactions

The dehydrogenation of light alkanes over bulk and supported molybdenum carbide and oxycarbide is reported for ethane,[54] propane[52, 55] and butane.[56-60] A relatively low number of studies concerning this topic reflects the difficulty involved in these reactions, which are characterised by deactivation, complex reaction networks, and the the dynamic nature of the carbide surface.

Dehydrogenation of ethane in the presence of CO_2 is presented by Solymosi *et al.* over the temperature range 550-700°C using a Mo_2C/SiO_2 catalyst.[54] At conversions of around 10%, the selectivity to ethylene is high (80-90%). With temperature, the conversion increases exponentially with increasing selectivity to both the hydrogenolysis and ethane reforming products. It is loosely hypothesised that the dehydrogenation is carried out on an 'oxycarbide' site via 'activated oxygen' attack at the ethane to form ethylene and water. There is no evidence provided.

In a series of more rigorous studies, Solymosi *et al.* present the dehydrogenation of propane over bulk and supported Mo_2C with and without the influence of CO_2.[52, 55] It is observed that in dry feed conditions over bulk Mo_2C, the dominant reaction product is propylene (S = 44% @ 600°C) with secondary products of methane and ethylene. The supported catalyst Mo_2C/SiO_2 is reported to show higher selectivity to propylene

under similar conditions. It is worth noting that the initial selectivity to propylene of the silica supported catalyst prepared *in situ* is zero, increasing with time on stream. This is in contrast to the passivated bulk catalyst, which is initially selective to propylene.

The reactions of butane over molybdenum oxycarbide catalyst have been extensively studied by Ledoux *et al.* [56, 60, 61] who describe a carbon-modified MoO_x 'oxycarbide' phase that is selective to C4 olefin products in a feed of $H_2/C_4H_{10}/H_2O$. Reduction of the steam partial pressure leads to reduction of the oxycarbide and increasing selectivity to hydrogenolysis. Also of note in this work is that reduced MoO_2 is also tested in the dehydrogenation of n-butane and found to show low conversion and selectivity to dehydrogenation products compared with the active oxycarbide phase.

A comparative study by Thompson *et al.* contrasts the relative product selectivities towards dehydrogenation, isomerisation and hydrogenolysis in n-butane activation over the group V and VI transition metal carbides and nitrides. For Mo_2C, the selectivity distribution given as relative reaction rates to dehydrogenation, isomerisation and hydrogenolysis are 1300, 91 and 703 nmol/gs respectively. This initially appears incommensurate with the claims of Ledoux *et al.* However, the TPR-carburization is to 600°C for 15 minutes and hydrogen pretreatment carried out at 480°C. Under these conditions the carburisation is incomplete and bulk oxygen, which is mobilised under the reaction conditions, will form an oxycarbide overlayer. In this study, it is observed also that the vanadium carbide and nitride materials were 100% selective for the dehydrogenation of n-butane.

3.2.3.3 Isomerisation reactions — C5-C8

The isomerisation of alkanes over transition metal carbides was first observed by Levy and Boudart for 2,2-dimethylpropane over a tungsten carbide surface.[62] Subsequently, a number of studies have been published concerning the isomerisation of alkanes over reduced, carbon-modified molybdenum catalysts.[61, 63-79] The wealth of findings for these isomerisation reactions has led to some debate over the nature of the active site for isomerisation.

In an early paper, Holl *et al.* proposed a mechanism involving Mo^0 as the active site. In this mechanism the reaction proceeds via a metallacycle intermediate to a carbene-

olefin, resulting in bond shift migration.[80] This was contested as it required the metal to present two active sites, one selective to hydrogenolysis and one selective to isomerisation, which was not supported in the data.

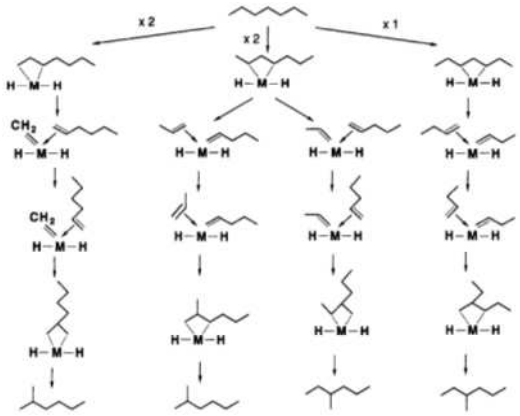

Figure 3.5: Metallacyclobutane intermediate mechanism of heptane isomerisation — reprinted from [69] with permission from the American Chemical Society.

Iglesia *et al.* present a cooperative mechanism in a study of oxygen-modified tungsten carbide catalysts.[81-83] It is assumed that WC_x sites activate C-C and C-H bonds and WO_x sites act as Brønsted acidic sites which catalyse the formation of carbenium-ions for bond-shift reactions. These findings are justified by NH_3 adsorption experiments combined with the observation that a metallacyclobutane intermediate mechanism (Figure 3.5) is inconsistent with the low selectivity for propylene metathesis reactions on WC/O.

This assertion is contrasted by the findings in a series of studies by Ledoux *et al.* on oxygen-modified Mo_2C catalysts.[66, 68-70, 84] The authors reject Mo_2C as unselective and propose the existence of a crystallographically distinct oxycarbide phase selective for isomerisation.[70] Contrary to Iglesia *et al.*, the metallacyclobutane mechanism is put forward, supported by an analysis of the product distribution.[69] In this theory, the absence of cyclic products is cited as being due to the enhanced carbon deposition, also a cause of deactivation. The presence of acidic sites is not discussed.

In an ongoing contribution to the discussion, Maire *et al.* present an electronic argument for a bifunctional catalyst.[72, 73] It is claimed that the electron rich metal centre Mo^{IV} is the active site for initial dehydrogenation and that $M\text{-}O^{\delta+}$ fixates the atomic hydrogen thus forming a Brønsted acidic site M-OH. However, Mo^{IV} as an

active species is generally refuted in the literature, even by Maire's own co-authors it would appear,[85] nonetheless the fundamental mechanism has merit.

In separate studies by Matsuda[75, 86, 87] and Torres-Garcia *et al.*[78, 79], a metallic MoO species distinct from Mo^{IV} is proposed as the active site for isomerisation. Matsuda *et al.* demonstrate the presence of Brønsted acidity in reduced MoO_x catalysts and suggest that the incorporation of H_2 from reduction combines to form the M-OH sites responsible for isomerisation, while broadly speculating on the presence of metallic Mo or Mo suboxide for initial dehydrogenation. This is elaborated by Torres-Garcia *et al.* in a study combining theoretical calculations and practice. It is claimed that a stoichiometric MoO *fcc* phase, which is predicted by quantum chemical calculations, can be observed in the XRD and TEM data. It is supposed that this stabilised phase is formed *in situ* upon reduction and that it is the oxycarbide phase that is identified by Ledoux *et al.* in previous studies.[74] The nature of the carbon species is further discussed with reference to electron energy loss spectroscopy (EELS), Raman and TPO data, and is concluded to be adventitious. The catalytic results are not discussed.

The conditions applied for alkane isomerisation (C4-C8) vary between 200-400°C and at pressures from 1-20 bar in the presence of hydrogen.

3.2.3.4 Other reactions of note – metathesis and RWGS

As well as the reactions of alkanes over Mo_2C/MoO_xC_y surfaces, it is worthwhile to note in the literature some further studies relating to the proposed research.

McBreen *et al.* and Tysoe *et al.* discuss in separate studies the surface interactions of light olefins over Mo_2C[88-92] and reduced MoO_x[93-103] surfaces respectively.

McBreen *et al.* show the formation and stability of alkene metathesis sites on Mo_2C by dissociative adsorption of carbonyl species over Mo to form an oxo-alkylidene surface complex (**Figure** 3.6). As well as the cyclopentylidene functionalised moeity shown here, it is demonstrated that various carbonyl species dissociate to form a highly stable (< 623°C) alkylidene functionalised surface that can undergo metathesis cycles in propylene. The observed surface species and cycled reaction products are consistent with the Chauvin mechanism.[104, 105] It is speculated by the authors, with respect to the low temperature metathesis reaction, that the trace quantities of acetone

and acetaldehyde seen to evolve during the induction period of propene metathesis are formed by a selective oxidation of the propene (presumably via MVK mechanism), and these species subsequently generate the active site via the previously described oxidative addition.[106]

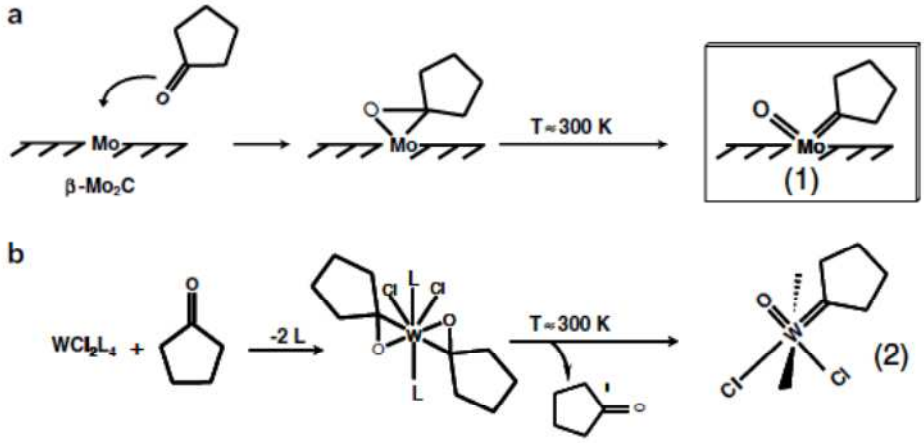

Figure 3.6: (a) Illustration of carbonyl bond scission to form a surface oxo-alkylidene complex on Mo2C. (b) Complementary organometallic mechanism for a tungsten complex. Reprinted from [89] with permission from Elsevier.

Tysoe et al. provide a complementary vision of light alkanes on Mo metal and MoO_x ($x < 3$) surfaces that is more focused on the catalytic properties of the surface than the exact mechanism of formation. By use of UV-photoelectron (UPS) and temperature-programmed desorption (TPD) spectroscopies it is shown that ethylene adsorbs dissociatively on an O-modified Mo(100) surface to form surface carbenes. These carbenes can react with adsorbed hydrogen to form methyl species and subsequently desorb as methane. It is shown that the rate-limiting step for this reaction is the hydrogenation of the methyl group with apparent activation energy of 97 kJ/mol.

The interactions of the C2-4 olefins with variously modified Mo surfaces are studied by TPDS of the adsorbed molecules from 80 – 800K. It is observed that at low oxygen coverage, the surface is highly active to C-C bond scission and subsequent CH_4 formation (Figure 3.7) for 2-butene and propylene, but not for ethylene. With increasing oxygen coverage the methane yield is seen to decrease for butylene, and conversely increase for ethylene and propylene to a maximum at ca. 0.6ML. At 1ML oxygen coverage the evolution of methane is not observed but instead the olefins are observed to adsorb and desorb molecularly.

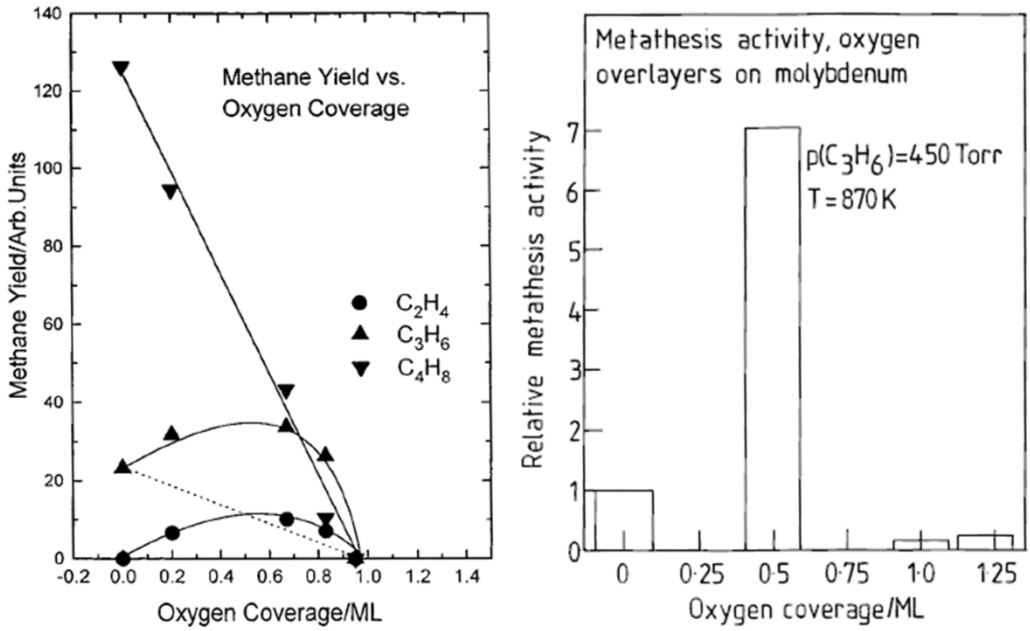

Figure 3.7: (left) methane yield from low temperature desorption experiments versus oxygen coverage over Mo(100). (Right) - observed recombinative hydrocarbon formation over oxygen modified Mo(100). Metathesis activity is defined as the rate of ethylene and butene formation — reprinted from [97] with permission from the American Chemical Society.

In their conclusions, the authors propose three pathways for the reactions of olefins on oxygen-modified Mo: they react to form alkanes; thermally decompose to form carbon and hydrogen; or dissociatively decompose to form carbene species. The carbene species were said to react via two different mechanisms depending upon the temperature: at low temperatures (> 377°C) via a Chauvin-type metathesis mechanism with low activation energy; and at higher temperatures via the recombination of carbene fragments at the surface (high apparent E_a). This has been erroneously termed 'high-temperature metathesis' but is more closely related to Fischer-Tropsch chemistry. As a more general description it will be refered to here as recombinative hydrocarbon formation. To explain the variation in methane yield for the different olefins, it is suggested that the C=C bond dissociation probability increases in the order ethylene < propylene < 2-butene and that the observed CH_4 is the result of hydrogenation of the carbene fragments following the decomposition on the surface.

An alternative explanation for these observations is put forward here: It is proposed in a theoretical study by Zhou *et al.* that the dehydrogenation of CH_4 over reduced Mo catalysts to form a surface CH_2 species is thermodynamically favoured over methyl

formation due to the formation of H_2.[45] This would suggest that these species play a key role in carbide formation and are strongly bound to the molybdenum atom. This is shown by McBreen *et al*. in which carbene species persist on the surface of Mo_2C to temperatures ca. 900K. The dissociative formation mechanism of surface carbenes from olefins is demonstrated for metallic molybenum in earlier papers from Tysoe,[100, 101] however, upon TPD of ethylene on Mo(100) there is no observation of CH_4.

A schematic diagram representing an oxygen-modified Mo surface with ML = 0, 0.5, and 1 is presented in Figure 3.8. The formation of surface alkylidenes over metallic Mo (a) is proposed to result in strongly bound species explainable through back donation of 4d electron density into the unoccupied p-states of the Fischer-type carbene species. With increasing oxygen coverage (b) the density of states at the Fermi edge is reduced and the carbene species is less strongly bound to the surface, therefore able to recombine with H atoms abstracted from the surface decomposition of olefins to carbonaceous residue. At higher coverage (c), the adsorption of olefins at low temperatures is non-dissociative and results in no CH_4 evolution (Figure 3.7). Therefore the origin of methane in the absence of oxygen is only observed for propylene and butene because they contain saturated alkyl groups that decompose on the metallic surface and subsequently desorb as CH_4. Over 0.5ML, the mechanism is a combination of alkyl group decomposition and carbene recombination and therefore is observed for ethylene as well. This increased mobility would also account for the recombinative hydrocarbon formation mechanism observed.

A small number of studies have investigated the suitability of Mo_2C for water-gas shift reactions.[107-110] In a theoretical (DFT) study into WGS over various Mo_2C surfaces by Rodriguez *et al*.[109] it is concluded that carbon- and molybdenum-terminated Mo_2C are less reactive than Cu surface (in that order) and that O-Mo-Mo_2C is the worst catalyst. However, O-C-Mo terminated Mo_2C is calculated to have a higher relative rate than that for Cu(111). This is supported in the finding of Thompson *et al.*, who report stable activity (48h) for WGS over Mo_2C which is greater than that of a commercial Cu-Zn-Al catalyst.[108, 110] The preparation detailed is also consistent with an oxygen-rich carbide phase.

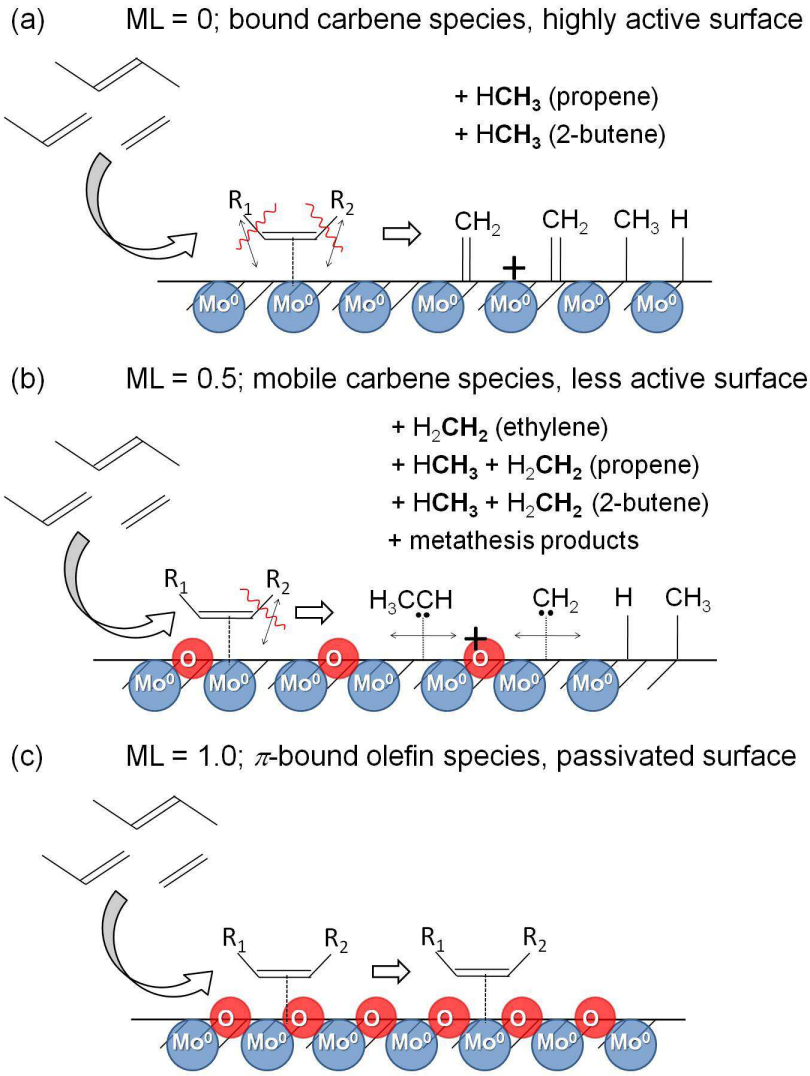

Figure 3.8: A schematic diagram of olefin TPD over oxygen-modified Mo: (a) Dissociative formation of M=CH_2 species over metallic Mo combined with C-C and C-H bond scission. CH_4 is formed from alkyl chains; (b) formation of less tightly bound M···:CH_2 species with surface recombination and CH_4 formation — most active recombinative surface; (c) at low temperatures over MoO surface, non-dissociative adsorption-desorption.

For the case of RWGS, there are surprisingly few studies that have concentrated on this reaction alone. Only one DFT study by Nagai *et al.* discusses CO_2 hydrogenation over Mo_2C using a cluster model of Mo_4C_2.[111] This study predicted the preferential formation of CO and H_2O over the cluster, and that the adsorbed CO_2 was preferentially hydrogenated to CO and OH species in the first step. The conclusions referred to experimental corroboration which was not detailed.

Two catalytic studies by Suzuki *et al.* approach RWGS over Mo-based catalysts. In the first paper MoO_3/ZnO and NiO/ZnO catalysts are compared for RWGS in 1:1

CO_2:H_2 conditions as well as excess CO.[112] The MoO_x in contrast to the NiO supported catalyst shows 100% selectivity to CO and no detectable carbon formation but lower overall conversion. Following a more rigorous pre-reduction it was observed that the MoO_x catalyst was also able to operate at equilibrium conversion (GHSV = 3000 h^{-1}). The second paper by Suzuki *et al.* presents a comparison of supported MoS_2 and WS_2 with supported Fe, Co, and Ni.[113] The activity for selective hydrogenation of CO_2 to CO was not as high as those observed for the 3d transition metals but with 100% selectivity to CO. It was observed that the sulfides had a preferential affinity for H_2 rather than CO_2.

3.3 Experimental

The experimental setup design is based around a plug flow-type reactor which consists of a gas delivery system connected to a quartz U-tube reactor whereby the effluent gas is analysed by gas chromatography. The apparatus was designed to fulfill a range of requirements and was constructed as a multi-purpose reactor for the analysis of light hydrocarbon reactions over solid catalysts. Further experimental constraints at times required the design of specific solutions which are discussed in this section. The plug flow reactor system was designed as a multi-purpose reactor for the partial oxidation of light hydrocarbons and can be seen in Figure 3.9.

Although the particular details of each experiment vary, some standard procedures were followed for the preparation of samples and for the reaction conditions applied. General experimental procedures are given later in this section. These reference the loading of solid catalyst in the reactor, catalytic conditions and subsequent data retrieval and analysis.

3.3.1 Experimental setup

3.3.1.1 U-tube catalytic reactor and furnace design

The U-tube catalytic reactor was custom designed and fabricated from two sections of 6mm OD SiO_2 tubing by Glasbläserei Müller in Adlershof (Figure 3.10). The reactor is fritless for cleaning purposes and the catalyst is sandwiched between two SiC beds, the bottom of which is prevented from flow-through by a plug of SiO_2 wool sitting on the internal shoulder. The geometry of the reactor is optimized for a top-down flow whereby the reactant gases are rapidly

purged in the narrow outlet (ID = 1 mm) to reduce the influence of gas phase reactions. The ID of the reactor at the catalytic bed is 4mm and the experimentally determined isothermal zone over the temperature range 200-700°C was determined to be 30 mm (± 0.5°C), 40 mm (± 1°C) and > 50 mm (± 2°C). All experiments were carried out within the smallest isothermal range (± 0.5°C) – see Figure 3.10).

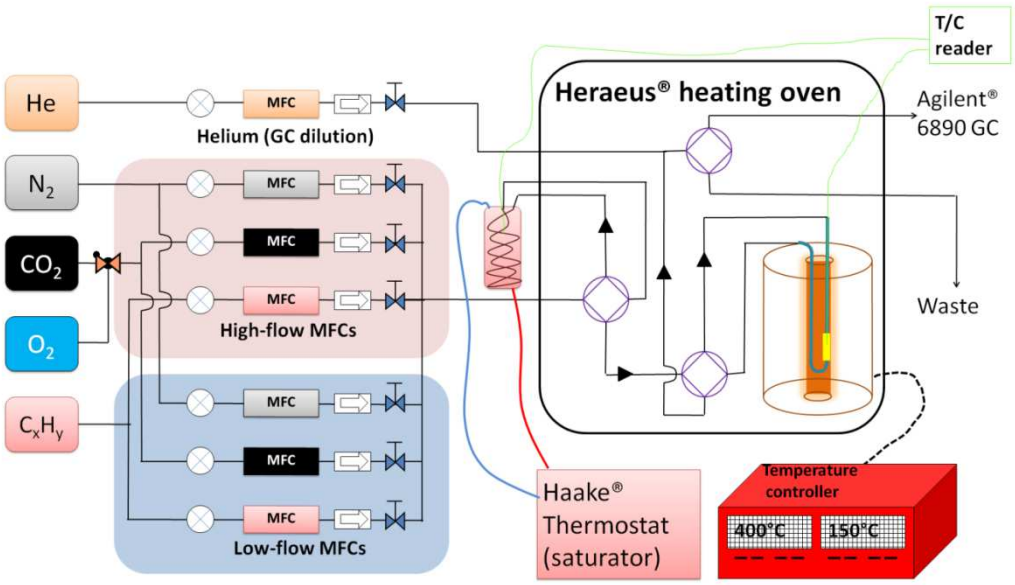

Figure 3.9: Graphical layout of the 'Taniwha' catalytic reactor system.

The heating furnace was adapted from a horizontal fixed tube furnace from Carbolite with a temperature range < 900°C. The heating tube and surrounding insulation were separated and mounted vertically on a crafted base with ceramic fibre stuffing used to prevent downwards heat loss. The heating is controlled by a Eurotherm 2416 PID controller via a solid-state relay and internal type-K thermocouple. The U-tube reactor mentioned earlier was mounted in the furnace tube by way of a machined ceramic sleeve, which also served to prevent heat flow within the tube.

The temperature at the catalyst bed was measured using a thermocouple introduced via a custom made T-junction on the tube adaptor. Temperature data from this thermocouple was recorded to the PC using a Picolog temperature logging system.

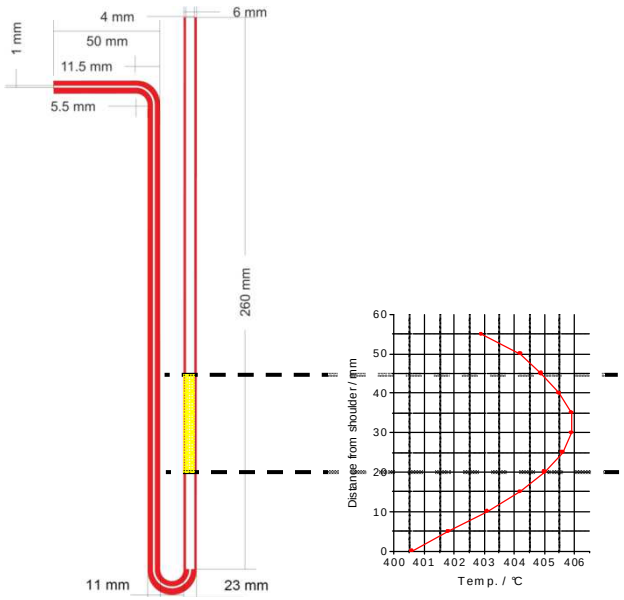

Figure 3.10: Schematic diagram of U-tube reactor (not to scale) with temperature profile mapped over catalyst bed (yellow). Temperature — 400°C; 100 sccm He.

For some experiments it was required for the catalyst to be introduced to the reactor without contact with the atmosphere or alternatively removed from the reactor to the glovebox directly. To facilitate this, a bypass setup was fabricated using a 4-way valve that allowed for the facile transfer of the reactor under inert conditions.

3.3.1.2 Gas delivery system

The basic layout of the gas delivery system is presented in Figure 3.9. Pressurised N_2, H_2, O_2 and He were obtained from a centralised gas supply (Westfalen; > 99.995% purity). C_3H_8 (Westfalen; > 99.95%), CO_2 (Westfalen; > 99.995%), and proofgas (CH_4/H_2, Westfalen; > 99.995%), were obtained from bottles kept in a dedicated gas storage cabinet. All gases, with the exception of water-steam, which was obtained by vapour-liquid saturation, were moderated by the use of mass flow controllers (MFCs) from Bronkhorst. The MFCs were operated via a PC interface and calibrated by 10-point calibration using a bubble-film flow meter from Horiba.

All gas supply lines were 1/8” stainless steel and the gas mixing manifold was purged preferentially with inert N_2 to reduce dead volume. Water-steam was introduced to the pre-mixed gas feed by introducing the feed to a glass saturator filled with bidistilled water via a 4-way Valco valve. The volume of water-steam in the gas feed was controlled by a thermostat (Haake) to raise or lower the water temperature and therefore vapour pressure in the saturator. The exact temperature of the outlet vapour

is monitored by a thermocouple logging device from Picolog and in the range 20-70°C was found to deviate < ±0.1°C.

The reactor is operated in an online/bypass mode through a 4-way Valco valve and the gas connection to the SiO_2 tubing using Ultratorr fittings from Swagelok. After the reactor the outlet gas line is directed through the sampling loops connected to the GC.

To prevent water condensation in the gas stream, the reactor and bypass valves are contained within a heating oven (Heraeus) and the gas lines from the saturator outlet and outlet to the GC are heated.

3.3.1.3 Product analytics

The gas analytics are carried out by GC (Agilent 5890) using a method developed for the (oxy) dehydrogenation of propane. The outlet gas is flowed continuously through the sampling loops atop the GC and automatically sampled by a series of pneumatic valves that divert the educt gas through the columns. The gas analysis is carried out using both a flame ionisation detector (FID) and a thermal conductivity detector (TCD) in parallel. The FID is used to detect flammable gases (hydrocarbons, organic molecules) while the TCD detects permanent gases (CO_2, O_2, N_2, CO, H_2O).

3.3.2 Experimental procedure

The preparation of solid samples for catalytic testing was carried out with reference to Chapter 9 of the *Handbook of Heterogeneous Catalysis*.[114] Materials to be subjected to catalytic conditions were pressed and sieved to give fractions $250 < x < 355\mu m$ before reaction. These values are deemed to be within the limit with respect to the avoidance of tunneling or axial temperature/concentration gradients in the reactor w.r.t. the ID. An exception was made for materials that were transferred directly from the glovebox, which were tested as loose powders. All carbide materials used in this study were obtained via TPR-carburisation in a rotary furnace as described in Chapter 2. In some cases, the materials were passivated after synthesis and for other cases the materials were used directly with aid of air-free transfer devices and glovebox work. An overview of the catalyst materials is given in Table 3.2.

Catalytic reactions over the carbides were carried out in all cases by ramping to the operating temperature while flowing N_2 (20 sccm) over the catalyst. At operating

temperature a bypass valve was switched exposing the catalyst to reaction atmosphere at temperature while initiating a GC run sequence. In this manner, the initial conversion was recorded with respect to time on stream. In the case of the temperature programmed catalytic reaction over *h*-$Mo_{1-x}V_xO_3$ precursor oxides, the temperature was gradually ramped (0.5°C/min) under reaction conditions. The temperature in the catalyst bed was monitored by an external thermocouple via Picolog PC interface.

All space velocities are given as weight hourly space velocities calculated as:

$$WHSV\ (ml/gh) = \frac{flow\ (\frac{mln}{t(h)})}{mass\ cat.(g)}$$

The calculation of product yield, selectivities and carbon balance was carried out as follows: the total outflow of each component was determined by normalizing with the N_2 signal. Secondly, the flow of carbonaceous components was converted to total carbon flow. The conversion (χ) was calculated as:

$$\chi = \frac{\sum carbon\ flow\ of\ products\ (\mu molC/\text{min})}{\sum total\ carbon\ flow\ \ (\mu molC/\text{min})}$$

Carbon-based selectivity to educt molecules was given as:

$$S = \frac{selected\ product\ carbon\ (\mu molC/\text{min})}{\sum total\ product\ carbon\ (\mu molC/\text{min})}$$

Carbon balance was calculated with reference to the bypass measurement:

$$Carbon\ Balance = \frac{\sum total\ product\ carbon}{bypass\ total\ carbon}$$

All rates are normalised to the mass of catalyst and for convenience are calculated as μmol C $min^{-1}g^{-1}$.

In the case of steady-state experiments, apparent activation energies were determined by plotting the natural logarithm of the rate against the reciprocal temperature (K^{-1}). The apparent activation energy was then calculated according to the formula:

$$\ln k = \ln A - \frac{E_a}{RT}$$

Where the slope is given by:

$$slope = -\frac{E_a}{R}$$

($R = 8.314\ Jmol^{-1}K^{-1}$)

Note: In any case, when discussing 'initial conversion' the term is used to mean the conversion that is observed over a fresh catalytic bed.

Table 3.2: (Mo1-xVx)2C catalysts used in the catalytic studies

Catalyst	Internal ID	Phase (XRD)	V/(Mo+V)	Pretreatment	BET (m^2g^{-1})	XRD - size (nm)	C wt.%
Mo_2C	8524	Mo_2C	0	Passivated	63	6.7	7.1
Mo_2C	9450	Mo_2C	0	Passivated	10	8	5.2
$(MoV)_2C$	8754	Mo_2C	0.11	Passivated	54	6.5	5.3
Mo_2C	8425	Mo_2C	0	Glovebox	69	7.1	5.2
$(MoV)_2C$	8478	Mo_2C	0.03	Glovebox	110	6.4	5.2
$(MoV)_2C$	8447	Mo_2C	0.08	Glovebox	106	5.5	5.1
$(MoV)_2C$	8486	Mo_2C	0.11	Glovebox	97	-	5.3

3.3.3 Notes on catalyst characterisation

Standard characterisation of post-catalytic materials was carried out by the following techniques:

- Powder XRD to determine crystalline phase composition
- N_2 physisorption for surface area and pore size distribution
- CHN analysis and Raman spectroscopy to determine carbon content

The details of these techniques can be found in the experimental section of Chapter 2 with the exception of Raman spectroscopy which is discussed in Chapter 4. Further in-depth characterisation and postmortem analysis will be presented in Chapter 4, which deals with surface characterisation and reactivity.

3.4 Results

3.4.1 Dehydrogenation vs. oxydehydrogenation vs. steam dehydrogenation

Investigative reactions into dehydrogenation, oxydehydrogenation and steam-dehydrogenation over Mo_2C were carried out over bulk Mo_2C synthesised by TPRC method in the UTP II rotating furnace reactor described in Chapter 2 and detailed in Table 3.2. All reactions were carried out over 295mg of Mo_2C mixed 1:1 (wt.%) with SiC (sieve fraction 250-355μm) with a total flow of 40 sccm giving a WHSV of 8250 $mlg^{-1}h^{-1}$. The concentration of C_3H_8 was kept constant at 10%. In the case of dehydrogenation, the balance was N_2 (90%). For steam dehydrogenation 10% water-steam was added to the feed with N_2 balance (80%). For oxydehydrogenation, 3.5% oxygen was added to the feed with N_2 balance (86.5%). Reactions conditions and details are outlined Table 3.3 below.

For each set of conditions the reaction was repeated with 3 different pretreatments of the passivated catalyst :

- No pre-treatment (passivated carbide)
- Reduction @500°C for 2 hours (20 sccm H_2)
- Reduction @675°C for 2 hours (20 sccm H_2)

Initial rates of propene formation observed for all conditions were subject to strong deactivation over the first two hours (Figure 3.11). The corresponding conversion of propane dropped to $\chi < 0.5\%$ in the case of ODH and DH, however, it was observed to approach a steady state of $\chi = 2\%$ for the steam containing feed.

For the reaction of propane in inert atmosphere (Figure 3.11a), it was observed that the initial rate of propene formation decreased with pre-reduction temperature and deactivation was achieved more quickly. Post-analysis by XRD reveals that the β-Mo_2C phase is retained. Similar propene formation rates are observed in the case of ODH. The initial conversion is relatively high (ca. 25% for passivated Mo_2C) with low selectivity to C_3H_6 and high selectivity to CO_x. After 3 hours on stream further deactivation occurs and the conversion approaches zero.

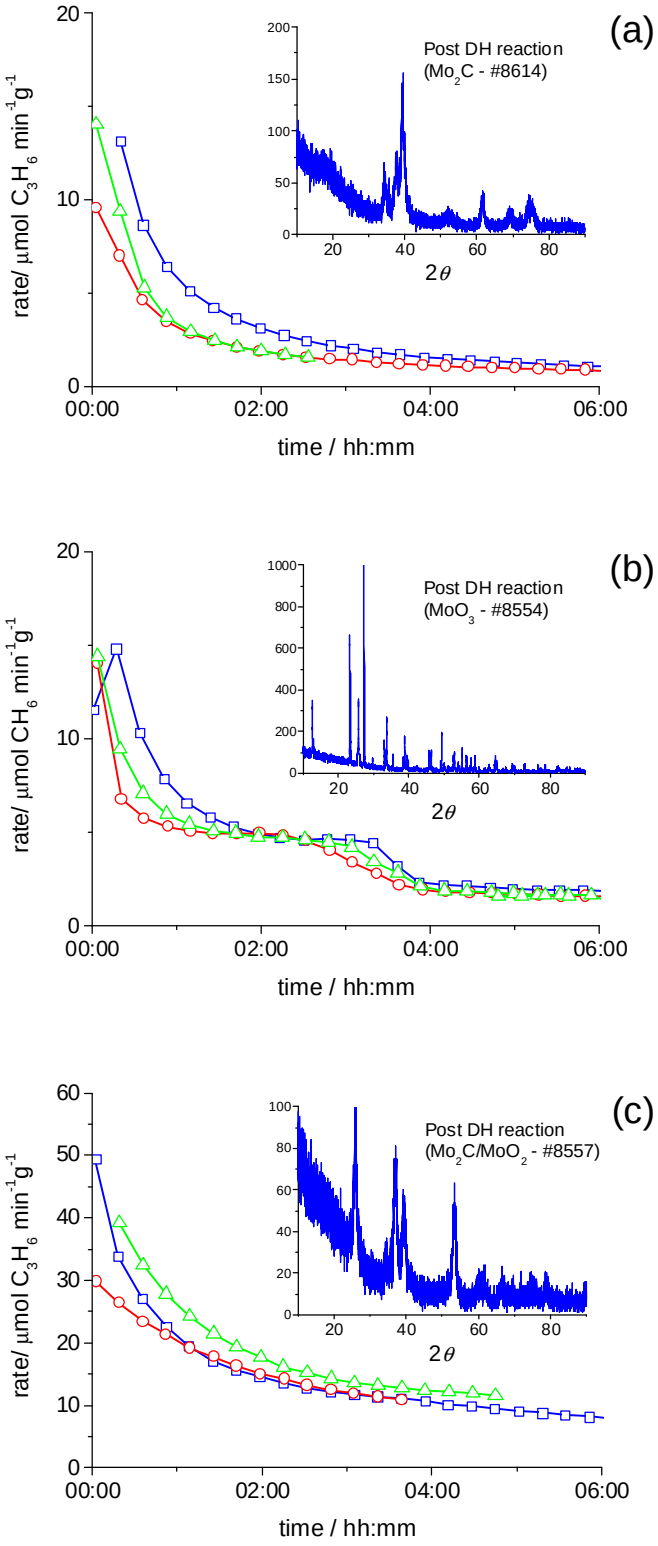

Figure 3.11: Propylene formation rates for: □ = no pre-reduction, Δ = 500°C pre-reduction, ○ = 675°C pre-reduction. Conditions, (a) inert conditions, (b) O_2 addition, (c) steam addion. Inset: post-mortem powder XRD of the catalyst (final patterns are the same for different pre-treatments).

Table 3.3: Comparison of Mo_2C (#8524) in: dehydrogenation, oxidatative dehydrogenation, and steam-dehydrogenation of propane with varying pre-treatment conditions.

Catalyst	Internal ID	Phase	Mo/ (Mo+V)	V/ (Mo+V)	Pre-treatment	Temperature	$C_3H_8/O_2/H_2O/N_2$	Post ID	XRD
Mo_2C	8524	Mo_2C	100	0	no	500°C	10/0/0/90	8614	Mo_2C
Mo_2C	8525	Mo_2C	100	0	500°C	500°C	10/0/0/90	8615	Mo_2C
Mo_2C	8526	Mo_2C	100	0	675°C	500°C	10/0/0/90	8616	Mo_2C
Mo_2C	8527	Mo_2C	100	0	no	500°C	10/3.5/0/86.5	8554	α-MoO_3
Mo_2C	8528	Mo_2C	100	0	500°C	500°C	10/3.5/0/86.5	8555	α-MoO_3
Mo_2C	8529	Mo_2C	100	0	675°C	500°C	10/3.5/0/86.5	8556	MoO_2 **
Mo_2C	8530	Mo_2C	100	0	no	500°C	10/0/10/80	8557	Mo_2C/ MoO_2
Mo_2C	8531	Mo_2C	100	0	500°C	500°C	10/0/10/80	8558	Mo_2C/ MoO_2
Mo_2C	8532	Mo_2C	100	0	675°C	500°C	10/0/10/80	8613	Mo_2C/ MoO_2

Analyses of post-reaction products reveal total oxidation of Mo_2C to α-MoO_3. It is also observed that increasing the temperature of reduction leads to faster deactivation. The steam-DH reactions show a much higher initial formation rate of propene *cf.* ODH and DH. The lowest is observed for Mo_2C pre-reduced at 675°C, however, all formation rates approach a similar value after 4 hours on stream. Conversion of propane approaches a steady state value of 2% after 5 hours on stream. XRD analyses of the catalysts after reaction show that the Mo_2C is partially transformed to MoO_2 with time on stream.

3.4.2 Propane activation in H_2

3.4.2.1 Comparison of passivated vs. freshly carburised materials

To determine the influence of surface oxygen passivation on the initial reactivity, two catalysts were compared under the same conditions. Passivated Mo_2C (#9450) and freshly prepared Mo_2C (#8425) were tested at WHSV = 5000 $mlg^{-1}h^{-1}$ under the reaction conditions: C_3H_8 = 25%, H_2 = 55%, N_2 = 20% at T = 500°C for 24 hours.

The reaction of propane over molybdenum carbide in the absence of oxygen gives primarily a mixture of C1-C3 products with C_3H_6 resulting as the principal product over time. In Figure 4.11 the initial conversion and selectivities for passivated (#9450) and unpassivated (#8425) Mo_2C at T = 500°C are shown. For the most part, the C_3H_8 conversion, formation rates and selectivities are very similar. Initial conversion in both cases is relatively high (> 40%), dropping exponentially over time to ca. 2.5% for both reactions after 4 hours on stream. The rate of C_3H_6 formation sharply increases in the first minutes on stream, but otherwise remains constant at 12-14 $\mu molg^{-1}min^{-1}$. The change in conversion is due the initially high selectivity to hydrogenolysis decreasing with time on stream. A ratio for $S(C_2H_4)/S(CH_4) \approx 0.5$ is observed with time on stream, but in the case of the passivated carbide, it is initially seen $S(C_2H_6) > S(CH_4)$. In this case, the selectivity to CH_4 initially increases. Another difference observed for the passivated Mo_2C *cf.* unpassivated is the initial formation of CO observed for the passivated material, which disappears after ca. 1 hour on stream. It can be observed that the pattern of selectivity to CO in this time is mirrored by $S(CH_4)$.

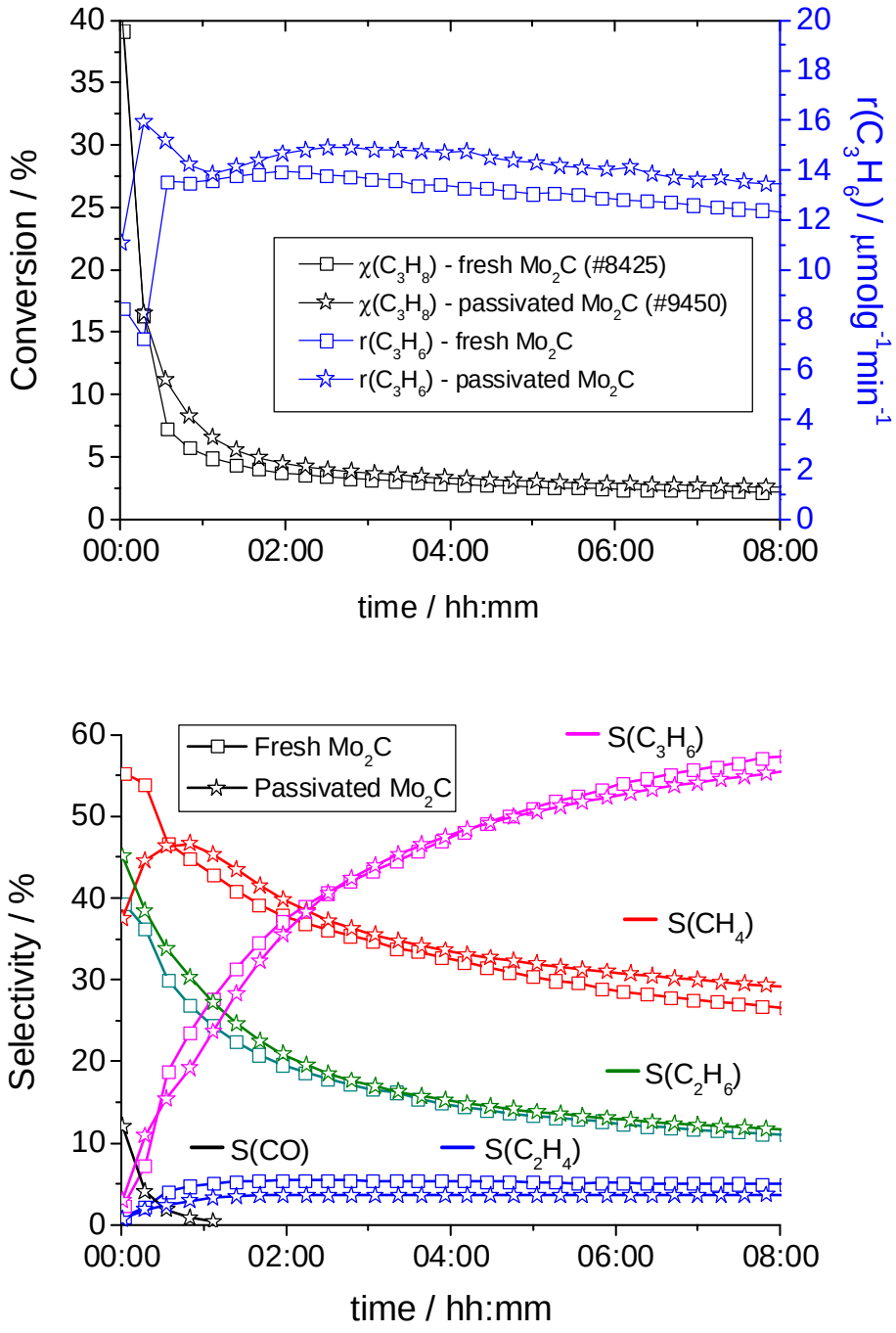

Figure 3.12: Activation of propane carried out at 500°C with WHSV = 5000 ml $g^{-1}h^{-1}$ over fresh Mo_2C (#8425, transferred from glovebox) and passivated Mo_2C (#9450).

Table 3.4: Propane dehydrogenation ($H_2/C_3H_8/N_2$) over different $(Mo_{1-x}V_x)_2C$ catalysts — influence of vanadium content and temperature

Catalyst	Internal ID	Phase	$C_{initial}$ (%)	V/ (Mo+V)	Pretreatment	T / °C	WHSV ($mlg^{-1}h^{-1}$)	$C_3H_8/H_2/N_2$	Post ID	XRD	C_{after} (%)
Mo_2C	8425	Mo_2C	5.2	0	Glovebox	500°C	5000	25/55/20	10935	Mo_2C	8.8
Mo_2C	8425	Mo_2C	5.2	0	Glovebox	550°C	5000	25/55/20	11004	Mo_2C	9.3
$(MoV)_2C$	8478	Mo_2C	5.2	3	Glovebox	500°C	5000	25/55/20	9751	Mo_2C	8.4
$(MoV)_2C$	8478	Mo_2C	5.2	3	Glovebox	550°C	5000	25/55/20	11006	Mo_2C	10.6
$(MoV)_2C$	8447	Mo_2C	5.1	8	Glovebox	500°C	5000	25/55/20	10980	Mo_2C	7.4
$(MoV)_2C$	8447	Mo_2C	5.1	8	Glovebox	550°C	5000	25/55/20	10996	Mo_2C	9.7
$(MoV)_2C$	8486	Mo_2C	5.3	11	Glovebox	500°C	5000	25/55/20	9752	Mo_2C	5.9
$(MoV)_2C$	8486	Mo_2C	5.3	11	Glovebox	550°C	5000	25/55/20	11034	Mo_2C	9.0

3.4.2.2 Influence of V content and temperature

The reactivity of a series of four Mo-V carbide catalysts was studied for the activation of propane in a hydrogen-rich environment. To prevent contamination of surface oxygen the materials were transferred under argon from the glovebox to the reactor. The carbides were synthesised by temperature-programmed reduction-carburisation as detailed in Chapter 3 and are detailed in Table 3.4. All reactions were carried out over 225mg of $(Mo_{1-x}V_x)_2C$ with a total flow of 19 sccm giving a WHSV of ca. 5000 $mlg^{-1}h^{-1}$. The concentration of C_3H_8 was 25%, with H_2 = 55% and the balance was N_2 (20%). For each catalyst, the initial conversion was measured at T = 500°C, 550°C. Additionally, after observing initial conversions at the highest temperature, a steady state conversion was approached and the temperature was varied between 400°C and 600°C to determine the apparent activation energies of each reaction component.

The effect of vanadium substitution on the catalytic conversion of propane in H_2/N_2 atmosphere at 550°C is illustrated in Figure 3.13. In Figure 3.13(a), the initial $\chi(C_3H_8)$ is shown to rise with increasing vanadium content. The rate of C_3H_6 formation is initially higher for #8486 and #8447 (the two highest V loadings), but over time the formation rates converge to ≈ 7 $\mu molg^{-1}min^{-1}$. For sake of clarity, only $S(CH_4)$ and $S(C_3H_6)$are shown in Figure 3.13(b). The samples with higher vanadium loadings show higher $S(CH_4)$ *cf*. Mo_2C. It is also shown that the increase in $S(CH_4)$ is at the expense of $S(C_3H_6)$.

Counter intuitively, increasing the temperature has the effect of decreasing the conversion. In Figure 3.14, the initial exponential decrease in conversion is observed for all conditions, but for T = 500°C; $\chi^{t=0}(C_3H_8) > 20\%$ for both $(Mo/V)_2C$ and Mo_2C, whereas at T = 550°C; $\chi^{t=0}(C_3H_8) \approx 10\text{-}15\%$. Due to experimental constraints, it is not possible to measure the instantaneous conversion at precisely t = 0, and the nature of the deactivation must be inferred from the data points available. Inset in Figure 3.14(a) shows the rate of C_3H_6 formation over time is higher at lower temperature and does not exhibit the same 'deactivation' that is observed at 550°C.

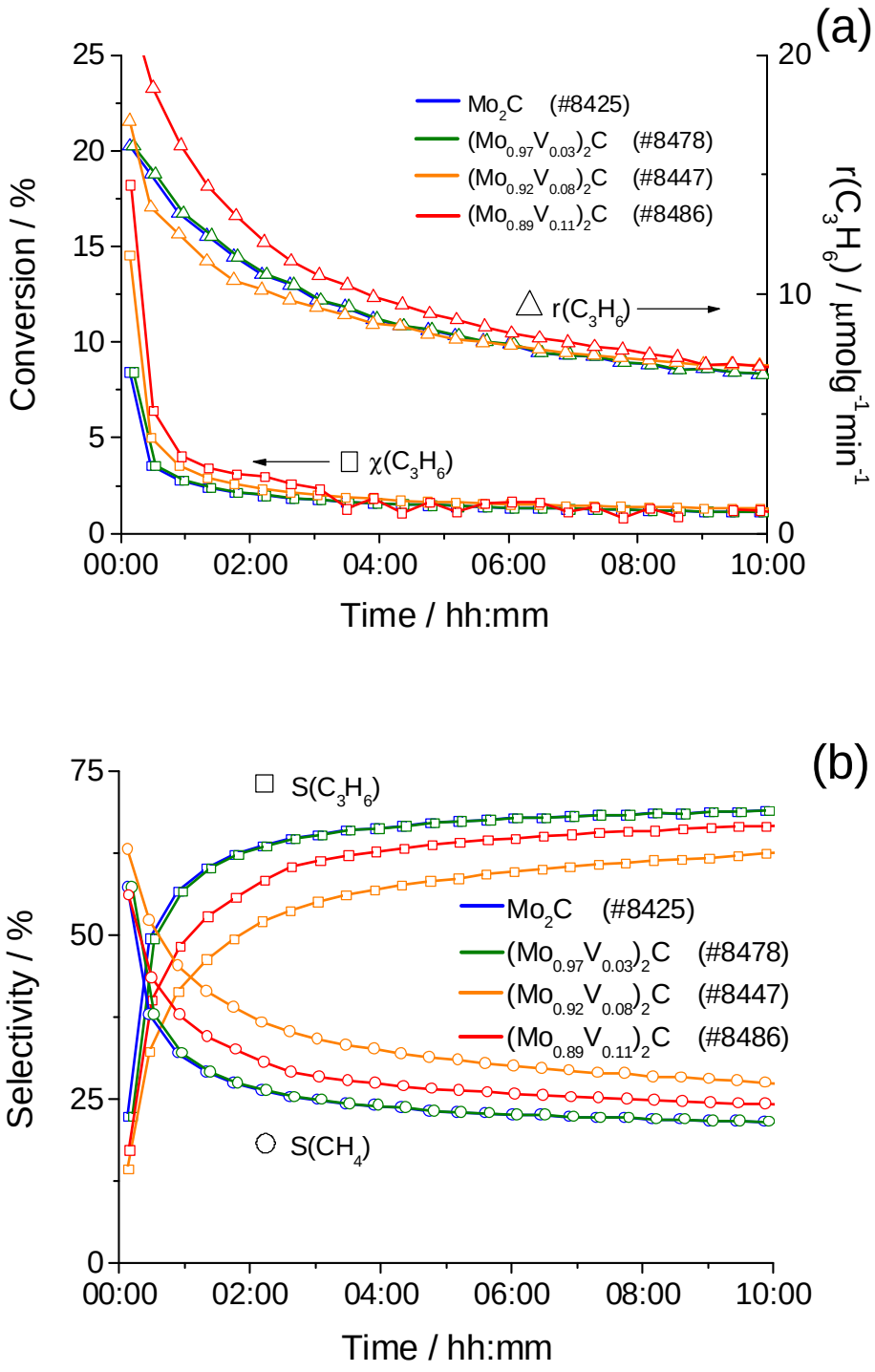

Figure 3.13: (a) Effect of increasing vanadium content on the conversion and rate of propene formation; T = 550°C under $H_2/C_3H_8/N_2$ at 5000 ml g^{-1} h^{-1}. (b): Comparison of $S(C_3H_6)$ vs. $S(CH_4)$; conditions as above.

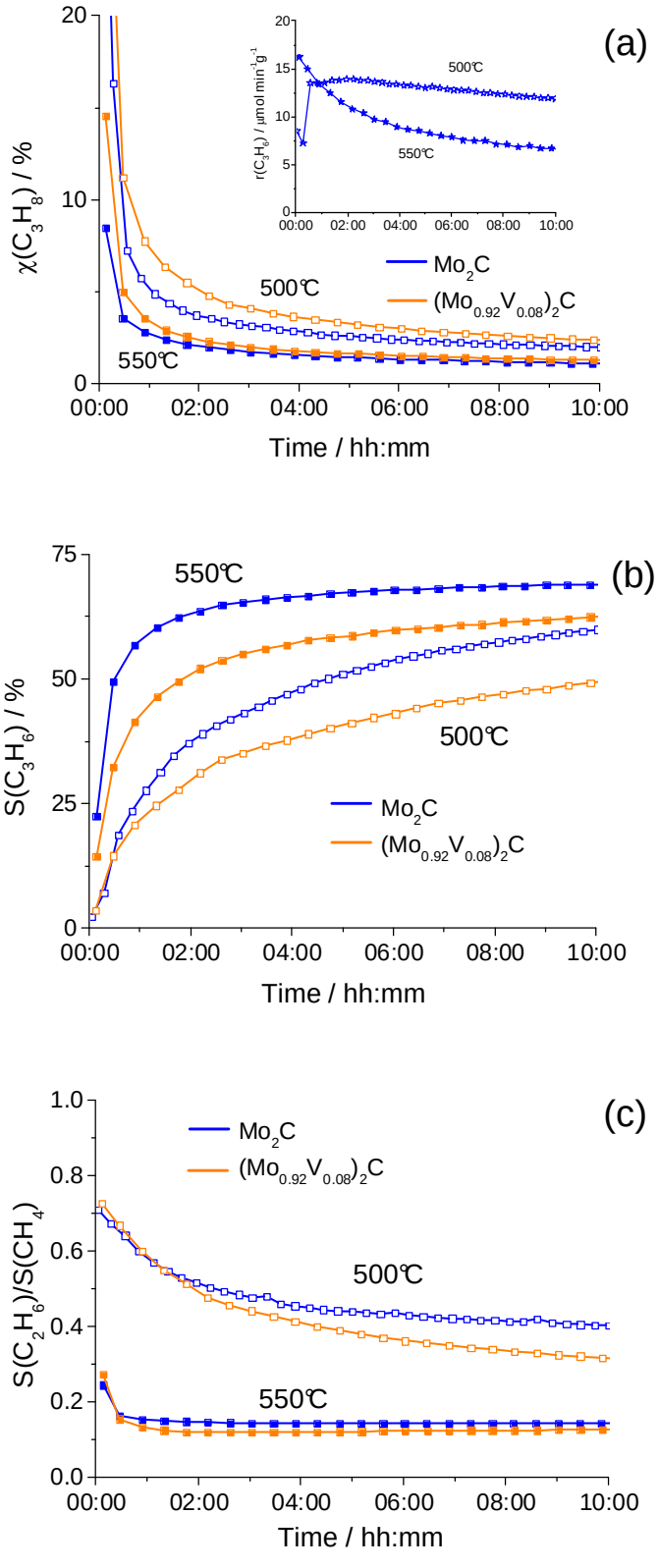

Figure 3.14: (a) Total conversion of propane vs. time at T = 500 & 550°C over fresh Mo_2C (#8425) and $(Mo_{0.92}V_{0.08})_2C$ (#8447). Inset: Propene formation rate at T = 500 & 550°C for #8425. (b) $S(C_3H_6)$ for #8425 & #8447 at T = 500, 550°C. (c): ratio of $S(C_2H_6)/S(CH_4)$ at varying conditions.

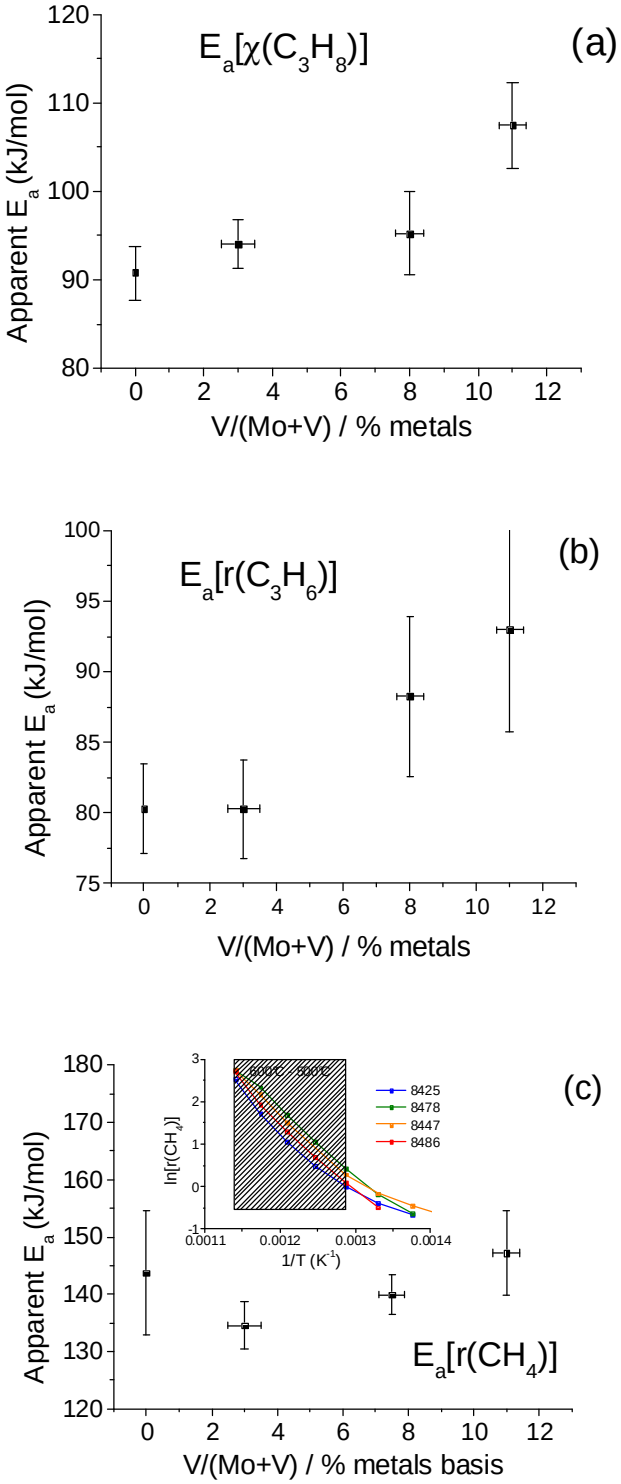

Figure 3.15: Apparent activation energies over 400 - 600°C derived from Arrhenius plots for: (a) apparent rate of propane consumption; (b) propene formation; (c) methane formation (500–600°C) — inset: non-linear behaviour observed for E_a[2].

With increasing temperature it is also observed that the ratio of the hydrogenolysis products changes (Figure 3.14(c)). At 500°C $S(C_2H_4)/S(CH_4) \approx 0.4\text{-}0.5$ which decreases to ≈ 0.15 at 550°C.

Comparison of the steady-state catalyst behaviour in Figure 3.15 shows some slight trends. The apparent activation energies for the conversion of propane increase with vanadium concentration from ca. 90 → 110 $kJmol^{-1}$. This is reflected in the increasing apparent activation energy observed for propene formation (80 → 90 $kJmol^{-1}$). The apparent activation energy for CH_4 formation is relatively high (135-145 $kJmol^{-1}$) but does not appear to be correlated with the vanadium content of the catalyst. The apparent $E_a(CH_4)$ is derived from the Arrhenius plots in the range 500-600°C. Below 500°C the plots deviate from linearity.

3.4.2.1 Variation of space velocity

In order to determine the dependence of the reaction products on space velocity, comparative measurements were taken at steady-state conversion over Mo_2C (450mg, #9450, Table 3.3) at 500°C. The sample was recarburised *in situ* by ramping to 675°C @5°C/min and holding for 1 hour before cooling to reaction temperature under N_2. Initial conversion was measured at a WHSV = 5000 $mlg^{-1}h^{-1}$ until it was determined that the conversion was at steady-state. Catalytic measurements were recorded at 1250, 2500, and 5000 $mlg^{-1}h^{-1}$.

By varying the space velocity over the Mo_2C catalyst at steady-state conditions (Figure 3.19) it can be observed which reactions are interdependent. Increasing the space velocity from 1250 to 5000 leads to a doubling of the rate of hydrogenolysis (CH_4 and C_2H_6), but only a marginal increase in the rate of dehydrogenation. This implies that the production of C_3H_6 has an element of dependency upon the hydrogenolysis reaction and is preferentially consumed with respect to C_3H_8.

The selectivity-conversion plot (Figure 3.16(b)) also provides important information about the reaction mechanism. The extrapolated trend lines shown for the products intersect the y-axis at conversion = 0 at various positions which sum to ca. 100%, implying that these 4 products are representative of the total. It's important to note that the extrapolated trendline for $S(C_2H_6)$ intersects the y-axis at close to the origin.

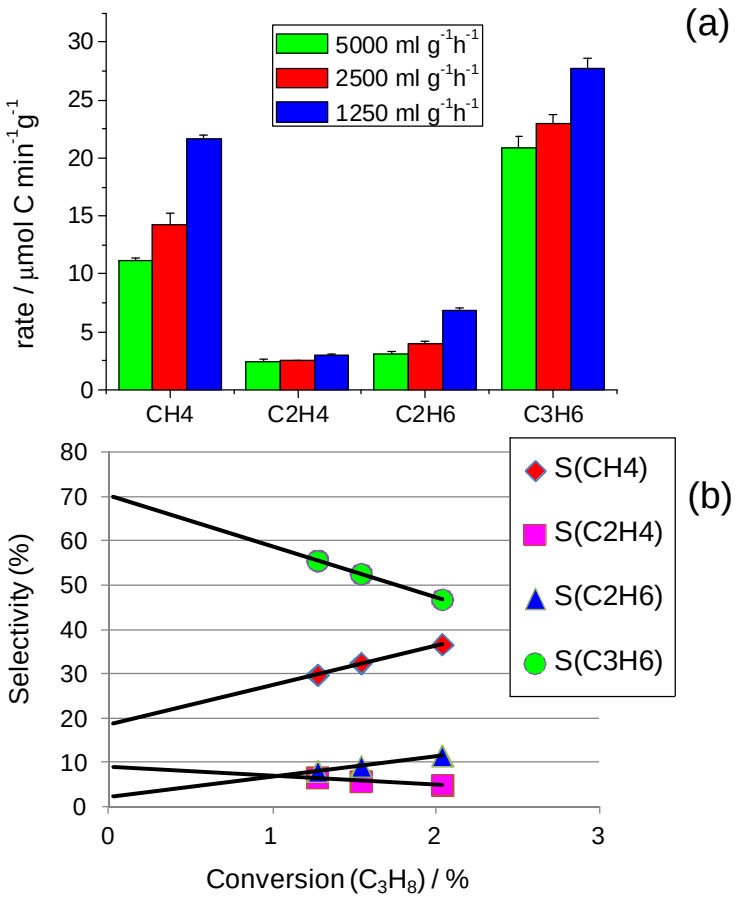

Figure 3.16: (a) Bar plot of formation rates for observed products in steady state $H_2/C_3H_8/N_2$ over Mo_2C (#9450). (b) Selectivity-conversion plot for observed products.

This is indicative of a secondary product for the reaction of propane on Mo_2C. If we consider the basic reaction network:

$C_3H_8 \rightarrow C_3H_6 + H_2$ — propane dehydrogenation (primary)

$C_3H_8 \rightarrow C_2H_4 + CH_4$ — partial hydrogenolysis (primary)

$C_2H_4 + H_2 \rightarrow C_2H_6$ — ethylene hydrogenation (secondary)

then this would appear to be consistent with the observed data. Unfortunately, the conversion was only observed over a small range and further, in-depth analysis is not possible with this data.

3.4.1 Propane activation in H_2/H_20

The influence of steam as an oxidant co-feed on the reactivity was determined by first carrying out series of preliminary experiments which led to a range of stable conditions for the Mo_2C phase.

Table 3.5: Details of carbide samples treated in $C_3H_8/H_2/H_2O$

Catalyst	Internal ID	Phase	$C_{initial}$ (%)	V/(Mo+V)	T / °C	WHSV ($mlg^{-1}h^{-1}$)	$C_3H_8/H_2/H_2O$	Post ID	XRD	C_{after} (%)	BET (m^2/g)
Mo_2C	9450	Mo_2C	5.3	0	500°C	5000	25/55/20	9663	Mo_2C	6.3	25
Mo_2C	9450	Mo_2C	5.3	0	550°C	5000	25/55/20	9476	Mo_2C	7.6	30
Mo_2C	9450	Mo_2C	5.3	0	600°C	5000	25/55/20	9515	Mo_2C	7.9	38
$(MoV)_2C$	8754	Mo_2C	5.1	0.10	500°C	5000	25/55/20	9420	Mo_2C/MoO_2	2.6	34
$(MoV)_2C$	8754	Mo_2C	5.1	0.10	550°C	5000	25/55/20	9327	Mo_2C/MoO_2	6.5	44
$(MoV)_2C$	8754	Mo_2C	5.1	0.10	600°C	5000	25/55/20	9368	Mo_2C/MoO_2	5.5	39
$(MoV)_2C$	8754	Mo_2C	5.1	0.10	650°C	5000	25/55/20	9388	Mo_2C/MoO_2	7.1	40

Table 3.6: Apparent activation energies calculated for steam-dehydrogenation of propane over Mo_2C.

Product	Apparent E_a (< 510°C) kJ/mol	Apparent E_a (> 510°C) kJ/mol
C3H8 (χ)	137	70
C3H6	120	54
C2H6	241	-
C2H4	195	-
CH4	185	-
CO	272	66
CO2	216	-

The conditions applied in the study were; C_3H_8 = 25%, H_2 = 55% and H_2O = 20% over a catalyst mass of 450mg (total flow 38 sccm) to give a WHSV = 5000 $mlg^{-1}h^{-1}$. Initial conversions were observed at 500, 550 and 600°C under the previously mentioned conditions for Mo_2C (#9450) and for $(Mo_{0.9}V_{0.1})_2C$ (#8754). The influence of reductive pre-treatment was also determined for both catalysts.

For the case of Mo_2C, the apparent activation energies of formation of the respective products were determined at steady-state conversion after reaction at 600°C for 24 hours.

The catalytic conversion of propane in steam conditions is a considerably more complex network of reactions. Beyond dehydrogenation and hydrogenolysis products, steam-reforming products and water-gas shift are observed to play a role. In Figure 3.17(a), the conversion and rate of propene formation are contrasted at 500, 550 and 600°C. As observed in the previous 'dry' study, the conversion of propane decreases more sharply with increasing temperature. At 500°C the conversion is steady at ca. 8% and the rate of propene formation is constant (ca. 25 $\mu molg^{-1}min^{-1}$). The initial conversion does not change significantly with increasing temperature, but exhibits an initial increase to a peak yield (t = 6h for 550°C, t = 3h for 600°C) before declining over time.

Analysis of the product selectivities (for T = 550°C – Figure 4.16b) shows a high initial selectivity to CO, a product of steam reforming, as well as dehydrogenation and hydrogenolysis products. This is followed at t = 5h by a peak in selectivity to CO_2 which precedes the peak production of C_3H_6. Over time the selectivity to C_3H_6 approaches 90%.

An Arrhenius plot for the formation rates of observed products in the steam-H_2 activation of propane shows a strong dependency on temperature (see

Figure 3.18). Below 510°C the behaviour is observed to be linear, but above 510°C the apparent E_a of all the products decreases indicating a change in the underlying material. This is reflected in the reactivity, which is observed to be steady state at T = 500°C but changes dramatically at higher temperatures. The apparent activation energies observed for the products are reported in Table 3.6.

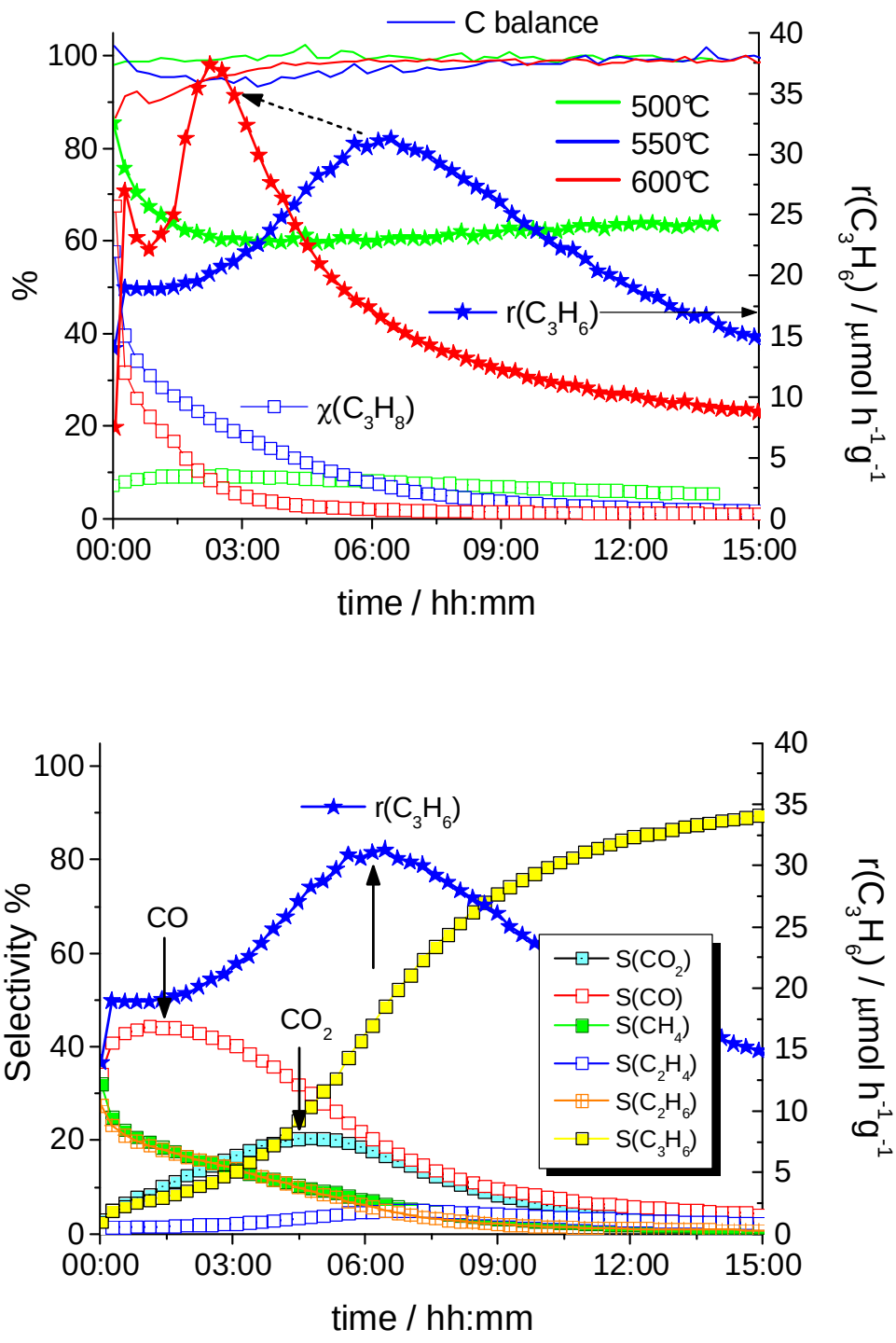

Figure 3.17: (a) Conversion and C_3H_6 rate plots over time for steam/H_2 propane activation over Mo_2C (#9450) at 500, 550 & 600°C. (b) Selectivity evolution with time on stream at 550°C.

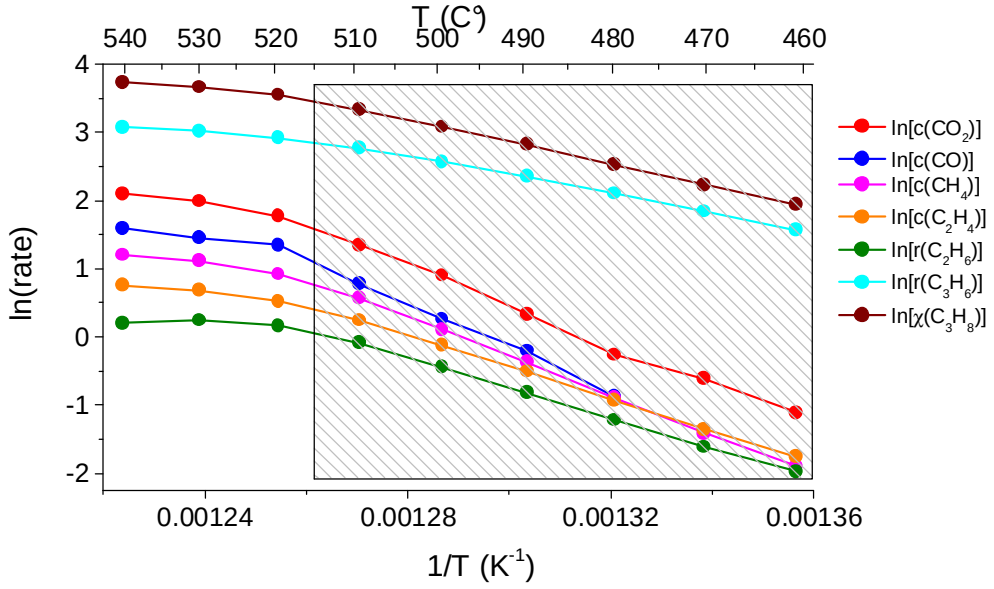

Figure 3.18: Arrhenius plot of ln(product formation rates) vs. 1/T for steam/H_2 activation of propane over Mo_2C (#9450) at steady-state for 460°C < T < 540°C. Region of linearity is shaded.

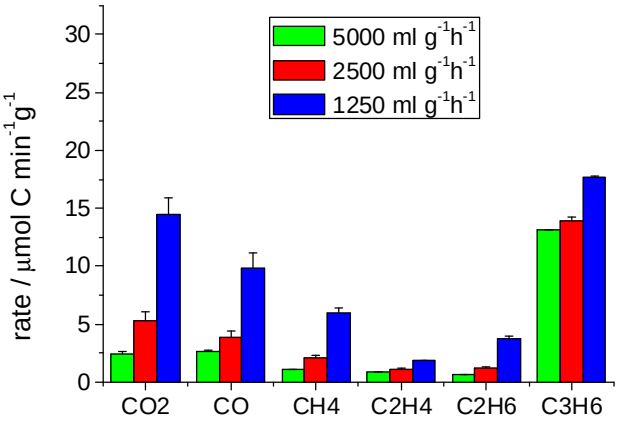

Figure 3.19: Variation of space velocity in steam/H_2 propane activation over Mo_2C (#9450) — product formation rates.

As is seen in the case of the H_2/C_3H_8 conditions, decreasing the space velocity from 5000 → 1250 affords only a slight increase in propene formation rate while the rates of CO_2, CO and CH_4 formation increase by more than double (Figure 3.19). This implies that the propene is preferentially consumed to form one or more of these products.

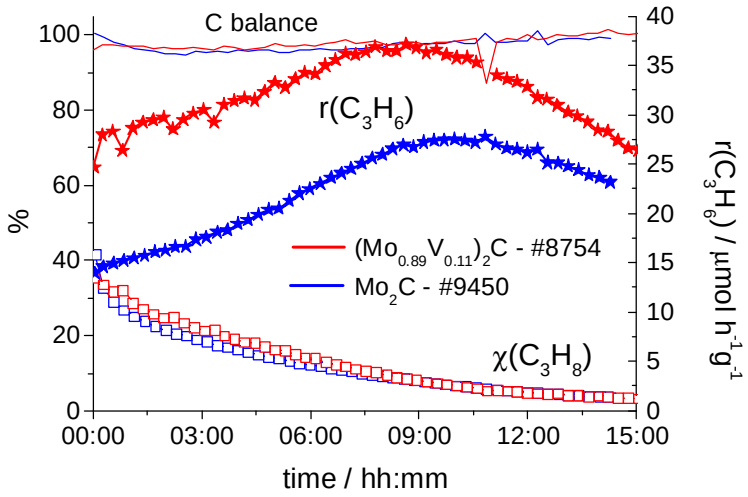

Figure 3.20: Conversion and rate of C_3H_6 formation for steam/H_2 propane activation over Mo_2C (#9450) and $(Mo_{0.89}V_{0.11})_2C$ at T = 550°C.

The influence of vanadium content differs to that observed for H_2/C_3H_8. The conversion of propane is not observed to change dramatically but the rate of propene formation is increased with respect to Mo_2C (Figure 3.20). However, the mixed Mo/V carbide is unstable to oxidation by steam under these conditions, and at a range of temperatures it can be seen in XRD powder diffraction that the catalyst is partially oxidised to MoO_2 (Figure 3.21).

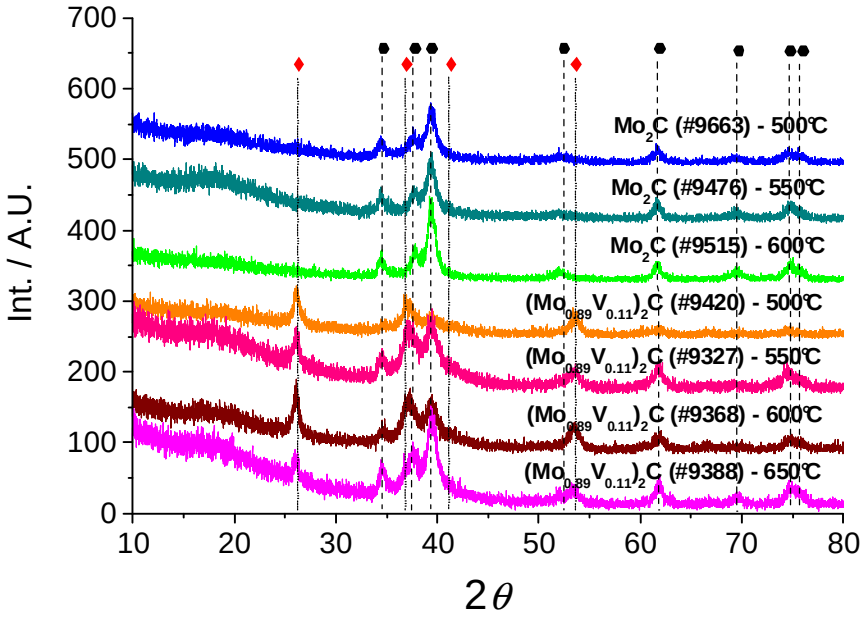

Figure 3.21: Post-catalytic X-ray powder diffraction patterns for steam/H_2 activation of propane at different temperatures over Mo_2C (#9450) and $(Mo_{0.89}V_{0.11})_2C$ (#8754). Phase composition: ♦ — Mo_2C (*hcp*), ● — MoO_2 (monoclinic).

It can be seen that at T = 500°C the post reaction product is largely MoO_2, however with increasing temperature, the stability of the carbide phase (Mo_2C) increases and at 650°C there is only a trace of MoO_2 visible. Mo_2C was stable under all tested conditions.

3.4.2 CO_2 as an alternative oxidant source

To contrast the effects of CO_2 and oxygen on the catalytic conversion of propane, CO_2 was added to the reaction mixture. The conditions applied in the study were; C_3H_8 = 25%, H_2 = 55% and CO_2 = 20% over a catalyst mass of 450mg (total flow 38 sccm) to give a WHSV = 5000 $mlg^{-1}h^{-1}$.

Initial conversions were observed at 500°C and 550°C under the above conditions for Mo_2C (#9450) and a pattern of behaviour similar to that observed for steam/H_2-DH was apparent.

As can be seen in Figure 3.22, the 'activation' is characterised by an initial bump in the rate of propylene formation as was seen for steam containing feeds (*cf.* Figure 3.17). For the same temperature (550°C), the rise in selectivity is more immediate in the case of CO_2. This implies that CO_2 is a stronger oxidant than H_2O.

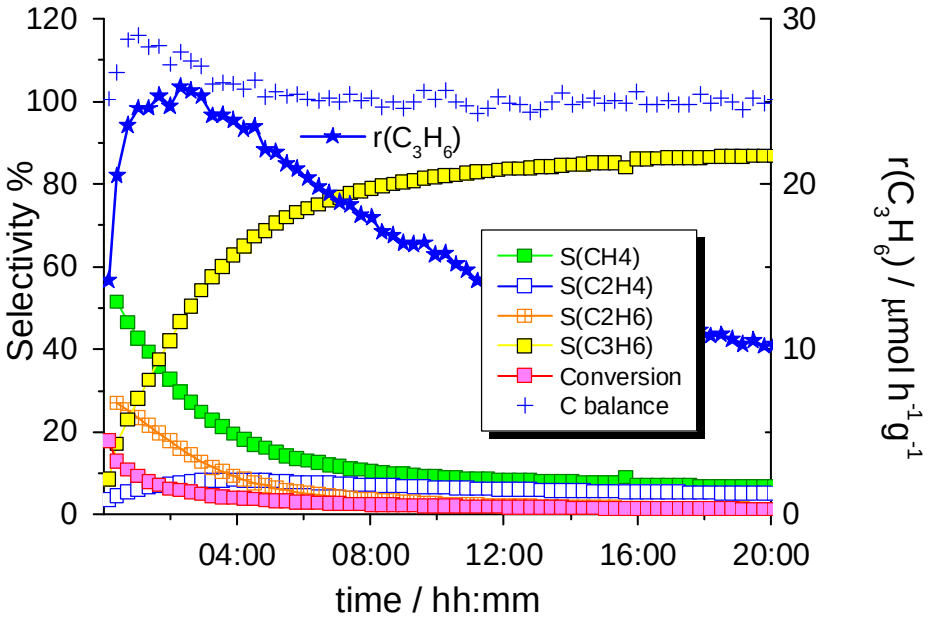

Figure 3.22: Initial selectivity, conversion and propylene formation rate of $CO_2/C_3H_8/H_2$ over Mo_2C (#9450) at 550°C. CO_x is excluded due to conflicting carbon-sources.

At steady-state conversion after reaction at 600°C for 24 hours, it was additionally attempted to determine the apparent activation energies of product formation. However, this proved to be unreliable due to the complication in extracting the data with a strong background of RWGS observed for the reaction. Further experiments to determine whether CO_2 hydrogenation reaction had an influence on the CO_2/H_2-DHP are detailed in the next section.

3.4.3 Reverse water-gas shift over Mo_2C

In the $C_3H_8/CO_2/H_2$ reactions, significant RWGS was observed. To investigate this reactivity, the reaction was carried out over freshly carburised Mo_2C (#9450). The conditions applied in this study were; N_2 = 25%, H_2 = 55% and CO_2 = 20% over a catalyst mass of 450mg (total flow 38 sccm) to give a WHSV = 5000 $mlg^{-1}h^{-1}$. No induction period was observed for the reaction and no significant deactivation was noted.

In Figure 3.23, the conversion of CO_2 is close to the RWGS equilibrium conversion as calculated for the reaction conditions. The ratio of selectivity for CO:CH_4 at 500°C is ca. 93:7.

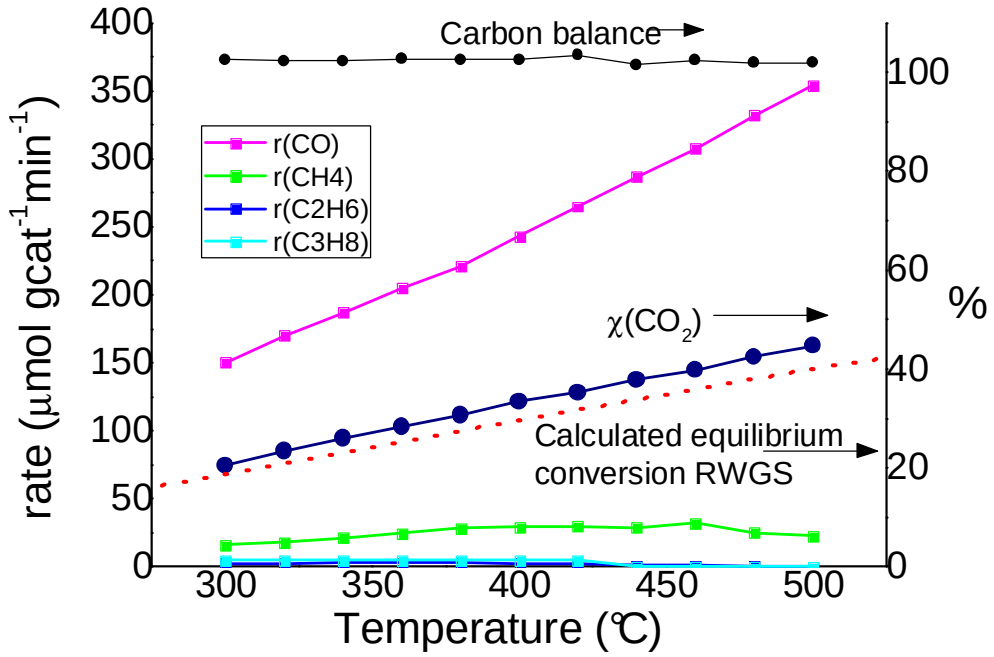

Figure 3.23: RWGS at WHSV = 5000 ml/gh over Mo_2C (#9450) after carburisation *in situ*.

As it was observed that there was very little information on RWGS over carbides some further preliminary experiments were made. By decreasing the catalyst mass to 20mg (#8425 – transferred from glovebox) with the same flow rate, a WHSV of 114000 (GHSV ≈ 220000) was achieved. Even at this high space velocity the reaction was observed to go to equilibrium conversion. At the increased GHSV the selectivity of CO:CH_4 was observed to be ≈ 99:1 and the carbon balance was ca. 95%.

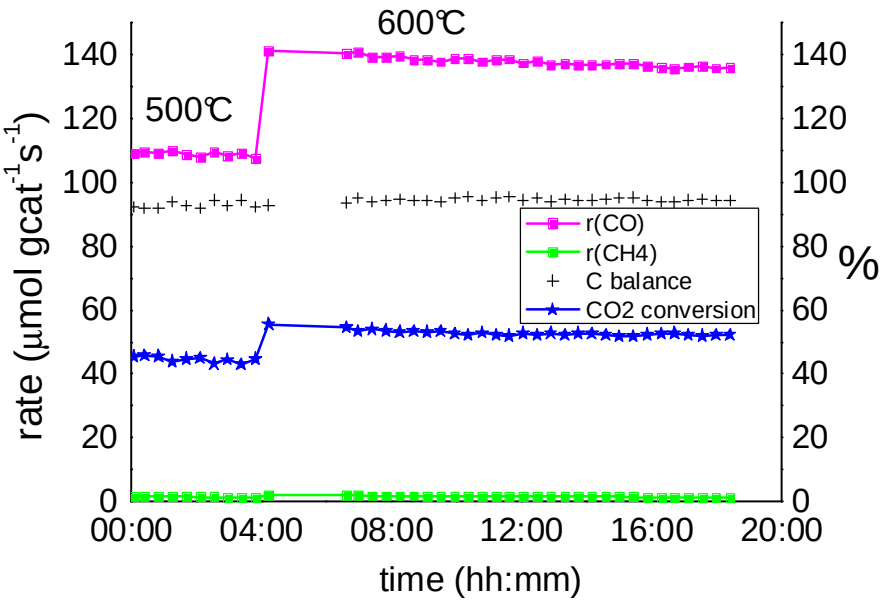

Figure 3.24: RWGS over Mo_2C (#8425) at GHSV = 220000

No significant deactivation was observed over 24 hours and the XRD and CHN post-mortem analysis indicated that there was no bulk phase change or deposition of carbon.

3.4.4 Temperature-programmed reduction-carburisation reaction – H_2/C_3H_8 over h-$Mo_{1-x}V_xO_3$

In the previous experiments, Mo_2C and $(Mo_{1-x}V_x)_2C$ are presented as a model system for the activation of propane on a strongly reduced catalyst. As a complementary study to link carbide formation and propane reactivity, temperature-programmed reduction was carried out under previous H_2/C_3H_8 conditions for each of the oxide precursors. The oxides were synthesised by co-precipitation as detailed in Chapter 2 and the reaction details are given in Table 3.7.

Table 3.7: Table of precursor oxides for TPR under $H_2/C_3H_8/N_2$

Precursor	Internal ID	Mo/ (Mo+V)	V/ (Mo+V)	pre BET (m^2/g)	WHSV ($mlg^{-1}h^{-1}$)	$C_3H_8/H_2/N_2$	Post ID	XRD	post-BET (m^2/g)
h-MoO_3	8650	100	0	<1	5000	25/55/20	11196	α-MoC_{1-x}	74
h-$Mo(V)O_3$	6702	97	3	<1	5000	25/55/20	11197	α-MoC_{1-x}	77
h-$Mo(V)O_3$	7911	92	8	<1	5000	25/55/20	11199	α-MoC_{1-x}	98
h-$Mo(V)O_3$	6601	89	11	1.6	5000	25/55/20	11211	α-MoC_{1-x}	112

All reactions were carried out over 225mg of $(Mo_{1-x}V_x)_2C$ with a total flow of 19 sccm giving a WHSV of ca. 5000 $mlg^{-1}h^{-1}$. The concentration of C_3H_8 was 25%, with H_2 = 55% and the balance N_2 (20%). The oxides were ramped at 5°C/min to 300°C and at 0.5°C/min from 300°C to 600°C, held for 2 hours and then cooled at 5°C/min to 500°C and held for 2 hours before cooling to RT. During the temperature program, GC samples were taken every 20 minutes to give a temperature resolution of ca. 10°C. After reaction the samples were removed to the glovebox for handling and post-analysis by BET, XRD, TEM and Raman spectroscopy (see Chapter 4).

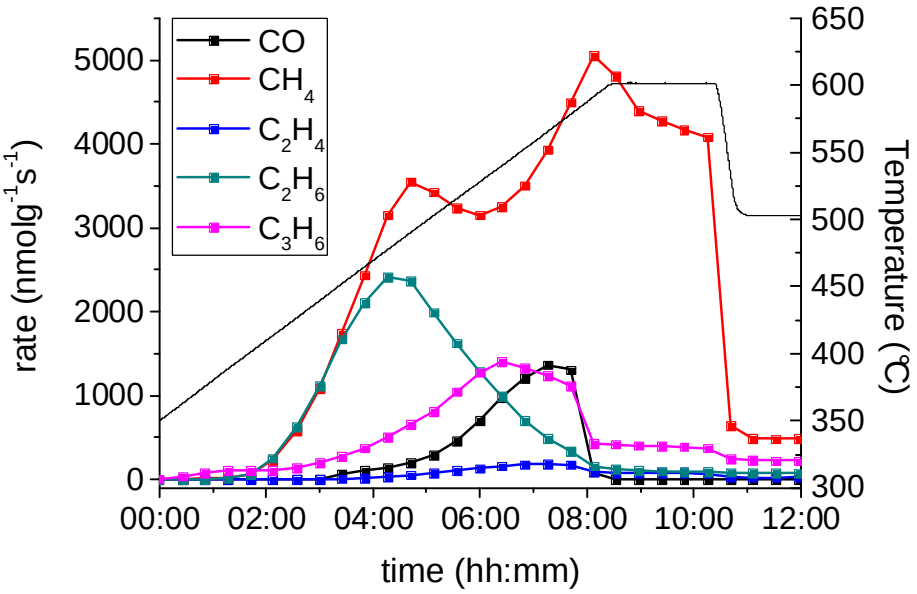

Figure 3.25: Product formation rates for temperature-programmed reaction of H_2/C_3H_8 over *h*-MoO_3.

As shown in Figure 3.25, the reaction product distribution of propane over *h*-MoO_3 changes considerably with the extent of reduction. For the case of undoped *h*-MoO_3

(#8650) the product evolution can be divided into three phases. The first is a sharp increase in the formation of methane and ethane above 400°C. This is followed by an increase in the C2 and C3 olefin products which coincides with the generation of CO via RWGS between 450-550°C. The final phase is the decrease in all rates except for that of methane. In the gas chromatograph the initial traces show that C1 and C2 species as well as C4 species are present in the outlet gas. In Figure 3.26 the gas chromatographs are shown for the temperature range 400-560°C. It can be seen that the formation of n- and iso-butane mirrors the formation of ethylene, while the unsaturated butenes are observed at higher temperatures.

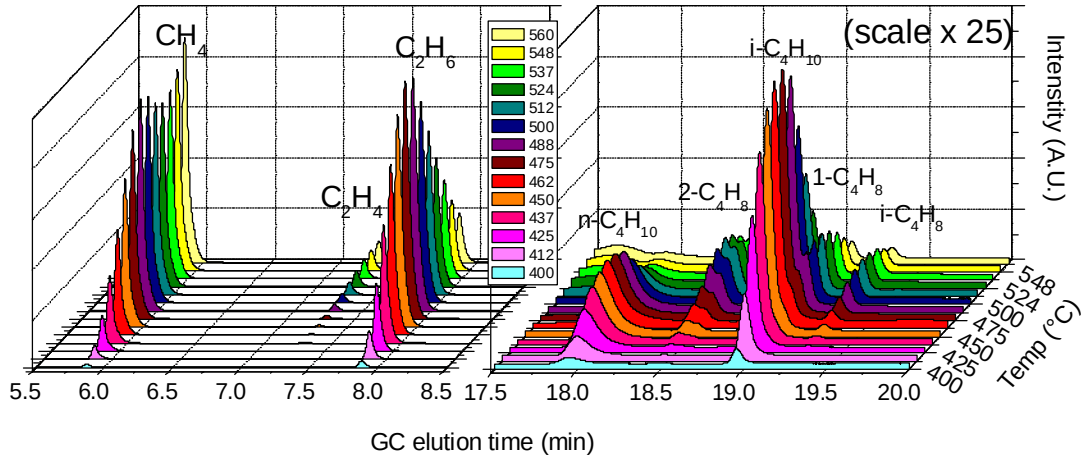

Figure 3.26: Gas chromatographs of C1, C2 and C4 products at increasing temperatures.

The variations observed for the *h*-Mo(V)O_3 oxide series can be seen in Figure 3.27. From the overall conversion of C_3H_8 there are some similarities with the observed TPRC profiles in Chapter 2. The oxides with lower vanadium content are reduced at lower temperatures resulting in a faster onset of activity. Overall, it is observed that the rate of methane formation for the undoped and 3% V doped oxides is significantly higher than for that of the V-rich samples, especially at higher reduction temperatures.

With respect to the onset of CO formation via RWGS, the V-poor samples show a small onset at ca. 450°C, but all the samples start properly at ca. 480°C indicating the integration of C into the MoO_x lattice. This temperature is much lower than is observed for CH_4 for reasons discussed in Chapter 1. It can be seen that the formation of dehydrogenation products directly precedes the carburisation process and is observed to peak just before the CO maximum. The formation rate of propylene is

remarkably similar for all the catalysts and does not appear to be correlated with the catalyst surface area before or after reduction.

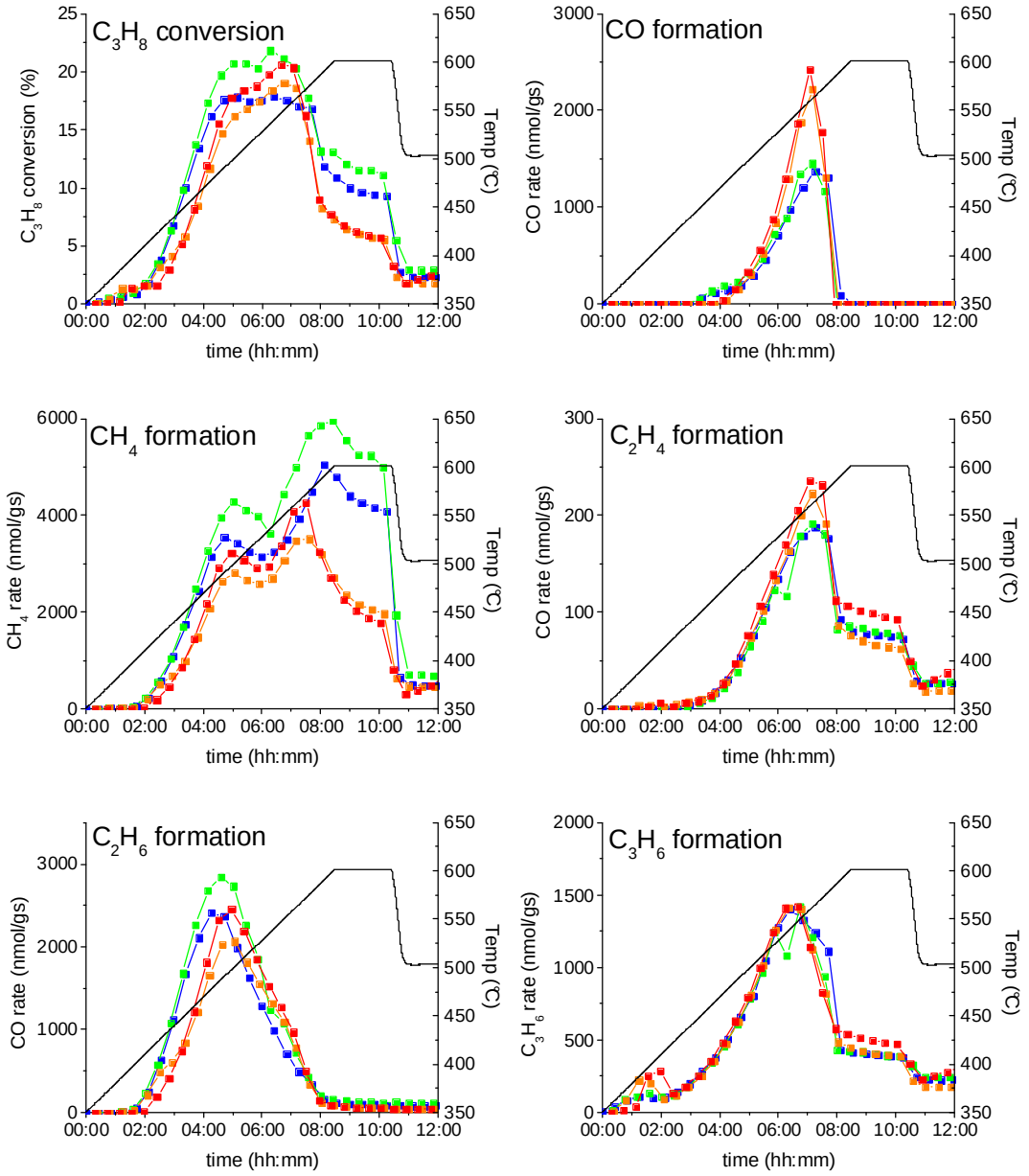

Figure 3.27: Temperature-programmed reduction of *h*-$Mo_{1-x}V_xO_3$ under $H_2/C_3H_8/N_2$ (55/25/20) at WHSV = 5000 ml/gh. ■ — *h*-MoO_3 (#8650); ■ — *h*-$Mo_{0.97}V_{0.03}O_3$ (#6702); ■ — *h*-$Mo_{0.92}V_{0.08}O_3$ (#7911); ■ — *h*-$Mo_{0.89}V_{0.11}O_3$ (#6601)

From the XRD patterns of the post-TPR samples below in Figure 3.28, it is apparent that the oxides have been carburised to the *fcc* α-MoC_{1-x} structure. It is well-known in the literature that for the carburisation of MoO_x by longer-chain hydrocarbons (> C2),

that the formation of cubic MoC_{1-x} is favoured.[38, 115-117] Here we see by the evolution of CO from the structure that the carburisation occurs over the temperature range 500-600°C (Figure 3.27).

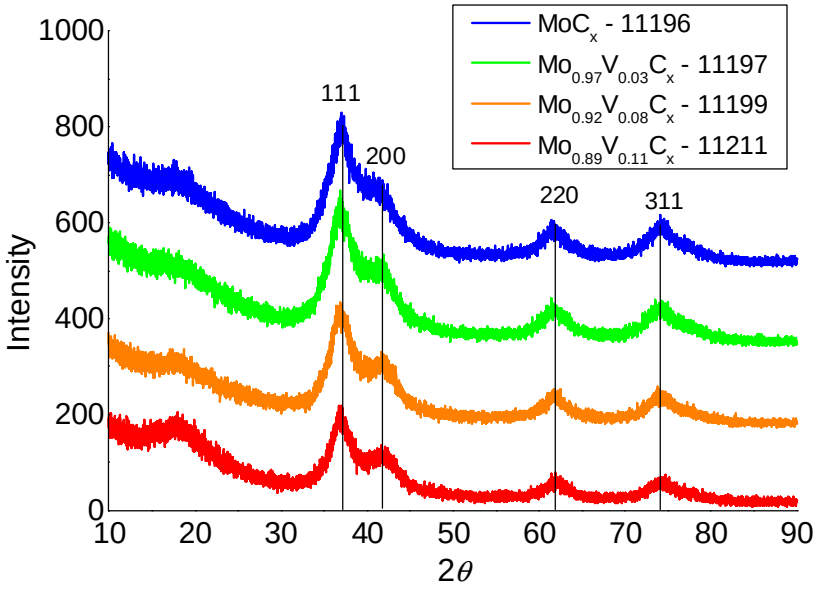

Figure 3.28: Post-mortem XRD patterns of TPR oxides after $H_2/C_3H_8/N_2$ to 600°C

3.5 Discussion

The various approaches to the activation of propane over Mo_2C and Mo/V carbides with respect to the carbide stability are summarised in Figure 3.29. From the results of preliminary experimentation it was observed that oxidative dehydrogenation conditions resulted in the oxidation of the carbide to MoO_3 and that under a less aggressive oxidant such as H_2O/CO_2 the carbide was partially oxidised to MoO_2. However, the addition of co-fed H_2 to the reaction resulted in a stable conversion of propane. Additionally, it was found that the dehydrogenation of propane over Mo_2C resulted in very fast deactivation due to carbon deposition. In this case H_2 was added to reduce carbon deposition.

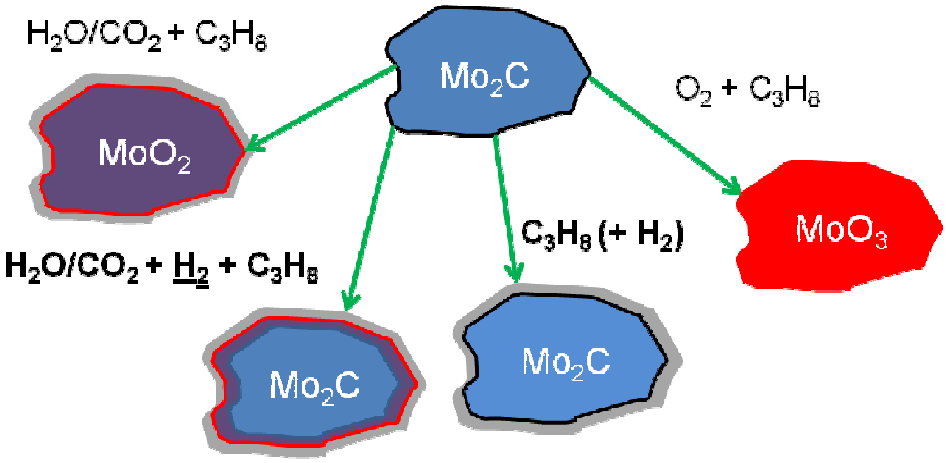

Figure 3.29: Summary of propane reactions over Mo_2C with respect to phase stability and surface carbon.

Therefore, two separate approaches were made to study the activation of propane over molybdenum carbide. The first was a non-oxidative route using a feed of $C_3H_8/N_2/H_2$ and the second was using alternatively H_2O or CO_2 as an oxidant source, which was co-fed with H_2 to stabilise the catalyst.

In the discussion of catalytic conversion of propane over molybdenum and mixed Mo-V carbides we can outline a number of basic reactions that could contribute to the formation of each product. For the case of H_2/C_3H_8:

$C_3H_8 \leftrightarrow C_3H_6 + H_2$	—	dehydrogenation/ hydrogenation
$C_3H_8 (+ H_2) \rightarrow C_2H_{4/6} + CH_4$	—	partial hydrogenolysis/cracking
$C_2H_6 \leftrightarrow C_2H_4 + H_2$	—	ethane dehydrogenation
$C_nH_{2n+2} + H_2 \leftrightarrow nCH_4$	—	total hydrogenolysis
$C_nH_{2n+2} \leftrightarrow nC + (n+1)H_2$	—	coking

For the case of propane dehydrogenation in steam there are additional reactions to take into account:

$C_3H_{6/8} + 3H_2O \leftrightarrow 3CO + 6/7H_2$	—	steam reforming of propane/ene
$C_2H_{4/6} + 2H_2O \leftrightarrow 2CO + 4/5H_2$	—	steam reforming of ethane/ene
$CH_4 + H_2O \leftrightarrow CO + 3H_2$	—	steam reforming of methane

$CO + H_2O \leftrightarrow CO_2 + H_2$ — water-gas shift reaction

$2CO \leftrightarrow CO_2 + C$ — Boudouard reaction

These reactions do not form an exhaustive list, nor are they intended to represent a mechanistic picture. However, by simplifying the complexities of the system we can begin to draw a picture of the reactivity over carbide/oxycarbide surfaces.

3.5.1 Reactions of propane/hydrogen over carbide surfaces

In the case of a fixed feed of C_3H_8/H_2 over undoped Mo_2C let us consider two principal variables for the reaction:

- The initial surface oxidation state of the catalyst.
- The temperature of reaction.

In Figure 3.12 we can see the differences between two distinctly different surface states of Mo_2C. The passivated sample (#9450) and the freshly carburised sample (#8425) show very similar activity with time on stream. This indicates that the surface of the catalyst becomes equilibrated quickly. The key differences observed between the oxidised and carbidic surface are in the relative selectivities of CH_4 and CO. During the equilibration process, the excess oxygen is extracted from the surface of #9450 via a reforming reaction in which the broken down C3 is incorporated and partially removed as CO and H_2O from the surface. During this process, the selectivity of CH_4 increases to the equilibrium level. At a basic level we can represent the formation of C1 and C2 products by a combination of the total and partial hydrogenolysis reactions.

$xC_3 \rightarrow yC_1 + zC_2$ $(y + 2z = 3x)$ — general hydrogenolysis eqn.

The influence of excess surface oxygen is then seen to favour partial hydrogenolysis ($y = z$) with reduction pushing the balance towards total hydrogenolysis ($y > z$).

Throughout both reactions, the rate of propylene formation initially rises and is roughly constant over 8 hours. The rate of hydrogenolysis products, however, decreases exponentially. A possible explanation for this is that the active site for dehydrogenation is distinct from the hydrogenolysis site.

If we then consider the time-dependent rate of C_2H_4 formation, we see that the selectivity remains constant from early on (t = 1h) while the conversion decreases (implying that the rate of formation is also decreasing). This is counter-intuitive if we are to believe that the C_2H_4 originates only from the dehydrogenation of C_2H_6, as we would expect the selectivity to mirror that of C_2H_6. Instead, the formation rate appears to be a function of both the hydrogenolysis and dehydrogenation rates. This can be understood by considering that the propylene is also consumed by the hydrogenolysis process to give C_2H_4. Evidence for this pathway is seen in the steady-state variation of GHSV over Mo_2C shown in Figure 3.16. The variation in GHSV from 5000 → 1250 ml/gh is observed to double the rate of hydrogenolysis but only marginally increase the rate of C_3H_6. In the selectivity-conversion plot the C_3H_6 is consumed by the hydrogenolysis process with increasing conversion. The selectivity-conversion plot also shows that the selectivity for C_2H_6 converges close to 0 at low conversions implying that it is likely to be a secondary product.

A schematic explanation for these observations is presented in Figure 3.30. It is stressed again that this schematic is merely a tool to provide explanation and is not intended as a mechanistic model.

The strong hydrogenolysis sites in this case are defined as those that can activate propane, whereas the weak sites are defined as those that can only activate propylene.

As seen in Figure 3.30 dehydrogenation is independent of other reactions while methane can be formed by hydrogenolysis of propane or propylene and by the methanation of deposited carbon. This creates a disparity between the selectivity to ethylene and methane which can be seen in Figure 3.14(c). As the reaction progresses at 500°C, the ‘strong’ hydrogenolysis sites are deactivated by carbon deposition and the relative contribution of carbon methanation is increased.

By increasing the temperature of reaction, not only is the rate of equilibration increased, but also the position of equilibrium. From comparison of $(Mo_{1-x}V_x)_2C$ at 500°C and 550°C in Figure 3.14 we see that the ultimate conversion is lower and that the rate of formation of C_3H_6 decreases over time. This implies that the active sites for dehydrogenation are consumed at this temperature.

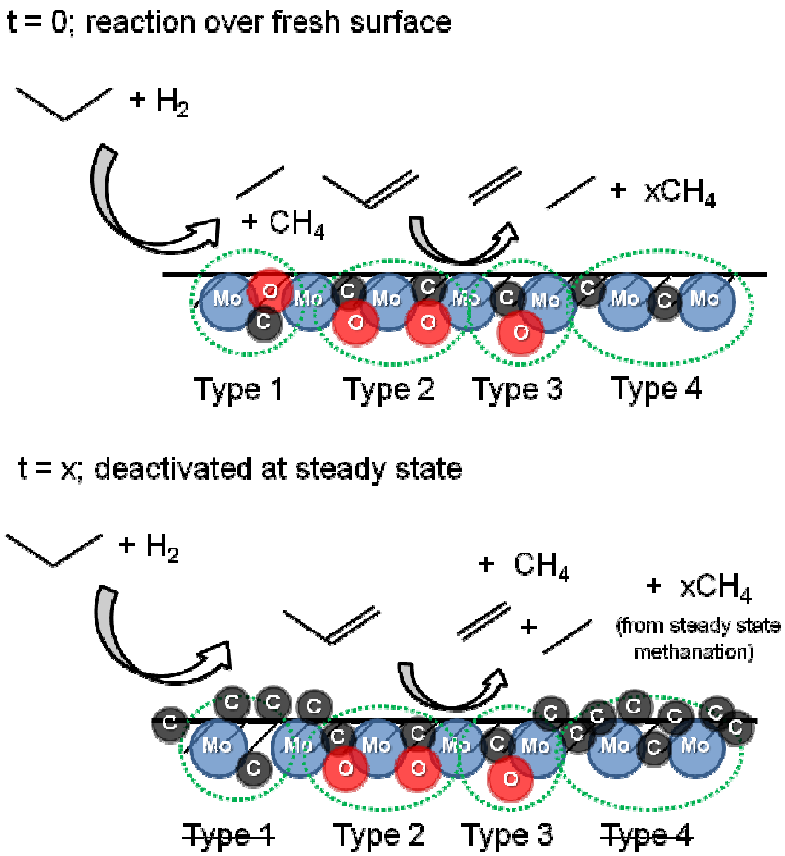

Figure 3.30: Schematic for propane reactivity over deactivated Mo_2C. Type 1 = alkyl-recombinative site; Type 2 = dehydrogenation site; Type 3 = weak hydrogenolysis site; Type 4 = strong hydrogenolysis site.

From the temperature-programmed reaction of *h*-Mo(V)O_3 discussed earlier, we see that the carburisation of the oxide under C_3H_8/H_2 occurs between 500-600°C. At 500°C, the residual oxygen content of the carbide persists throughout the course of the reaction, also at the surface whereas at 550°C the oxygen is stripped from the surface, destroying dehydrogenation sites.

The temperature-programmed reaction experiments shown in Figure 3.25 – Figure 3.27 provide further information on the temperature dependence of product selectivity for this reaction. Apart from the fact that we see carburisation occur between 500-600°C (as evidenced by the evolution of CO), at lower temperatures (400-500°C) the evolution of CH_4, C_2H_6 and C_4H_{10} are observed as products of recombinative hydrocarbon formation as discussed by Tysoe *et al.*[93, 101, 102] Propylene is formed even at low temperatures (< 400°C) but does not increase dramatically in rate until ca. 450°C, which coincides with the very beginning of CO evolution. The C_3H_6

formation rate peaks at ca. 520°C, just before the peak of CO evolution. At this time it can be seen that the C_2H_4 formation rate, while meagre, mirrors the CO evolution with the implication that the carbide is a likely hydrogenolysis site. As the reaction temperature increases, the methane has a second peak which is observed at 550°C for the V-rich oxides, and at 600°C for *h*-$Mo_{0.97}V_{0.03}O_3$ & *h*-MoO_3. This peak is associated with the total hydrogenolysis of propane and it is observed to decay to a steady-state value, presumably as the active sites are titrated by surface carbon.

The influence of vanadium in the activation of propane over the freshly prepared carbide series $(Mo_{1-x}V_x)_2C$ is difficult to quantify. Most notably, an increase in vanadium increases the initial conversion of propane and formation rate of methane (Figure 3.13). With time on stream, the selectivity to hydrogenolysis of V-rich samples is observed to be higher than that of Mo_2C. At steady-state conditions there is a trend observed for the apparent activation energy of propylene formation. With increasing V content, the apparent E_a is observed to increase from 80 ± 5 kJ/mol to 95 ± 5 kJ/mol in a roughly linear fashion (Figure 3.15). This is not reflected in the E_a determined for methane formation, which would indicate that the most likely pathway is independent of the surface – hydrogenation of surface carbon.

In the TPR experiment, we observe the inverse situation. Over the course of reaction the conversion is higher for the V-poor *h*-$Mo_{1-x}V_xO_3$ & *h*-MoO_3 and especially so with methane formation. As was discussed in Chapter 2, the V-substituted oxides are more stable to reduction which is reflected by the delayed onset of activity (Figure 3.27). Most interestingly we observe that the area under the CO peak is larger for the V-containing oxides. This is also contrary to observations for the TPR-carburisation of $Mo(V)O_x$ in CH_4/H_2.

It must be noted here that the resultant carbide is different in the case of TPRC under C_3H_8/H_2 (*fcc* MoC_{1-x}) vs. CH_4/H_2 (*hcp* Mo_2C). However, the relevance of these observations is not insignificant and the relation between these two phases will be discussed in more depth in the next chapter.

3.5.2 Reactions of propane/steam (or CO_2)/hydrogen over carbide surfaces

Much of the discussion relating to the reactivity of propane in the previous section is applicable to the situation observed for steam.

The conversion of propane and selectivity to propylene is observed to be higher for the case of steam/CO_2 containing feeds. At 500°C, the conversion of propane is roughly constant (8-10%) with a constant rate of propylene formation. For temperatures > 500°C the initial conversion of propane is ca. 40% which is principally due to formation of CO, CH_4 and C_2H_6 (Figure 3.17). It seems that just above 500°C lies a critical temperature which is hinted at in the previous experiments. It can be seen quite clearly in the Arrhenius plots for various products (Figure 3.18) that between 510-530°C, there is a disjoint in the nature of the catalytic surface. This is particularly evident in the Arrhenius plot for CO formation, which gives an apparent activation energy; Ea<510°C = 272 kJ/mol & Ea>510°C = 66 kJ/mol.

If we look at the initial conversion plot for the reaction at 550°C (Figure 3.17b) at t = 0, we note the predominant selectivities are to CO, CH_4 and C_2H_6. With reference to the observed alkyl-group recombination that was observed in the TPR of the oxides we can tentatively propose that the initially passivated Mo_2C surface catalyses the reaction:

$$nC_3H_8 \rightarrow xCH_4 + yC_2H_6 + zC_4H_{10} \quad (3n = x + 2y + 4z)$$

— recombinative hydrocarbon formation

and that in the meanwhile;

$$C_3H_8 + 3H_2O \rightarrow 3CO + 7H_2$$ — steam reforming of C_3H_8

is combined with the carburisation of MoO_xC_y to give:

$$MoO_x + C_3H_8 \rightarrow MoC_x + CO + H_2O$$ — carburisation of MoO_x

The CO peak is subsequently followed by a peak in the selectivity to CO_2 which possibly arises via the formation of an oxycarbide surface which is active for WGS:[110]

$CO + H_2O \leftrightarrow CO_2 + H_2$ — water-gas shift reaction

This last assumption is based on the fact that the rate of CO_2 never exceeds CO formation and that the decline in selectivity mirrors that observed for CO.

Finally, the rate of propylene formation is observed to peak soon after the WGS peak, which is reported to be most active over oxycarbide surfaces.[109] Overall with temperatures > 500°C the reaction strongly deactivates over time, most likely due to carbon deposition (discussed in Chapter 4). This is also notable in the post-catalytic CHN analyses, where the reaction carried out at 500°C has 6.3 wt.% carbon (5.92 wt.% is stoichiometric) after reaction whereas the reactions carried out at 550 & 600°C have 7.3 and 7.9 wt.% carbon, respectively.

Vanadium is observed to increase the selectivity of propylene but the conversion does not change. This is contrary to the observations for the H_2/C_3H_8 feed, however, the mechanistic differences are significant and it is difficult to ascribe specific reasoning except that in O-rich conditions V_xO_y is a better DH catalyst.

3.6 Summary

In this chapter we have observed that the activation of propane over molybdenum carbide is strongly dependent upon the oxidation state of the surface of the catalyst. In the direct dehydrogenation of propane we observe that freshly reduced material is highly active but only moderately selective to propylene. With time on stream, however, the hydrogenolysis products are observed to decrease while the rate of dehydrogenation stays roughly constant. The addition of vanadium is observed to increase the overall activity of the catalyst but it does not increase the selectivity to propylene.

The activation of propane in soft-oxidising conditions (H_2O/CO_2) increases productivity of the catalyst to propylene in all cases. In this case vanadium is seen to be beneficial to the reactivity initially but the overall stability of the catalyst to oxidation is reduced. In the case of H_2O containing feeds, steam-reforming of propane over the catalyst is observed. Additionally, a critical temperature for surface reduction (~520°C) is noted for the catalyst, above which the chemical potential of the reactor results in strong deactivation of the catalyst, most likely due to carbon formation. The

addition of CO_2 has a similar effect on the productivity to propylene but in this case there is also a strong contribution of reverse water-gas-shift.

In a separate study into the reverse water-gas shift reaction, Mo_2C is found to be an efficient catalyst for the hydrogenation of CO_2 with high selectivity to CO (> 90%). The reaction went to equilibrium conversion even at very high space velocities over a range of temperatures (GHSV > 200000, 500°C < T < 700°C).

For the temperature-programmed reaction of *h*-$Mo_{1-x}V_xO_3$ precursor oxide materials in propane the catalytic activity was observed to increase dramatically as the oxide is reduced and the selectivities evolved with temperature mirroring the reduction state of the oxide. In all cases the phase resulting after reaction was observed to be the metastable *fcc* MoC_{1-x}.

3.7 References

[1] C. F. Cullis, Industrial and Engineering Chemistry 1967, 59, 18.
[2] F. Cavani, F. Trifiro, Catalysis Today 1999, 51, 561.
[3] F. Cavani, F. Trifiro, Catalysis Today 1995, 24, 307.
[4] W. Ueda, Y.-S. Yoon, K.-H. Lee, Y. Moro-oka, Korean Journal of Chemical Engineering 1997, 14, 474.
[5] W. Ueda, N. F. Chen, K. Oshihara, Kinetics and Catalysis 1999, 40, 401.
[6] T. G. Alkhazov, K. Y. Adzhamov, F. M. Poladov, Reaction Kinetics and Catalysis Letters 1977, 7, 65.
[7] T. V. Andrushkevich, L. M. Plyasova, G. G. Kuznetsova, V. M. Bondareva, T. P. Gorshkova, I. P. Olenkova, N. I. Lebedeva, Reaction Kinetics and Catalysis Letters 1979, 12, 463.
[8] J. S. Lee, M. Boudart, Catalysis Letters 1993, 20, 97.
[9] R. Schlögl, A. Knop-Gericke, M. Hävecker, U. Wild, D. Frickel, T. Ressler, R. E. Jentoft, J. Wienold, G. Mestl, A. Blume, O. Timpe, Y. Uchida, Topics in Catalysis 2001, 15, 219.
[10] N. Ballarini, A. Battisti, F. Cavani, A. Cericola, C. Lucarelli, S. Racioppi, P. Arpentinier, Catalysis Today 2006, 116, 313.
[11] R. Horn, N. Degenstein, K. Williams, L. Schmidt, Catalysis Letters 2006, 110, 169.
[12] M. Y. Sinev, G. A. Vorobeva, V. N. Korchak, Kinetics and Catalysis 1986, 27, 1007.
[13] M. Y. Sinev, Z. T. Fattakhova, Y. P. Tulenin, P. S. Stennikov, V. P. Vislovskii, Catalysis Today 2003, 81, 107.
[14] B. Savova, D. Filkova, D. Crisan, M. Crisan, M. Raileanu, N. Dragan, L. Petrov, J. C. Védrine, Applied Catalysis A: General 2009, 359, 55.
[15] M. Baerns, Technische chemie, Wiley-VCH, Weinheim, 2006.
[16] A. K. M. Hatano, European Patent 1988, 318.
[17] K. O. T. Ushikubo, A. Kayo, T. Umezawa, K. Kiyona, I. Sawaki, European Patent 1992, 529.
[18] R. K. Grasselli, D. J. Buttrey, J. D. Burrington, A. Andersson, J. Holmberg, W. Ueda, J. Kubo, C. G. Lugmair, A. F. Volpe, Topics in Catalysis 2006, 38, 7.
[19] A. C. Sanfiz, T. W. Hansen, D. Teschner, P. Schnorch, F. Girgsdies, A. Trunschke, R. Schlogl, M. H. Looi, S. B. A. Hamid, Journal of Physical Chemistry C 2010, 114, 1912.
[20] A. T. L. Csepei, R. Schloegl data to be published 2011.
[21] P. Beato, A. Blume, F. Girgsdies, R. E. Jentoft, R. Schlogel, O. Timpe, A. Trunschke, G. Weinberg, Q. Basher, F. A. Hamid, S. B. A. Hamid, E. Omar, L. M. Salim, Applied Catalysis a-General 2006, 307, 137.
[22] A. T. L. Csepei, R. Schloegl private discussions 2011.
[23] P. Mars, D. W. van Krevelen, Chemical Engineering Science 1954, 3, 41.
[24] J. S. Lee, L. Volpe, F. H. Ribeiro, M. Boudart, Journal of Catalysis 1988, 112, 44.
[25] C. Bouchy, S. B. D. A. Hamid, E. G. Derouane, Chemical Communications 2000, 125.
[26] K. Page, J. Li, R. Savinelli, H. N. Szumila, J. P. Zhang, J. K. Stalick, T. Proffen, S. L. Scott, R. Seshadri, Solid State Sciences 2008, 10, 1499.

[27] I. P. Olenkova, L. M. Plyasova, S. D. Kirik, Reaction Kinetics and Catalysis Letters 1981, 16, 81.
[28] S. Crouch-Baker, P. G. Dickens, Solid State Ionics 1989, 32-33, 219.
[29] J. Song, X. Ni, L. Gao, H. Zheng, Materials Chemistry and Physics 2007, 102, 245.
[30] L. Dupont, D. Larcher, M. Touboul, Journal of Solid State Chemistry 1999, 143, 41.
[31] T. G. Kuznetsova, G. K. Boreskov, T. V. Andrushkevich, Y. A. Grigorkina, N. G. Maksimov, I. P. Olenkova, L. M. Plyasova, T. P. Gorshkova, Reaction Kinetics and Catalysis Letters 1982, 19, 405.
[32] B. Darriet, J. Galy, Journal of Solid State Chemistry 1973, 8, 189.
[33] M. Baca, A. Pigamo, J. L. Dubois, J. M. M. Millet, Topics in Catalysis 2003, 23, 39.
[34] A. P. E. York, J. B. Claridge, A. J. Brungs, S. C. Tsang, M. L. H. Green, Chemical Communications 1997, 39.
[35] J. B. Claridge, A. P. E. York, A. J. Brungs, C. Marquez-Alvarez, J. Sloan, S. C. Tsang, M. L. H. Green, Journal of Catalysis 1998, 180, 85.
[36] A. P. E. York, T.-c. Xiao, M. L. H. Green, J. B. Claridge, Catalysis Reviews 2007, 49, 511
[37] D. C. LaMont, A. J. Gilligan, A. R. S. Darujati, A. S. Chellappa, W. J. Thomson, Applied Catalysis a-General 2003, 255, 239.
[38] T. C. Xiao, A. P. E. York, V. C. Williams, H. Al-Megren, A. Hanif, X. Y. Zhou, M. L. H. Green, Chemistry of Materials 2000, 12, 3896.
[39] D. C. LaMont, W. J. Thomson, Chemical Engineering Science 2005, 60, 3553.
[40] A. R. S. Darujati, D. C. LaMont, W. J. Thomson, Applied Catalysis a-General 2003, 253, 397.
[41] D. C. LaMont, W. J. Thomson, Applied Catalysis A: General 2004, 274, 173.
[42] F. Solymosi, J. Cserényi, A. Szöke, T. Bánsági, A. Oszkó, Journal of Catalysis 1997, 165, 150.
[43] K. Oshikawa, M. Nagai, S. Omi, J. Phys. Chem. B 2001, 105, 9124.
[44] S. Liu, L. Wang, R. Ohnishi, M. Ichikawa, Journal of Catalysis 1999, 181, 175.
[45] T. J. Zhou, A. M. Liu, Y. R. Mo, H. B. Zhang, Journal of Physical Chemistry A 2000, 104, 4505.
[46] S. Yuan, S. B. Derouane-Abd Hamid, Y. Li, P. Ying, Q. Xin, E. G. Derouane, C. Li, Journal of Molecular Catalysis A: Chemical 2002, 180, 245.
[47] S. Liu, R. Ohnishi, M. Ichikawa, Journal of Catalysis 2003, 220, 57.
[48] D. Mckay, J. S. J. Hargreaves, R. F. Howe, Catalysis Letters 2006, 112, 109.
[49] M. Toosi, M. Peyrovi, R. Mondgarian, Reaction Kinetics and Catalysis Letters 2009, 98, 133.
[50] D. Wang, J. H. Lunsford, M. P. Rosynek, Journal of Catalysis 1997, 169, 347.
[51] R. K. Grasselli, Catalysis Today 1999, 49, 141.
[52] E. Solymosi, R. Nemeth, L. Ovari, L. Egri, Journal of Catalysis 2000, 195, 316.
[53] S. Xing, D. Zhou, L. Cao, X. Li, Chinese Journal of Catalysis 2010, 31, 415.
[54] F. Solymosi, R. Nemeth, Catalysis Letters 1999, 62, 197.
[55] F. Solymosi, R. Németh, A. Oszkó, J. J. S. E. Iglesia, T. H. Fleisch, in Studies in Surface Science and Catalysis, Vol. Volume 136, Elsevier, 2001, pp. 339.
[56] M. J. Ledoux, F. Meunier, B. Heinrich, C. Pham-Huu, M. E. Harlin, A. O. I. Krause, Applied Catalysis a-General 1999, 181, 157.

[57] M. K. Neylon, S. Choi, H. Kwon, K. E. Curry, L. T. Thompson, Applied Catalysis a-General 1999, 183, 253.
[58] M. E. Harlin, A. O. I. Krause, B. Heinrich, C. Pharm-Huu, M. J. Ledoux, Applied Catalysis a-General 1999, 185, 311.
[59] H. Kwon, L. T. Thompson, J. Eng, J. G. Chen, Journal of Catalysis 2000, 190, 60.
[60] M. Volpe, G. Tonetto, H. de Lasa, Applied Catalysis a-General 2004, 272, 69.
[61] C. Bouchy, C. Pham-Huu, B. Heinrich, E. G. Derouane, S. B. Derouane-Abd Hamid, M. J. Ledoux, Applied Catalysis a-General 2001, 215, 175.
[62] R. B. Levy, M. Boudart, Science 1973, 181, 547.
[63] Y. Holl, R. Touroude, G. Maire, A. Muller, P. A. Engelhard, J. Grosmangin, Journal of Catalysis 1987, 104, 202.
[64] Y. Holl, F. Garin, G. Maire, A. Muller, P. A. Engelhard, J. Grosmangin, Journal of Catalysis 1987, 104, 211.
[65] M. Yamada, J. Yasumaru, M. Houalla, D. M. Hercules, Journal of Physical Chemistry 1991, 95, 7037.
[66] M. J. Ledoux, P. H. Cuong, J. Guille, H. Dunlop, Journal of Catalysis 1992, 134, 383.
[67] S. T. Oyama, Catalysis Today 1992, 15, 179.
[68] M. J. Ledoux, C. Phamhuu, H. Dunlop, J. Guille, L. Portela, E. Iglesia, J. W. Geus, G. Maire, J. C. Volta, Z. Paal, G. Leclercq, Studies in Surface Science and Catalysis 1993, 75, 955.
[69] E. A. Blekkan, P. H. Cuong, M. J. Ledoux, J. Guille, Industrial & Engineering Chemistry Research 1994, 33, 1657.
[70] P. Delporte, C. PhamHuu, M. J. Ledoux, Applied Catalysis a-General 1997, 149, 151.
[71] P. DelGallo, F. Meunier, C. PhamHuu, C. Crouzet, M. J. Ledoux, Industrial & Engineering Chemistry Research 1997, 36, 4166.
[72] A. Katrib, V. Logie, M. Peter, P. Wehrer, L. Hilaire, G. Maire, Journal De Chimie Physique Et De Physico-Chimie Biologique 1997, 94, 1923.
[73] A. Katrib, V. Logie, N. Saurel, P. Wehrer, L. Hilaire, G. Maire, Surface Science 1997, 377, 754.
[74] C. Bouchy, C. Pham-Huu, B. Heinrich, C. Chaumont, M. J. Ledoux, Journal of Catalysis 2000, 190, 92.
[75] T. Matsuda, Y. Hirata, S. Suga, H. Sakagami, N. Takahashi, Applied Catalysis a-General 2000, 193, 185.
[76] P. Wehrer, L. Hilaire, G. Maire, Applied Catalysis a-General 2001, 208, 259.
[77] T. C. Xiao, H. T. Wang, J. W. Da, K. S. Coleman, M. L. H. Green, Journal of Catalysis 2002, 211, 183.
[78] E. Torres-GarcÃ-a, G. RodrÃ-guez-Gattorno, J. A. Ascencio, L. O. AlemÃ¡n-VÃ¡zquez, J. L. Cano-DomÃ-nguez, A. MartÃ-nez-HernÃ¡ndez, P. Santiago-Jacinto, The Journal of Physical Chemistry B 2005, 109, 17518.
[79] G. Rodriguez-Gattorno, A. Martinez-Hernandez, L. O. Aleman-Vazquez, E. Torres-Garcia, Applied Catalysis a-General 2007, 321, 117.
[80] Y. Holl, F. Garin, G. Maire, Journal of Catalysis 1988, 113, 569.
[81] F. H. Ribeiro, M. Boudart, R. A. Dallabetta, E. Iglesia, Journal of Catalysis 1991, 130, 498.
[82] E. Iglesia, F. H. Ribeiro, M. Boudart, J. E. Baumgartner, Catalysis Today 1992, 15, 455.

[83] E. Iglesia, F. H. Ribeiro, M. Boudart, J. E. Baumgartner, Catalysis Today 1992, 15, 307.
[84] C. Phamhuu, M. J. Ledoux, J. Guille, Journal of Catalysis 1993, 143, 249.
[85] P. Wehrer, C. Bigey, L. Hilaire, Applied Catalysis a-General 2003, 243, 109.
[86] H. Sakagami, Y. Asano, T. Ohno, N. Takahashi, H. Itoh, T. Matsuda, Applied Catalysis A: General 2006, 297, 189.
[87] T. Ohno, Z. Li, N. Sakai, H. Sakagami, N. Takahashi, T. Matsuda, Applied Catalysis A: General 2010
In Press, Accepted Manuscript.
[88] M. Siaj, N. Dubuc, P. H. McBreen, The Journal of Physical Chemistry C 2009.
[89] M. Siaj, I. Temprano, N. Dubuc, P. H. McBreen, Journal of Organometallic Chemistry 2006, 691, 5497.
[90] M. Siaj, C. Maltais, E. M. Zahidi, H. Oudghiri-Hassani, J. Q. Wang, F. Rosei, P. H. McBreen, Journal of Physical Chemistry B 2005, 109, 15376.
[91] H. Oudghiri-Hassani, E. Zahidi, M. Siaj, J. Wang, P. H. McBreen, Applied Surface Science 2003, 212, 4.
[92] J. Wang, M. Castonguay, J. Deng, P. H. McBreen, Surface Science 1997, 374, 197.
[93] G. F. Wu, W. T. Tysoe, Abstracts of Papers of the American Chemical Society 1999, 217, U608.
[94] B. Bartlett, M. M. Hossain, W. T. Tysoe, Journal of Catalysis 1998, 176, 439.
[95] G. F. Wu, B. Bartlett, W. T. Tysoe, Journal of Molecular Catalysis a-Chemical 1998, 131, 91.
[96] G. F. Wu, W. T. Tysoe, Surface Science 1998, 397, 197.
[97] G. F. Wu, B. Bartlett, W. T. Tysoe, Langmuir 1998, 14, 1435.
[98] G. Wu, B. Bartlett, W. T. Tysoe, Journal of Catalysis 1998, 173, 172.
[99] B. F. Bartlett, W. T. Tysoe, Catalysis Letters 1997, 46, 101.
[100] W. T. Tysoe, Langmuir 1996, 12, 78.
[101] B. Bartlett, V. Shneerson, W. T. Tysoe, Catalysis Letters 1995, 32, 1.
[102] B. Bartlett, C. Soto, R. Wu, W. T. Tysoe, Catalysis Letters 1993, 21, 1.
[103] L. P. Wang, C. Soto, W. T. Tysoe, Journal of Catalysis 1993, 143, 92.
[104] Y. Chauvin, Angewandte Chemie-International Edition 2006, 45, 3740.
[105] J. L. Herisson, Y. Chauvin, Makromolekulare Chemie 1971, 141, 161.
[106] M. Siaj, C. Reed, S. T. Oyama, S. L. Scott, P. H. McBreen, Journal of the American Chemical Society 2004, 126, 9514.
[107] M. Nagai, A. M. Zahidul, Y. Kunisaki, Y. Aoki, Applied Catalysis A: General 2010, 383, 58.
[108] J. A. Schaidle, A. C. Lausche, L. T. Thompson, Journal of Catalysis 2010, 272, 235.
[109] P. Liu, J. A. Rodriguez, The Journal of Physical Chemistry B 2006, 110, 19418.
[110] J. Patt, D. J. Moon, C. Phillips, L. Thompson, Catalysis Letters 2000, 65, 193.
[111] H. Tominaga, M. Nagai, Applied Catalysis A: General 2005, 282, 5.
[112] T. Suzuki, H. I. Iwanami, T. Yoshizawa, H. Yamazaki, Y. Yoshida, International Journal of Hydrogen Energy 1995, 20, 823.
[113] T. Osaki, N. Narita, T. Horiuchi, T. Sugiyama, H. Masuda, K. Suzuki, Journal of Molecular Catalysis A: Chemical 1997, 125, 63.
[114] G. Ertl, H. Knözinger, F. Schüth, J. Weitkamp, Handbook of heterogeneous catalysis, Second, completely rev. and enl. ed., VCH, Weinheim, 2008.

[115] N. Ji, T. Zhang, M. Zheng, A. Wang, H. Wang, X. Wang, Y. Shu, A. L. Stottlemyer, J. G. Chen, Catalysis Today 2009, 147, 77.
[116] A. Hanif, T. C. Xiao, A. P. E. York, J. Sloan, M. L. H. Green, Chemistry of Materials 2002, 14, 1009.
[117] T. Xiao, A. P. E. York, K. S. Coleman, J. B. Claridge, J. Sloan, J. Charnock, M. L. H. Green, Journal of Materials Chemistry 2001, 11, 3094.

Chapter 4: Reactivity of propane over Mo/V carbide II: Surface reactivity studies and post-catalytic characterisation

4.1 Abstract

In this section we address the chemical nature of the catalyst surface in relation to the observed catalytic activity. Using *in situ* Raman spectroscopy and *ex*- and *in situ* X-ray photoelectron spectroscopy (XPS), it was possible to gain insight into the nature of the active material and observe the progression of the surface chemistry under reaction conditions. Finally, in conjunction with transmission electron microscopy (TEM) techniques, we were able to characterise the samples after reaction to give a 'post-mortem' analysis of the catalysts.

Using Raman microscopy, adventitious carbon was observed to form on the surface of the catalyst, selectively blocking sites that were active for the hydrogenolysis/cracking of propane to lighter molecules. The nature of the carbon species was dependent on the reaction conditions and was found to evoke a higher sp^2 character (less amorphous) with a co-oxidant feed (H_2O, CO_2).

The oxy-carbidic nature of the surface layer is apparent from *ex situ* XPS of the freshly prepared carbides. It is also observed for the V-containing materials that the surface layer is enriched with vanadium in the form of V=O. Results of *in situ* XPS experimentation reveal a strong dependency of the catalytic activity with the surface oxidation state of the carbide. Dehydrogenation of propane was observed to increase with the oxidation state, whereas formation of C2 and C4 products is favoured by an increased electron density at the Fermi edge. No formation of adventitious carbon was observed.

The comparison of pre- and post-mortem carbide catalysts shows a considerable surface rearrangement as well as carbon deposition. Selected area electron diffraction (SAED) of the freshly prepared carbides is indicative of *hcp* β-Mo_2C with agglomerated crystallite morphology. After reaction the catalysts are observed to be quite heterogeneous with regards to carbon deposition and structural rearrangement. The SAED reveals a mixture of *hcp* β-Mo_2C as well as the presence of *fcc* α-MoC_{1-x} however, the powder XRD shows only β-Mo_2C.

Post-mortem analysis of the oxide precursors after TPR in H_2/C_3H_8 shows primarily *fcc* α-MoC_{1-x} with extensive carbon deposition as both graphitic overlayers and carbon-rich carbidic phases.

4.2 Introduction

The comprehensive surface characterisation of molybdenum carbides is a complex area of research and one that hinders efforts to develop mechanistic insights into their reactivity. Due to their dark nature, many light-based spectroscopic techniques are ineffective for the characterisation of surface species or adsorbates. The difficulties of exact characterisation are compounded by the reactive nature of molybdenum carbide and the tendency to incorporate oxygen into the structure of the carbide. Freshly reduced Mo_2C is pyrophoric and burns on contact with bulk oxygen. It is therefore necessary to passivate the surface layers under a low partial pressure of oxygen in order to handle the material in atmosphere. This surface modification by oxygen leads to significant changes in the reactivity and hence it is common in catalytic studies for the carbide to be formed *in situ* prior to the catalytic reaction in question.

As well as surface contamination by oxygen, the process of carburisation leads to the deposition of adventitious carbon on the surface of Mo_2C. As is discussed in Chapter 1, this is a function of the chemical potentials of carbon and hydrogen in the gas phase during the synthesis, and may be reduced by considering the thermodynamics situation. However, the necessary crossover of the maximum temperature of the thermodynamic coking limit and the minimum temperature required to remove oxygen from the system, means that there is generally some aliphatic carbon formed during the synthesis. In the literature, a pretreatment under H_2 is regularly applied to remove surface carbon. Specific methanation of the surface carbon may be achieved under ideal (i.e. single crystal) conditions but in most cases it is applied as a rule of thumb and has been shown to result in an overly metallic character of the final surface depending upon conditions.[1] Just as the production of high-quality materials presents a challenge to the synthetic chemist, determining the nature of the surface with respect to observed catalytic activity is challenging and is aided by the use of an array of techniques including; TPD/R/O, TEM, physisorption and chemisorptions experiments, Raman microscopy, X-ray absorption spectroscopy (XAS) and XPS.

4.2.1 Motivation and experimental goals

The goal of this study is to shed light on the nature of the carbide surface in the activation of propane under varying conditions. It also examines the mechanistic influence of vanadium as a dopant atom in the Mo_2C lattice under conditions of high reducing potential in hydrocarbon reactions.

As has been discussed in the previous chapter, the operation of metal oxide catalysts for selective oxidation reactions in industrial conditions is rigorous and demanding on materials and engineering. At equilibrium conversions over large scale reactors, the chemical potential varies greatly over the range of the catalytic bed and can therefore influence the degree of reduction/ carburisation which in turn can influence the product distribution.

For these reasons, it is interesting to examine the reactivity of oxide surfaces with respect to their oxidation state, structure and carbon coverage. As the surface composition of a catalyst is a function of the chemical potential in the gas phase, it is necessary to employ the use of *in situ* techniques such as XPS and Raman, and also by the post-mortem characterisation of catalyst samples.

Specifically the goals of this study are to:

- compare and contrast the formation of surface carbon species using Raman spectroscopy
- to conduct transmission electron microscopy studies comparing pre- and post-mortem samples of Mo_2C and $(Mo_{1-x}V_x)_2C$ following treatment under propane by way of local chemical and structural analysis
- to correlate the specific catalytic activity with the surface chemical composition and oxidation state by use of *in situ* XPS technique.

4.2.2 Previous studies and literature review

An exhaustive review on the surface characterisation of molybdenum catalysts is not practical within the scope of this work. However, it is important to outline some key studies that relate to the techniques applied in this thesis. Also presented are studies that contribute to the mechanistic understanding of reactivity on molybdenum carbide/oxycarbide surfaces.

4.2.2.1 Mo_2C single crystal studies

There are relatively few papers in the literature that deal with surface studies of Mo_2C single crystals. Considerable contributions to the field have been made by Otani *et al.* with a series of papers studying the surface structure and oxygen adsorption on α-(0001)-Mo_2C.[2-5] The principal techniques used in these studies were LEED (low-energy electron diffraction), XPS and TPD.

In a paper with Oyama, Otani *et al.* discuss the surface composition and structure of Mo_2C. It is observed with the use of LEED and angle-resolved photoelectron spectroscopy (ARPES), that at lower temperatures (< 823°C) the surface is characterised by Mo termination. At higher temperatures (> 1023°C) the surface is found to be predominantly C-terminated.[2] This distinction of metallic/carbidic character is important when considering the adsorption of hydrocarbons on the surface.

In a review of transition metal surface chemistry, Chen *et al.* discuss the interaction of ethylene on metal and carbide terminated surfaces using TPD and HREEL spectroscopies.[6] On clean Mo(110), ethylene is found to decompose to C and H, with the latter desorbed as H_2 at ca. 120°C. Similar behaviour was observed for the carbon modified surface, however, with the presence of 0.25 ML of surface oxygen, the reactivity is almost entirely suppressed. The high resolution electron energy loss spectra (HREELS) indicate that the reaction pathway for the metal and carbide is different. The adsorption of C_2H_4 on the pure metal surface is observed to decompose the C-H bonds at very low temperatures (< 80K) leading to the formation of an acetylene-like adsorbate, which decomposes at 75°C. The carbide surface is observed to adsorb the ethylene in a di-sigma-bound mode before forming a MoC_x-CCH_3 ethylidyne-like species, comparable to an organometallic moiety. In a subsequent study by Grossman *et al.*[7] this change in behaviour is suggested to arise from C(sp)-Mo(4d) hybridisation observed for molybdenum carbides, which modifies the density of states (DOS).

These differences are outlined in a paper by Kelly *et al.* which considers the reactivity of butane over C-modified Mo(100) surfaces.[8] The TD spectra are compared for a series of surfaces and it observed that at a surface carbon coverage of ca. $\theta_c = 0.6$, the H_2 peak associated with decomposition is decreased and the desorption of butene is

observed to increase. The above studies indicate that the reactivity of the carbide is specifically altered *cf.* Mo^0 surface, however it is still active for the dissociation of hydrocarbon molecules. It is also noted that the reactivity may be strongly moderated by the introduction of surface oxygen.

The effect of surface oxygen on the reactivity is again addressed by Otani *et al.*[4] who find that the $Mo_2C(0001)$ surface is active to O_2 adsorption with a very high sticking probability, and that the adsorbed O atoms interact with both Mo and C atoms to form an 'oxycarbide' at temperatures < 523°C. Above 523°C, the oxygen is observed to bind only to Mo atoms. Interestingly, the metallic character of the carbide is observed to persist with oxygen exposure (10 ML) at temperatures < 823°C. The observed density of states at the Fermi edge is enhanced by exposure to oxygen by the formation of an oxygen-induced state at E_F, the origin of which is later hypothesised to be due to increased Coulomb interaction between the Mo 4p and 4d electrons.[5] This behaviour is attributed to the fact that, in contrast to group IV/V transition metal carbides, the highest occupied state is mostly composed of Mo4d orbitals rather than the C2p orbitals. Hence, the attacking oxygen preferentially bonds with Mo in the second layer rather than attacking C and desorbing as CO.

4.2.2.2 Mo_2C polycrystalline studies in 'metathesis' reactions

The complex interactions of Mo_2C with hydrocarbon molecules are explored by McBreen *et al.* in a series of studies using reflectance-absorbance infrared spectroscopy measurements, combined with XPS to probe the interactions of aldehydes and alkenes with Mo_2C.[9, 10] Using a polycrystalline foil, the dissociation of a cyclic aldehyde is observed to result in the formation of Mo=O oxo species as well as surface alkylidene species. Subsequent treatment of the surface in propene results in the evolution of metathesis products of the cyclic alkylidene, as well as regenerating the alkylidene active sites in the form of methylidene and propylidene species (see Figure 4.1). The persistence of metathesis with temperature is observed to extend from ca. 100°C– 275°C which is at the upper end of the range reported for metathesis activity over Mo-based catalysts. The results presented are commensurate with the operation of a Chauvin-type mechanism of metathesis.[11, 12]

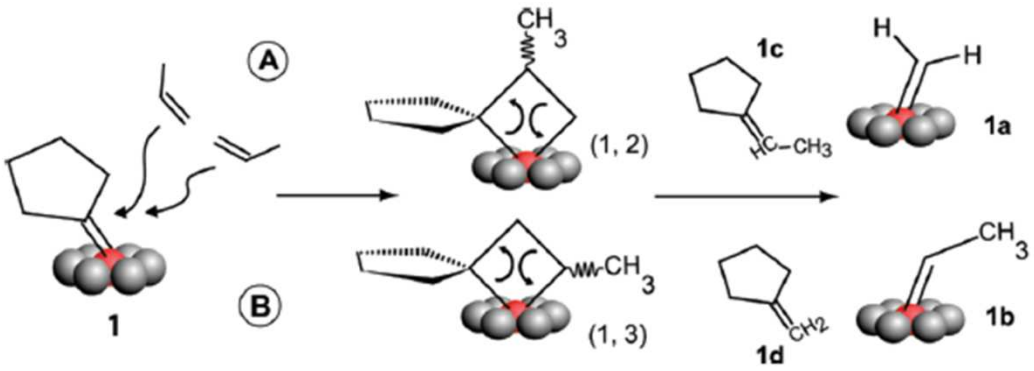

Figure 4.1: The Chauvin mechanism for metathesis shown for propylene attack over a cyclopentylidene functionalised carbene site — reprinted from [9] with the permission of Elsevier.

Tysoe *et al.* observed the metathesis-like behaviour (recombinative hydrocarbon formation) of ethylene and propylene over various Mo surfaces at considerably higher temperatures (323–623°C) than normally applied.[13] In the reaction of ethane over Mo foil, a distribution of products from C1–C6 is observed, which fits a Schulz-Flory distribution. The apparent activation energy for this reaction is observed to be ca. 230 kJ/mol, much higher than the reported 30-40 kJ/mol for low temperature metathesis. The mechanism proposed involves the decomposition of incident alkenes to carbene species followed by the recombination of these species to give a range of products in a similar manner to that proposed for Fischer-Tropsch product formation. In the case of propylene, it is shown that the principle products are; C1, C2 C3 and C4 products. The product distribution could be modeled by a modified Shultz-Flory equation and is commensurate with the recombination of surface methyl carbene species with hydrogen (carbene destruction), another methylidene, ethylidene or propylidene species respectively.

The addition of oxygen to the surface of Mo is observed to have a significant impact on the reactivity. In a further study, MoO_2 is shown to catalyse both low temperature metathesis and recombinative formation of alkenes quite effectively.[14] For temperatures > 375°C, the mechanism is observed to change from a Chauvin metallacyclobutane mechanism to a carbene-polymerisation mechanism, which gives decreasing selectivity to metathesis products with increasing temperature (Figure 4.2).

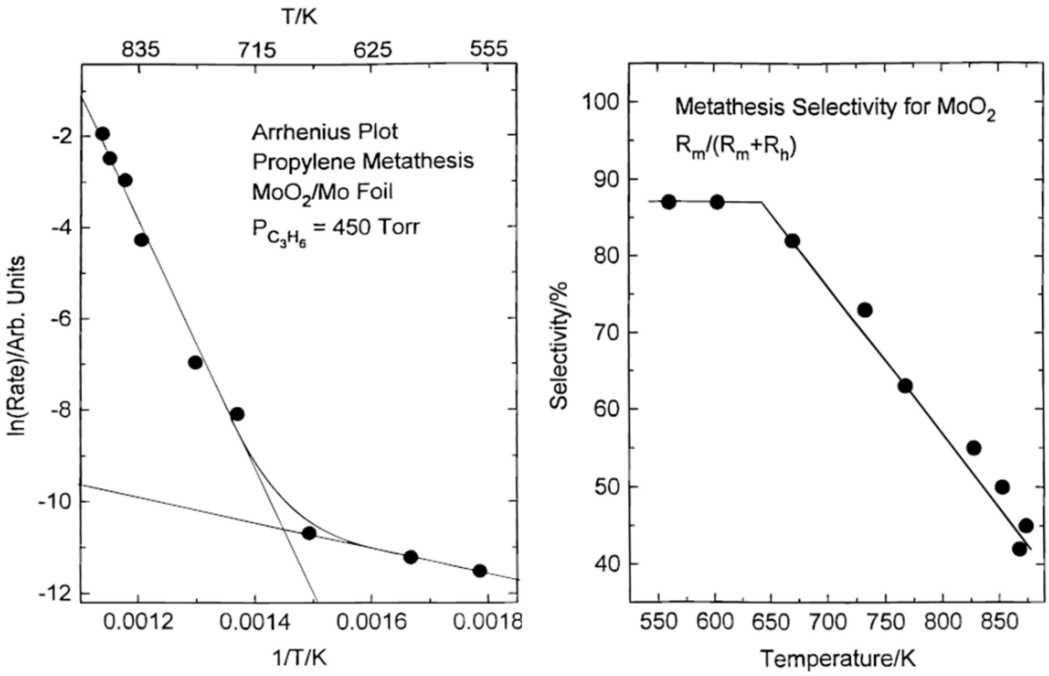

Figure 4.2: Plot illustrating propylene metathesis over MoO_2; two different mechanisms of ethylene/butylene formation depending on temperature — reprinted from [14] with the permission of The American Chemical Society.

4.2.2.3 Bulk spectroscopic Mo_2C studies in alkane transformation reactions

Solymosi *et al.* report the adsorption of propane and propylene on Mo_2C/SiO_2 observed by FTIR spectroscopy.[15] At low temperatures (< RT) propane is observed to bind weakly and reversibly. After treatment at temperatures between 100–300°C the formation σ & π-bonded propylene is observed, and at the highest temperature there is evidence for formation of propylidene moieties. These species are also observed to persist in this temperature range with the co-adsorption of CO_2.[16] Furthermore, it is observed by FTIR and TDS that CO_2 adsorbs irreversibly, dissociating to CO and O on the surface at T > 500°C, which subsequently desorbs at ca. 550°C. Bulk oxidation of the surface is observed to take place slowly at T > 600°C.

In several studies by Rodriguez-Gattorno *et al.* the isomerisation of *n*-heptane over carbon modified MoOx surfaces is discussed with reference the development of a surface carbon layer as observed by Raman spectroscopy and TPO.[17, 18] In this study, pre-reduced MoO_3 is treated at 370°C under *n*-heptane with increasing conversion observed concomitantly with the evolution of the D and G bands of carbon in the

Raman spectra. It is claimed that the evolution of an active Mo-O phase is stabilised by the deposition of more ordered carbon species, which present a higher temperature TPO peak.

4.2.2.4 Transmission electron microscopy studies on Mo_2C and oxycarbide materials

A long-standing discussion related to the interpretation of TEM and XRD data for the characterisation of the 'oxycarbide' phase exists in the literature. First reported by Ledoux *et al*,[19] it is posited to be the active phase in alkane isomerisation. The formation of this phase occurs via an initial low temperature (350–400°C) reduction of MoO_3 under H_2 to partially reduce the structure, which introduces shear planes into the orthorhombic lattice by selectively forming interlayer vacancies (Figure 4.3). This is followed by treatment in flowing hydrocarbon to introduce carbon and stabilise an intermediate MoO_xC_y phase with *fcc* symmetry and lattice parameters of 4.1 ± 0.1 Å.[19-24] This hypothesised structure was later supported by theoretical calculations for a structure of the oxycarbide fitting observed SAED patterns.[24] The cell parameters of the oxycarbide compare closely to those observed for the *fcc* carbide α-MoC_{1-x} (4.24 Å), however it is claimed that the decreased cell parameter is due to the high ratio of oxygen to carbon, which leads to an inversion in the intensities of the principal reflections ((111) & (200)). Moreover, the phase was considered to have superior catalytic properties due to improved geometric constraints and chemopotential that promoted the operation of a metallacyclobutane-type one step mechanism.

In the previously discussed paper by Rodriguez-Gattorno *et al.*, the oxycarbide argument is refuted in favour of a cubic Mo-O active phase.[17] In micrographs obtained from a spent isomerisation catalyst, it is observed that multiple MoO_x phases are present and that *fcc* phase is present and found embedded as small aggregates within the oxide matrix. Based on these TEM observations as well as theoretical calculations, it is postulated that the cubic Mo-O phase is metallic in nature with cell parameter 4.07 Å. In the proposed mechanism, it acts as a centre for the dehydrogenation-hydrogenation, while the isomerisation is carried out via a conventional bifunctional mechanism with the carbocation stabilised by acid MoO_x sites. A similar argument is presented by Matsuda *et al.*[25-27] which is based on the

titration of acid sites on MoO_x. The measurements were determined by ammonia-TPD and 1-propanol dehydration.

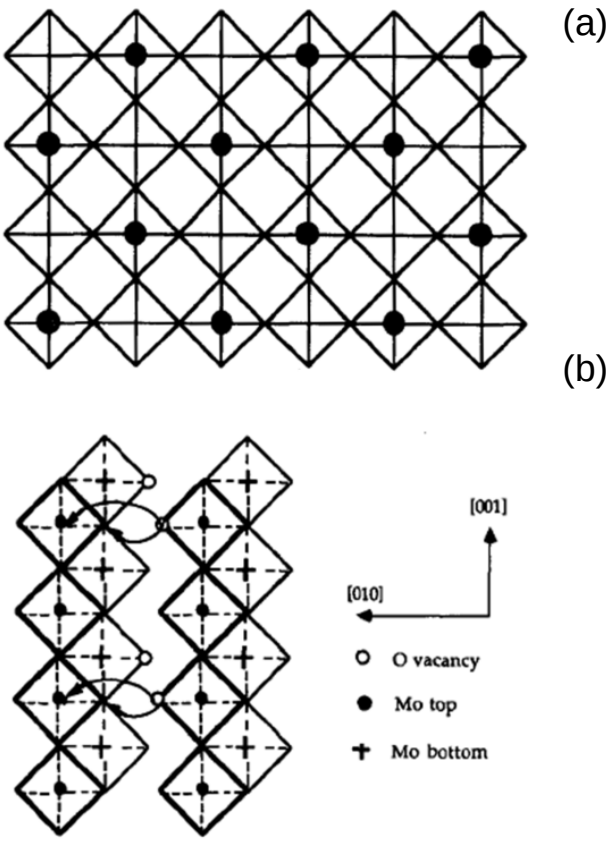

Figure 4.3: Proposed mechanism of formation of a shear plane in α-MoO_3 via: (a) reorganization of the oxygen vacancies in the (010) plane; (b) reorganization of layers in the (100) plane — adapted from [19] with the permission of Elsevier.

In two studies by Schlögl *et al.* the phenomenon of beam-induced transformation is addressed with respect to the MoO_x system.[28, 29] MoO_3 is observed to reductively decompose to an *fcc* MoO structure by a radiolysis enhanced diffusion of oxygen along the layer planes of MoO_3 (Figure 4.4), facilitating the formation of shear structure in an epitaxial process. Energy loss near edge structure (ELNES) spectroscopy supports a one-to-one Mo:O stoichiometry which pre-supposes the Mo-O rock salt-like structure put forward by Rodriguez-Gattorno *et al.* It is also hypothesised that the lack of bulk-structure evidence points to its presence as nano-domains embedded in a larger oxide matrix.

In an interesting study by Green *et al.*, the deactivation of Mo_2C and WC in methane reforming reactions is discussed with specific reference to TEM data attained from post-mortem samples.[30] It was observed in the partial oxidation/steam and dry reforming of methane that the deactivation rate reflected the strength of oxidant: O_2 > $H_2O \approx CO_2$. The initially nanoporous carbides are highly disordered with multiple stacking faults. After reaction, they exhibit an increased structural order with regular crystallites and terraces on which oxygen decorates the step edges. It is claimed that this structural rearrangement is the cause of deactivation via the formation of a kinetically more hindered system..

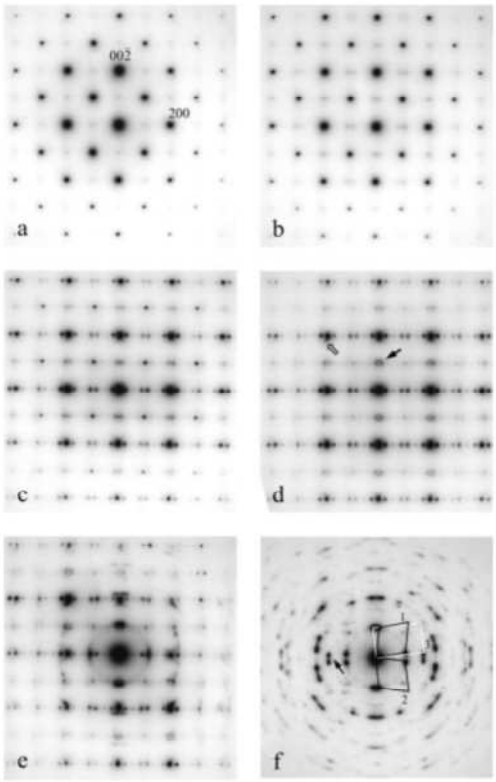

Figure 4.4: 'MoO' cubic phase formed by radiolytic mechanism under electron beam. Reprinted from [29] with the permission of John Wiley and Sons.

4.2.2.5 XPS studies on Mo_2C and reduced Mo systems

There is a great deal of literature relating to photoelectron studies of Mo-based systems. This review aims to narrow the scope to catalytic studies of particular relevance and to studies which present findings pertinent to the accurate assignment and interpretation of peaks in our analyses.

Mo presents a difficult system for analysis by XPS due the large number of potential oxidation states, coupled with a number of more complex physical nuances in the electronic structure found in the intermediate oxidation states. Molybdenum carbide in this sense is a special case and is often referred to as a metalloid having mixed covalent and metallic character. Nemoshkalenko *et al.* determine that the valence band of Mo_2C is made up of two sub-bands of states that participate in metallic bonding and covalent bonding; the latter being exclusive to *p*-electrons, while the metallic character is made up of contributions from the *d*-electron states with some metallic bonding coming from the *p*-electrons.[31]

In the discussion pertaining to Mo metal, it is largely accepted that a reasonable value for the $3d_{5/2}$ binding energy on a clean metal surface is ca. 227.8 ± 0.1 eV.[32-35] Hüfner *et al.* determine the singularity index (relating to the peak asymmetry) for the Mo core lines to be $\alpha = 0.12$[36] and Minni *et al.* determine the FWHM of the metal to be ca. 0.8.[33]

Minni, Stair, McIntyre and others have approached the analysis of intermediate oxidation states of molybdenum with varying results (see Table 4.1).[33-35, 37-42] It can be seen from the overview that the metallic peak assignment is largely agreed upon, as is the assignment for Mo(VI). However, further assignment is less obvious. From the literature pertaining to Mo_2C in particular, the binding energy assignment of 228.2 eV is consistent,[43] and by analogy it can also be considered to be consistent with the Stair model for shifts in the metallic binding energy with increasing oxygen coverage.

Table 4.1: Assignments for Mo3d doublet peaks found in the literature

[a]Mo(IV) is defined in these cases as the unscreened doublet resulting from final state effects

	Mo(0)	Mo(II)	Mo(III)	MoO_2	Mo(IV)[a]	Mo(V)	MoO_3
Minni	227.8			228.7			232.8
Stair	227.7	228.0		229.3			
McIntyre	227.8	228.2		229.2	230.1	231.2	232.7
Olefjord	227.9			229.5	231.1		232.7
Freund	227.7			229.3	230.9		

For the remaining possible oxidation states, the argument can be made that assignment of various peaks must have some physical meaning. From a chemical

consideration, it can be expected that there are only Mo(0), Mo(IV) and Mo(VI). If this is the case, then one must consider the final state effects related to MoO_2 which induce such a complex peak structure. Minni *et al.* ascribe this effect of multiplet peak splitting to the number of unpaired electrons. In MoO_2, the Mo ions have a formal $4d^2$ configuration that favours the 3d-hole-4d-electron interaction which manifests as an observed line-broadening relative to Mo(0). The asymmetry of the Mo(0) and MoO_2 peaks is a direct result of the density of states (DOS) at the Fermi edge, which is high for the conducting oxide. This unusual conduction phenomenon is the result of a characteristic metal-metal dimerisation resulting from a Peierls-type instability.[44-46] The edge-sharing chains of Mo octahedra that make up the structure become distorted by the formation of Mo-Mo pairs (Figure 4.5).[45, 46]

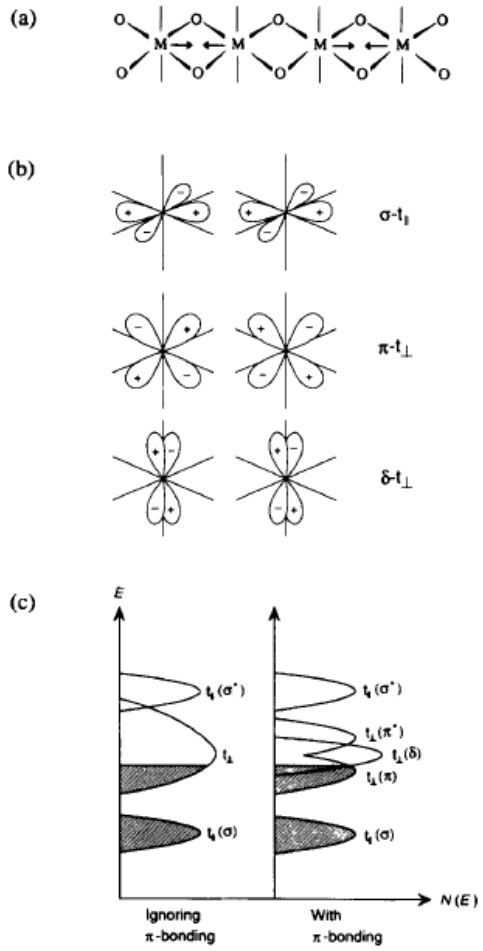

Figure 4.5: (a) Schematic representation of the rutile structure showing the Peierls distortion allowing metallic bonding in MoO_2. (b) origin of orbital overlaps for σ, π & δ states. (c) schematic energy level diagrams for MoO_2 without and with π–π interactions — reprinted from [45] with the permission of The Royal Chemical Society.

This reduction in symmetry results in non-bonding Mo-4d π states that are free to contribute to the Fermi edge. According to Scanlon *et al.*, the resulting spectrum of MoO_2 (Figure 4.6) consists of a pair of doublet peaks at ca. 229.3 and 231 eV. The so called 'screened' peaks at lower binding energies are a result of well-screened final states in which the core hole is filled by an itinerant conduction electron. This is in contrast to the unscreened peaks in which the localised level remains empty. It is proposed that the energy separation between the screened and unscreened $3d_{5/2}$ peaks (1.63 eV) is approximately equal to the plasmon energy loss ,which is measured for MoO_2 by EELS.[45] This interpretation therefore attributes the unscreened peaks to unusually strong plasmon satellite features of MoO_2. The large observed FWHM for this unscreened state is attributed to lifetime broadening characteristic to the final state screening process.

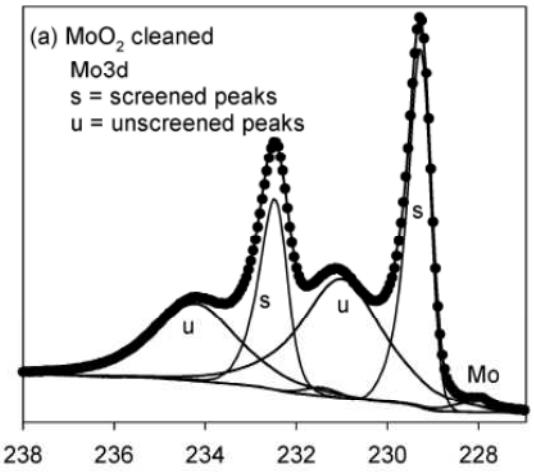

Figure 4.6: MoO_2 multiplet splitting — reprinted from [47] with the permission of the American Chemical Society.

The interpretation of these Mo3d spectra appears to be intrinsically different to that given in much of the catalysis literature. It is noteworthy then to recall the binding energy value given by Minni *et al.* for single crystal MoO_2 – 228.8 eV (Figure 4.7).[33] Here we see that there is a distinct reduction in the unscreened states, which can perhaps be considered an indicator of a highly metallic ordered MoO_2. Hence we see that the assignment of XPS peaks for Mo species is highly variable and dependent on the atomic uniformity of the sample. Mo(IV) may be a chemically valid oxidation state but the observed electronic and physical properties are extremely structure dependent. A structurally well-ordered MoO_2 (or MoO_x for that matter) can give rise

to Peierls-type distortions in the lattice, which results in the freeing up of conduction band electrons. These electrons can subsequently screen the electron hole pair resulting in a large overall decrease in binding energy relative to the oxidation state ($\Delta_{Mo(0)\text{-}Mo(IV)}$ = 1.5 eV *cf.* $\Delta_{Mo(0)\text{-}Mo(VI)}$ = 5 eV).

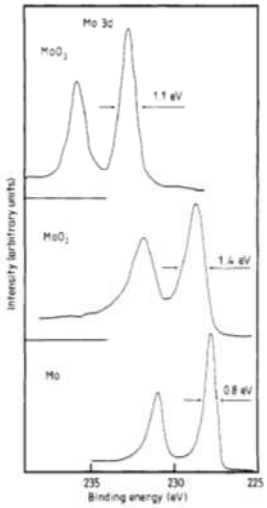

Figure 4.7: Mo3d peak structures — reprinted from [33] with the permission of the Insitute of Physics.

The reason for the subsequent broadening observed for the unscreened peaks is of course very difficult to quantify without good reference spectra or theoretical calculations, but for our purposes may be modeled as a broad doublet, which is acknowledged to contain information on the disordered Mo(IV) species that may or may not be attributed to 'Mo(V)'-type species.

Finally, it should be noted that an important indicator can be obtained from valence band spectra with regards to the observed intensity of Mo(IV) unscreened peaks. An increase in DOS at the Fermi edge indicates a high degree of metallicity of MoO_2 and therefore an increase in the ratio of screened to unscreened peak areas.

4.2.2.6 Notes on Raman fitting for carbon peaks

A recent paper by Sadezky *et al.* outlines a method for the spectral analysis of Raman spectra obtained from carbon samples,[48] particularly pertaining to soot and related carbonaceous materials. The method proposes the decomposition of the spectral features known in spectra of graphite-like materials as 'D' and 'G' bands. It is proposed that the known 'G' band at ca. 1580cm^{-1} , corresponding to the ideal graphitic lattice vibration with E_{2g} symmetry is accompanied by 4 'D' (defect) bands,

which represent varying structural disorder and compositional variation from the ideal lattice. The principal D band is assigned to D1 and appears at 1360cm^{-1} corresponding to a graphitic lattice vibration with A_{1g} symmetry. This peak was supposed to arise from the grapheme layer vibrations in the vicinity of lattice terminations or heteroatom inclusions. A second peak, D2, related to the graphitic lattice vibration modes is found at 1620cm^{-1} as a shoulder on the G band relating to a mode with E_{2g} symmetry and is related to the vibrations of surface graphene layers. The D3 band is assigned to a broad peak at ca. 1500cm^{-1} and is proposed to originate from the amorphous carbon fraction of soot by means of mixed vibrations from organic molecules, fragments and functional groups. The final band, D4, relates to a shoulder commonly found on the D1 peak at ca. 1180cm^{-1} and is attributed to the sp^2-sp^3 stretching vibrations of polyene-like structures. Figure 4.8 is taken from the paper by Sadezky *et al.* and illustrates the band assignments given for the Raman spectra of a diesel soot sample.[48]

Although it is clear that such decomposition of Raman spectra is overly simplistic model for the complexity of carbon materials, it can provide a useful comparative tool for carbonaceous species that have a significant amorphous fraction. For these reasons I have included interpretations of spectra obtained from post-mortem samples to complement data obtained from CHN analyses and EELS-EDX spectra obtained for the catalysts before and after treatment.

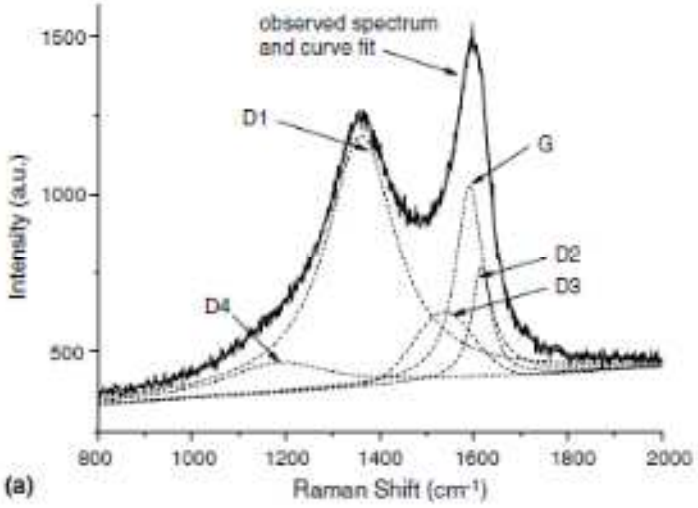

Figure 4.8: The decomposition of Raman D and G bands — reprinted from [48] with the permission of Elsevier.

4.3 Experimental

4.3.1 Raman studies

Raman spectra were obtained for the pre- and post-mortem catalysts with the use of a Horiba Jobin LABRAM microscope. Samples were prepared as pressed wafers (13mm; 1.5T, 2min) or alternatively by flattening a powder sample between two glass slides. All spectra unless otherwise stated were recorded for 60s with the average of 3 accumulations at a magnification of 100X using an MPlan Olympus objective with an aperture value of 0.9. The light sources was a 20mW He-Ne laser with λ = 632.8nm and an observed power density of 3mW at the sample. Calibration of the spectra was carried out by standard comparison with the phonon excitation at 521cm^{-1} observed for Si (111). Spectra were recorded between the ranges of 200 – 1000cm^{-1} (Mo and V oxide peaks) and 1100 – 1800cm^{-1} (carbon D and G band excitations) using a diffraction grating with 1800mm^{-1}. The principal laser line was excluded by the use of a holographic notch filter (± 150cm^{-1}) from Kaiser Optical Systems.

Spectra of carbonaceous species were treated using a peak fitting method for the D and G bands developed by Sadezky *et al.*[48] Integrated peak areas are given only for comparison between samples and for discussion purposes.

Quasi *in situ* Raman spectra were obtained by the use of a custom designed SiO_2 cell which is illustrated in Figure 4.9. For the measurements a pressed wafer (200mg, 3T, 10min) was used which was supported by SiO_2 wool. The design of the cell allowed for the sample to be heated in a tube furnace under reaction conditions (gas flow, temperature, educt analysis by GC) and periodically removed to record Raman spectra through a SiO_2 window (2mm).

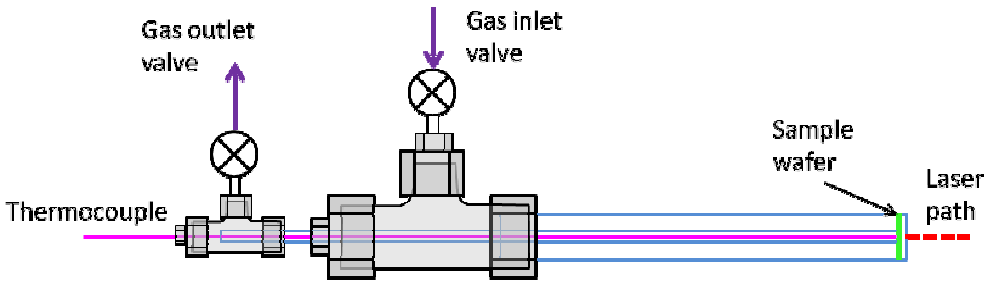

Figure 4.9: *In situ* Raman cell design for the dehydrogenation of propane.

4.3.2 XPS

In situ and *ex situ* X-ray photoelectron spectra were recorded at the ISISS (Innovative Station for In Situ Spectroscopy) beamline at the BESSY (Berliner Elektronspeicherring-Gesellschaft für Synchrotronstrahlung) synchrotron facility in Berlin using the high brilliance X-ray source of the undulator U49/2. All samples were prepared in the glovebox at FHI-AC as pressed powders and mounted on to sapphire sample holders. These were then transferred to the sample chamber without contact to atmosphere using a vacuum transfer apparatus. The sample was mounted ca. 2mm in front of a differentially pumped electrostatic lens system mounted at 55° relative to the incident X-ray beam. The electron lens directed the photoelectron stream to a commercial hemispherical electron analyser (PHOIBOS 150, Spec-GmbH).

For *in situ* measurements, the sample chamber may be maintained at a constant pressure < 5 mbar under flow conditions by the use of leak valves and mass flow controllers. The gas phase composition is monitored by a quadrupole mass spectrometer (Pfeiffer 300) and a Micro-GC from Varian. The sample is heated by a laser, which is incident on the stainless steel backing plate of the sample holder, and the temperature is measured by a type-K thermocouple mounted across the sample surface.

Ex situ spectra were recorded for each of the four fresh $(Mo_{1-x}V_x)_2C$ (8425, 8478, 8447, 8486; x = 0, 0.03, 0.08, 0.11) samples at two positions on each sample. Survey spectra at excitation energies of 1000 and 1010 eV and a step value of 1 eV were acquired to correlate the Auger peaks. To gain depth information, scans were carried out with different excitation energies to collect photons of specific kinetic energies, in this case 150 eV and 600 eV. For each energy range, 10 scans were acquired for the C 1s edge, the O 1s edge, the Mo3d edge and the V 2p edge at a step value of 0.05 eV. The Fermi edge was measured at each energy to correct for charging phenomena. Spectra were treated using SpecsLab™ software for energy adjustment and scaling before exporting to account for variations in peak positions and variable photon flux. Background subtraction (Shirley) and peak fitting was carried out using CasaXPS™ software, and the peak assignments and parameters were made with careful consideration of the literature (to be discussed). Relative surface compositions were

determined by normalising the integrated peak areas with a factor derived from physically measured parameters:

$$Area_{normalised} = \frac{Area}{CS \times (1 + AP \times 0.5065) \times Flux}$$

Where CS is the energy dependent cross-section of the element, AP is the asymmetry parameter, and the Flux is the measured energy-dependent photon flux.

In situ XPS measurements were carried out over Mo_2C (#10000) with the use of a reference material, MoO_2 (Aldrich). The Mo_2C pre-pressed wafer (50mg, 8mm; 1.5T, 5min) was initially measured at the Mo L edge, C K edge and O K edge under UHV conditions for survey purposes. Following this, the sample was reduced in H_2 (0.3mbar, 5sccm) by ramping the temperature at 10°C/min to 600°C and holding for 10 minutes before cooling to a working temperature of 500°C. After reduction, spectra were acquired under flowing H_2 at the Mo L edge, C K edge and O K edge at constant kinetic energies of 200eV and 600eV. Fermi edge spectra were acquired to account for energy shifts. After reduction, the sample was exposed to a flowing reaction atmosphere of $C_3H_8/CO_2/H_2$ (0.3 mbar, 1.25/1.25/2.5 sccm) at 500°C and spectra were continuously acquired at 3 x KE = 200 eV (Mo L edge, C K edge, O K edge, FE Mo & FE O edges) and 1 x KE = 600 eV (Mo L edge, C K edge, O K edge, FE Mo & FE O edges).

The experiment was repeated with a fresh sample under the same conditions of pre-treatment in a C-rich, oxidant-free atmosphere. The conditions applied were under flowing $C_3H_8/He/H_2$ (0.3 mbar, 2.5/1.25/1.25 sccm) at 500°C. Spectra were recorded continuously as in the previous experiment.

4.3.3 TEM

TEM characterisation was carried out for selected samples of the precursor oxides (6600 – *h*-MoO_3, 6697 – h-$Mo_{0.92}V_{0.08}O_3$) as well as the freshly prepared $(Mo_{1-x}V_x)_2C$ carbide series (7484 – Mo_2C, 8447 – $(Mo_{0.92}V_{0.08})_2C$). Post-mortem analysis was carried out for samples that had been treated under C_3H_8/H_2 (11004, 11006, 10996) and for samples from the oxide series that were subjected to temperature-programmed reaction under H_2/C_3H_8 (11196, 11197, 11211).

Using a combination of selected area electron diffraction (SAED), energy dispersive X-ray (EDX) and electron energy loss (EEL) spectroscopies, as well as high angle annular dark field-scanning transmission electron microscopy (HAADF-STEM) and high resolution (HR) microscopy techniques we were able to investigate the local crystal structure, the elemental composition in the bulk, and near surface regions of the material.

Transmission electron microscopy (TEM) investigation was carried out with a Philips CM 200 FEG (Philips, Eindhoven, The Netherlands) TEM-operated at 200 kV and equipped with a Gatan Image Filter (Gatan, Warrendale, PA) and a charge-coupled device (CCD) camera. HAADF-STEM and HRTEM investigations were carried out on a TITAN 80-300 (FEI) equipped with a Cs-corrector.

4.4 Results and discussion

4.4.1 Raman studies of fresh and used catalysts

Raman spectra of the passivated carbide series are shown for the range 1100 – 1800 cm^{-1} (Figure 4.10). The spectra are baseline corrected but show no evidence of bulk C deposition.

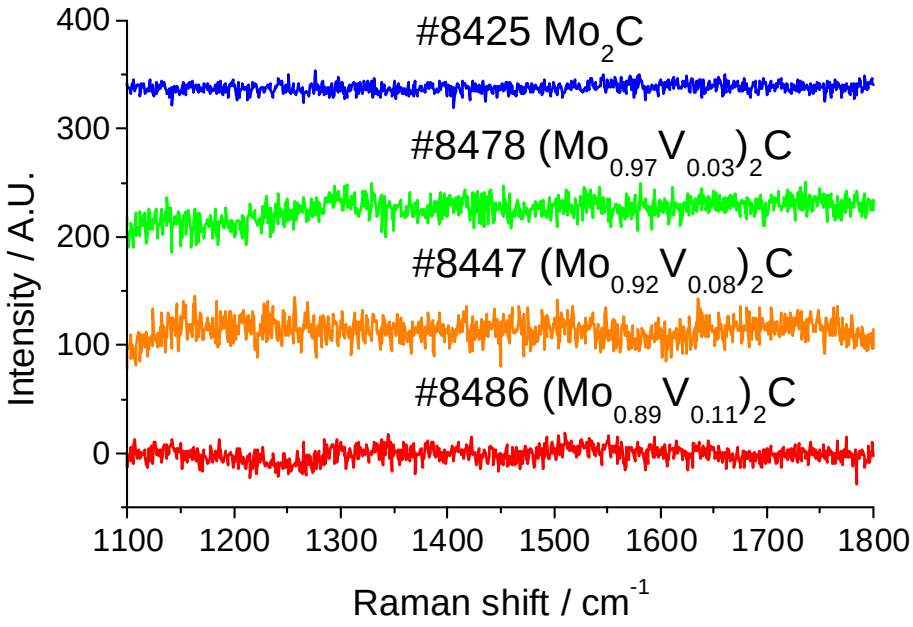

Figure 4.10: Raman spectra of freshly prepared carbides

For Raman spectra recorded in the range 200 – 1100cm^{-1} , it is observed with all carbide samples that there is no initial peak structure and with time under the laser light, broad signals begin to evolve at ca. 800cm^{-1} indicative of Mo=O. However, it is concluded that these peaks are due to the local oxidation of the sample and not due to an oxycarbide overlayer.

Table 4.2: $Mo(V)_2C$ samples treated under C_3/H_2.

Catalyst	Starting material	Phase (XRD)	V/(Mo+V)	Treatment	Temp (°C)	C before (wt.%)	C after wt.%
Mo_2C	8425	Mo_2C	0	H_2/C_3H_8	550	5.2	9.2
Mo_2C	8478	Mo_2C	0.03	H_2/C_3H_8	550	5.2	10.7
$(MoV)_2C$	8447	Mo_2C	0.08	H_2/C_3H_8	550	5.1	9.7
Mo_2C	8486	Mo_2C	0.11	H_2/C_3H_8	550	5.3	9.2

Figure 4.11 shows the normalised Raman spectra of the D and G bands for $(Mo_{1-x}V_x)_2C$ samples post-catalytic treatment at 550°C (H_2/C_3H_8 – see Chapter 3). For all samples there appears to be a carbonaceous overlayer, which is reasonably amorphous by consideration of the very broad D and G band overlap. This overlap can be attributed to the contribution of a broad D3 peak which arises due to the combined vibrational intensities of amorphous carbon material. It is possible to determine slight differences throughout the series of $(Mo_{1-x}V_x)_2C$, however it is not practical to carry out comparative analysis due to the uncertainty involved in background subtraction.

A comparison between post-mortem samples was carried out for Mo_2C (9540) that has been treated in H_2/C_3H_8 (DH), $H_2/C_3H_8/H_2O$ (H_2O-DH), $H_2/C_3H_8/CO_2$ (CO_2-DH) and H_2/CO_2 (RWGS). The spectra show that the samples treated under propane have gained an overlayer of carbon as seen in Figure 4.12. The samples show an increasing level of amorphous character in the order: 9965 < 9990 < 9886. The samples treated under CO_2 and H_2O (9965 & 9990) show a significant increase in graphitic character *cf*. 9886, which was treated under C_3H_8 only (Figures 4.12 & 4.13)

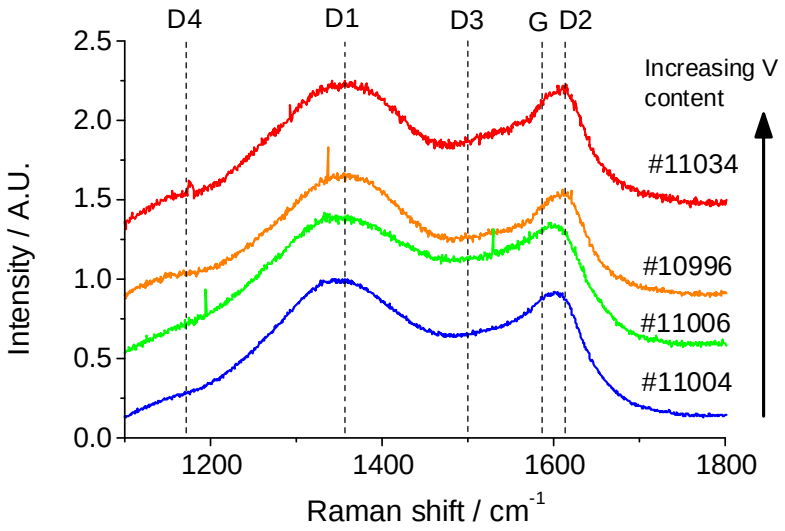

Figure 4.11: Raman spectra of Mo_2C after treatment in C_3H_8/H_2 at 550°C.

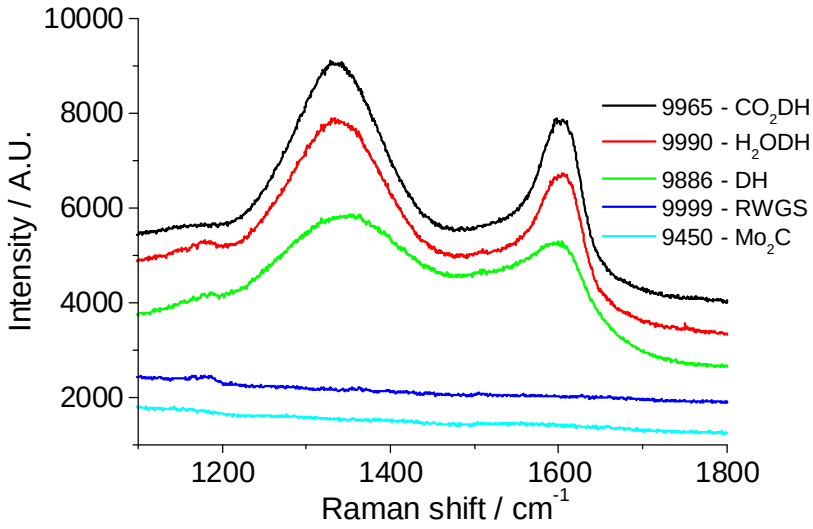

Figure 4.12: Raman spectra of Mo_2C after treatment under various atmospheres at 550°C.

We can speculate that the formation of carbonaceous species on each surface is either the result of differing formation mechanisms or the increase in graphiticity is due the preferential destruction of more reactive disordered carbon under the influence of steam or CO_2. It is interesting to note that the carbide treated under the influence of CO_2 exhibits a higher degree of graphitic character than the sample treated under H_2O despite the similarity in oxidising potential of CO_2 vs. H_2O.[49, 50] From the spectra it would appear that the sample treated under RWGS conditions (9999) shows no

deposition of carbon, with the exception of what may be a peak at ca. 1180cm^{-1}. CHN analysis confirms that there is minimal carbon deposition over the course of reaction (Table 4.2)

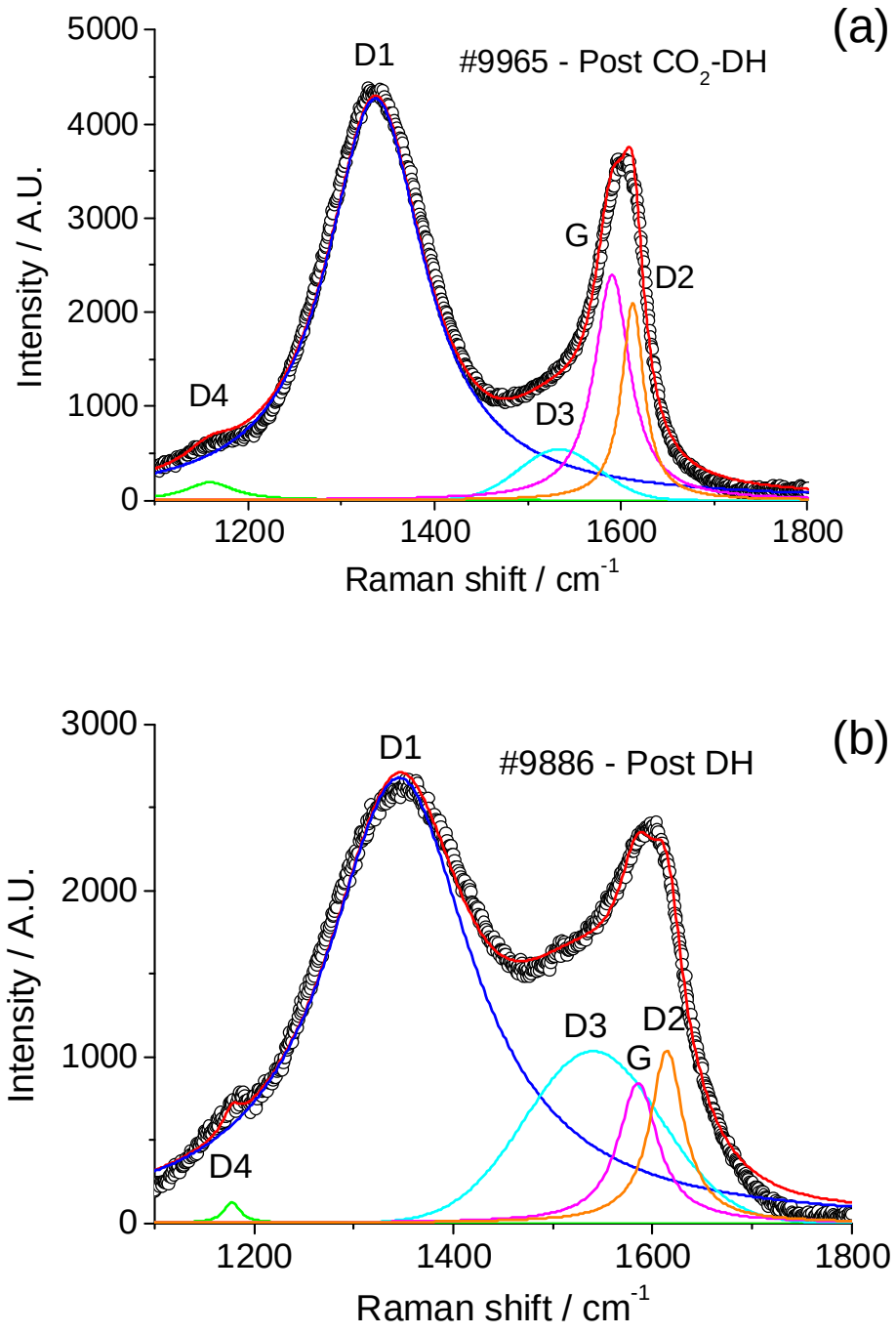

Figure 4.13: Raman spectra showing D and G band peak fitting for Mo_2C treated under: (a) $C_3H_8/H_2/CO_2$, (b) $C_3H_8/H_2/N_2$ at 550°C.

Table 4.3: Carbon deposition over Mo_2C in various atmospheres at 550°C.

	9965	9990	9886	9999
Precursor	9450	9450	9450	9450
Phase	Mo_2C	Mo_2C	Mo_2C	Mo_2C
Pretreatment	$H_2/CO_2/C_3H_8$	$H_2/H_2O/C_3H_8$	H_2/C_3H_8	H_2/CO_2
Temp. (°C)	550	550	550	550
C content (%)	7.7	8.2	8.5	5.7
D1 position	1336	1339	1346	-
D1 Area	70	71	70	-
D1 FWHM	128	145	195	-
D2 position	1613	1616	1612	-
D2 Area	8	8	11	-
D2 FWHM	29	33	52	-
D3 position	1534	1538	1531	-
D3 Area	5	6	12	-
D3 FWHM	101	99	141	-
D4 position	1159	1171	1170	-
D4 Area	2	2	1	-
D4 FWHM	63	49	41	-
G position	1590	1593	1578	-
G Area	15	13	6	-
G FWHM	46	48	55	-

4.4.2 In situ Raman

In situ Raman spectroscopy was used to evaluate the real-time deposition of carbon on the surface of Mo_2C during reaction under H_2/C_3H_8 and $H_2/CO_2/C_3H_8$. In both cases it was observed that the deposition of surface carbon correlated with a strong deactivation of the hydrogenolysis reaction pathway. In Figure 4.14(a) it can be seen that the relative formation rates of C_2H_4 and C_3H_6 remain constant over 20h reaction time, whereas the formation rate of CH_4 and C_2H_6 decays exponentially over time to less than 25% of initial activity within 4h. Simultaneously, it can be observed in the Raman spectra (Figure 4.14b) that the D and G bands associated with carbon deposition are already formed within two hours of beginning the reaction.

It is reasonable to assume that the hydrogenolysis reactions are correlated with the mechanism of carbon deposition on the surface of the catalyst, and that the initially high activity is reduced by blocking of the hydrogenolysis sites by carbon. In contrast, it is observed that the dehydrogenation of C3H8 → C3H6 remains relatively constant implying that the catalytic sites active for dehydrogenation are not those sites that facilitate hydrogenolysis.

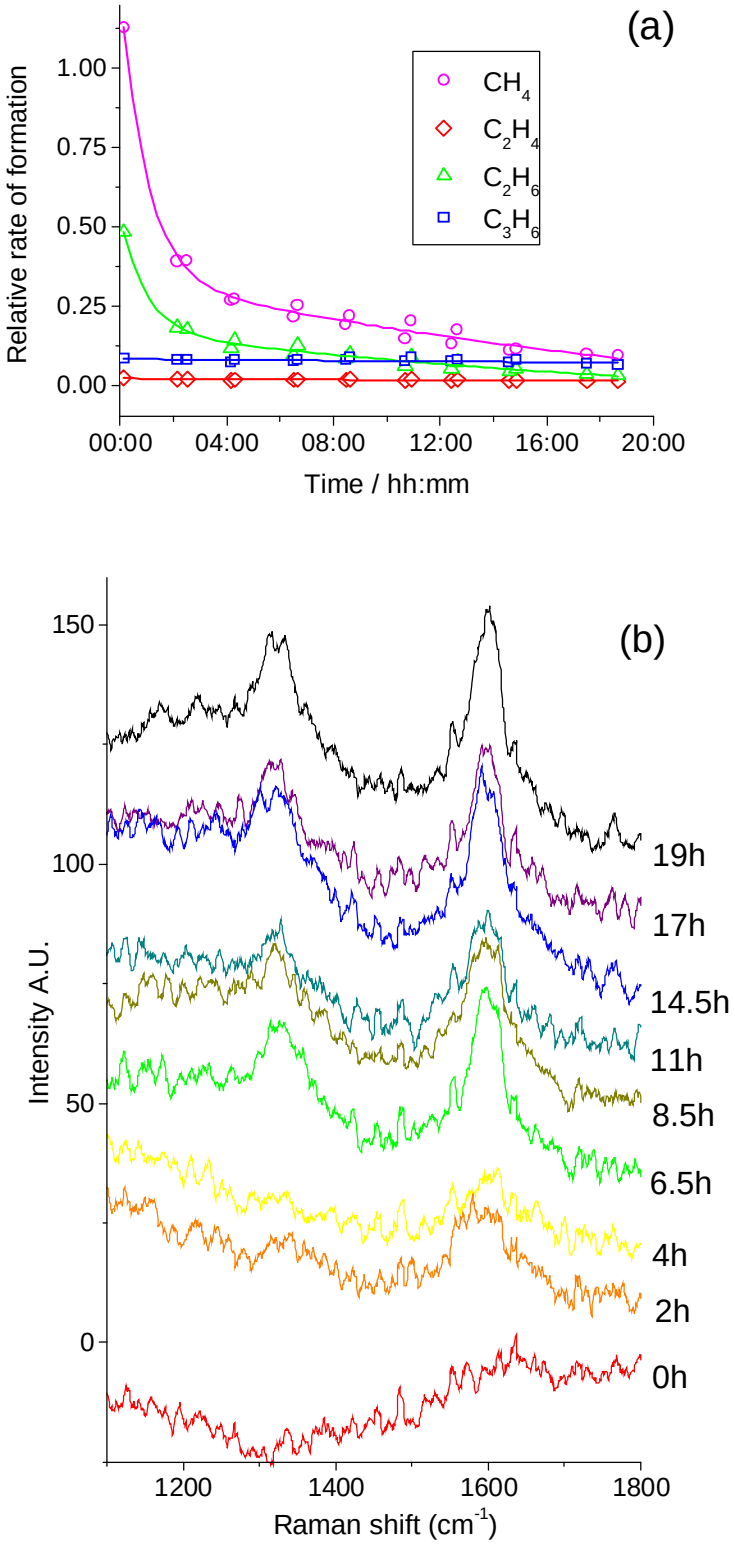

Figure 4.14: *In situ* Raman experiment. Figure (a): relative product formation rates over time; (b) Raman spectra showing evolution of D and G bands from carbon deposition. T = 500°C, $C_3H_8/H_2/N_2$ = 20/55/25, total flow = 20 sccm.

4.4.3 XPS studies

4.4.3.1 Ex situ XPS of MoV carbide catalysts

Ex situ analysis of a series of 4 catalysts of the form $(Mo_{1-x}V_x)_2C$ was carried out at the ISISS beamline at BESSY. The freshly carburised samples were transferred to the sample chamber without contact to atmosphere to examine the surface of the carbide materials without pre-treatment. In Figure 4.15, the Mo 3d edge is shown at two different kinetic energies – 150 eV and 600 eV – corresponding to an information depth of approximately 1nm and 2nm respectively (according to the 'universal curve' – Figure 4.16).[51] The peaks were assigned following careful consideration of the literature for Mo_2C and Mo metal and MoO_2.

For the freshly carburised samples, there is no observation of metallic Mo (227.8 eV) under the conditions applied. Instead, a doublet is observed with $3d_{5/2}$ peak centred at 228.2 eV, which is assigned to Mo_2C and is found to be self-consistent throughout all the analyses. In the absence of any literature or reference materials, these peaks are modeled with mixed Gaussian-Lorentzian (30:70) functions and are found to have a reasonable FWHM (0.4 - 0.8). The next doublet has $3d_{5/2}$ peak centred at BE = 228.8 eV and is fitted with asymmetric peak function comprised of a Doniach-Sunjic/GL convolution. This peak is assigned tentatively to a molybdenum oxycarbide species, which is supported by the findings of Otani *et al.*[4] It is observed in a single crystal study of $Mo_2C(0001)$ that the partially oxidized surface exhibits an enhanced DOS at the Fermi edge that persists at temperatures < 523°C. This metallic MoOC doublet peak is accompanied by a broad doublet with $3d_{5/2}$ centred at ca. 231 eV, which is assigned to the unscreened MoOC peak, a catch-all state which accounts for shake-up and final state effects. The final doublet (in the case of KE = 150 eV) has a $3d_{5/2}$ centred at 232.7 eV and is assigned to the Mo(VI) oxidation state.

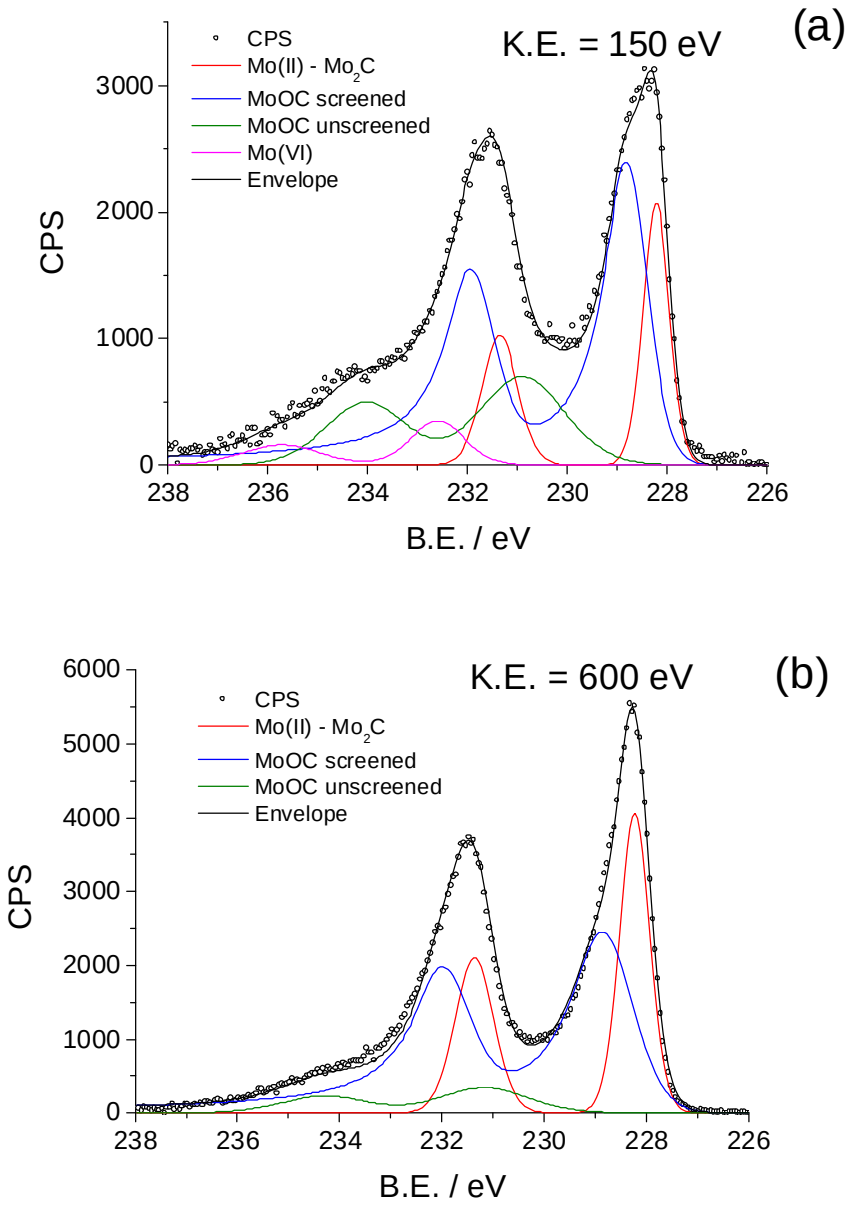

Figure 4.15: Mo3d XP spectra of as prepared Mo_2C (#8425) at: (a) 200 eV kinetic energy; (b) 600eV kinetic energy.

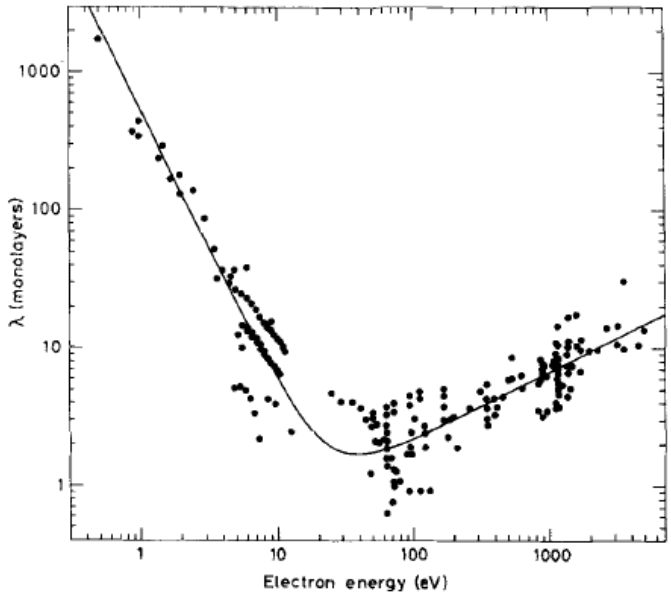

Figure 4.16: The 'Universal Curve' for determining the inelastic mean free path of electrons through a solid — reprinted from [51] with the permission of John Wiley and Sons.

Figure 4.15 illustrates the Mo3d peak fitting comparison for the freshly prepared Mo_2C sample (#8425). It can be seen from the observed fits that the surface of the carbide is rich in oxygen but remains in an overall reduction state below MoO_2. The spectra taken at higher kinetic energy indicate that the subsurface is mostly carbidic. C1s spectra of the carbides series shown in Figure 4.17 show two distinct maxima at ca. B.E. = 285 eV and B.E. = 283.3 ± 0.1 eV,which relate to surface carbon (C-C, C-H) and carbidic carbon (Mo-C), respectively. The spectra recorded with K.E. 150 and 600 eV indicate that the surface is dominated by adventitious carbon with respect to the lower surface, and that with increasing V-content there is a larger contribution from free carbon species at the surface and in the subsurface. It is also observed that the carbidic component of the C1s spectra is shifted by ca. 0.3-0.4 eV, which could be attributed to a contribution of VC (B.E. = 282.2 eV), however, the shift is within a margin of error.

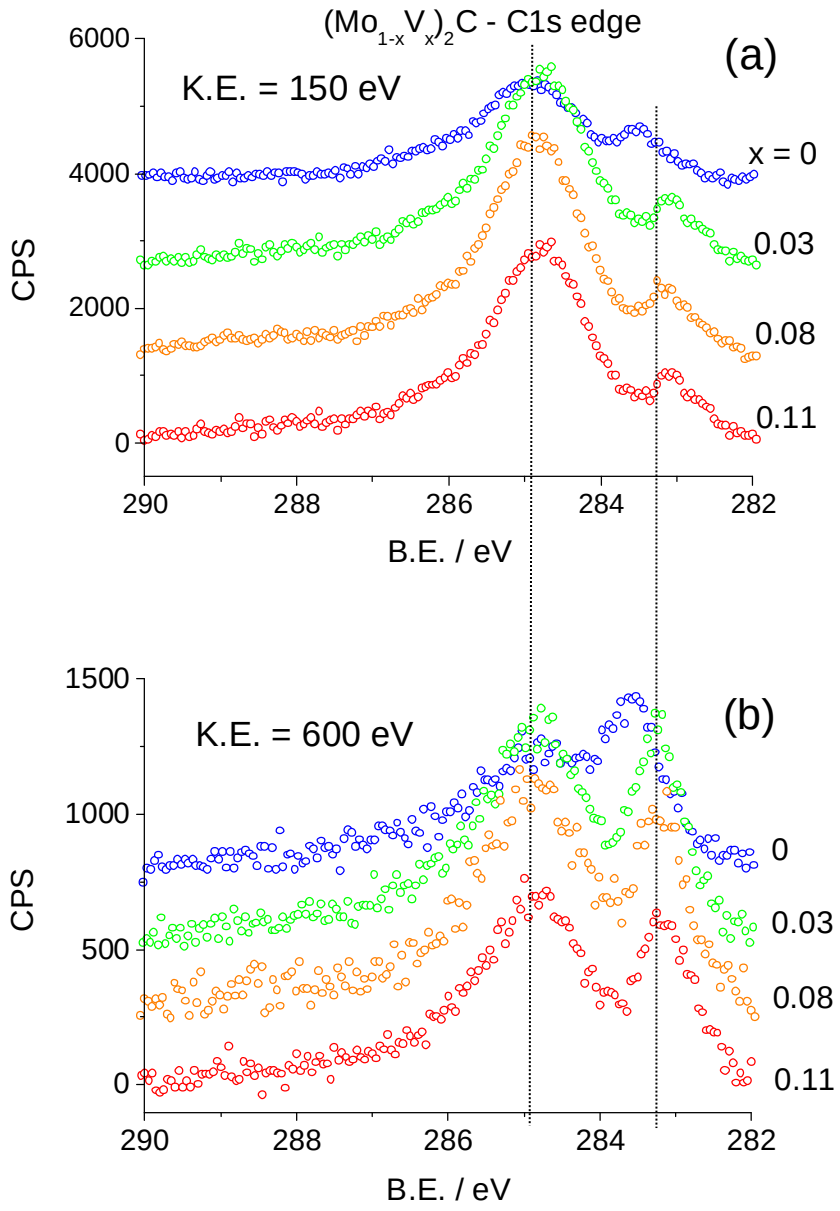

Figure 4.17: C1s spectra of $(Mo_{1-x}V_x)_2C$ at (a) 150 eV (b) 600 eV.

Quantification of the surface composition with respect to the observed Mo content (Figure 4.18) shows an increasing surface fraction of oxygen and carbon species with increasing bulk vanadium content. In Figure 4.18a, it appears that the immediate surface layer is highly enriched in V as well (V/Mo ≈ 0.5 for #8486-11Vc). At higher energies (K.E. 600 eV) the concentration of vanadium is more reflective of the measured bulk value, however, an increase in subsurface carbon is observed in comparison to the undoped Mo_2C. These observations suggest that the formation of the carbide has either resulted in mobilisation of the V atoms towards the surface or

that the initial growth of dislocation defects proceed preferentially along V-rich seams in the precursor lattice.

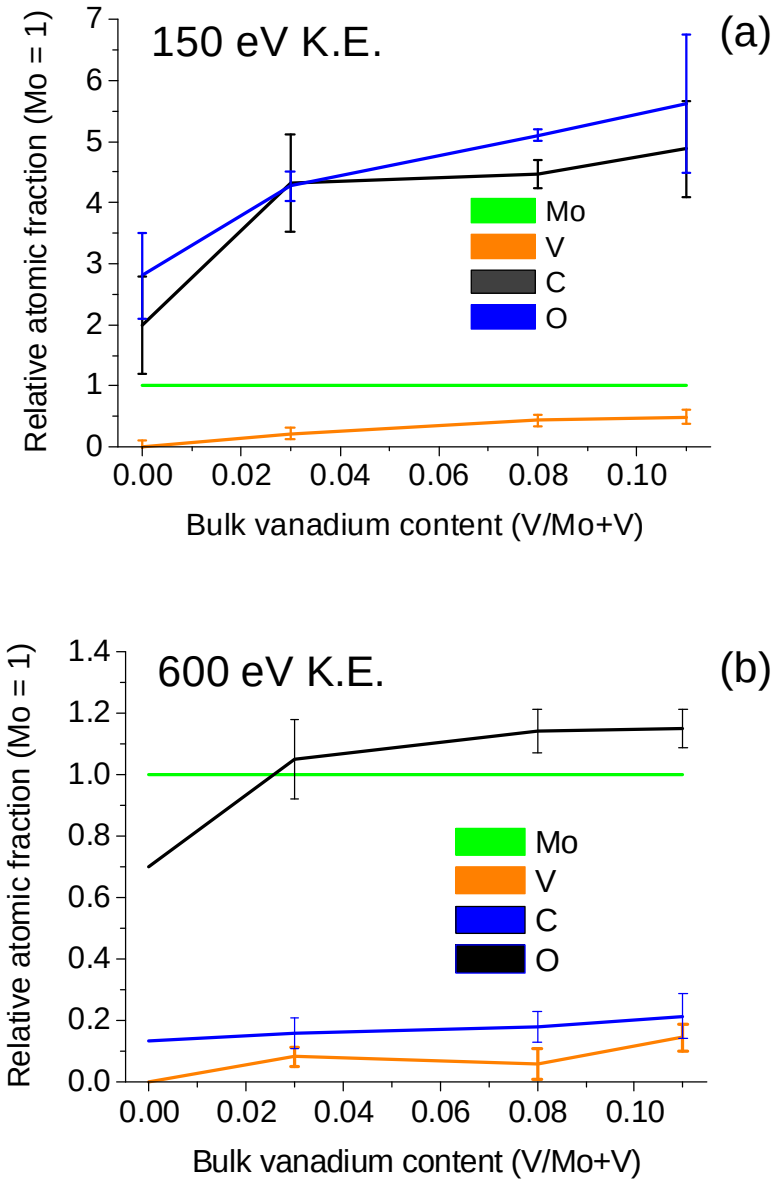

Figure 4.18: Variation of surface composition of freshly prepared carbide with respect to vanadium content.

The quality of the V2p spectra obtained (Figure 4.19) are not sufficient for a detailed fitting procedure, but a qualitative analysis of the general features indicates that the primary structure consists of a broad doublet centred at $3d_{5/2} \approx 515.8$ eV. Comparison with energies reported in the literature suggests that the V atom is in a reduced oxidation state such as found in V_2O_3.[52] However, inspection of the peak edge at lower binding energies suggests the contribution of a more reduced phase, such as a

carbide/nitride as well. By comparison with a study carried out by Freund *et al.*[53] the vanadium peak can tentatively be assigned to a V=O –like compound. The presence of vanadium as vanadyl species in the structure is also seen in EEL spectra obtained in the following TEM study. This is not unexpected when one considers the high temperatures (ca. 900°C) required to form VC by TPR-carburisation.[54]

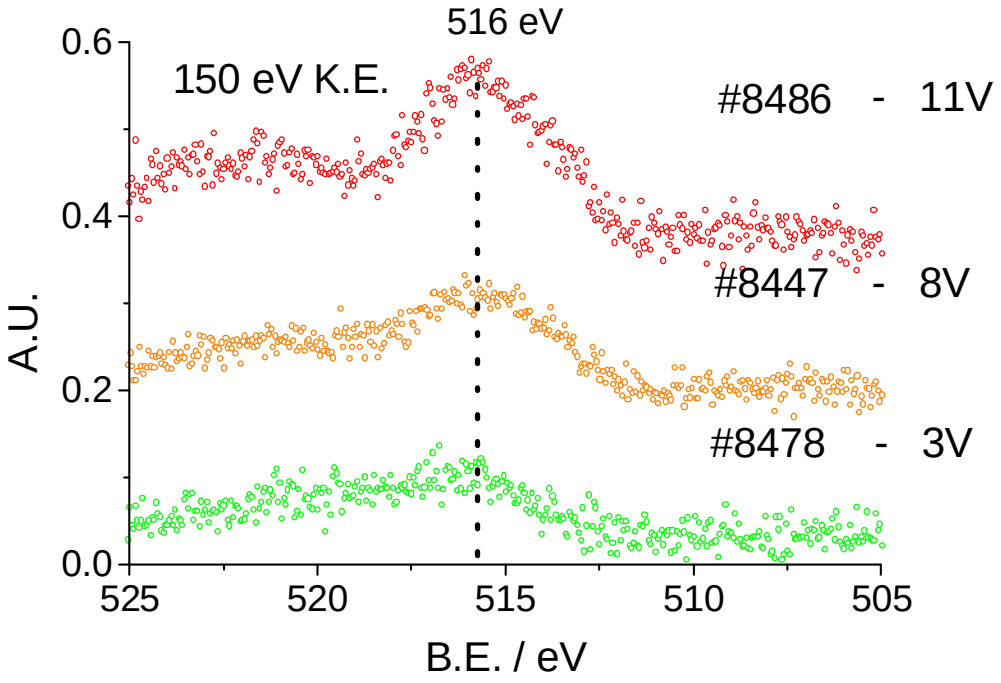

Figure 4.19: V2p edge of $(Mo_{1-x}V_x)_2C$ catalysts.

4.4.3.2 In situ XPS

In situ XPS analysis was carried out at the ISISS beamline at BESSY. The sample investigated was pressed to form wafers and subsequently recarburised before mounting in sapphire sample holders.

For the first experiment, the spectra recorded before and after H_2 pre-treatment can be seen in Figure 4.20. The main observed difference is in the C1s spectra where it can be seen that the peak at 285 eV relating to aliphatic carbon is vanishing. This loss of surface carbon could account for the decrease in intensity for the O1s edge around 531 eV from C=O species. The peak at B.E. = 283.3 eV can be assigned to the carbidic species. As a result of the double-carburisation, the Mo3d edge of the initial sample shows little change after H_2 treatment at 600°C.

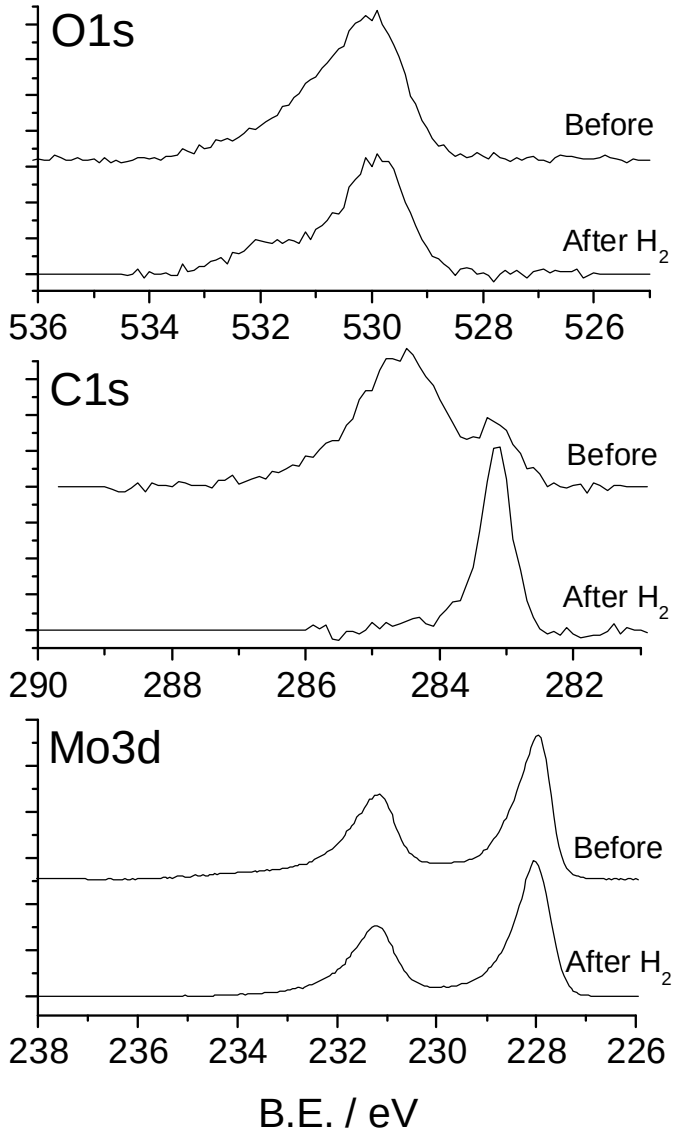

Figure 4.20: *In situ* XPS of Mo_2C before and after H2 treatment recorded at KE = 200eV.

Product formation was observed during the course of reaction under $C_3H_8/CO_2/H_2$. This was in keeping with the observed reactivity from plug flow experiments outlined in Chapter 3. Due to the nature of the analytics, not all reaction products could be seen by GC. For instance, it was observed that the H_2 concentration strongly distorted some peaks such as C_3H_6 preventing their accurate detection. However, it was possible to measure peaks for CO, CO_2 and C_2H_4, which correlates strongly to the evolution of C_3H_6 as a dehydrogenation product. Thus, it is observed in Figure 4.21(a) that the initial rate of formation of C_2H_4 decreases inversely to the rate of CO formation via reverse water-gas-shift. The initial increase in r(CO) coincides with a decrease in the O1s peak (Figure 4.21(b); red → green). The next spectrum at t =

14:12 (green → blue) decreases slightly as the r(CO) appears to level off. After some time, the rate of CO formation has decreased and the O1s peak has regained its original intensity. The Mo3d and C1s peaks are characteristic of the reduced Mo_2C throughout.

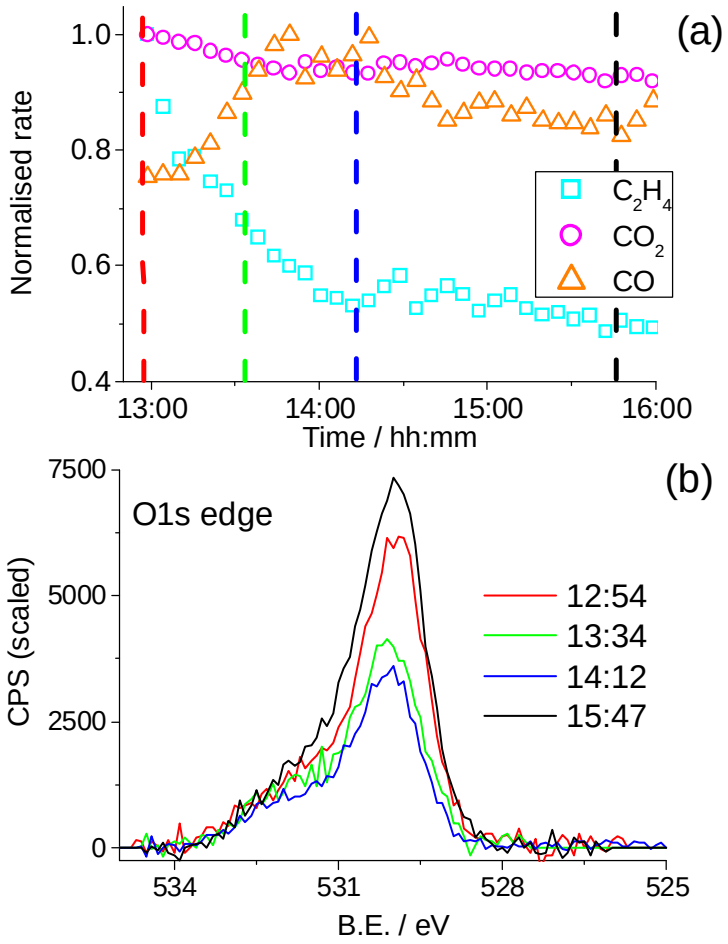

Figure 4.21: *In situ* XPS of Mo_2C (#10000) — (a) normalised product formation rate over time on stream under $H_2/C_3H_8/CO_2$ (2:1:1); (b) evolution of O1s peak with time on stream.

Due to the relatively high partial pressure of H_2 the carbide remains in a reduced form despite the oxidising CO_2. This observation supports the theory that an oxygen-moderated carbide phase is more active for the dehydrogenation of alkanes. It is also interesting to note that there is no observed bulk change during the RWGS. It is expected in this case that the overall degree of reduction influences the rate of CO formation via the dissociative adsorption of CO_2 on the oxygen-starved surface.

The second experiment was carried out under a flowing atmosphere of $C_3H_8/He/H_2$ (2:1:1) after a H_2 pre-treatment as described earlier. The original design of the

experiment aimed to study the effect of a rich hydrocarbon stream over the catalyst to observe carbon deposition and propane activation in the absence of oxidising feed. However, during the course of reaction it was observed that the surface of the carbide became progressively oxidised (Figure 4.22). It was finally determined that the oxidation of the sample was not due to external influences (i.e. leak) but came about from the mobilisation of residual oxygen in carbide migrating to the surface. This was observed for this reaction and not for the previous reaction, because the relative concentration of hydrogen was half of that used previously and below the critical concentration required to maintain a reduced surface. The resulting slow oxidation coupled with the observed product distributions over time illustrates a picture of surface reactivity with respect to surface oxidation. In Figure 4.22 a selection of the Mo3d spectra recorded *in situ* at K.E. = 200 eV are shown. The peak assignments and positions are outlined in Table 4.4. As has been discussed in the literature review, the reliable and accurate assignment of peaks in such a multiplet structure is very difficult. The complex electronic nature of molybdenum suboxides prevents their exact determination and instead attempts have been made to present a self consistent pattern of fitting for the data that may be gauged against the observed reactivity as monitored by MS and GC.

As is consistent with the literature, metallic (Mo^0) and carbidic (Mo^{II}) peaks have been assigned to $3d_{5/2} \approx 227.8$ and 228.3 eV respectively. Mo^{IV} is divided into two separate species; the metallic, screened peak at $3d_{5/2} \approx 229.3$ eV and a contribution from the unscreened states which accounts which is observed as a very broad doublet with $3d_{5/2} \approx 231$ eV. Finally, a small contribution of intensity observed to at $Mo3d_{5/2} = 232.7$ is attributed to Mo^{VI} but it should be noted that this may also coincide with a shake-up peak of Mo^0 (227.8 + 5.1 eV).[55]

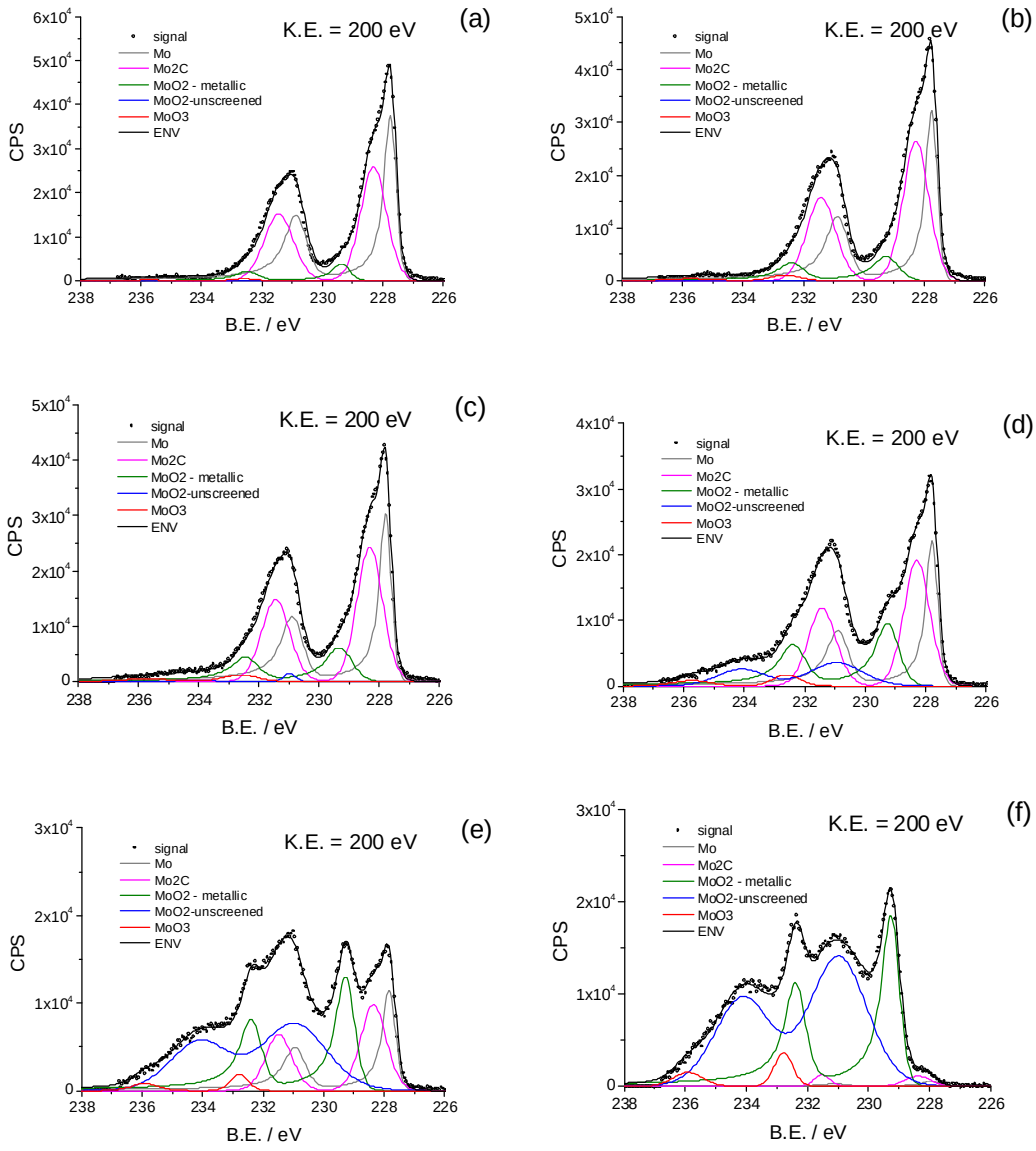

Figure 4.22: *In situ* XPS of Mo_2C - evolution of Mo3d multiplet peak with time on stream under C_3H_8/H_2/He (2:1:1). (a) t = 00:50, (b) t = 01:57, (c) t = 03:21, (d) t = 04:45, (e) t = 05:52, (f) t = 10:41.

Table 4.4: Evolution of Mo3d peak positions (KE = 200eV) over time during in situ XPS in $C_3H_8/H_2/He$.

Run #	Time (hh:mm)	Mo^0	Mo^{II}	Mo^{IV}(S)	Mo^{IV}(U)	Mo^{VI}*
1	0:50	227.77	228.31	229.40	231.20	232.60
2	1:24	227.78	228.28	229.35	230.90	232.60
3	1:57	227.78	228.28	229.31	230.90	232.60
4	2:48	227.78	228.26	229.27	230.94	232.60
5	3:21	227.80	228.31	229.37	230.98	232.60
6	3:54	227.80	228.29	229.35	231.20	232.60
7	4:45	227.81	228.29	229.30	230.95	232.60
8	5:19	227.83	228.29	229.30	231.02	232.87
9	5:52	227.86	228.35	229.31	230.97	232.79
10	6:43	227.84	228.21	229.28	230.94	232.74
11	10:41	228.00	228.39	229.29	230.98	232.78
12	11:12	228.00	228.31	229.25	230.95	232.74
Std dev.		0.08	0.04	0.04	0.10	0.10

The observed changes in surface oxidation are represented by the peak integrals plotted over time (Figure 4.23a). It is observed that the metallic and carbidic character of the surface is slowly oxidised over the first four hours with a steadily growing contribution from Mo^{IV} (screened). At around four hours the oxidative conversion is rapid and results in a large increase in the unscreened Mo^{IV} doublet. The corresponding picture of the surface reactivity is represented in Figure 4.23b. The initial rate of C_3H_6 formation is high and drops as the formation rates of C_2H_4 and C_4H_8 increase rapidly between t = 0 and t = 2h. These recombinative hydrocarbon formation products (C_2H_4 and C_4H_8) are observed to decrease again at t = 5h and t = 4h respectively. From this we can deduce that the oxidation of the surface is detrimental for this mechanism of reaction (alkylidene recombination). Also, because the C_2H_4 deactivates at a later time than the C_4H_8, it is likely that the mechanism of product formation is slightly different for each educt.

If we consider the valence band (VB) spectra recorded during the *in situ* run we can gain some more insight into the mechanism of reaction. In Figure 4.24a the VB spectra are shown for the course of reaction with the final spectra displayed at the front.

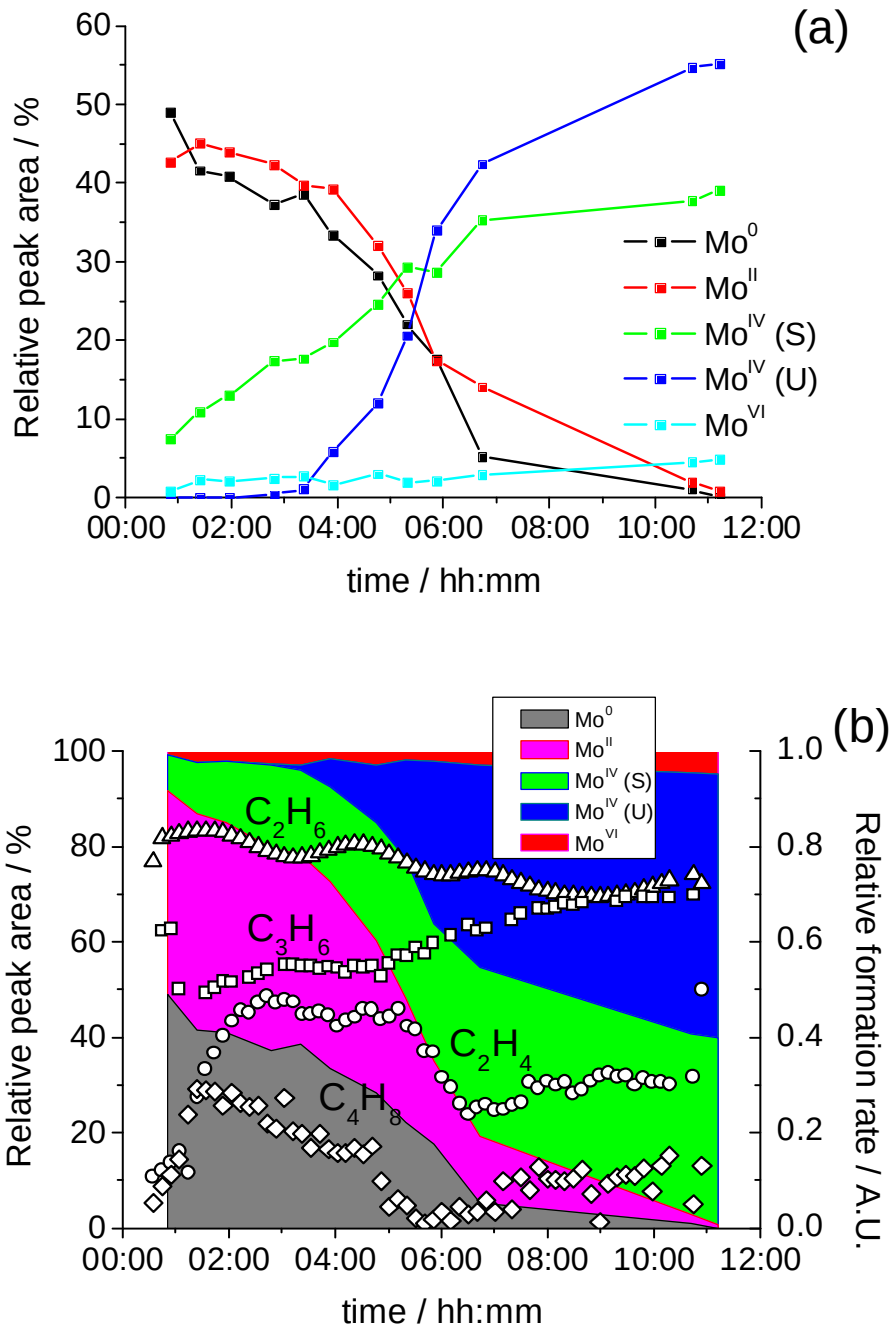

Figure 4.23: *In situ* XPS — (a) Mo species over time as determined by Mo3d peak areas. (b) Stacked area plot of oxidation states overlaid with selected relative product distributions.

It can be seen that throughout the reaction there is a non-zero DOS at the Fermi edge, implying that the system remains metallic in character. However, the VB spectra show a decreasing electronic density at states close to the Fermi edge, and in the final spectra it can be seen that the overlap between the Mo4d and O2p bands is strongly decreased to the point that the bands are almost discrete.

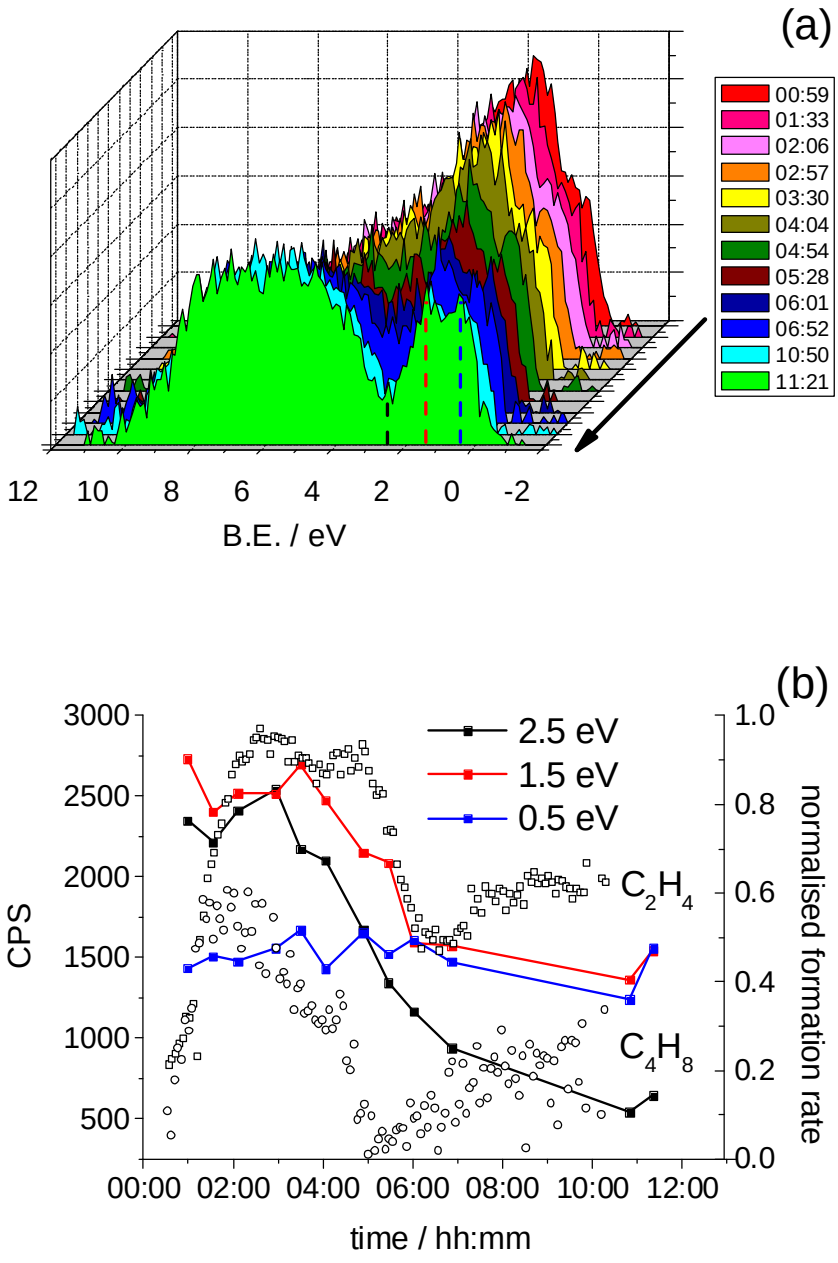

Figure 4.24: ***In situ*** **XPS — (a) valence band spectra of #10000 over time on stream. (b) Plot of cross sections taken from 0.5, 1.5 & 2.5 eV from the Fermi edge compared with normalised rates of C_2H_4 and C_4H_8.**

In Figure 4.24b, a cross-section is taken through the VB spectra at B.E. = 0.5, 1.5 & 2.5 eV to give a picture of electron density at the Fermi edge, the Mo4d state, and at the overlapping region between the 4d and O2p states.

The result is that while the DOS at the Fermi edge (0.5 eV) remains unchanged, the electron density in the Mo4d VB decreases strongly from t = 05:00-06:00 in concert with the observed C_2H_4 formation. Moreover, the separation between the Mo4d and O2p states occurring from t = 04:00, is observed to coincide with the decrease in C_4H_8 formation rate.

4.4.4 TEM study of Mo/V materials after reaction in H_2/C_3H_8

TEM characterisation of the precursor oxides and the prepared carbides is presented in Chapter 2 of this thesis and will only be referenced briefly in this section. The post-mortem studies refer to the $(Mo_{1-x}V_x)_2C$ materials after H_2/C_3H_8 treatment and also to the *h*-$Mo_{1-x}V_xO_3$ after temperature-programmed reaction in H_2/C_3H_8.

4.4.4.1 $(Mo_{1-x}V_x)_2C$ after C_3H_8/H_2

The post-mortem analyses of $(Mo_{1-x}V_x)_2C$ materials using HRTEM after reaction reveal significant changes in both the surface and structural features of the catalysts after reaction. From the HRTEM images, we can observe a variety of morphologies including densely-packed particles as well as porous agglomerates with particle domain sizes 5–15 nm (Figure 4.25). It can be seen by the contrast that in the immediate surface of the particles is a layer of loosely ordered carbon covering the particles. The overall morphology is not significantly different from that observed for the as-prepared carbide, but there appears to mesoporous aspect to the agglomerate structure.

Structurally the changes are more profound. By powder XRD, only *hcp* β-Mo_2C is evident in the diffraction pattern, however, it is observed in the SAED of individual domains that there is also α-MoC_{1-x} present in the sample (Figure 4.26). These cubic sub-domains appear to be integrated within the matrix of the bulk carbide and potentially come about via a high temperature recrystallisation of the surface oxycarbide layer, which was seen to prevail in the XPE spectra of the freshly prepared carbides. This surface restructuring also appears to be more prevalent in the V-containing samples which have a higher concentration of surface oxygen.

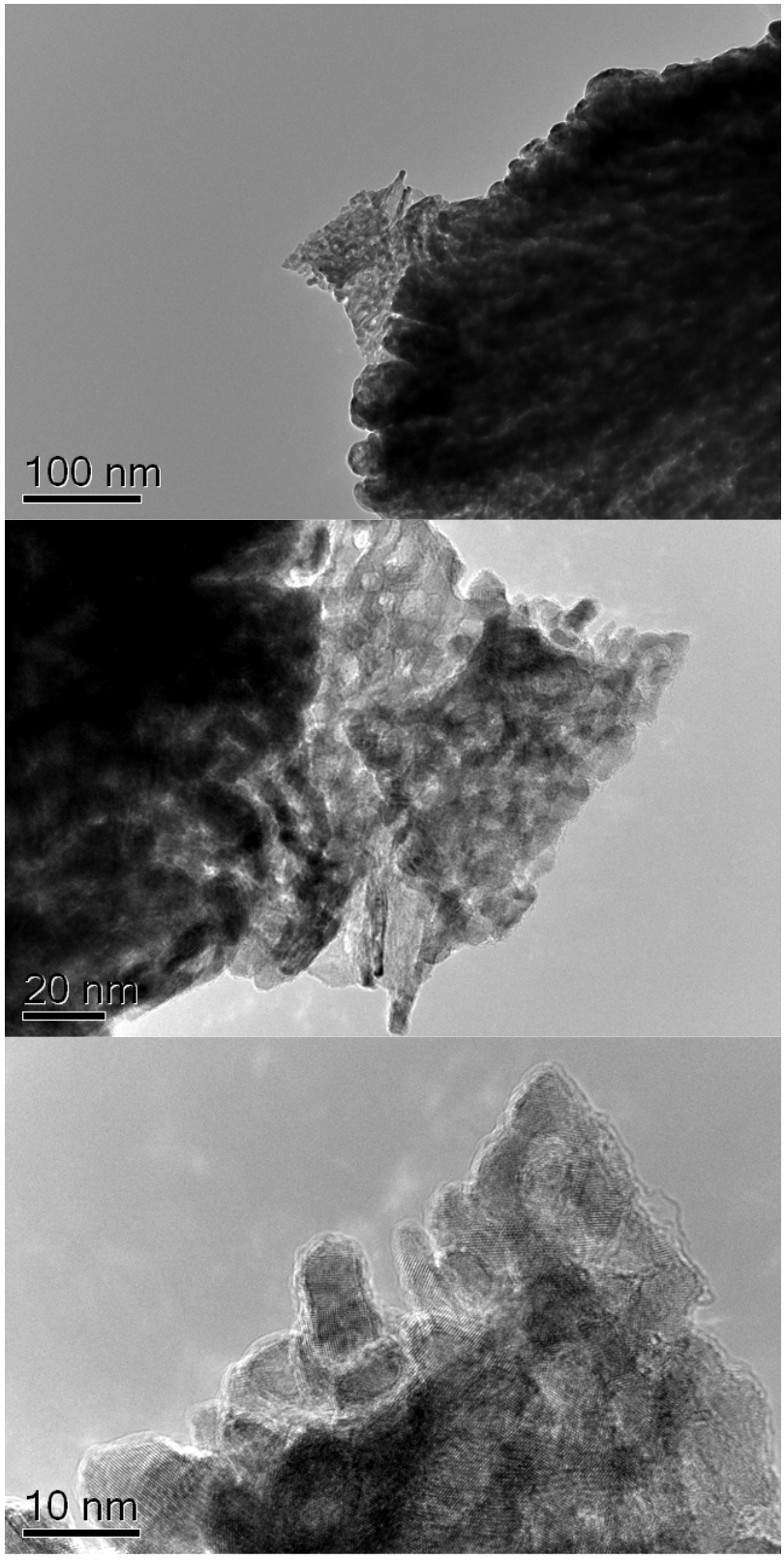

Figure 4.25: TEM images of 11004 — post mortem sample of Mo_2C after H_2/C_3H_8 treatment.

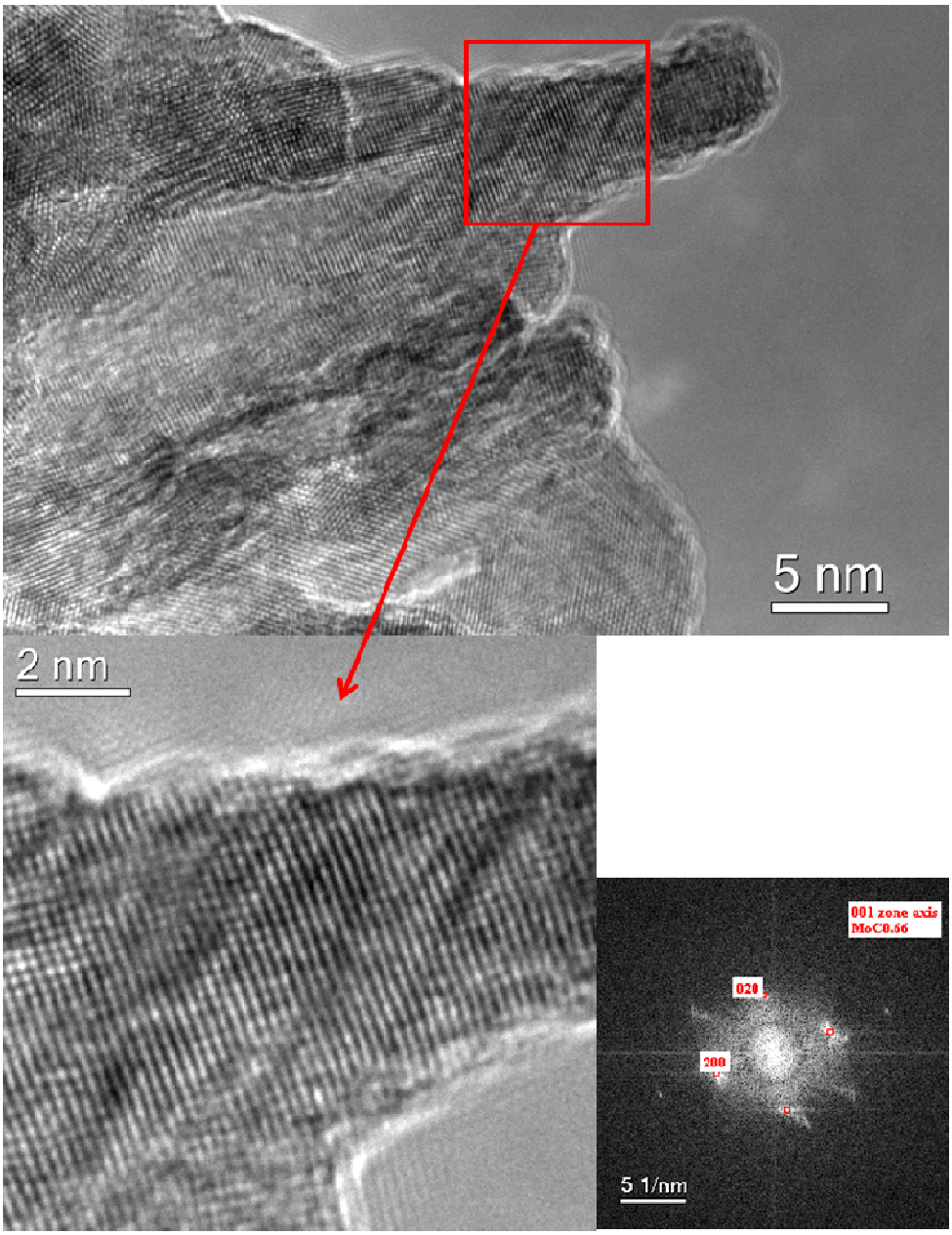

Figure 4.26: SAED of 11004 showing α-MoC_{1-x} phase reconstruction.

Analysis of the local elemental composition by energy-dispersive X-ray (EDX) spectroscopy was carried out for the $Mo(V)_2C$ samples in the microscope. In this case, exact determination of the element ratios was complicated by the fact that a low energy Mo M edge interferes strongly with the carbon K edge which is necessary for quantification. It is observed that the Mo M edge is only sometimes present, which may be due to orientational effects.

Overall, semi-quantitative information can be obtained using sophisticated background subtraction techniques (see above), but the determination of carbon tends

to be under-represented. The carbide samples after reaction, as seen in Figure 4.25 and Figure 4.27, exhibit visible heterogeneity, which is apparent from the EDX spectra. Figure 4.28 shows considerable deviation in the EDX quantification collected at three spots with respect to carbon content. In spot 1, the sample appears to be carbon poor while in spot 3, we can see that the structure is carbon rich. This induced structural and compositional heterogeneity appears to be linked with areas of *fcc* MoC_{1-x} tending to exhibit higher carbon contents. However, it was not deemed worthwhile to collect statistical data given the apparent inhomogenous nature of the material and the difficulty in quantifying spectra.

Electron energy loss spectra (EELS) were obtained for the samples to give information about the chemical states of the elements present in the matrix. As can be seen in Figure 4.29, the Mo M edge is rather broad and has a small feature (M 4,5) at ca. 227 eV and further features visible at 393 and 410 eV (M3 ,M2). A large peak was observed for the C K-edge, which is indicative of the presence of sp^2-bonded carbon that is in agreement with Raman spectra discussed previously. The final feature of note is the doublet peak observed at ca. 515 eV for the V L-edge. As was observed for the *ex situ* XPS the energy range of the $3d^{5/2}$ peak suggests that the vanadium is in a intermediate oxidation state reminiscent of V=O.

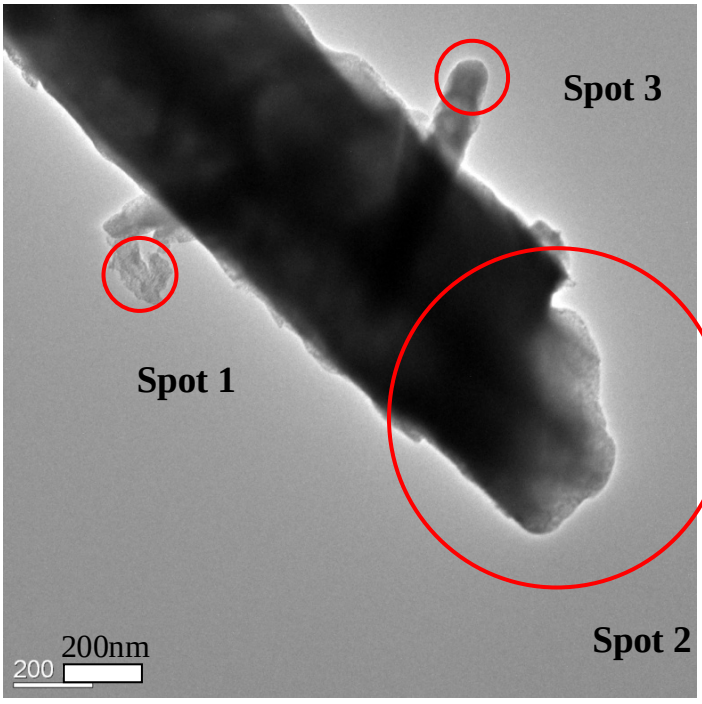

Figure 4.27: TEM micrograph of EDX area for $(Mo_{0.92}V_{0.08})_2C$ (#10996).

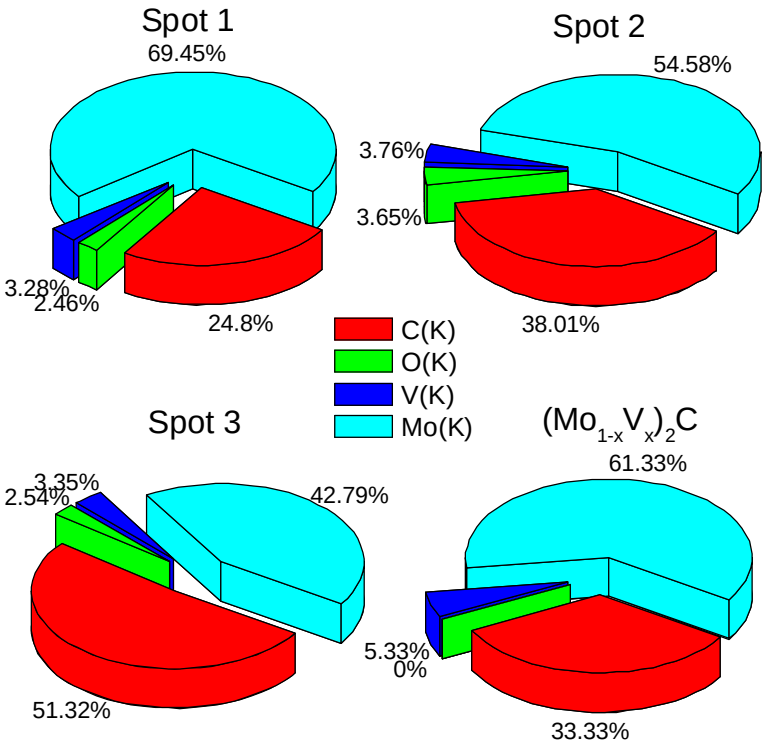

Figure 4.28: Graphic representation of EDX spectra as received for Figure 4.27 with reference.

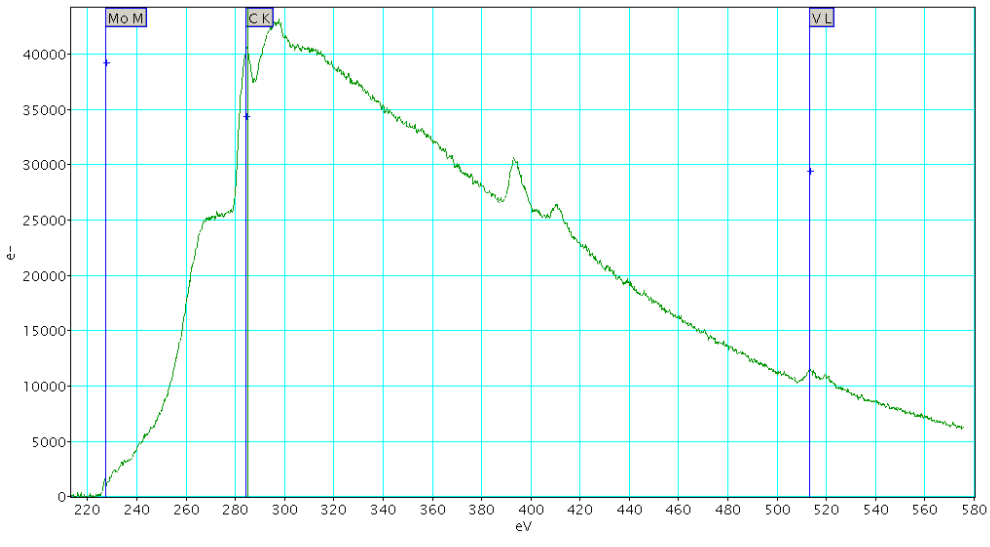

Figure 4.29: EELS spectra of $(Mo_{0.92}V_{0.08})_2C$ (#10996). The major energy edges are assigned to Mo-Medge, C K-edge and V L-edge.

4.4.4.2 h-$Mo_{1-x}V_xO_3$ after C_3H_8/H_2

In contrast to the post-mortem carbides discussed above, the Mo/V oxides were carburised under reaction conditions with propane rather than methane and form preferentially the *fcc* α-MoC_{1-x} carbide phase. As is discussed in the introduction and in Chapter 1, *fcc* α-MoC_{1-x} is a metastable carbide phase and exhibits variable occupancy with respect to C and O. The lattice parameter of a = 4.23 Å is very close to the values between 4.0 – 4.2 Å, which are assigned variously in the literature to the 'MoO_xC_y' and 'MoO' oxycarbide and cubic oxide phases to which it bears remarkable similarity. Overall, the parent morphology of the post-reaction oxides is retained in a pseudomorphic fashion as is observed for the carburisation process. Due to the reported topotactic nature of the transformation $MoO_3 \rightarrow \alpha$-MoC_{1-x} ,the received crystallite domains are very small (typically < 5 nm) and form a mesoporous agglomerated material as seen for sample #11211 in

Figure 4.30. Although it is observed that the sample largely consists of *fcc* α-MoC_{1-x}, it is evident from SAED that there is also *hcp* β-Mo_2C present as well as MoO_2.

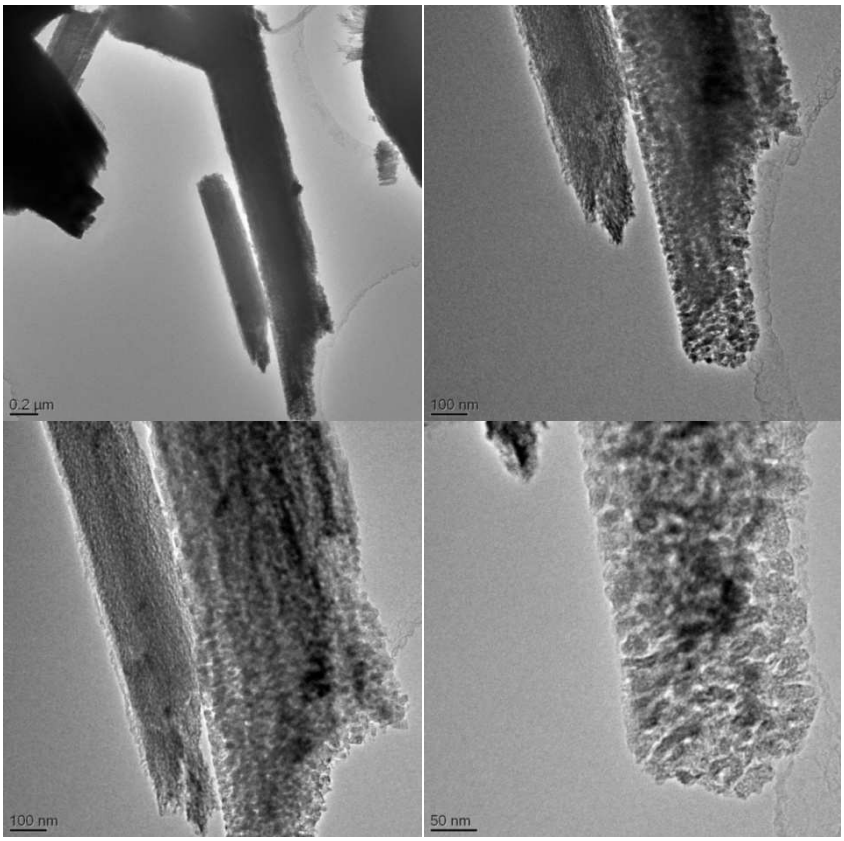

Figure 4.30: Post-TPR *h*-$Mo_{0.89}V_{0.11}O_3$ (#11211) showing pseudomorphism.

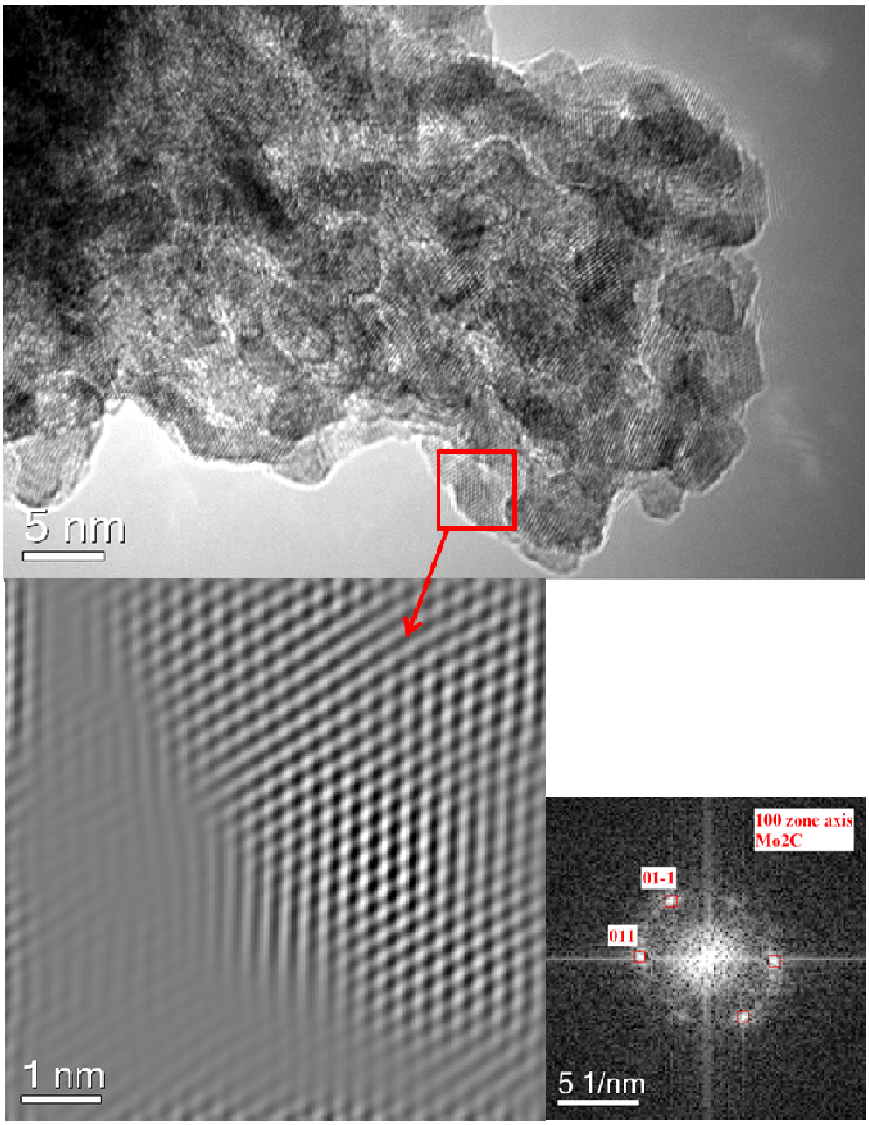

Figure 4.31: SAED of *h*-$Mo_{0.97}V_{0.03}O_3$ (11197) post TPR under H_2/C_3H_8 showing *hcp* carbide phase.

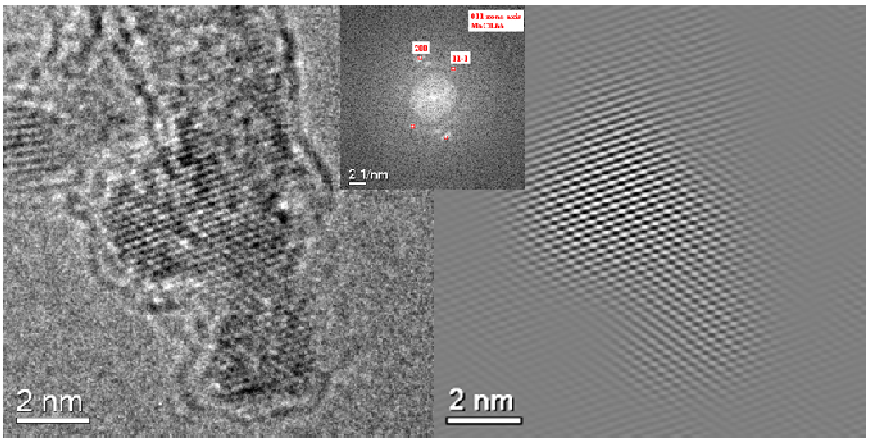

Figure 4.32: SAED of *h*-$Mo_{0.89}V_{0.11}O_3$ (11211) post TPR under H_2/C_3H_8 showing *fcc* carbide phase.

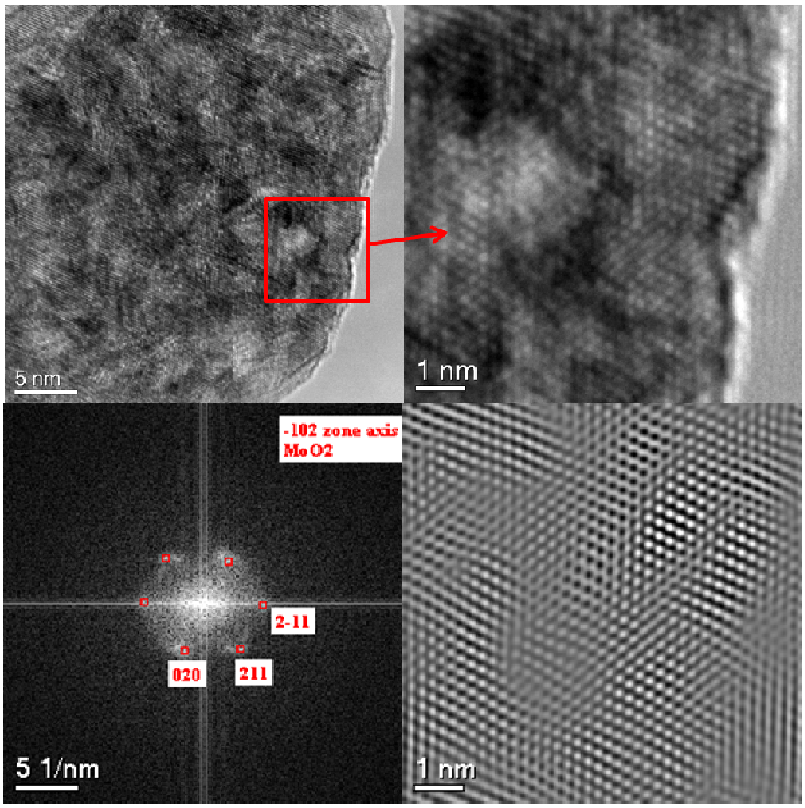

Figure 4.33: SAED of *h*-$Mo_{0.89}V_{0.11}O_3$ (11197) post TPR under H_2/C_3H_8 showing MoO_2 phase.

Figures 4.32–4.34 show SAED patterns indicative of Mo_2C, MoC_{1-x} and MoO_2 structures, exhibiting the dynamic reconstruction of the precursor oxide under rigorous reaction conditions to give various phases. The structural dependency on the reactive hydrocarbon is discussed in Chapter 1 and is clearly illustrated here. Due to the meta-stable nature of the *fcc* α-$MoC_{1-x,}$ the *hcp* carbide may be formed due to excess local heating or is formed concurrently with the cubic phase in local regions due to mass transport limitation of the initial reduction.

It was noted in Chapter 2 that the carburisation of Mo/V precursor oxides resulted in formation of ribbon or fibre-like morphologies in the resultant carbides. This phenomenon is also noted in the case of the TPR of precursor oxides. As can be seen in Figure 4.34, a high aspect-ratio crystallite sits on the edge of the holey carbon film and distinctive ribbon-like features surround a solid core. As was observed for the TPR-carburisation samples in Chapter 2, the fibres run along the length of the (presumable) *c*-axis from the parent oxide.

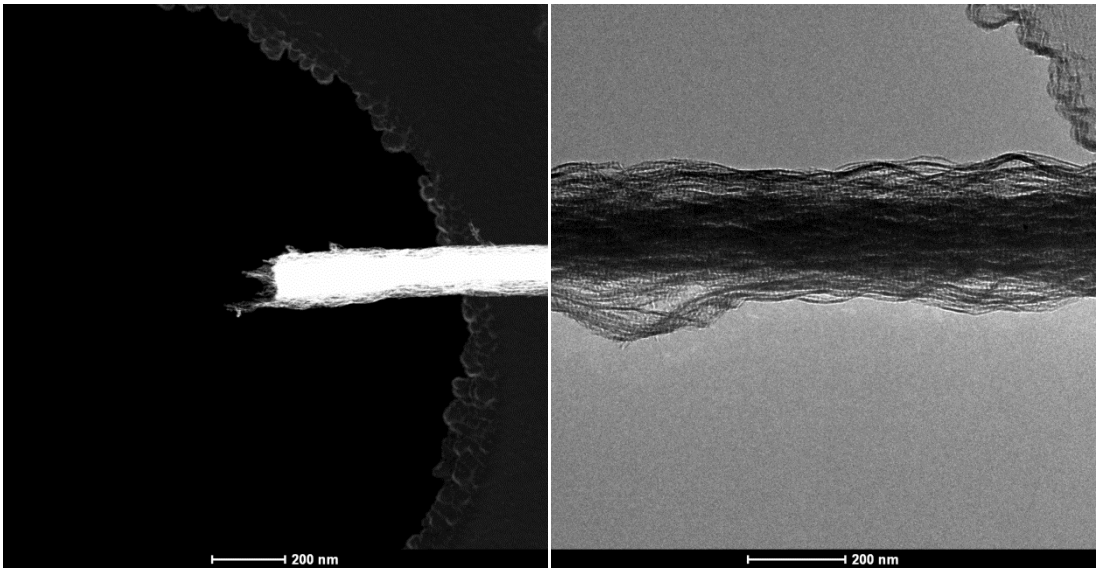

Figure 4.34: (left) STEM-HAADF image of post-TPR *h*-$Mo_{0.89}V_{0.11}O_3$ (#11211) showing fibrous structure. (Right): TEM image of same.

The carbon content of the TPR samples as determined by EDX spectroscopy is observed to be quite high in comparison to the stoichiometric carbide. Due to the highly dislocated nature of the *fcc* structure and higher relative surface area (see Chapter 1 and 3), the post-reaction oxides appear to support higher levels of carbon deposition *cf.* the post-treated Mo_2C samples. In Figure 4.35, EDX spectra taken across a larger particle surrounded by smaller particles shows the smaller particles to be saturated with carbon (70-80 at.%) and it also shows strong variations in the vanadium content. To confirm a suspicion that the variations in vanadium content in this sample (*h*-$Mo_{0.97}V_{0.03}O_3$) originate from the poor statistics/background subtraction for vanadium, the same particle was inspected using STEM-HAADF with element-specific filtering to give an elemental map (Figure 4.36).

As can be seen the elemental distribution across the particle is quite homogenous and as seen in EDX, the particle appears to be saturated with carbon. EELS spectra of the post-TPR oxides (Figure 4.37) show a doublet for the V L-edge with $3p^{3/2}$ centred around ca. 516 eV. Inset in the figure is a reference spectra for V=O which shows a similar excitation energy. This assignment is also in line with the observed oxidation state of vanadium in the prepared and post-reaction Mo/V carbide series.

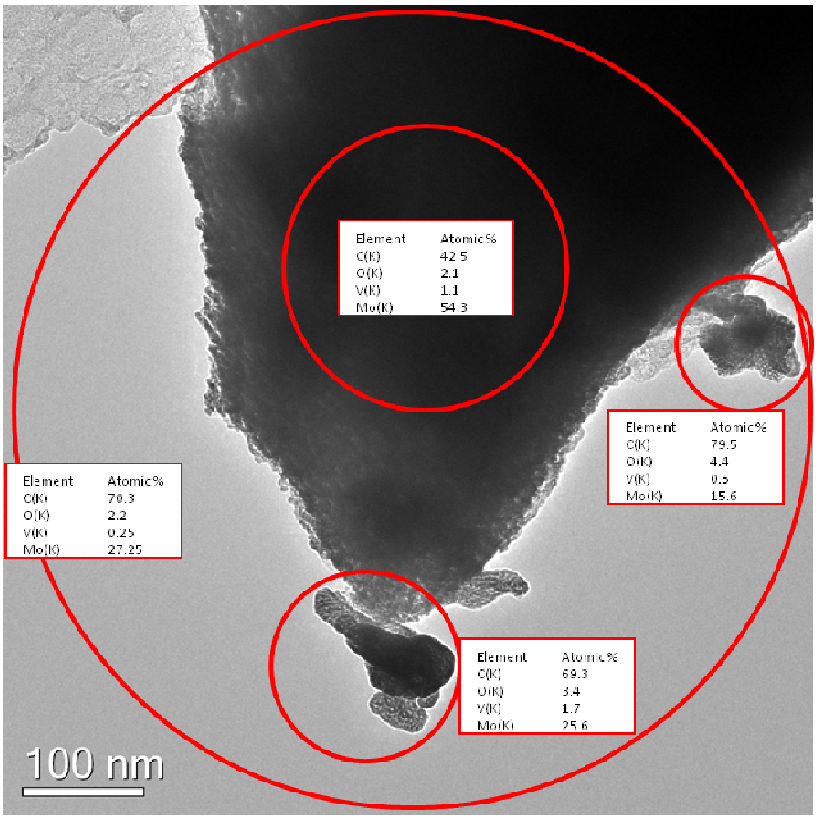

Figure 4.35: EDX spectra of a selected area of post-TPR *h*-$Mo_{0.97}V_{0.03}O_3$ (#11197)

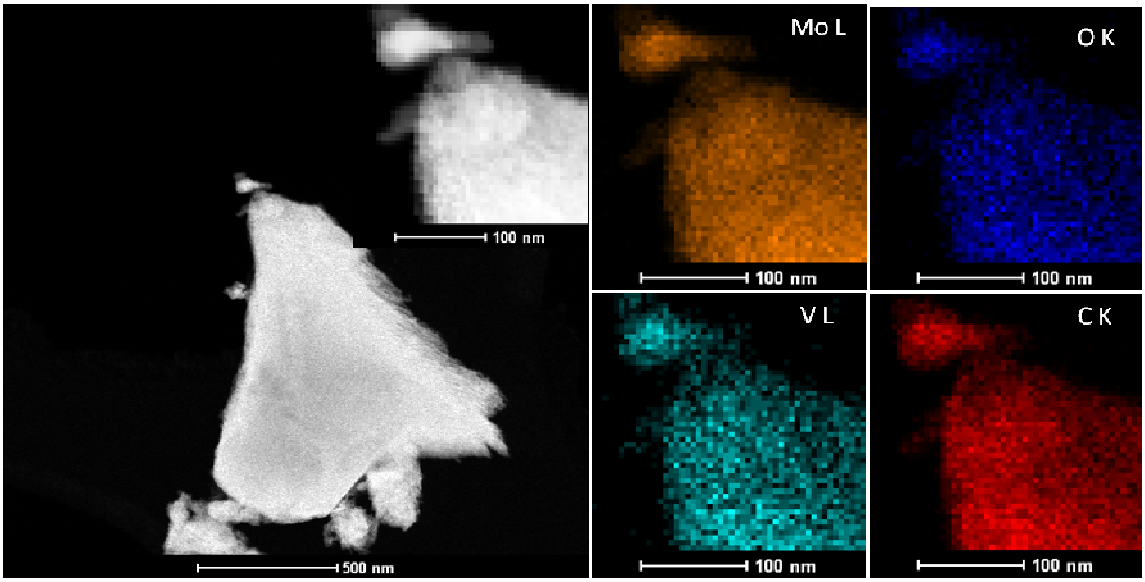

Figure 4.36: STEM-HAADF micrograph of particle in Figure 4.35 (upside down) showing elemental distribution.

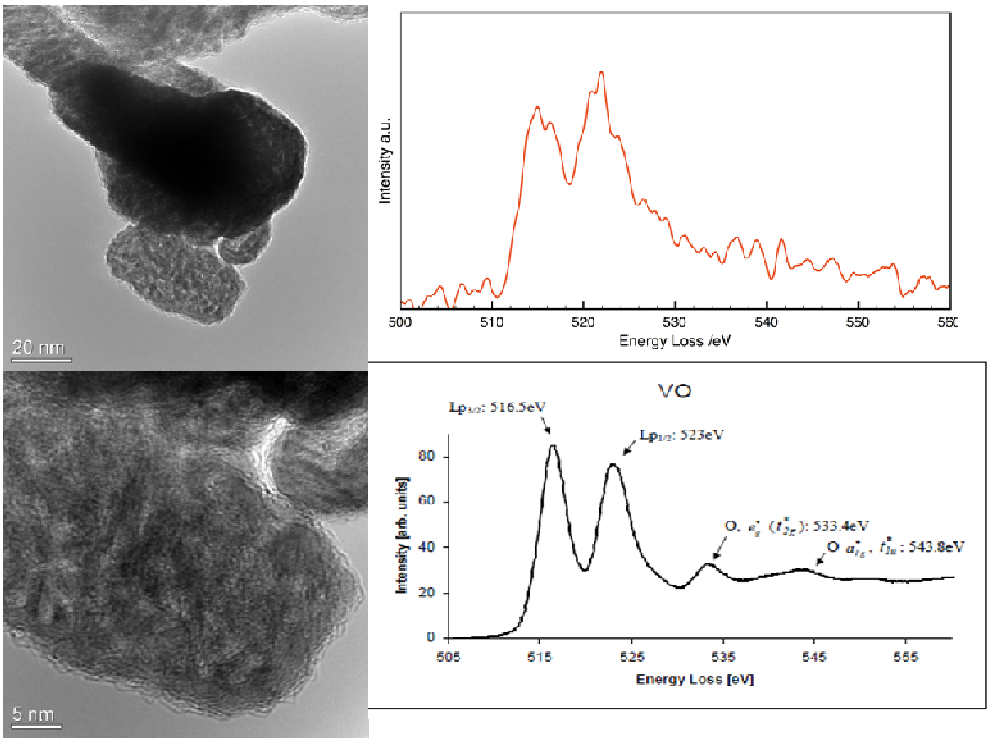

Figure 4.37: Vanadium EELS spectra of post-TPR *h*-$Mo_{0.97}V_{0.03}O_3$ (#11197). Reference EEL spectra in lower right reprinted with the permission of Willinger.[56]

4.5 Discussion

4.5.1 Raman microscopy studies

The use of Raman microscopy for observing freshly carbided surfaces is of limited value due to the absence of spectroscopic information. It was observed in the region 200-1000cm^{-1} that bands began to evolve around 800cm^{-1} with irradiation time, and it is concluded that even at low power, Mo_2C as prepared is beam sensitive.

The principle use of Raman microscopy in this study is to monitor and characterise the deposition of surface carbon following the catalyst's exposure to the reactant atmosphere. In this case, we observe two distinct modes of deposition. In the first instance, the reaction of propane in H_2 over the surface of Mo_2C results in a relatively amorphous carbon with a strong and broad underlying D3 peak at ca. 1500cm^{-1}. As was determined in the previous chapter, this carbon is the result of overactive total hydrogenolysis resulting in the deactivation of the surface by bulk carbon build up.

In contrast, the carbon formed by the treatment of Mo_2C in $H_2/C_3H_8/H_2O$ or $H_2/C_3H_8/CO_2$ is formed under an oxidative environment and total hydrogenolysis of

the propane is not observed. In this case, the carbon is considerably more graphitic in nature. However, more information is required to make an analysis of this mechanism.

4.5.2 XPS studies

It was hoped to gain insight into the coking process by XPS studies. However, throughout all the attempted experiments, there was no observed carbon deposition, likely due to the reduced pressure of the *in situ* XPS at ISISS. Despite the lack of coking, or possibly because of it, we are able to draw a clearer picture of the reactivity of propane over molybdenum carbide/oxycarbide surfaces.

Ex situ XPS results for the as-prepared $Mo(V)_2C$ catalysts show the surface of the carbides to be a relatively disordered array of Mo, C and O (see Figure 4.38). On H_2 activation, the surface carbon is largely removed but resulted in a partially metallic surface.

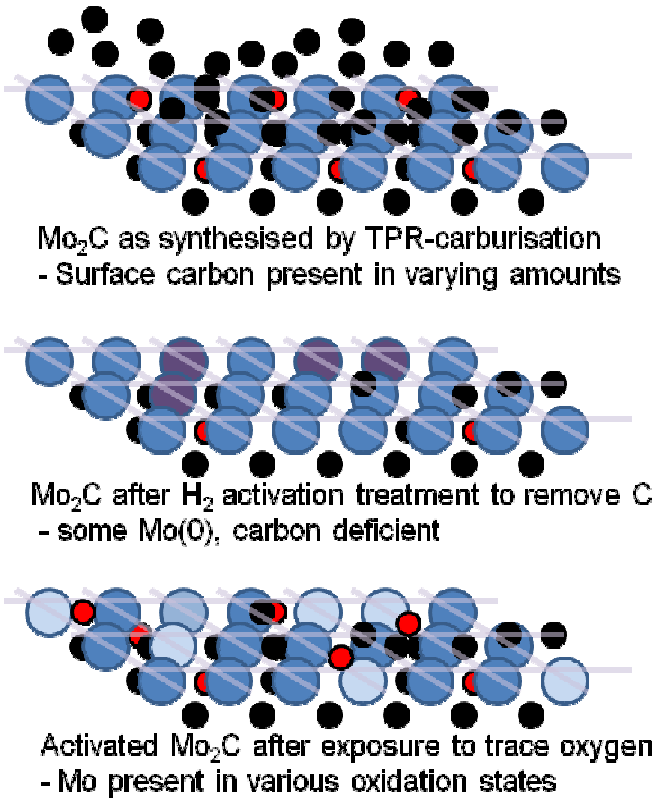

Figure 4.38: Mo_2C surface model.

The inclusion of vanadium is seen to increase the level of surface C and O significantly (Figure 4.18) and it was observed that the surface was enriched in

vanadium relative to the bulk. The increasingly oxy-carbidic nature of the $(Mo_{1-x}V_x)_2C$ surfaces can be attributable to the increased oxo-philicity of V relative to Mo which serves to decrease oxygen mobility in the solid. This is observed in the *ex situ* XPS as V=O species.

In the *in situ* XPS experiments, the surface of the active carbide under the reaction is observed to be supplied with residual oxygen from the bulk, which is subsequently trapped and forms an oxidic layer. The evolving surface catalyses the transformation of propane with an initially high relative rate, which is observed to drop after a short time on stream as the formation rate of C_2H_4 and butanes increase (Figure 4.39)

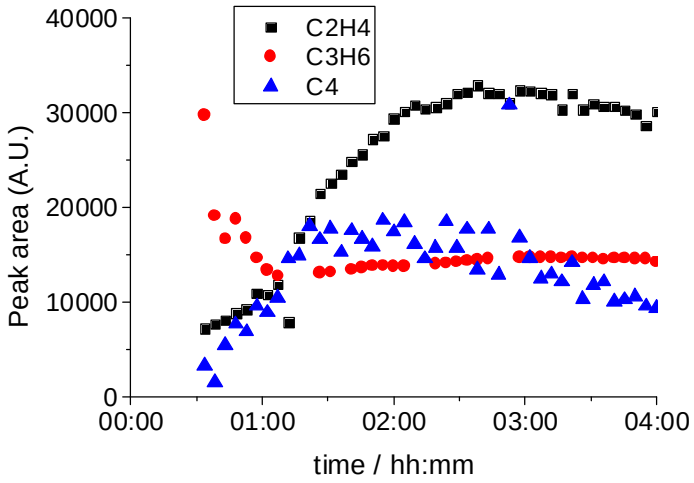

Figure 4.39: detail from *in situ* XPS experiment of C_3/H_2/He over Mo_2C (Figure 4.23).

This observation is consistent with the notion of a recombinative hydrocarbon formation mechanism as put forward by Tysoe *et al.*[13] The initial surface under these conditions is observed to catalyse the dehydrogenation of propane to propylene. As the surface slightly increases in oxygen concentration it becomes more active for the dissociative adsorption of propylene. During this time (t = 00:30 → 01:00), propylene titrates the catalyst surface forming bound methylidene and ethylidene species, which recombine with each other and with surface bound atomic H to form C1, C2, C3, and C4 species. As seen in Figure 4.24, the formation of C_2H_4 and C4 species do not precisely mirror each other. The formation of C_2H_4 is partly due to hydrogenolysis and partly due to the recombinative hydrocarbon formation mechanism. As can be seen in the valence band spectra, the strong mixing between

the Mo4d and O2p states begins to decline at ca. t = 04:00. At this point the activity for recombinative hydrocarbon formation begins to decrease.

4.5.3 TEM studies

From the TEM studies of pre- and post-mortem catalysts, it is clear that surface-restructuring and to a certain extent bulk-restructuring occurs upon heating in reaction conditions. It is well known that *fcc* MoC_{1-x} is a metastable phase that may be transformed on heating to Mo_2C.[57] However, in the case of $Mo(V)_2C$, we see that the reverse is also true in this case and that the action of propane on the carbide induces a structural rearrangement to form MoC_{1-x} sub-domains.

From the TEM imagery of the carbide materials there is evidence of carbon deposition and carbon rich areas, but there is no suggestion of large-scale elemental segregation between Mo and V. The post-catalytic materials are distinctly more heterogeneous compared with the freshly prepared carbides and the microstructure is observed in some cases to be densely packed, while in other areas there is visible mesoporosity. The local distribution of carbon is also observed to be non-uniform but is difficult to quantify exactly due to signal interference.

In the case of the post-TPR oxides the materials are even less ordered. Due to the use of propane as a carburising agent, the structure is irregularly bloated with carbon-rich areas and the material exhibits an array of microstructural characteristics.

4.6 Conclusions

Using Raman microscopy, adventitious carbon was observed to form on the surface of the catalyst which selectively blocked sites that were active for the hydrogenolysis/cracking of propane to lighter molecules. The nature of the carbon species was dependent on the reaction conditions and was found to evoke a higher sp^2 character (less amorphous) with a co-oxidant feed (H_2O, CO_2).

From *ex situ* XPS of the freshly prepared carbides the oxy-carbidic nature of the surface layer is apparent and it is also observed for the V-containing materials that the surface layer is enriched with vanadium in the form of V=O. Results of *in situ* XPS experimentation reveal a strong dependency of the catalytic activity with the surface oxidation state of the carbide. Dehydrogenation of propane was observed to increase

with an increasing oxidation state, whereas formation of C2 and C4 products is favoured by an increased electron density at the Fermi edge. No formation of adventitious carbon was observed.

The comparison of pre- and post-mortem carbide catalysts shows considerable surface rearrangement and carbon deposition. Selected area electron diffraction (SAED) of the freshly prepared carbides is indicative of *hcp* β-Mo_2C with agglomerated crystallite morphology. After reaction, the catalysts are observed to be quite heterogeneous with regards to carbon deposition and structural rearrangement. The SAED reveals a mixture of *hcp* β-Mo_2C as well as the presence of *fcc* α-MoC_{1-x} however, the powder XRD shows only β-Mo_2C.

Post-mortem analysis of the oxide precursors after TPR in H_2/C_3H_8 shows primarily *fcc* α-MoC_{1-x} with extensive carbon deposition as both graphitic overlayers and carbon-rich carbidic phases.

4.7 References

[1] W. C. Wu, Z. L. Wu, C. H. Liang, P. L. Ying, Z. C. Feng, C. Li, Physical Chemistry Chemical Physics 2004, 6, 5603.

[2] T. P. St. Clair, S. T. Oyama, D. F. Cox, S. Otani, Y. Ishizawa, R.-L. Lo, K.-i. Fukui, Y. Iwasawa, Surface Science 1999, 426, 187.

[3] M. Sugihara, K. Ozawa, K. Edamoto, S. Otani, Solid State Communications 2001, 121, 1.

[4] K. Edamoto, M. Sugihara, K. Ozawa, S. Otani, Surface Science 2004, 561, 101.

[5] M. Kato, T. Sato, K. Ozawa, K. Edamoto, Y. Nakadai, S. Otani, Surface Science 2007, 601, 201.

[6] J. G. Chen, Chem. Rev. 1996, 96, 1477.

[7] J. C. Grossman, A. Mizel, M. Cote, M. L. Cohen, S. G. Louie, Physical Review B 1999, 60, 6343.

[8] D. G. Kelly, M. Salmeron, G. A. Somorjai, Surface Science 1986, 175, 465.

[9] M. Siaj, I. Temprano, N. Dubuc, P. H. McBreen, Journal of Organometallic Chemistry 2006, 691, 5497.

[10] M. Siaj, N. Dubuc, P. H. McBreen, The Journal of Physical Chemistry C 2009.

[11] Y. Chauvin, Angewandte Chemie-International Edition 2006, 45, 3740.

[12] J. L. Herisson, Y. Chauvin, Makromolekulare Chemie 1971, 141, 161.

[13] B. Bartlett, V. Shneerson, W. T. Tysoe, Catalysis Letters 1995, 32, 1.

[14] W. T. Tysoe, Langmuir 1996, 12, 78.

[15] E. Solymosi, R. Nemeth, L. Ovari, L. Egri, Journal of Catalysis 2000, 195, 316.

[16] F. Solymosi, R. Németh, A. Oszkó, J. J. S. E. Iglesia, T. H. Fleisch, in Studies in Surface Science and Catalysis, Vol. Volume 136, Elsevier, 2001, pp. 339.

[17] E. Torres-GarcÃ-a, G. RodrÃ-guez-Gattorno, J. A. Ascencio, L. O. AlemÃ¡n-VÃ¡zquez, J. L. Cano-DomÃ-nguez, A. MartÃ-nez-HernÃ¡ndez, P. Santiago-Jacinto, The Journal of Physical Chemistry B 2005, 109, 17518.

[18] G. Rodriguez-Gattorno, A. Martinez-Hernandez, L. O. Aleman-Vazquez, E. Torres-Garcia, Applied Catalysis a-General 2007, 321, 117.

[19] P. Delporte, F. Meunier, C. Phamhuu, P. Vennegues, M. J. Ledoux, J. Guille, Catalysis Today 1995, 23, 251.

[20] P. Delporte, C. PhamHuu, M. J. Ledoux, Applied Catalysis a-General 1997, 149, 151.

[21] P. DelGallo, F. Meunier, C. PhamHuu, C. Crouzet, M. J. Ledoux, Industrial & Engineering Chemistry Research 1997, 36, 4166.

[22] M. J. Ledoux, F. Meunier, B. Heinrich, C. Pham-Huu, M. E. Harlin, A. O. I. Krause, Applied Catalysis a-General 1999, 181, 157.

[23] M. E. Harlin, A. O. I. Krause, B. Heinrich, C. Pharm-Huu, M. J. Ledoux, Applied Catalysis a-General 1999, 185, 311.

[24] C. Bouchy, C. Pham-Huu, B. Heinrich, C. Chaumont, M. J. Ledoux, Journal of Catalysis 2000, 190, 92.

[25] F. Uchijima, T. Takagi, H. Itoh, T. Matsuda, N. Takahashi, Physical Chemistry Chemical Physics 2000, 2, 1077.

[26] T. Matsuda, Y. Hirata, S. Suga, H. Sakagami, N. Takahashi, Applied Catalysis a-General 2000, 193, 185.

[27] T. Ohno, Z. Li, N. Sakai, H. Sakagami, N. Takahashi, T. Matsuda, Applied Catalysis A: General 2010
In Press, Accepted Manuscript.
[28] R. Schlögl, A. Knop-Gericke, M. Hävecker, U. Wild, D. Frickel, T. Ressler, R. E. Jentoft, J. Wienold, G. Mestl, A. Blume, O. Timpe, Y. Uchida, Topics in Catalysis 2001, 15, 219.
[29] D. Wang, D. S. Su, R. Schlögl, Zeitschrift Fur Anorganische Und Allgemeine Chemie 2004, 630, 1007.
[30] J. B. Claridge, A. P. E. York, A. J. Brungs, C. Marquez-Alvarez, J. Sloan, S. C. Tsang, M. L. H. Green, Journal of Catalysis 1998, 180, 85.
[31] V. V. Nemoshkalenko, V. P. Krivitskii, A. P. Nesenjuk, L. I. Nikolajev, A. P. Shpak, Journal of Physics and Chemistry of Solids 1975, 36, 277.
[32] P. Mikušík, R. Nyholm, N. Mårtensson, Czechoslovak Journal of Physics 1981, 31, 1165.
[33] F. Werfel, E. Minni, Journal of Physics C-Solid State Physics 1983, 16, 6091.
[34] E. Minni, F. Werfel, Surface and Interface Analysis 1988, 12, 385.
[35] G. H. Smudde, P. C. Stair, Surface Science 1994, 317, 65.
[36] H. Höchst, P. Steiner, G. Reiter, S. Hüfner, Zeitschrift für Physik B Condensed Matter 1981, 42, 199.
[37] M. Shimoda, T. Hirata, K. Yagisawa, M. Okochi, A. Yoshikawa, Journal of Materials Science Letters 1989, 8, 1089.
[38] K. Oshikawa, M. Nagai, S. Omi, J. Phys. Chem. B 2001, 105, 9124.
[39] P. C. Stair, Langmuir 1991, 7, 2508.
[40] N. S. McIntyre, D. D. Johnston, L. L. Coatsworth, R. D. Davidson, J. R. Brown, Surface and Interface Analysis 1990, 15, 265.
[41] P. A. Spevack, N. S. Mcintyre, Journal of Physical Chemistry 1992, 96, 9029.
[42] P. A. Spevack, N. S. McIntyre, The Journal of Physical Chemistry 1993, 97, 11020.
[43] M. Xiang, D. Li, J. Zou, W. Li, Y. Sun, X. She, Journal of Natural Gas Chemistry 2010, 19, 151.
[44] V. Eyert, et al., Journal of Physics: Condensed Matter 2000, 12, 4923.
[45] A. Gulino, S. Parker, F. H. Jones, R. G. Egdell, Journal of the Chemical Society-Faraday Transactions 1996, 92, 2137.
[46] T. Schroeder, J. Zegenhagen, N. Magg, B. Immaraporn, H. J. Freund, Surface Science 2004, 552, 85.
[47] D. O. Scanlon, G. W. Watson, D. J. Payne, G. R. Atkinson, R. G. Egdell, D. S. L. Law, The Journal of Physical Chemistry C 2010, 114, 4636.
[48] A. Sadezky, H. Muckenhuber, H. Grothe, R. Niessner, U. Pöschl, Carbon 2005, 43, 1731.
[49] D. C. LaMont, A. J. Gilligan, A. R. S. Darujati, A. S. Chellappa, W. J. Thomson, Applied Catalysis a-General 2003, 255, 239.
[50] A. R. S. Darujati, D. C. LaMont, W. J. Thomson, Applied Catalysis a-General 2003, 253, 397.
[51] M. P. Seah, D. Briggs, Practical surface analysis by Auger and X-ray photoelectron spectroscopy, Wiley, Chichester, 1983.
[52] J. Chastain, J. F. Moulder, Handbook of X-ray photoelectron spectroscopy a reference book of standard spectra for identification and interpretation of XPS data, Physical Electronics, Eden Prairie, Minn., 1995.

[53] M. A. Haija, S. Guimond, Y. Romanyshyn, A. Uhl, H. Kuhlenbeck, T. K. Todorova, M. V. Ganduglia-Pirovano, J. Döbler, J. Sauer, H. J. Freund, Surface Science 2006, 600, 1497.
[54] R. Kapoor, S. T. Oyama, Journal of Solid State Chemistry 1995, 120, 320.
[55] G. M. Bancroft, B. D. Boyd, D. K. Creber, Inorganic Chemistry 1978, 17, 1008.
[56] M. Willinger, Diploma Thesis 2002.
[57] T. Xiao, A. P. E. York, K. S. Coleman, J. B. Claridge, J. Sloan, J. Charnock, M. L. H. Green, Journal of Materials Chemistry 2001, 11, 3094.

Chapter 5: Summary and Conclusions

5.1 Summary of achieved project goals

An outline of the core results of this project is as follows:

- Molybdenum carbide was chosen as the basis for a model system to represent the surface of a reduced oxide catalyst operating in industrial conditions
- A series of oxide precursors were synthesised as potential precursors for carbide materials
- The TPR-carburisation of these oxides was studied using *in situ* X-ray diffraction and characterised using N_2-sorption to determine the most suitable precursor materials
- A series of mixed Mo-V complex molybdate (*h*-$Mo_{1-x}V_xO_3$) was chosen as a precursor due to the tunable composition and the high resulting surface area of the carbides
- TPR-carburisation of the oxides was studied using *in situ* XRD, TPR-MS and TG-MS, and the oxide precursors and carbide products were characterised by elemental analysis, N_2-sorption, TGA-DSC, XRD, XPS, SEM-EDX and TEM
- The solid-state kinetics of the oxide carburisations were analysed by means of temperature-programmed experimentation combined with model-free kinetic analysis and master plot method
- Handling techniques, apparatus and materials were developed to scale the synthesis to multi-gram quantities such that all procedures were without contact to air
- Large-scale synthesis was optimised to produce activated materials of high quality for catalytic testing in a variety of reactions
- A catalytic test reactor (Taniwha) was designed and constructed for the testing of light alkane dehydrogenation and selective oxidation reactions
- The materials were tested for the activation of propane in varying atmospheres including $H_2/H_2O/CO_2$
- *In situ* characterisation of the materials was carried out at the ISISS beamline at BESSY and a rationalised approach to the data analysis was pursued
- A series of complementary temperature programmed reactions were carried

out to provide context to both the catalytic and *in situ* XPS experimentation and compare the influence of oxidation state on reactivity

- A systematic characterisation study of the post catalytic materials was performed in order to better understand the process of reduction/carburisation in systems of high carbon potential

5.2 The synthesis of Mo/V carbides

A series of bimetallic Mo/V carbides was synthesised by carbothermal reduction of corresponding *h*-(MoV)O_3 mixed metal oxide precursors. The oxides were synthesised by precipitation and the subsequent carbide phase development was monitored using *in situ* XRD and outgas analysis of the TPR-carburisation. The observed structural evolution is combined with analysis of the solid state kinetic data and the reduction mechanism is discussed.

Inclusion of vanadium is observed to retard the onset of reduction as well as strongly influencing the kinetics of oxide reduction. The reduction proceeds via a complex mechanism involving initial formation of a suboxide MoO_{3-x} which is subsequently reduced to MoO_2. Increasing the content of vanadium content retards the onset of the overall reduction as well as the onset of carburisation in the step $MoO_2 \rightarrow Mo_2C$. Importantly it was noted that the carburisation of the oxide materials did not initiate at the stoichiometric point MoO_2 but rather at $MoO_{\sim 1.33}$. This is a clear indication of either the existence of atomically reduced Mo^0 or alternatively a suboxide of Mo such as Mo^{II} or Mo^{III}. However, by XRD no crystallographic phases are observed which reflect species other than MoO_2 and Mo_2C. The formation of the substoichiometric oxide lies clearly at the boundary point between the two and is best described as XRD amorphous.

The carbides exhibit a trend in morphological growth with vanadium concentration from a particulate-agglomerate material towards a densely packed, nano-fibrous morphology.Transmission electron microscopy investigation of the fibrous material using selected area electron diffraction (SAED) reveals that the high aspect-ratio crystallites exhibit pseudomorphism, and in the case of the vanadium containing materials, it is observed that there is some preferential orientation of crystal grains. Characterisation of the materials by N_2 adsorption reveals an increasing mesoporosity

associated with the fibrous morphology, as well as an exceptionally high surface area (80–110m^2/g).

The synthesis was subsequently scaled up from the *in situ* XRD preparation using a specially adapted rotary furnace to perform the temperature-programmed reduction-carburisation. By adapting the heating rate, gas flow and pre-treatment conditions it was possible to produce carbide materials with comparable physical properties to those obtained from the small scale. As a result, it was possible to synthesise Mo_2C materials in multi-gram quantities (5–15 g) with BET surface areas ranging from 50–100 m^2/g, among the highest values reported in literature.

The kinetics of reduction for the precursor oxides were investigated yielding insight into the differences in mechanism between the oxide series. The observed TPR profiles were in agreement with the findings of Ressler and Lalik and suggested that the mobility of atomic oxygen in the lattice is affected by the back-exchange of oxygen between Mo^{VI} and Mo^{IV} and that increasing the temperature of reduction counter-intuitively leads to an increase in the apparent activation energy. The inclusion of vanadium as a dopant was observed to modify this mechanism considerably and it was noted that the onset of oxygen mobility, or reducibility, was retarded significantly. Furthermore the competitive back-exchange of oxygen was reduced resulting in a singular reduction mechanism which conformed to the Jander model of 3-dimensional diffusion for oxygen in the lattice. Finally the onset of reduction-carburisation for $Mo(V)O_x \rightarrow Mo(V)_2C$ is seen to be delayed. It is unclear if this is the result of structural inhibition or whether it is because of a more subtle electronic effect. However, it was observed that vanadium inclusion was correlated with a more uniform, evolved mesoporosity in the product carbide.

5.3 The reactivity of Mo/V carbides

In this chapter, mixed molybdenum-vanadium carbide catalysts are studied in the activation of propane. The catalysts are tested in a plug flow reactor under reducing conditions in order to maintain the phase composition and the influence of temperature, surface oxidation, vanadium content and surface carbon deposition are observed on the reaction network.

In the presence of H_2/C_3H_8, Mo/V carbides are shown to catalyse the dehydrogenation of propane to propylene with a selectivity which approaches 50%, as well as carrying out the hydrogenolysis of propane to CH_4 and C_2H_6 on apparently distinct catalytic sites. Addition of H_2O or CO_2 as an oxidant to the feed greatly increases the yield and selectivity of the dehydrogenation reaction (S > 90%), as well as introducing products from the dry/steam reforming of propane and reverse water-gas shift. A strongly favoured initial reaction pathway is via a hydrogenolysis-like mechanism. Upon closer inspection, this mechanism is observed to comprise two aspects, one of preferential methane formation and the other a surface recombination of alkyl fragments resulting in the formation of Fischer-Tropsch-like products (C2–C4). Depending upon the reaction temperature and surface oxidation state of the catalyst the recombinative mechanism played a role in product formation. Vanadium was observed to reduce the stability of the carbide to oxidation; in the case of O_2 to α-MoO_3, and in the case of H_2O and CO_2, to MoO_2. In the activation of propane, vanadium increases the apparent activation energy for dehydrogenation and for hydrogenolysis.

In a separate study into the reverse water-gas shift reaction, Mo_2C is found to be an efficient catalyst for the hydrogenation of CO_2 with high selectivity to CO (> 90%). The reaction went to equilibrium conversion even at very high space velocities over a range of temperatures (GHSV > 200000, 500°C < T < 700°C).

In the temperature programmed reaction of *h*-$Mo_{1-x}V_xO_3$ materials in H_2-C_3H_8 it was observed that the oxides were reduced to the *fcc* α-MoC_{1-x} carbide with evidence of carburisation occuring at much lower temperatures than observed for methane-hydrogen mixtures. In these cases, the effect of vanadium was similarly seen to retard the onset of reduction-carburisation but to a much lesser extent. Upon reduction the catalytic activity was observed to increase dramatically and the selectivity evolved with temperature mirroring the reduction state of the oxide.

Importantly from the results of this section we can see that the freshly prepared carbide surface is not selective for dehydrogenation reactions at high temperatures. However, with the addition of a small amount of oxygen derived from the reactant gases, or residual in the structure, the passivated surface is quite selective to propane dehydrogenation. The strongly oxophilic nature of the fresh carbide surface is

illustrated by the extremely fast rate observed for reverse water-gas-shift in which the oxygen of CO_2 is abstracted by the carbide surface and subsequently reduced to H_2O. As seen in the steam-moderated dehydrogenation of propane, the temperature at which the chemisorbed oxygen is reduced to form the carbide is a function of the temperature and chemical potential of the gas atmosphere. Below this critical point, oxygen is irreversibly chemisorbed to the carbide altering the surface potential.

5.4 Characterisation of Mo/V carbides

Using Raman microscopy, adventious carbon was observed to form on the surface of the catalyst which selectively blocked sites which were active for the hydrogenolysis/cracking of propane to lighter molecules. The nature of the carbon species was dependent upon the reaction conditions and was found to evoke a higher sp^2 character (less amorphous) with a co-oxidant feed (H_2O, CO_2).

From *ex situ* XPS of the freshly prepared carbides the oxy-carbidic nature of the surface layer is apparent and it is also observed for the V-containing materials that the surface layer is enriched with vanadium in the form of V=O. Results of *in situ* XPS experimentation reveal a strong dependency of the catalytic activity with the surface oxidation state of the carbide. Dehydrogenation of propane was observed to increase with an increasing oxidation state whereas formation of C2 and C4 products is favoured by an increased electron density at the Fermi edge. No formation of adventitious carbon was observed.

The comparison of carbide catalysts before and after reaction shows evidence of considerable surface rearrangement and carbon deposition. Selected area electron diffraction (SAED) of the freshly prepared carbides is indicative of *hcp* β-Mo_2C with agglomerated crystallite morphology. After reaction the catalysts are observed to be quite heterogeneous with regards to carbon deposition and structural rearrangement. The SAED reveals a mixture of *hcp* β-Mo_2C as well as the presence of *fcc* α-MoC_{1-x} however, the powder XRD shows only β-Mo_2C.

Post-mortem analysis of the oxide precursors after TPR in H_2/C_3H_8 using XRD and TEM shows primarily *fcc* α-MoC_{1-x} structured Mo/V carbide with extensive carbon deposition as both graphitic overlayers and carbon-rich carbidic phases. The carbide crystallites are in many cases elongated needle-like structures and show preferred

orientation, similar to that seen in the case of methane-carburisation. The dispersed nature of the crystallites within a matrix of graphitic carbon suggests interplay of carbon deposition and carburisation during the formation leading to a distinctive structure which is mesoporous in appearance. The observed voids in this structure are mosy likely carbon rich spaces which maintain the pore structure and prevent sintering of the particles.

5.5 Conclusions

From a variety of different methods and experiments I have tried to draw together a picture of reactivity for a broadly defined system of molybdenum-based oxides and carbides in reductive, carbonaceous atmospheres.

From the temperature programmed reduction-carburisation study it is clear that vanadium plays an important role in such oxide structures even in very low concentrations. The doped carbides were seen to have an exceptional morphology and surface area with the addition of only 3% V (metals basis). These qualitative findings are backed up the solid-state kinetic analysis which shows a strong influence of the vanadium dopant via modification of oxygen mobility in the lattice. This 'oxygen mobility' is evidenced by the higher observed activation energy of reduction-carburisation and is also observed in the V EEL spectra which shows that the vanadium is primarily present as a V=O like species. It can also be interpreted on an electronic basis; the conduction mechanism of MoO_2 relies upon a Peierls distortion of co-planar MoO_2 units. This mechanism not exceptional but it certainly seems likely that the presence of vanadium could inhibit such a regular distortion, reducing the free electron density. This reduced density of free electrons would prevent the early decomposition of CH_4, resulting in more distinct stepwise reduction and then carburisation.

These hypotheses are supported with respect to the temperature-programmed reaction of the oxide precursors in propane. It is observed that the V-containing materials are delayed in their reduction and subsequently are not as active for the hydrogenolysis of propane to CH_4. At this point we must admit that the understanding of the system is not complete because with respect to the catalytic dehydrogenation of propane, it was observed that vanadium doping increased the initial conversion of propane but

decreased selectivity to propylene. It was observed in this case that the precarburised Mo/V materials were more active to hydrogenolysis with increasing V content.

In soft-oxidative feeds (CO_2, H_2O) the carbide surface is oxidised, promoting the dehydrogenation reaction. Notably, Mo_2C is an excellent catalyst for the hydrogenation of CO_2 via reverse water-gas shift reaction. *In situ* XPS experiments correlate propane dehydrogenation activity with an oxycarbide surface modification and recombinative hydrocarbon formation products are observed in concert with clear changes in the valence band spectra. Post-mortem analyses of the catalysts by transmission electron microscopy reveal significant surface and bulk restructuring as well as the recrystallisation of metastable phases and inhomogeneous bloating of the structure by carbonaceous material.

Vanadium is proposed to exert a stabilising influence due to its strongly oxophilic nature, resulting in the formation of V=O moieties which kinetically hinder the mobility of oxygen and carbon through the oxide/carbide lattice. The resulting higher initial activity for propane activation is attributed to the increased activity of sites selective to hydrogenolysis. Hexagonal $(Mo/V)_2C$ is proposed to be a reasonable model for bronze-like multi-metal oxide catalysts in propane activation. This is because the dynamic recrystallisation of *hcp* Mo_2C to metastable *fcc* MoC_{1-x} under reaction conditions, and the interchangeability of the reactivities of these materials, renders an equivalence by which the surface structure is controlled principally by the chemical potential of the reaction atmosphere.

With respect to the multi-metallic oxide MoVTe system for the selective oxidation of propane to acrylic acid the following statements can be made:

1. The carburisation of Mo/V oxides under the influence of methane/hydrogen proceeds at a considerably higher temperature (570–600°C) than the operating temperature for selective oxidation (350–400°C).
2. However, when propane is used as a carbon source, the beginning of carburisation, as indicated by the observation of reformate CO, is at the considerably lower temperature of ~450°C. This temperature, although higher than the operational temperature of MoVTe, is not unimaginable in an exothermic reaction at high conversion.

3. The bulk is observed to persist under the conditions of steam or CO_2 and the reactivity observed is consistent with that observed over an oxycarbidic surface.
4. The high activity of carbide/oxycarbide surfaces towards steam reforming and reverse water-gas shift result in a high selectivity of CO with respect to CO_2. This pattern of reactivity is also observed in the $MoVTeO_x$ system and these processes provide a possible explanation for this preferential selectivity which is not easily explained by the current models.
5. In the selective oxidation of propane over $MoVTeO_x$ catalysts it is observed that the secondary oxygenate product is acetic acid, a C-2 compound. In addition to this, under some conditions maleic anhydride is observed in the reaction outlet. The formation of these C-2 and C-4 oxygenates is not discussed in the literature and it is difficult to understand their presence in the framework of the current understanding. In the reduced carbide/oxycarbide system, a similar distribution of C-2 and C-4 hydrocarbons is observed due to recombinative formation from alkyl/alkylidene fragments on the surface of the catalyst.
6. If we consider catalysis to be predominantly a surface phenomenon the implication is that only the uppermost layer of atoms participates in the reaction. As we go from methane → propane → propylene → acrylic acid the potential of carbon in the system increases greatly and considering a number other factors such as the surface adsorption it is conceivable that the formation of a surface carbide may take place at considerably lower temperatures than would otherwise be predicted.

The above considerations alone do not implicate carbidic or oxycarbidic species as contributing to the reactivity in selective oxidation catalysis but they do present an alternative mechanistic pathway whereby such byproducts can be rationalised. Although a great deal of work has been done to bring selective oxidation catalysis to the point at which it is at today there is still a large gap of understanding in our way to the rational design of catalysts for such processes.

Appendix A: Acknowledgements for permission to reprint published material

- Figure 1.2 is reprinted from *Journal of Catalysis*, Vol. 180, J.B. Claridge, A.P.E. York, A.J. Brungs, C. Marquez-Alvarez, J. Sloan, S.C. Tsang, and M.L.H. Green, *New catalysts for the conversion of methane to synthesis gas: Molybdenum and tungsten carbide*, pp. 92, Copyright (1998), with permission from Elsevier
- Figure 3.4 is reprinted from *Journal of Catalysis*, Vol. 165, F. Solymosi, J. Cserényi, A. Szöke, T. Bánsági, A. Oszkó, *Aromatization of Methane over Supported and Unsupported Mo-Based Catalysts*, pp. 155, Copyright (1997), with permission from Elsevier
- Figure 3.5 is reprinted from *Industrial & Engineering Chemistry Research*, Vol. 33, E. A. Blekkan, P. H. Cuong, M. J. Ledoux, J. Guille, *Isomerization of n-Heptane on an Oxygen-Modified MolybdenumCarbide Catalyst*, pp. 1663, Copyright (1994), with permission from the American Chemical Society
- Figures 3.6 & 4.1 are reprinted from *Journal of Organometallic Chemistry*, Vol. 691, M. Siaj, I. Temprano, N. Dubuc, P. H. McBreen, *Preparation and olefin-metathesis activity of cyclopentylidene-oxo initiator sites on a molybdenum carbide surface*, pp. 5501, Copyright (2006), with permission from Elsevier
- Figure 3.7 is reprinted from *Langmuir*, Vol. 14, G. F. Wu, B. Bartlett, W. T. Tysoe, *Surface and Catalytic Chemistry of Small Hydrocarbons on Oxidized Molybdenum*, pp. 1441, Copyright (1998), with permission from the American Chemical Society
- Figure 4.2 is reprinted from *Langmuir*, Vol. 14, G. F. Wu, B. Bartlett, W. T. Tysoe, *Surface and Catalytic Chemistry of Small Hydrocarbons on Oxidized Molybdenum*, pp. 1437, Copyright (1998), with permission from the American Chemical Society
- Figure 4.3 is reprinted from *Catalysis Today*, Vol. 23, P. Delporte, F. Meunier, C. Phamhuu, P. Vennegues, M. J. Ledoux, J. Guille, *Physical Characterization of Molybdenum Oxycarbide Catalyst - TEM, XRD and XPS*, pp. 261–262, Copyright (1995), with permission from Elsevier

- Figure 4.4 is reprinted from *Zeitschrift für Anorganische und Allgemeine Chemie*, Vol. 630, D. Wang, D. S. Su, R. Schlögl, *Electron Beam Induced Transformation of MoO_3 to MoO_2 and a New Phase MoO*, pp. 1009, Copyright (2004), with permission from John Wiley and Sons
- Figure 4.5 is reprinted from *Dalton Transactions*, Vol. 92, A. Gulino, S. Parker, F. H. Jones, R. G. Egdell, *Influence of metal-metal bonds on electron spectra of MoO_2 and WO_2*, pp. 2139, Copyright (1996), with permission from the Royal Society of Chemistry
- Figure 4.6 is reprinted from *The Journal of Physical Chemistry C*, Vol. 114, D. O. Scanlon, G. W. Watson, D. J. Payne, G. R. Atkinson, R. G. Egdell, D. S. L. Law, *Theoretical and Experimental Study of the Electronic Structures of MoO_3 and MoO_2*, pp. 4641, Copyright (2010), with permission from the American Chemical Society
- Figure 4.7 is reprinted from *Journal of Physics C — Solid State Physics*, Vol. 16, F. Werfel, E. Minni, *Photoemission-Study of the Electronic-Structure of Mo and Mo Oxides*, pp. 6093, Copyright (1983), with permission from the Institute of Physics
- Figure 4.8 is reprinted from *Carbon*, Vol. 43, A. Sadezky, H. Muckenhuber, H. Grothe, R. Niessner, U. Pöschl, *Raman microspectroscopy of soot and related carbonaceous materials: Spectral analysis and structural information*, pp. 1737, Copyright (2005), with permission from Elsevier
- Figure 4.16 is reprinted from *Practical Surface Analysis by Auger and X-ray Electron Spectroscopy*, ISBN 0-471-26279-x, M. P. Seah, D. Briggs, Figure 5.5, Copyright (1983), with permission from John Wiley and Sons

List of Figures

Chapter 1

Chapter 2

Chapter 3

Chapter 4